62 /3/2024

JOURNAL OF THEORETICAL AND APPLIED MECHANICS

WARSAW 2024, QUARTERLY, VOLUME 62, INDEX 365238, ISSN 1429-2955

POLISH SOCIETY OF THEORETICAL AND APPLIED MECHANICS ptmts

POLISH SOCIETY OF THEORETICAL AND APPLIED MECHANICS

JOURNAL OF THEORETICAL AND APPLIED MECHANICS

No. 3 • Vol. 62

Quarterly

WARSAW, July 2024

JOURNAL OF THEORETICAL AND APPLIED MECHANICS
(until 1997 Mechanika Teoretyczna i Stosowana, ISSN 0079-3701)

Beginning with Vol. 45, No. 1, 2007, *Journal of Theoretical and Applied Mechanics* (JTAM) has been selected for coverage in Thomson Reuters products and custom information services. Now it is indexed and abstracted in the following:

- **Science Citation Index Expanded** (also known as SciSearch®)
- **Journal Citation Reports/Science Edition**

* * * * *

Editorial Office

Al. Armii Ludowej 16, room 650; 00-637 Warsaw, Poland
phone (+48) 664 099 345, e-mail: biuro@ptmts.org.pl

www.jtam.pl

* * * * *

Rozwój kwartalnika naukowego *Journal of Theoretical and Applied Mechanics*, ISSN 1429-2955, jest dofinansowany ze środków Ministra Edukacji i Nauki przyznanych z pomocy *de minimis* w ramach programu „Rozwój czasopism naukowych", umowa RCN/SN/0056/2021/1. Niniejszy numer został sfinansowany przez ministerstwo w ramach projektu: Doskonała nauka – Wsparcie konferencji naukowych. V Polski Kongres Mechaniki-25 Międzynarodowa Konferencja Metod Komputerowych Mechaniki, umowa DNK/SN/548136/2022.

JOURNAL OF THEORETICAL AND APPLIED MECHANICS
62, 3, pp. 461-476, Warsaw 2024
https://doi.org/10.15632/jtam-pl/188882

AN APPROXIMATE ANALYTICAL SOLUTION OF A 4-DOF VARIABLE-LENGTH PENDULUM MODEL

Godiya Yakubu, Paweł Olejnik

Lodz University of Technology, Department of Automation, Biomechanics and Mechatronics, Łódź, Poland
e-mail: godiesluv59@gmail.com; pawel.olejnik@p.lodz.pl

In this work, we employ the multiple scale method to introduce a novel analytical solution for an extended four-degrees-of-freedom dynamical system modeled on a swinging Atwood machine. We provide a methodology for obtaining the asymptotic solution up to the second-order approximation for both the swinging and modified swinging Atwood machine, demonstrating its solvability through the multiple scale approach. Subsequently, we present a comparative analysis of time histories between numerical and analytical solutions. These analytical solutions are of particular significance in applied mechanics, given their practical applications in parametric dynamical models grounded in the pendulum concept.

Keywords: analytical solutions, asymptotic solutions, swinging Atwood machine, multiple scale method

1. Introduction

Analytical solutions find extensive applications across physics, engineering, and mathematics. Their versatility allows for simulating a wide range of systems, from elementary pendulums to intricate electromagnetic fields. Furthermore, these solutions prove invaluable in validating numerical methods, offering a reliable benchmark for precise comparison and assessment.

Drawing from the existing body of literature on variable-length pendulums (Yakubu *et al.*, 2022), it becomes apparent that the modeling and analysis of parametric dynamical models for such pendulums can be intricate and demanding. The applications of such pendulums in mechanical and mechatronic systems provide a compelling motivation for undertaking research in this area, and they have a strong presence in both theoretical and practical engineering applications.

The multiple scale approach is a widely utilized technique for finding analytical solutions of dynamical systems, as evidenced by various authors in the following references: Abady *et al.* (2022), Abohamer *et al.* (2023a,b), Awrejcewicz *et al.* (2022), Starosta *et al.* (2017), Manafian and Allahverdiyeva (2022). A recent publication by Prokopenya (2021) tackled the problem of finding solutions to the equations of motion of swinging Atwood machine, a system comprised of two equal masses that oscillate and are in a state of dynamic equilibrium. The author derived the system differential equations of motion and computed them in the form of a power series with a small parameter.

Obtaining an analytical solution for novel 4-degrees of freedom (4-DOF) modified swinging Atwood machine (SAM) holds immense significance. This is primarily due to its ability to provide fast, stable, and precise solutions that can be readily understood and explicitly expressed due to its parameter dependencies (Manafian and Allahverdiyeva, 2022; Seadawy and Manafian, 2018; Starosta *et al.*, 2017).

To explore the potentially intricate dynamics of a variable-length pendulum in a range of engineering and mechatronic systems, we introduce a novel 4-DOF variable-length pendulum model. This pendulum is analytically solved, and a comparative analysis is performed to identify

correlative features between analytical and numerical solutions, thus verifying the accuracy of the computational model. The primary objective of this analysis is to uncover the system internal structure by identifying all the existing resonances. The analytical solution presented allows for the resolution of resonance issues by making appropriate adjustments to the forcing term when the model is applied in engineering and mechatronic systems. This ensures that the pendulum operates optimally in various practical applications.

In this paper, we utilized the multiple scale method, which allowed us to derive an asymptotic solution up to the second-order approximation of the SAM. The objective was to gain insight into applying the same technique for analytically solving the novel modified SAM with 4-DOF. Accordingly, we applied the same multiple scale method and derived the analytical solution for the modified SAM.

Before delving into procedures for finding solutions, the main assumptions are presented in Section 1.1. This approach ensures that the reader has a clear understanding of the underlying assumptions that are used in developing the analytical solution. Furthermore, by establishing the key assumptions upfront, the subsequent steps in the solution-finding process are grounded in a well-defined set of criteria. Therefore, by clearly stating the main assumptions at the outset, we can ensure that the subsequent analysis is rigorous, transparent, and logically consistent.

1.1. Main assumptions

To approximate the solution to the differential equation, a series expansion based on powers of a small parameter is employed (Awrejcewicz *et al.*, 2022). Each term in the series represents a distinct time or length scale (Abohamer *et al.*, 2023b; Awrejcewicz *et al.*, 2022). In order to streamline the resulting equations, the higher-order terms associated with the small parameter are neglected.

The precision of a multiple scale solution relies on the small parameter size and the number of terms incorporated in the series expansion. Generally, a more accurate solution is achieved when more terms are added in the expansion (Awrejcewicz *et al.*, 2022; Nayfeh, 2005). However, it is important to acknowledge that despite the potential for increased accuracy with more terms, the complexity of the equations often requires limiting Taylor's series expansion to the inceptive terms only.

Considering the assumptions mentioned earlier, we have neglected the impact of frictional forces in the model equations. To make the system suitable for investigation, we transformed the equations of motion into a dimensionless form to make it solvable using multiple scales. In doing so, we introduced specific dimensionless terms. Furthermore, we offset the time-dependent variables $x(t)$ and $\dot{\phi}(t)$ in the SAM model, and $x_1(t)$ and $\dot{\phi}_1(t)$ in the modified SAM model by an independent variable designated by λ.

2. The swinging Atwood machine

The SAM is a classical mechanics concept that can aid in comprehending the variable-length pendulum. In this particular system, the pendulum body oscillates within a two-dimensional plane, displaying a diverse range of dynamic behavior while remaining disconnected from another mass known as the counterweight (Elmandouh, 2016; Prokopeny, 2017; Tufillaro, 1985). In the initial approach, the two bodies are linked by an unyielding weightless string suspended on two pulleys devoid of friction (Tufillaro, 1994), as demonstrated in Fig. 1a.

The behavior of the SAM can be described by employing concepts of circular motion, centripetal force, and energy conservation. The tension in the string creates the centripetal force which enables the pendulum, mass m, to move horizontally to follow a circular trajectory, and the counterweight of mass M to move vertically, solely influenced by the force of gravity only

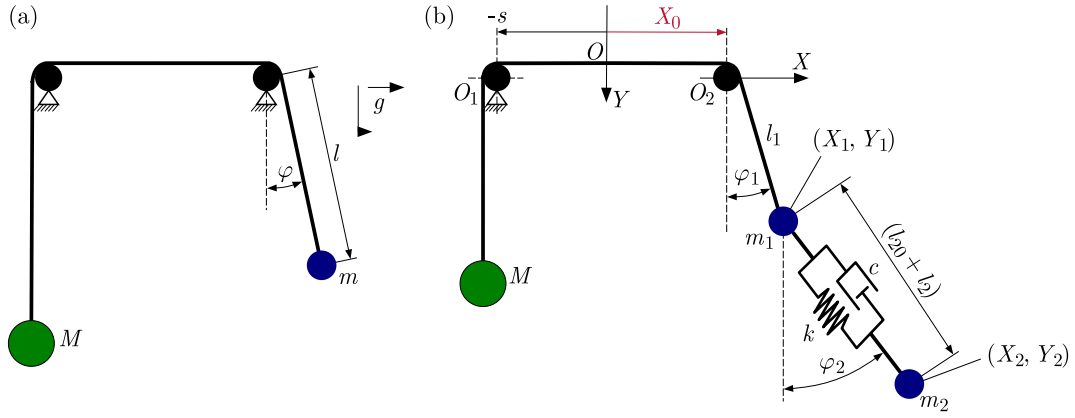

Fig. 1. (a) The initial physical model of the 2-DOF SAM: M – counterweight, m – pendulum body; (b) the proposed original Modified SAM

(Elmandouh, 2016; Tufillaro *et al.*, 1988). By analyzing motion of this system, various physical phenomena can be explored, such as conservation of angular momentum and the impact of centripetal force on object motion. Due to the pendulum reactive centrifugal force opposing the weight of the counterweight mass M, the dynamic response of the system can exhibit characteristics such as singularity or non-singularity, chaos or quasi-periodicity, boundedness or unboundedness, and even discontinuity (Casasayas *et al.*, 1990; Tufillaro, 1986; Nunes *et al.*, 1995; Pujol *et al.*, 2010; Yehia, 2006).

2.1. Equations of motion

The system being examined possesses two degrees of freedom. First, by utilizing the Lagrangian L, one can deduce the equation of motion (Elmandouh, 2016) for T and U, which respectively denote the kinetic and potential energy. The equations of motion for the SAM as described by Prokopenya (2021), Elmandouh (2016), Tufillaro *et al.* (1988), Tufillaro (1994), Casasayas *et al.* (1990), Nunes *et al.* (1995), Pujol *et al.* (2010), Yehia (2006), Tufillaro (1985) are presented below.

Upon considering the initial state-space variable, we observe that the two ordinary differential equations (ODEs) encompass the dynamics along the two independent degrees of freedom, i.e., $\varphi(t)$ and $l(t)$

$$\frac{\partial L}{\partial \varphi} = \frac{d}{dt}\Big(\frac{\partial L}{\partial \dot{\varphi}}\Big) \qquad \frac{\partial L}{\partial l} = \frac{d}{dt}\Big(\frac{\partial L}{\partial \dot{l}}\Big) \tag{2.1}$$

Based on the presented model illustrated in Fig. 1a, we express the following

$$T = \frac{1}{2}M\dot{l}^2(t) + \frac{1}{2}m[\dot{l}^2(t) + l^2(t)\dot{\varphi}^2(t)] \qquad U = Mgl(t) - mgl(t)\cos\varphi(t) \tag{2.2}$$

where M is the non-swinging mass, m – pendulum mass as it swings, $l(t)$ – distance from the pivot point to the center of the swinging pendulum body.

We determine the Lagrangian as $L = T - U$, i.e.

$$L = \frac{1}{2}M\dot{l}^2(t) + \frac{1}{2}m[\dot{l}^2(t) + l^2(t)\dot{\varphi}^2(t)] - Mgl(t) + mgl(t)\cos\varphi(t) \tag{2.3}$$

Given that the Hamiltonian $H = T + U$ is defined in terms of the canonical momenta p_l and p_φ, we obtain the following

$$H = \frac{p_l^2}{2(M+m)} + \frac{p_\varphi^2}{2ml^2(t)} + Mgl(t) - mgl\cos\varphi(t) \tag{2.4}$$

where: $p_l = (M+m)\dot{l}(t)$, $p_\varphi = ml^2(t)\dot{\varphi}(t)$.

The equations governing dynamical behavior in the state-space variables φ and l can be obtained based on the aforementioned assumptions

$$\begin{aligned} &l(t)\ddot{\varphi}(t) + 2\dot{l}(t)\dot{\varphi}(t) + g\sin\varphi(t) = 0 \\ &ml(t)\dot{\varphi}^2(t) - Mg + mg\cos\varphi(t) = (M+m)\ddot{l}(t) \end{aligned} \tag{2.5}$$

Taking into account the mass ratio $\mu_m = M/m$, then Eq. $(2.5)_2$ becomes

$$(\mu_m + 1)\ddot{l}(t) - l(t)\dot{\varphi}^2(t) + g[\mu_m - \cos\varphi(t)] = 0 \tag{2.6}$$

In order to find the solution of the systems using the MSM method, the following parameters are employed

$$\begin{aligned} &\omega_2^2 = \frac{g}{l} \qquad \omega_4^2 = \frac{\omega_2^2}{\omega_1^2} \qquad \sigma_1 = \frac{\lambda^3}{(\mu+1)\omega_1^2} + \frac{\mu\omega_4^2}{\mu+1} - \frac{\omega_4^2}{\mu+1} \\ &\sigma_2 = \frac{\lambda^2}{(\mu+1)\omega_1^2} \qquad \sigma_3 = \frac{\omega_4^2}{3(\mu+1)} \qquad \zeta_5 = \frac{1}{\lambda} \qquad \sigma_4 = \frac{2\lambda^2}{(\mu+1)\omega_1} \\ &\sigma_5 = \frac{2\lambda}{(\mu+1)\omega_1} \qquad \sigma_6 = -\frac{\lambda}{\mu+1} \qquad \sigma_7 = \frac{1}{\mu+1} \qquad \zeta_1 = \omega_4^2 \\ &\zeta_2 = \frac{\omega_4^2}{6} \qquad \zeta_3 = \frac{2}{\omega_1} \qquad \zeta_4 = \frac{2}{\lambda} \end{aligned} \tag{2.7}$$

Moreover, we employed the Taylor series to incorporate an additional approximation. In particular, we considered only the first term of Taylor's expansion, resulting in the following expression

$$\sin\phi(t) = \phi(t) - \frac{\phi^3(t)}{6} \qquad \cos\phi(t) = 1 - \frac{\phi^2(t)}{2} \tag{2.8}$$

By utilizing the parameters specified in Eqs. (2.7) and (2.8), Eqs. (2.5) are transformed into their final dimensionless form, which can be expressed as follows

$$\begin{aligned} &\sigma_1 + \sigma_2 x(\tau) + \sigma_3\phi(\tau)^2 + \sigma_4\dot{\phi}_1(\tau) + \sigma_5 x(\tau)\dot{\phi}(\tau) + \sigma_6\dot{\phi}(\tau)^2 + \sigma_7 x(\tau)\dot{\phi}(\tau)^2 + \ddot{x}(\tau) = 0 \\ &\zeta_1\phi(\tau) - \zeta_2\phi(\tau)^3 + \zeta_3\dot{x}(\tau) + \zeta_4\dot{\phi}(\tau)\dot{x}(\tau) + \ddot{\phi}(\tau) + \zeta_5 x(\tau)\ddot{\phi}(\tau) = 0 \end{aligned} \tag{2.9}$$

where τ represents the dimensionless time, $x(\tau)$ and $\phi(\tau)$ are dimensionless forms of $l(t)$ and $\varphi(t)$, respectively. ω_1 is first associated with $\dot{\phi}(\tau)$, then λ is introduced into both $x(\tau)$ and $\dot{\phi}(\tau)$ as a way to partially linearize the nonlinear terms ensuring that they appear in the equation where they should be. This effectively helps in decoupling the left-hand side of the approximate solution using the multiple scale method.

2.2. The multiple scale approach technique

In this Section, we apply the multiple scale approach to obtain asymptotic solutions for the equations mentioned in Eqs. (2.9). In accordance with the multiple scale technique, we examine the dynamics of the systems under consideration within a close range around their static equilibrium position (Abohamer *et al.*, 2023a; Awrejcewicz *et al.*, 2022). In order to characterize the amplitudes of oscillations within this region, we introduce a small parameter denoted as $0 < \varepsilon << 1$, which allows us to establish the following relationship

$$x(\tau) = \varepsilon\alpha(\tau : \varepsilon) \qquad \phi(\tau) = \varepsilon\gamma(\tau : \varepsilon) \tag{2.10}$$

This enabled us to consider the following approximations

$$\begin{aligned} &\sigma_1 = \varepsilon^2\widetilde{\sigma}_1 \qquad \sigma_4 = \varepsilon^1\widetilde{\sigma}_4 \qquad \sigma_7 = \varepsilon^{-1}\widetilde{\sigma}_7 \\ &\zeta_2 = \varepsilon^{-1}\widetilde{\zeta}_2 \qquad \zeta_3 = \varepsilon\widetilde{\zeta}_3 \qquad \zeta_5 = \varepsilon^0\widetilde{\zeta}_5 \end{aligned} \tag{2.11}$$

where ε is a parameter used for bookkeeping, having no impact on the computation and not appearing in the final approximate solution. Its purpose is to ensure that all other terms from the original equations are included in the solution process. We assume that ε is small enough to avoid computational errors.

In accordance with the multiple scale approach, the time-dependent variable $x(\tau)$, and $\phi(\tau)$ can be considered as a power series of ε

$$x(\tau)=\sum_{k=1}^{2}\varepsilon^k x_{,k}(\tau_0,\tau_1)+O(\varepsilon^k) \qquad \phi(\tau)=\sum_{k=1}^{2}\varepsilon^k \phi_{,k}(\tau_0,\tau_1)+O(\varepsilon^k) \tag{2.12}$$

where $\tau_n=\varepsilon^n\tau(n=0,1)$ with τ_0 being the fastest and τ_1 being the slowest.

To convert the derivatives with respect to τ to the new time scales τ_n, the following operators are employed

$$\frac{d}{d\tau}=\frac{\partial}{\partial\tau_0}+\varepsilon\frac{\partial}{\partial\tau_0} \qquad \frac{d^2}{d\tau^2}=\frac{\partial^2}{\partial\tau_0^2}+2\varepsilon\frac{\partial^2}{\partial\tau_0\partial\tau_1}+O(\varepsilon^2) \tag{2.13}$$

It is worth noting that these operators neglect terms of $O(\varepsilon^2)$ and higher orders. To obtain the partial differential equation (PDE) groups corresponding to different powers of ε, we substitute equations (2.10)-(2.13) into the dimensionless form of governing equations (2.9). This procedure leads to derivation of the preceding four linear PDEs. Based on the perturbation parameter ε, the splitting method is employed for obtaining these PDEs (Awrejcewicz *et al.*, 2022). These equations are the orders of ε and ε^2:

— first-order equations (coefficient 1 at ε^1)

$$\frac{\partial^2\alpha_1}{\partial\tau_0^2}+\sigma_2\alpha_1=0 \qquad \frac{\partial^2\gamma_1}{\partial\tau_0^2}+\zeta_1\gamma_1=0 \tag{2.14}$$

— second-order equations (coefficient 2 at ε^2)

$$\begin{aligned}&\widetilde{\sigma}_1+\sigma_2\alpha_2+\sigma_3\gamma_1^2+\widetilde{\sigma}_4\gamma_1\frac{\partial\gamma_1}{\partial\tau_0}+\sigma_5\alpha_1\gamma_1\frac{\partial\gamma_1}{\partial\tau_0}+\sigma_6\Big(\frac{\partial\gamma_1}{\partial\tau_0}\Big)^2\\&\quad+\widetilde{\sigma}_7\alpha_1\Big(\frac{\partial\gamma_1}{\partial\tau_0}\Big)^2+2\frac{\partial^2\alpha_1}{\partial\tau_0\partial\tau_1}+\frac{\partial^2\alpha_2}{\partial\tau_0^2}=0\\&\zeta_1\gamma_2-\widetilde{\zeta}_2\gamma_1^3+\widetilde{\zeta}_3\frac{\partial\alpha_1}{\partial\tau_0}+\zeta_4\frac{\partial\alpha_1}{\partial\tau_0}\frac{\partial\gamma_1}{\partial\tau_0}+2\frac{\partial^2\gamma_1}{\partial\tau_0\partial\tau_1}+\widetilde{\zeta}_5\alpha_1\frac{\partial^2\gamma_1}{\partial\tau_0^2}+\frac{\partial^2\gamma_2}{\partial\tau_0^2}=0\end{aligned} \tag{2.15}$$

where α_1 and γ_1 represent the solution of the first-order approximations of the time-dependent variables $x(\tau)$ and $\phi_1(\tau)$, respectively. Also, α_2 and γ_2 are the solution of the second-order approximations of the time-dependent variables $x(\tau)$ and $\phi_1(\tau)$. Meanwhile, α and γ will represent the respective general solutions of the time-dependent variables.

The solutions to Eqs. (2.15) are required to be solved in a specific order. Notably, the solutions obtained from the first group hold significant importance. Therefore, our initial emphasis lies in acquiring the general solutions to Eq. (2.14). The resulting established solutions are presented as follows

$$\alpha_1=\mathrm{e}^{\mathrm{i}\sigma_2\tau_0}B_1(\tau_1)+\mathrm{e}^{-\mathrm{i}\sigma_2\tau_0}\widetilde{B}_1(\tau_1) \qquad \gamma_1=\mathrm{e}^{\mathrm{i}\zeta_1\tau_0}B_3(\tau_1)+\mathrm{e}^{-\mathrm{i}\zeta_1\tau_0}\widetilde{B}_3(\tau_1) \tag{2.16}$$

Consequently, by substituting solutions (2.16) into the second group of PDEs (2.15), we obtain the following second-order solutions with B_i and $\widetilde{B}_i$ being τ_1 dependent, where $i = 1, 2$

$$\begin{aligned}
\alpha_2 &= -\frac{-2\zeta_1^2\sigma_6 B_2(\tau_1)\widetilde{B}_2(\tau_1) - 2\sigma_3 B_2(\tau_1)\widetilde{B}_2(\tau_1) + \widetilde{\sigma}_1}{\sigma_2^2} + \frac{\mathrm{i}\sigma_5 B_1(\tau_1)B_2(\tau_1)\mathrm{e}^{\mathrm{i}\tau_0(\zeta_1+\sigma_2)}}{\zeta_1+2\sigma_2} \\
&\quad - \frac{\mathrm{e}^{2\mathrm{i}\zeta_1\tau_0}[\zeta_1^2\sigma_6 B_2(\tau_1)^2 - \sigma_3 B_2(\tau_1)^2]}{(2\zeta_1-\sigma_2)(2\zeta_1+\sigma_2)} + \frac{\mathrm{i}\zeta_1\widetilde{\sigma}_4 B_2(\tau_1)\mathrm{e}^{\mathrm{i}\zeta_1\tau_0}}{(\zeta_1-\sigma_2)(\zeta_1+\sigma_2)} - \frac{\zeta_1\widetilde{\sigma}_7 B_1(\tau_1)B_2(\tau_1)^2\mathrm{e}^{\mathrm{i}\tau_0(2\zeta_1+\sigma_2)}}{4(\zeta_1+\sigma_2)} \\
&\quad + \frac{\mathrm{i}\sigma_5 B_2(\tau_1)\widetilde{B}_1(\tau_1)\mathrm{e}^{\mathrm{i}\tau_0(\zeta_1-\sigma_2)}}{\zeta_1-2\sigma_2} - \frac{\zeta_1\widetilde{\sigma}_7 B_2(\tau_1)^2\widetilde{B}_1(\tau_1)\mathrm{e}^{\mathrm{i}\tau_0(2\zeta_1-\sigma_2)}}{4(\zeta_1-\sigma_2)} + CT \qquad (2.17)\\
\gamma_2 &= -\frac{\widetilde{\zeta}_2 B_2(\tau_1)^3\mathrm{e}^{3\mathrm{i}\zeta_1\tau_0}}{8\zeta_1^2} - \frac{\mathrm{e}^{\mathrm{i}\tau_0(\zeta_1+\sigma_2)}[\zeta_1^2\widetilde{\zeta}_5 B_1(\tau_1)B_2(\tau_1) + \zeta_1\zeta_4\sigma_2 B_1(\tau_1)B_2(\tau_1)]}{\sigma_2(2\zeta_1+\sigma_2)} \\
&\quad + \frac{\mathrm{i}\sigma_2\widetilde{\zeta}_3 B_1(\tau_1)\mathrm{e}^{\mathrm{i}\sigma_2\tau_0}}{(\sigma_2-\zeta_1)(\zeta_1+\sigma_2)} + \frac{\mathrm{e}^{\mathrm{i}\tau_0(\zeta_1-\sigma_2)}[\zeta_1^2\widetilde{\zeta}_5 B_2(\tau_1)\widetilde{B}_1(\tau_1) - \zeta_1\zeta_4\sigma_2 B_2(\tau_1)\widetilde{B}_1(\tau_1)]}{\sigma_2(2\zeta_1-\sigma_2)} + CT
\end{aligned}$$

where CT represents the conjugates of the preceding terms.

2.3. Modulation equations

The modulation equations are a group of four first-order ODEs that describe the modulation of amplitudes and phases, since the procedures for solving them are complemented by initial conditions.

Secular terms in Eqs. (2.18) appear when the previous solutions are substituted into second--order Eqs (2.17). These terms act as conditions for solvability, which must be eliminated to obtain the modulation equations.

In order to eliminate the secular terms from the equations, we use a method that involves introducing new, unknown complex value functions that are defined in Eq. (2.19). These functions are then substituted into the secular terms. Canceling them effectively allows us to obtain the modulation equations. This, in turn, enables us to arrive at the final asymptotic solution. These secular terms in α_2 and γ_2 follow

$$\begin{aligned}
\alpha_{2,s} &= -2\zeta_1^2 B_1(\tau_1)B_2(\tau_1)\widetilde{\sigma}_7(\tau_1)\widetilde{B}_2(\tau_1) - 2\mathrm{i}\sigma_2\frac{\partial B_1(\tau_1)}{\partial\tau_1} \\
\gamma_{2,s} &= 3\widetilde{\zeta}_2 B_2(\tau_1)^2\widetilde{B}_2(\tau_1) - 2\mathrm{i}\zeta_1\frac{\partial B_2(\tau_1)}{\partial\tau_1}
\end{aligned} \qquad (2.18)$$

and

$$B_k = \frac{1}{2}a_k(\tau)\mathrm{e}^{\mathrm{i}\psi_k} \qquad \widetilde{B}_k = \frac{1}{2}a_k(\tau)\mathrm{e}^{-\mathrm{i}\psi_k} \qquad k = 1, 2 \qquad (2.19)$$

where the order ψ_j and a_j represent the phases and amplitude of the solutions α and γ, respectively, for $j = 1, 2$.

Once we removed the secular terms from α_2 and γ_2, we arrived at the ensuing modulation equations

$$\dot{a}_1(\tau) = 0 \qquad \dot{a}_2(\tau) = 0 \qquad \dot{\psi}_1(\tau) = \frac{\zeta_1^2 a_2(\tau)^2\sigma_7}{4\sigma_2} \qquad \dot{\psi}_2(\tau) = -\frac{3a_2(\tau)^2\zeta_2}{8\zeta_1} \qquad (2.20)$$

Once we reconstituted the modulation equations for nonresonant cases and took into account established equations (2.20), we obtained the final asymptotic solution up to the second-order

approximations, with a_i and ψ_i being dependent on τ_1 for $i = 1, 2$. The resulting solution is as follows

$$\begin{aligned}
\alpha = {} & \frac{a_2(\tau)^2(\zeta 1^2\sigma_6 + \sigma_3) - 2\sigma_1}{2\sigma_2^2} + a_1(\tau)\cos(\sigma_2\tau + \psi_1(\tau)) \\
& + \frac{a_2(\tau)^2(\sigma_3 - \zeta_1^2\sigma_6)\cos[2(\zeta_1\tau + \psi_2(\tau))]}{8\zeta_1^2 - 2\sigma_2^2} - \frac{\sigma_5 a_1(\tau)a_2(\tau)\sin[\tau(\zeta_1 + \sigma_2) + \psi_1(\tau) + \psi_2(\tau)]}{2(\zeta_1 + 2\sigma_2)} \\
& - \frac{\sigma_5 a_1(\tau)a_2(\tau)\sin[\tau(\zeta_1 - \sigma_2) - \psi_1(\tau) + \psi_2(\tau)]}{2(\zeta_1 - 2\sigma_2)} \\
& - \frac{\zeta_1\sigma_7 a_1(\tau)a_2(\tau)^2\cos[\tau(2\zeta_1 + \sigma_2) + \psi_1(\tau) + 2\psi_2(\tau)]}{16(\zeta_1 + \sigma_2)} - \frac{\zeta_1\sigma_4 a_2(\tau)\sin(\zeta_1\tau + \psi_2(\tau))}{\zeta_1^2 - \sigma_2^2} \\
& - \frac{\zeta_1\sigma_7 a_1(\tau)a_2(\tau)^2\cos[\tau(2\zeta_1 - \sigma 2) - \psi_1(\tau) + 2\psi 2(\tau)]}{16(\zeta_1 - \sigma_2)} \\
\gamma = {} & a_2(\tau)\cos(\zeta_1\tau + \psi_2(\tau)) + \frac{\zeta_1 a_1(\tau)a_2(\tau)(\zeta_1\zeta_5 - \zeta_4\sigma_2)\cos[\tau(\zeta_1 - \sigma_2) - \psi_1(\tau) + \psi_2(\tau)]}{2\sigma_2(2\zeta_1 - \sigma_2)} \\
& - \frac{\zeta_1 a_1(\tau)a_2(\tau)(\zeta_1\zeta_5 + \zeta_4\sigma_2)\cos[\tau(\zeta_1 + \sigma_2) + \psi_1(\tau) + \psi_2(\tau)]}{2\sigma_2(2\zeta_1 + \sigma 2)} + \frac{\zeta_3\sigma_2 a_1(\tau)\sin(\sigma_2\tau\psi_1(\tau))}{\zeta_1^2 - \sigma_2^2} \\
& - \frac{\zeta_2 a_2(\tau)^3\cos[3(\zeta_1\tau + \psi_2(\tau))]}{32\zeta_1^2}
\end{aligned} \tag{2.21}$$

2.4. Comparison between analytical and numerical solutions using time histories

To compare the dimensionless form of equations of motion (2.9) with second-order asymptotic solution (2.21), we present a time history based on the data provided in Eqs. (2.22).

In Figs. 2a,b, we depict the time histories for two degrees of freedom of the dynamical system, namely, $x(\tau)$ and $\phi_1(\tau)$, respectively. It is noteworthy that both the analytical and numerical solutions demonstrate satisfactory accuracy of the obtained approximation. Hence, even a simplified model of the dynamical system can be efficiently solved analytically using the presented approach.

$$\begin{array}{llll}
\sigma_1 = 0.0025 & \sigma_2 = 1.01 & \sigma_3 = 0.06 & \sigma_4 = 0.014 \\
\sigma_5 = 0.06 & \sigma_6 = 0.01 & \sigma_7 = 0.05 & \zeta_1 = 1.0 \\
\zeta_2 = 0.1667 & \zeta_3 = 0.0005 & \zeta_4 = 0.01 & \zeta_5 = 0.005 \\
x(\tau) = 0.04 & \dot{x}(\tau) = 0 & \phi(\tau) = 0.01 & \dot{\phi}(\tau) = 0
\end{array} \tag{2.22}$$

The obtained solutions are then compared by plotting them in time history plots. The masses of pendulums and length of the string greatly influence the simulation results. Furthermore, these results can be utilized to gain more insights into energy transfers, tension in the string, and other critical characteristics of the system.

2.4.1. Compliance error

To ensure solution dependability and precision, time histories of compliance errors in the results are presented. This not only aids potential computation optimization but also contributes to advancing numerical methods. These histories, integrated with the results, enhance visualization of discrepancies in individual time intervals. Additionally, the Root Mean Square Error (RMSE) and Mean Absolute Error (MAE) are computed using $\sum_{n=1}^{N}[Num_i - Apr_i)^2]/n$ and $\sum_{n=1}^{N}[|Num_i - Apr_i|]/n$, respectively. Here, Num is the numerical solution, Apr is the approximate solution, and N is the number of observations. These metrics provide additional tools

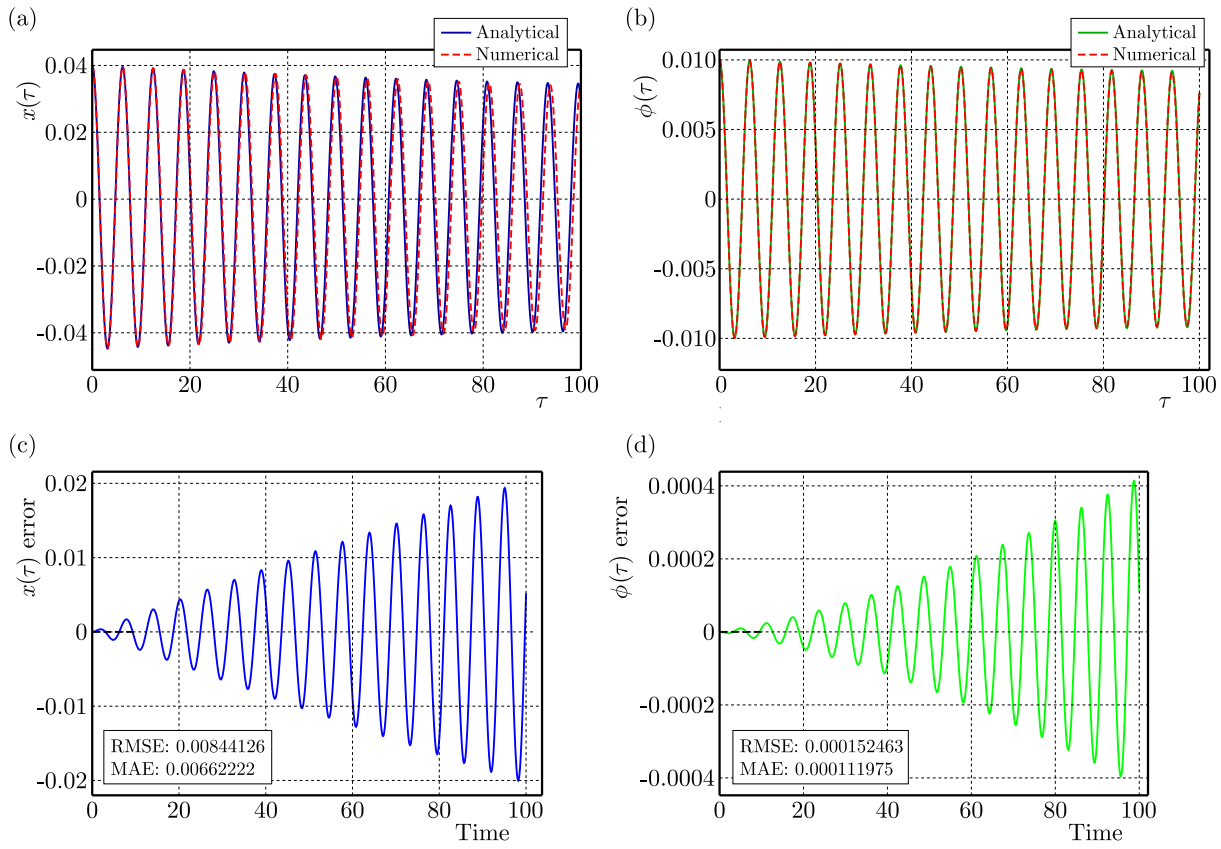

Fig. 2. (a) Comparison between the analytical (in blue, Eq. $(2.9)_1$) and numerical (in red, Eq. $(2.21)_1$) solution using the parameters given in Eqs. (2.22). (b) Comparison between analytical ($\phi(\tau)$ in green, Eq. $(2.9)_2$) and numerical (β in red, Eq. $(2.21)_2$) solution using the parameters presented in Eqs. (2.22). (c) Compliance error for $x(\tau)$ with RMSE = 0.00844126 and MAE = 0.00662222. (d) Compliance error for $\phi(\tau)$ with RMSE = 0.000152463 and MAE = 0.000111975

for a thorough assessment of solution accuracy, offering a more comprehensive understanding of overall performance.

Figures 2c and 2d depict the deviation between numerical and approximate solutions along the x-axis (representing time). The y-axis shows the compliance error at each point. Peaks or shifts in error plots signify notable deviations between solutions, while a declining trend suggests convergence of the numerical solution. Oscillations in the compliance errors indicate sensitivity to parameters and initial conditions. RMSE and MAE values are very small, affirming improved performance of the method and appropriateness of the dataset.

Moving forward to the next Section, we show a more advanced version of the variable-length pendulum with 4-DOF. The process used to obtain the solutions for this system closely mirrors the one employed earlier, encompassing all the fundamental assumptions and culminating in generating and comparing the results in time history plots.

3. The original modification of SAM

We introduce a novel and innovative modification to the SAM model based on the work presented in (Yakubu *et al.*, 2022). This modified version demonstrates potentially richer dynamics, as depicted in Fig. 1b. To achieve this, we have added a second spring pendulum to the non-swinging mass M, on the opposite end. The two pendulums, with masses of m_1 and m_2, are connected by a suspension configuration with a stiffness k and a damper c. Point 0_2 is free to rotate and

subject to oscillation in the (X, Y) plane, while point 0_1 is fixed, allowing for the variability of length l_1 and the double pendulum configurations. The distance of l_20 is measured between the two pendulums, and l_2 denotes the extension caused by the spring between them. The original Modified SAM model can be applied to various scenarios, including wave variability, suspension systems, elastic robotic links, and load-lifting equipment such as cranes. $X_0 = f_0 \sin(\omega t + \theta)$ is a time function that represents the periodic kinematic excitation. The displacement is measured from the origin of the coordinate system O specifically in the direction of the x-axis. Here, f_0 is the excitation force, ω and θ represent the angular frequency and phase shift of the excitation, respectively, while s denotes the distance in the X direction from the point O to the fixed support point O_1.

3.1. Equations of motion

The equation of motion for the 4-DOF MSAM model is derived in (Yakubu *et al.*, 2022) using Newton's second law and the Lagrangian mechanics. The system equations of motion, when friction in pulley bearing is neglected, are

$$
\begin{aligned}
\ddot{l}_1 &= \frac{1}{m_1 + M}[T_2 \cos(\varphi_2 - \varphi_1) - (M + m_1 \sin\varphi_1)\ddot{X}_0 + m_1(l_1\dot{\varphi}_1^2 + g\cos\varphi_1) - Mg] \\
\ddot{l}_2 &= \frac{1}{2m_1m_2(m_1+M)}\Big(\{Mm_1T_2[\cos(2(\varphi_2-\varphi_1))] - 1\}Mm_1m_2\{\ddot{X}_0[2\cos(\varphi_2-\varphi_1) \\
&\quad + \sin(\varphi_2 - 2\varphi_1) - \sin\varphi_2] + g\} + 2m_1m_2[Ml_1\dot{\varphi}_1^2\cos(\varphi_2-\varphi_1) + (m_1+M)(l_1+l_{20})\dot{\varphi}_2^2] \\
&\quad - 2m_1T_2(m_1+m_2+M)\Big) \\
\ddot{\varphi}_1 &= \frac{T_2\sin(\varphi_2-\varphi_1) - m_1(2\dot{l}_1\dot{\varphi}_1 + \ddot{X}_0\cos\varphi_1 + g\sin\varphi_1)}{m_1l_1} \\
\ddot{\varphi}_2 &= \frac{1}{2(m_1^2 + Mm_1)(l_2+l_{20})}\Big\{[-MT_2\sin(2(\varphi_2-\varphi_1)) - Mgm_1(2\sin(\varphi_2-\varphi_1)) \\
&\quad + \sin(\varphi_2 - 2\varphi_1) + \sin\varphi_2] - Mm_1\ddot{X}_0[2\sin(\varphi_2-\varphi_1) - \cos(\varphi_2-2\varphi_1) + \cos\varphi_2] \\
&\quad - 2Mm_1l_1\dot{\varphi}_1^2\sin(\varphi_2-\varphi_1) - 4m_1\dot{l}_2\dot{\varphi}_2(m_1+M)\Big\}
\end{aligned}
\tag{3.1}
$$

where $T_2 = (c\dot{l}_2 + kl_2)$ and l_1, l_2, φ_1, φ_2 are t dependent variables.

Besides the assumptions outlined in Section 1.1, it is worth noting that the length l_1 exhibits motion opposite to that of l_2. Thus, to transform the system to a solvable form using the multiple scale method, we introduce dimensionless parameters presented in Appendix A.1 to adhere to the system investigational process.

$x_1(\tau)$, $x_2(\tau)$, $\phi_1(\tau)$ and $\phi_2(\tau)$ are dimensionless forms of $l_1(t)$, $l_2(t)$, $\varphi_1(t)$ and $\varphi_2(t)$, respectively. ω_1 is first associated with $\dot{\phi}_1(\tau)$, then λ is introduced into both $x_1(\tau)$ and $\dot{\phi}_1(\tau)$ for the same reasons stated in Section 2.1. Additionally, we employ the following approximation based on the Taylor series. In this approximation, we retain only the first term of Taylor's expansion, which can be expressed as follows

$$
\begin{aligned}
&\sin\phi_i(t) = \phi_i(t) - \frac{(\phi_i(t))^3}{6} \qquad \cos\phi_i = 1 - \frac{(\phi_i(t))^2}{2} \\
&\sin[2(\phi_{i+1}(t) - \phi_i(t))] = 2[\phi_{i+1}(t) - \phi_i(t)] \qquad \cos[2(\phi_{i+1}(t) - \phi_i(t))] = 1 \\
&\sin(\phi_{i+1}(t) - \phi_i(t)) = \phi_{i+1}(t) - \phi_i(t) \qquad \cos(\phi_{i+1}(t) - \phi_i(t)) = 1 \\
&\sin(\phi_{i+1}(t) - 2\phi_i(t)) = \phi_{i+1}(t) - 2\phi_i(t) \qquad \cos(\phi_{i+1}(t) - 2\phi_i(t)) = 1
\end{aligned}
\tag{3.2}
$$

Using the parameters in Appendix A.1, then the final dimensionless form of Eqs. (3.1) can be written as it is presented in Appendix A.2.

3.2. The multiple scale method

Our analysis concentrates on a small region near the system static equilibrium. To characterize the amplitudes of the oscillations within this region, we use a small parameter, denoted by $0 < \varepsilon << 1$

$$\begin{aligned} x_1(\tau) &= \varepsilon\alpha(\tau:\varepsilon) \qquad & x_2(\tau) &= \varepsilon\beta(\tau:\varepsilon) \\ \phi_1(\tau) &= \varepsilon\gamma(\tau:\varepsilon) \qquad & \phi_2(\tau) &= \varepsilon\Gamma(\tau:\varepsilon) \end{aligned} \tag{3.3}$$

By assuming a small area around the system static equilibrium position and the amplitude of oscillations within that area, as is consistent with the MSM, we can make the following approximations (Abohamer *et al.*, 2023a; Awrejcewicz *et al.*, 2022)

$$\begin{aligned} &b = \varepsilon\widetilde{b} \qquad F = \varepsilon\widetilde{F} \qquad c_1 = \varepsilon\widetilde{c}_1 \qquad G_2 = \varepsilon\widetilde{G}_2 \qquad \omega_0 = \varepsilon\widetilde{\omega}_0 \\ &\sigma_1 = \varepsilon^2\widetilde{\sigma}_1 \qquad \sigma_2 = \varepsilon^2\widetilde{\sigma}_2 \qquad \sigma_3 = \varepsilon\widetilde{\sigma}_3 \qquad \sigma_4 = \varepsilon^{-1}\widetilde{\sigma}_4 \qquad \sigma_6 = \varepsilon\widetilde{\sigma}_6 \\ &\sigma_9 = \varepsilon^{-1}\widetilde{\sigma}_9 \qquad A = \varepsilon\widetilde{A} \qquad b_2 = \varepsilon\widetilde{b}_2 \qquad b_3 = \varepsilon\widetilde{b}_3 \qquad G = \varepsilon^{-1}\widetilde{G} \\ &G_1 = \varepsilon^{-1}\widetilde{G}_1 \qquad \delta_2 = \varepsilon\widetilde{\delta}_2 \qquad \delta_3 = \varepsilon\widetilde{\delta}_3 \qquad \delta_5 = \varepsilon^{-1}\widetilde{\delta}_5 \qquad \delta_7 = \varepsilon\widetilde{\delta}_7 \\ &\delta_8 = \varepsilon\widetilde{\delta}_8 \qquad \delta_9 = \varepsilon\widetilde{\delta}_9 \qquad \delta_1 = \varepsilon^2\widetilde{\delta}_1 \qquad y = \varepsilon\widetilde{y} \qquad c_2 = \varepsilon\widetilde{c}_2 \\ &\zeta_3 = \varepsilon\widetilde{\zeta}_3 \qquad \zeta_2 = \varepsilon^{-1}\widetilde{\zeta}_2 \qquad h = \varepsilon^{-1}h \qquad \xi_1 = \varepsilon\widetilde{\xi}_1 \qquad \xi_6 = \varepsilon^{-1}\widetilde{\xi}_6 \\ &\xi_9 = \varepsilon^{-1}\widetilde{\xi}_9 \qquad \xi_{10} = \varepsilon^{-1}\widetilde{\xi}_{10} \qquad \xi_{11} = \varepsilon^{-2}\widetilde{\xi}_{11} \end{aligned} \tag{3.4}$$

In line with the methodology of the multiple scale approach, the time-dependent variables $x_1(\tau)$, $x_2(\tau)$, $\phi_1(\tau)$ and $\phi_2(\tau)$ can be considered as power series of ε

$$\begin{aligned} x_1(\tau) &= \sum_{k=1}^{2}\varepsilon^k x_{1,k}(\tau_0,\tau_1) + O(\varepsilon^k) \qquad & x_2(\tau) &= \sum_{k=1}^{2}\varepsilon^k x_{2,k}(\tau_0,\tau_1) + O(\varepsilon^k) \\ \phi_1(\tau) &= \sum_{k=1}^{2}\varepsilon^k \phi_{1,k}(\tau_0,\tau_1) + O(\varepsilon^k) \qquad & \phi_2(\tau) &= \sum_{k=1}^{2}\varepsilon^k \phi_{2,k}(\tau_0,\tau_1) + O(\varepsilon^k) \end{aligned} \tag{3.5}$$

It is worth emphasizing that these operators exclude terms of $O(\varepsilon^2)$ and higher orders. To derive the PDE groups associated with different powers of ε, we substitute Eqs. (3.3)-(3.5) into the dimensionless form of governing equations (A.2) in Appendix. This process involves a splitting method based on the perturbation parameter ε (Awrejcewicz *et al.*, 2022). Then, we derive the preceding 8 linear PDEs, each corresponding to a specific order of ε and ε^2:
— first-order equations (coefficient 1 at ε^1)

$$\frac{\partial^2\alpha_1}{\partial\tau_0^2} + w^2\alpha_1 = 0 \qquad \frac{\partial^2\beta_1}{\partial\tau_0^2} + \beta_1 = 0 \qquad \frac{\partial^2\gamma_1}{\partial\tau_0^2} + \omega_4^2\gamma_1 = 0 \qquad \frac{\partial^2\Gamma_1}{\partial\tau_0^2} + \xi_4^2\Gamma_1 = 0 \tag{3.6}$$

— second-order equations (coefficient 2 at ε^2) (refer to Appendix A.3) where α_1, β_1, γ_1, Γ_1 represent the solutions of the first-order approximations of the time-dependent variables $x_1(\tau)$, $x_2(\tau)$, $\phi_1(\tau)$, $\phi_2(\tau)$, respectively. Also, α_2, β_2, γ_2, Γ_2 are the solutions of the second-order approximations of the time-dependent variables $x_1(\tau)$, $x_2(\tau)$, $\phi_1(\tau)$, $\phi_2(\tau)$. Meanwhile, the general solutions of the time-dependent variables will be represented by α, β, γ, and Γ, respectively.

The solutions to obtained Eqs. (a.3) in Appendix, which can be solved in a particular sequence, emphasize the importance of the solutions in the first category. Thus, our primary focus is on obtaining the general solutions to Eqs. (3.6). The solutions obtained are as follows

$$\begin{aligned} \alpha_1 &= \mathrm{e}^{\mathrm{i}w\tau_0}B_1(\tau_1) + \mathrm{e}^{-\mathrm{i}w\tau_0}\widetilde{B}_1(\tau_1) \qquad & \beta_1 &= \mathrm{e}^{\mathrm{i}\tau_0}B_2(\tau_1) + \mathrm{e}^{-\mathrm{i}\tau_0}\widetilde{B}_2(\tau_1) \\ \gamma_1 &= \mathrm{e}^{\mathrm{i}\omega_4\tau_0}B_3(\tau_1) + \mathrm{e}^{-\mathrm{i}\omega_4\tau_0}\widetilde{B}_3(\tau_1) \qquad & \Gamma_1 &= \mathrm{e}^{\mathrm{i}\xi_4\tau_0}B_4(\tau_1) + \mathrm{e}^{-\mathrm{i}\xi_4\tau_0}\widetilde{B}_4(\tau_1) \end{aligned} \tag{3.7}$$

As a result, by substituting solutions (3.7) into the second group of PDEs (A.3) in Appendix, we derive the 2-order solutions as α_2, β_2, γ_2 and Γ_2, where B_i and $\widetilde{B}_i$ depend on τ_1, i takes values of $1, \ldots, 4$.

3.3. Modulation equations

The modulation equations constitute a set of eight first-order ODEs describing the amplitude and phase modulation. These equations necessitate initial conditions for the effective solution, which complement the solving procedures.

Secular terms, as observed in Eqs. (3.8), emerge when inserting the previously derived solutions into the second-order equations (refer to Eqs. (A.3) in Appendix). While serving as solvability conditions, these secular terms must be eliminated to obtain the modulation equations.

To eliminate the secular terms (see Eqs. (3.8)), we employ a method introducing new complex-valued functions, defined in Eqs. (3.9). Substituting these functions into the secular terms eliminates them, allowing derivation of the modulation equations. The final asymptotic solution is then obtained through these equations. The secular terms in α_2, β_2, γ_2 and Γ_2 are expressed as

$$\begin{aligned}
\alpha_{2,s} &= -2\omega_4^2\widetilde{\sigma}_9 B_1(\tau_1)B_3(\tau_1)\widetilde{B}_3(\tau_1) - 2\mathrm{i}w\frac{\partial B_1(\tau_1)}{\partial\tau_1} \\
\beta_{2,s} &= -\widetilde{b}_2 B_2(\tau_1) - \widetilde{b}_3 B_2(\tau_1) + 2\xi 4^2\widetilde{G}B_2(\tau_1)B_4(\tau_1)\widetilde{B}_4(\tau_1) - 2\mathrm{i}\frac{\partial B_2(\tau_1)}{\partial\tau_1} \\
&\quad + 2\xi 4^2\widetilde{G}_1 B_2(\tau_1)B_4(\tau_1)\widetilde{B}_4(\tau_1) - \mathrm{i}\widetilde{c}_1 B_2(\tau_1) - \mathrm{i}\widetilde{\delta}_7 B_2(\tau_1) - \mathrm{i}\widetilde{\delta}_8 B_2(\tau_1) \\
\gamma_{2,s} &= 3\widetilde{\zeta}_2 B_3(\tau_1)^2\widetilde{B}_3(\tau_1) - 2\mathrm{i}\omega_4\frac{\partial B_3(\tau_1)}{\partial\tau_1} \\
\Gamma_{2,s} &= -2\omega_4^2\widetilde{\xi}_{10}B_3(\tau_1)B_4(\tau_1)\widetilde{B}_3(\tau_1) - 3\widetilde{\xi}_6 B_4(\tau_1)^2\widetilde{B}_4(\tau_1) - 2\mathrm{i}\xi_4\frac{\partial B_4(\tau_1)}{\partial\tau_1}
\end{aligned} \tag{3.8}$$

and

$$B_j = \frac{1}{2}a_j(\tau)\mathrm{e}^{\mathrm{i}\psi_j(\tau_1)} \qquad \widetilde{B}_j = \frac{1}{2}a_j(\tau)\mathrm{e}^{-\mathrm{i}\psi_j(\tau_1)} \tag{3.9}$$

where ψ_j and a_j represent the phases and amplitude of the solutions α, β, γ, and Γ, respectively. For $j = 1, 2, 3, 4$.

After eliminating the secular terms from α_2, β_2, γ_2 and Γ_2, the modulation equations are obtained as

$$\begin{aligned}
&\dot{a}_1(\tau) = 0 \qquad \dot{a}_3(\tau) = 0 \qquad \dot{\psi}_1(\tau) = \frac{\omega_4^2 a_3(\tau)^2\sigma_9}{4w} \\
&\dot{\psi}_3(\tau) = -\frac{3a_3(\tau)^2\zeta_2}{8\omega_4} \qquad \dot{a}_2(\tau) = -\frac{1}{2}a_2(\tau)(c_1 + \delta_7 + \delta_8) \qquad \dot{a}_4(\tau) = 0 \\
&\dot{\psi}_2(\tau) = \frac{1}{4}[2b_2 + 2b_3 + \xi_4^2 a_4(\tau)^2(G + G_1)] \qquad \dot{\psi}_4(\tau) = \frac{2\omega_4^2 a_3(\tau)^2\xi_{10} + 3a_4(\tau)^2\xi_6}{8\xi_4}
\end{aligned} \tag{3.10}$$

After reconstituting the modulation equations for nonresonant cases and considering the equations established in Eq. (3.7), the final asymptotic solution up to the second-order approximation for α, β, γ and Γ, with a_i and ψ_i being dependent on τ_1, where $i = 1, 2, 3, 4$, have been obtained.

3.4. Comparison between analytical and numerical solutions using time histories

For comparison, the dimensionless form of the equations of motion (see Eqs. (A.1) and (A.2) in Appendix) and the asymptotic solution up to the second-order approximation are shown in

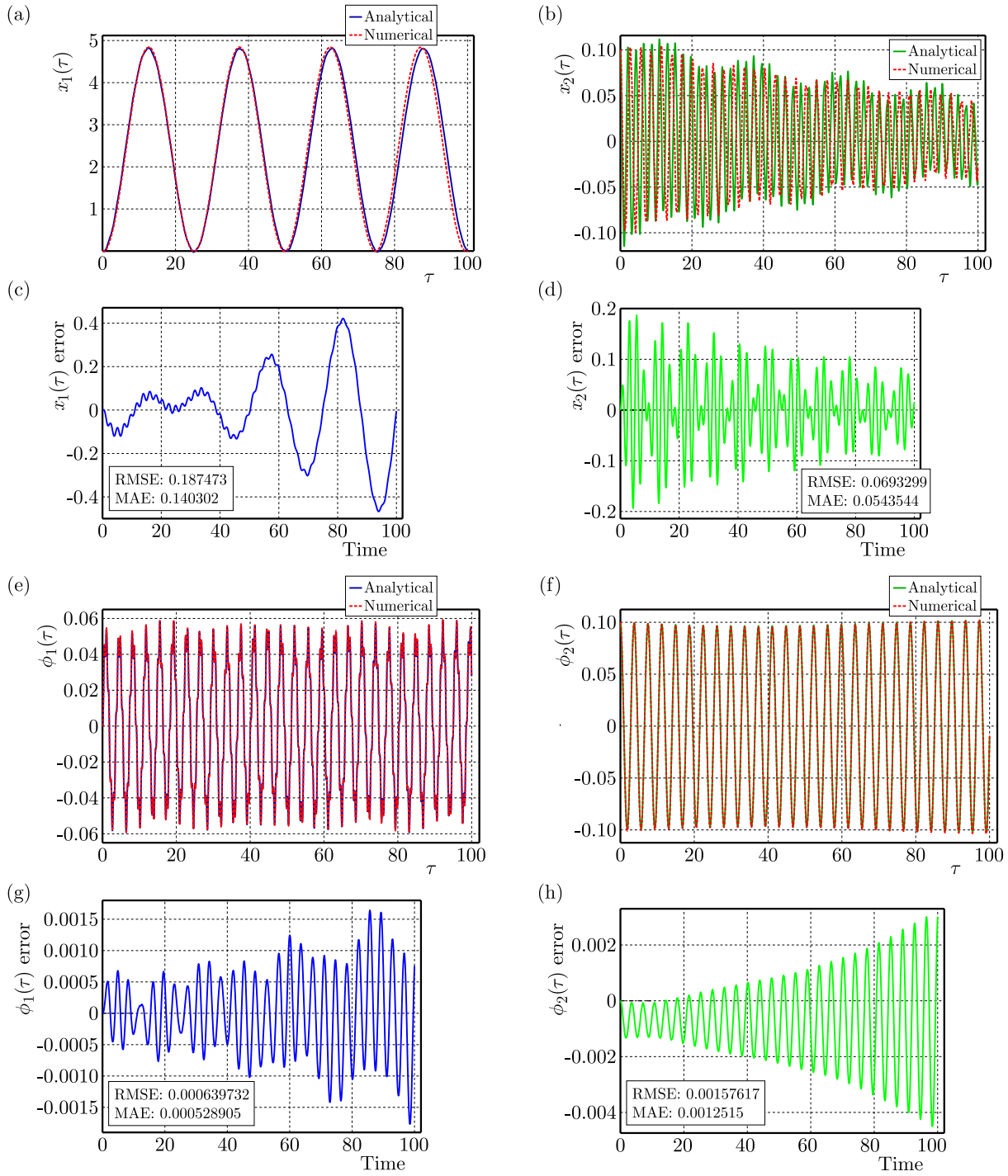

Fig. 3. (a) Comparison between analytical (in blue) and numerical (in red) solutions using the parameters presented in Eq. (3.11). (b) Comparison between analytical (in green) and numerical (in red) solutions using the parameters presented in Eq. (3.11). (c) Compliance error for $x_1(\tau)$ with RMSE = 0.187473 and MAE = 0.140302. (d) Compliance error for $x_2(\tau)$ with RMSE = 0.0693299 and MAE = 0.0543544. (e) Comparison between analytical (in blue) and numerical (in red) solutions using the parameters presented in Eq. (3.11). (f) Comparison between analytical (in green) and numerical (in red) solutions using the parameters presented in Eq. (3.11). (g) Compliance error for $\phi_1(\tau)$ with RMSE = 0.000639732 and MAE = 0.000528905. (h) Compliance error for $\phi_2(\tau)$ with RMSE = 0.00157617 and MAE = 0.0012515

the time history using the data in below. All initial conditions, except for $x_2(0) = \phi_2(0) = 0.1$, are set to zero

$$\begin{array}{lllll} A = 0.5 & c_1 = c_2 = \xi_1 = \xi_3 = \delta_3 = 0.01 & \sigma_5 = \zeta_3 = 0.0001 & \xi_4 = 1.61 & \\ \omega_5 = \xi_2 = 0.002 & \sigma_6 = \sigma_7 = \xi_{10} = \xi_{11} = 0.0002 & \sigma_8 = 0.0004 & & \\ \xi_{12} = 0.00004 & \xi_5 = 0.005 & \sigma_9 = \xi_{14} = \zeta_4 = 0.00005 & \delta_2 = 0.001 & \\ \delta_4 = 0.003 & \delta_5 = 0.00008 & \xi_7 = 0.0012 & h = \omega_0 = 1 & \\ \delta_8 = 0.008 & \delta_9 = 0.00009 & \delta_0 = 0.00002 & \xi_6 = 0.00008 & \\ \xi_9 = 0.000021 & \omega = 10 & \xi_{13} = 0.00015 & \sigma_1 = 0.15 & \\ \sigma_2 = 0.464 & b_2 = 2.11 & b_3 = 1.63 & G = 0.8 & G_1 = 0.1 \\ F = 0.81 & \omega_4 = 1.72 & \zeta_1 = 0.05 & \sigma_3 = 1.15 & w = 0.25 \end{array} \tag{3.11}$$

Figure 3a, 3b, 3e and 3f represent the time history for $x_1(\tau)$, $x_2(\tau)$, $\phi_1(\tau)$ and $\phi_2(\tau)$, respectively. As we can observe, both the analytical and numerical solutions indicate the accuracy of the system equation. Figure 3c, 3d, 3g and 3h depicts the deviation between the numerical and approximate solutions for $x_1(\tau)$, $x_2(\tau)$, $\phi_1(\tau)$ and $\phi_2(\tau)$, respectively. The compliance error for the modified SAM follows the same trend as that of the SAM. Therefore, it aligns with the presumption stated in Section 2.4.1. It becomes evident that the 4-DOF system can be effectively solved analytically by employing the multiple scale approach. However, it comes with a drawback in that it offers an approximate solution, and its accuracy depends on the number of time scales used. As a result, it becomes crucial to identify particular traits between the analytical and numerical solutions to compare them accurately and guarantee their correctness.

4. Conclusions

This publication focuses on the modeling and analysis challenges posed by variable-length pendulums, with a particular emphasis on the 4-DOF system. The attainment of an analytical solution not only validates the model but also contributes to improved efficiency, accuracy, and theoretical advancements. These analytical solutions serve as crucial tools for the investigation of dynamical systems, finding applications across diverse scientific and engineering fields. Furthermore, the study identifies promising directions for future research, urging exploration into steady-state solutions and conducting thorough stability analyses.

The publication highlights the practical applications of the analyzed models, revealing their potential in studying dynamic entities like robots and load-lifting devices. For instance, the study suggests examining a system comprising three inverted pendulums to represent different segments of the human body or analyzing the dynamics of load-lifting devices such as cranes. This approach extends the utility of the findings, offering insights into a broader applicability of the studied parametric dynamical models. Notably, the potential application of these insights in the field of energy harvesting is also underscored, adding a dimension of practical significance to the theoretical advancements presented in the publication.

A. Appendix

A.1. Dimensionless parameters for the modified SAM

$$A = \frac{l_{20}}{l} \qquad G = \frac{M}{(m_1 + M)} \qquad G_1 = \frac{m_1}{(m_1 + M)} \qquad \omega_2^2 = \frac{g}{l} \qquad \omega_3^2 = \frac{k}{m_1}$$

$$\omega_1^2=\frac{k}{m_1+M}\qquad \lambda^2=\frac{\omega_1^2\omega_1}{G_1}\qquad c_1=\frac{c}{(m_1+M)\omega_1}\qquad F=\frac{f_0\omega^2}{l\omega_1^2}$$
$$c_2=\frac{c}{\lambda\omega_1}\qquad b_1=\frac{M}{m_1}\qquad b_2=\frac{M}{m_2}\qquad b_3=\frac{m_1}{m_2}\qquad \omega_4^2=\frac{\omega_2^2}{\omega_1^2}$$
$$\omega_5^2=\frac{\omega_3^2}{\lambda\omega_1^2}\qquad \sigma_1=\omega^2\lambda+G\omega_4^2-\frac{\omega^2\omega_1^2\omega_4^2}{\lambda^2}\qquad \sigma_2=FG\qquad \sigma_3=\frac{F\omega^2\omega_1^2}{\lambda^2}$$
$$\sigma_4=\frac{F\omega^2\omega_1^2}{6\lambda^2}\qquad \sigma_5=\frac{\omega^2\omega_1^2\omega_4^2}{2\lambda^2}\qquad \sigma_6=\omega^2\omega_1\qquad \sigma_7=\frac{\omega^2\omega_1^2}{\lambda}$$
$$\sigma_8=\frac{2\omega^2\omega_1^2}{\lambda}\qquad \sigma_9=\frac{\omega^2\omega_1^2}{\lambda^2}\qquad \delta_0=G\lambda\qquad \delta_1=\frac{G\lambda^3}{\omega_1^2}+\frac{5G\omega_4^2}{2}$$
$$\delta_2=\frac{G\lambda^2}{\omega_1^2}\qquad \delta_3=FG\omega_0\qquad \delta_4=\frac{G\omega_4^2}{4}\qquad \delta_5=\frac{FG}{12}\qquad \delta_6=\frac{2G\lambda}{\omega_1}\tag{A.1}$$
$$\delta_7=b_2c_1\qquad \delta_8=b_3c_1\qquad \delta_9=\frac{2G\lambda^2}{\omega_1}\qquad \zeta_1=\frac{F}{3}+\frac{5G\omega_4^2}{2}$$
$$\zeta_2=\frac{\omega_4^2}{6}\qquad \zeta_3=\frac{2}{\omega_1}\qquad \zeta_4=\frac{1}{\lambda}\qquad \xi_1=\frac{G\lambda^3}{A\omega_1^2}+2G\omega_4^2$$
$$\xi_2=\frac{G\lambda^2}{A\omega_1^2}\qquad \xi_3=G\omega_5^2\qquad \xi_4^2=\frac{G\lambda^3}{A\omega_1^2}+G\omega_4^2\qquad \xi_5=\frac{hFG}{4}$$
$$\xi_6=\frac{G\omega_4^2}{12}\qquad h=1\qquad \xi_7=c_2G\qquad \xi_8=\frac{2G\lambda^2}{A\omega_1}\qquad xi_9=\frac{2G\lambda}{A\omega_1}$$
$$\xi_{10}=\frac{G\lambda}{A}\qquad \xi_{11}=\frac{G}{A}\qquad \xi_{12}=\frac{2G}{A}\qquad \xi_{13}=\frac{2G_1}{A}\qquad \xi_{14}=\frac{1}{A}$$

A.2. The final dimensionless form of the modified SAM equations of motion

$$\begin{aligned}
&\sigma_1-\sigma_2\sin(\overline{\omega}\tau)-w^2x_1(\tau)-\omega_0x_2(\tau)-\sigma_3\sin(\overline{\omega}\tau)\phi_1(\tau)+\sigma_4\sin(\overline{\omega}\tau)\phi_1^3(\tau)+\sigma_5\phi_2^2(\tau)\\
&\quad-c_1\dot{x}_2(\tau)-\sigma_6\phi_1(\tau)-\sigma_7\dot{\phi}_1^2(\tau)-\sigma_8x_1(\tau)\dot{\phi}_1(\tau)-\sigma_9x_1(\tau)\dot{\phi}_1^2(\tau)-\ddot{x}_1(\tau)=0\\
&\delta_1-\sigma_2\sin(\overline{\omega}\tau)+\delta_2x_1(\tau)-x_2(\tau)-b_2x_2(\tau)-b_2x_2(\tau)-b_3x_2(\tau)+\delta_3\sin(\overline{\omega}\tau)\phi_1(\tau)\\
&\quad-\delta_4\phi_2^2(\tau)-\delta_5\sin(\overline{\omega}\tau)\phi_2^3(\tau)-c_1\dot{x}_2(\tau)-\delta_7\dot{x}_2(\tau)-\delta_8\dot{x}_2(\tau)+\delta_9\dot{\phi}_1(\tau)\\
&\quad+\delta_6x_1(\tau)\dot{\phi}_1(\tau)+\delta_0\dot{\phi}_1^2(\tau)+Gx_1(\tau)\dot{\phi}_1^2(\tau)+\frac{1}{2}AG(\tau)\dot{\phi}_2^2(\tau)+AG_1(\tau)\dot{\phi}_2^2(\tau)\\
&\quad+G_1x_2(\tau)\dot{\phi}_2^2(\tau)-\ddot{x}_2(\tau)=0\\
&F\sin(\overline{\omega}\tau)-\omega_4^2\phi_1+\omega_5^2x_2(\tau)\phi_1(\tau)+\zeta_1\phi_1^3(\tau)-\zeta_1\sin(\overline{\omega}\tau)\phi_1^2(\tau)-\omega_5^2x_2(\tau)\phi_2(\tau)\\
&\quad-\zeta_3\dot{x}_1(\tau)-c_2\phi_1(\tau)\dot{x}_2(\tau)+c_2\phi_2(\tau)-\dot{x}_2(\tau)-2\zeta_4\dot{x}_1(\tau)\dot{\phi}_1(\tau)-\zeta_4x_1(\tau)\ddot{\phi}_1(\tau)\\
&\quad-\ddot{\phi}_1(\tau)=0\\
&\xi_1\phi_1(\tau)+h\sigma_2\sin(\overline{\omega}\tau)\phi_1(\tau)+\xi_2x_1(\tau)\phi_1(\tau)+\xi_3x_1(\tau)\phi_1(\tau)-\xi_4^2\phi_2(\tau)-h\sigma_2\sin(\overline{\omega}\tau)\phi_2(\tau)\\
&\quad-\xi_2x_1(\tau)\phi_2(\tau)-\xi_3x_2(\tau)\phi_2(\tau)-\xi_5\sin(\overline{\omega}\tau)\phi_2^2(\tau)-\xi_6\phi_2^3(\tau)+\xi_7\phi_1(\tau)\dot{x}_2(\tau)\\
&\quad-\xi_7\phi_2(\tau)\dot{x}_2(\tau)+\xi_8\phi_1(\tau)\dot{\phi}_2^2(\tau)+\xi_9x_1(\tau)\phi_1(\tau)\dot{\phi}_2^2(\tau)-\xi_8\phi_2(\tau)\dot{\phi}_1^2(\tau)\\
&\quad-\xi_9x_1(\tau)\phi_2(\tau)\dot{\phi}_1^2(\tau)+\xi_{10}\phi_1(\tau)\dot{\phi}_1^2(\tau)\xi_{11}x_1(\tau)\phi_1(\tau)\dot{\phi}_1^2(\tau)-\xi_{10}\phi_2(\tau)\dot{\phi}_1^2(\tau)\\
&\quad-\xi_{11}x_1(\tau)\phi_2(\tau)\dot{\phi}_1^2(\tau)+\xi_{12}\dot{x}_2(\tau)\dot{\phi}_2^2(\tau)+\xi_{13}\dot{x}_2(\tau)\dot{\phi}_2^2(\tau)-\xi_{14}x_2(\tau)\ddot{\phi}_2(\tau)-\ddot{\phi}_2(\tau)=0
\end{aligned}\tag{A.2}$$

A.3. Second-order equations of the modified SAM

$$\widetilde{\sigma}_1 - \widetilde{\sigma}_2\sin(\omega\tau_0) - w^2\alpha_1 - \omega_0\beta_1 - \widetilde{\sigma}_3\gamma_1\sin(\omega\tau_0) + \widetilde{\sigma}_4\gamma_1^3\sin(\omega\tau_0) + \widetilde{\sigma}_5\Gamma_1^2\sin(\omega\tau_0) - \widetilde{c}_1\frac{\partial\beta_1}{\partial\tau_0}$$
$$- \widetilde{\sigma}_6\frac{\partial\gamma_1}{\partial\tau_0} - \sigma_8\alpha_1\frac{\partial\gamma_1}{\partial\tau_0} - \sigma_7\Big(\frac{\partial\gamma_1}{\partial\tau_0}\Big)^2 - \widetilde{\sigma}_6\alpha_1\Big(\frac{\partial\gamma_1}{\partial\tau_0}\Big)^2 - 2\frac{\partial^2\alpha_1}{\partial\tau_0\partial\tau_1} - \frac{\partial^2\alpha_2}{\partial\tau_0^2} = 0$$
$$\widetilde{\delta}_1 - \widetilde{\delta}_2\sin(\omega\tau_0) + \widetilde{\delta}_2\alpha_1 - \widetilde{b}_2\beta_1 - \widetilde{b}_3\beta_1 - \beta_1 + \widetilde{\delta}_3\gamma_1\sin(\omega\tau_0) - \widetilde{\delta}_4\Gamma_1^2 - \widetilde{\delta}_5\Gamma_1^3\sin(\omega\tau_0) - \widetilde{c}_1\frac{\partial\beta_1}{\partial\tau_0}$$
$$- \widetilde{\delta}_7\frac{\partial\beta_1}{\partial\tau_0} - \widetilde{\delta}_8\frac{\partial\beta_1}{\partial\tau_0} + \widetilde{\delta}_9\frac{\partial\gamma_1}{\partial\tau_0} + \delta_6\alpha_1\frac{\partial\gamma_1}{\partial\tau_0} + \delta_0\Big(\frac{\partial\gamma_1}{\partial\tau_0}\Big)^2 + \widetilde{G}\alpha_1\Big(\frac{\partial\gamma_1}{\partial\tau_0}\Big)^2 + \frac{1}{2}\widetilde{A}\widetilde{G}\Big(\frac{\partial\Gamma_1}{\partial\tau_0}\Big)^2$$
$$+ \widetilde{A}\widetilde{G}_1\Big(\frac{\partial\Gamma_1}{\partial\tau_0}\Big)^2 + \widetilde{G}\beta_1\Big(\frac{\partial\Gamma_1}{\partial\tau_0}\Big)^2 + \widetilde{G}_1\beta_1\Big(\frac{\partial\Gamma_1}{\partial\tau_0}\Big)^2 - 2\frac{\partial^2\beta_1}{\partial\tau_0\partial\tau_1} - \frac{\partial^2\beta_2}{\partial\tau_0^2} = 0$$
$$\widetilde{F}\sin(\omega\tau_0) + \omega_5^2\beta_1\gamma_1 - \zeta_1\gamma_1^2\sin(\omega\tau_0) + \zeta_2\gamma_1^3 - \omega_4^2\gamma_2 - \omega_5^2\beta_1\Gamma_1 - \zeta_3\frac{\partial\alpha_1}{\partial\tau_0} - 2\zeta_4\frac{\partial\alpha_1}{\partial\tau_0}\frac{\partial\gamma_1}{\partial\tau_0} \quad \text{(A.3)}$$
$$- 2\frac{\partial^2\gamma_1}{\partial\tau_0\partial\tau_1} - \zeta_4\alpha_1\frac{\partial^2\gamma_1}{\partial\tau_0^2} - \frac{\partial^2\gamma_2}{\partial\tau_0^2} = 0$$
$$\widetilde{\xi}_1\gamma_1 + \widetilde{h}\widetilde{\sigma}_2\gamma_1\sin(\omega\tau_0) + \xi_2\alpha_1\gamma_1 + \xi_2\beta_1\gamma_1 - \widetilde{h}\widetilde{\sigma}_2\Gamma_1\sin(\omega\tau_0) - \xi_2\alpha_1\Gamma_1 - \xi_3\beta_1\Gamma_1$$
$$- \xi_5\Gamma_1^2\sin(\omega\tau_0) - \widetilde{\xi}_6\Gamma_1^3 - \xi_4^2\Gamma_2 + \xi_7\gamma_1\frac{\partial\beta_1}{\partial\tau_0} - \xi_7\Gamma_1\frac{\partial\beta_1}{\partial\tau_0} + \xi_8\gamma_1\frac{\partial\gamma_1}{\partial\tau_0} + \widetilde{\xi}_9\alpha_1\gamma_1\frac{\partial\gamma_1}{\partial\tau_0}$$
$$- \xi_8\Gamma_1\frac{\partial\gamma_1}{\partial\tau_0} - \widetilde{\xi}_9\alpha_1\Gamma_1\frac{\partial\gamma_1}{\partial\tau_0} + \widetilde{\xi}_{10}\gamma_1\Big(\frac{\partial\gamma_1}{\partial\tau_0}\Big)^2 + \widetilde{\xi}_{11}\alpha_1\gamma_1\Big(\frac{\partial\gamma_1}{\partial\tau_0}\Big)^2 - \widetilde{\xi}_{10}\Gamma_1\Big(\frac{\partial\gamma_1}{\partial\tau_0}\Big)^2$$
$$- \widetilde{\xi}_{11}\alpha_1\Gamma_1\Big(\frac{\partial\gamma_1}{\partial\tau_0}\Big)^2 + \xi_{12}\frac{\partial\beta_1}{\partial\tau_0}\frac{\partial\Gamma_1}{\partial\tau_0} + \xi_{13}\frac{\partial\beta_1}{\partial\tau_0}\frac{\partial\Gamma_1}{\partial\tau_0} - 2\frac{\partial\Gamma_1}{\partial\tau_0\partial\tau_1} - \xi_{14}\beta_1\frac{\partial^2\Gamma_1}{\partial\tau_0^2} - \frac{\partial^2\Gamma_2}{\partial\tau_0^2} = 0$$

Acknowledgments

This research was funded by the National Center of Science (Narodowe Centrum Nauki) grant number 2019/35/B/ST8/00980 (NCN Poland). The authors contributed equally to this work.

References

1. Abady I.M., Amer T.S., Gad H.M., Bek M.A., 2022, The asymptotic analysis and stability of 3DOF non-linear damped rigid body pendulum near resonance, *Ain Shams Engineering Journal*, **13**, 2, 101554

2. Abohamer M.K., Awrejcewicz J., Amer T.S., 2023a, Modeling and analysis of a piezoelectric transducer embedded in a nonlinear damped dynamical system, *Nonlinear Dynamics*, **31**, 1, 1-16

3. Abohamer M.K., Awrejcewicz J., Amer T.S., 2023b, Modeling of the vibration and stability of a dynamical system coupled with an energy harvesting device, *Alexandria Engineering Journal*, **63**, 377-397

4. Awrejcewicz J., Starosta R., Sypniewska-Kamińska G. (Edit.), 2022, *Asymptotic Multiple Scale Method in Time Domain: Multi-Degree-of-Freedom Stationary and Nonstationary Dynamics*, 1st ed., Boca Raton, United States: Taylor and Francis Group

5. Awrejcewicz J., Starosta R., Sypniewska-Kamińska G., 2014, Asymptotic analysis and limiting phase trajectories in the dynamics of spring pendulum, [In:] *Applied Non-Linear Dynamical Systems*, Awrejcewicz J. (Ed.), Springer Proceedings in Mathematics and Statistics, Springer, Cham, vol. 93

6. Casasayas J., Nunes A., Tufillaro N.B., 1990, Swinging Atwood's machine: integrability and dynamics, *Journal de Physique II*, **51**, 1693-1702

7. Elmandouh A.A., 2016, On the integrability of the motion of 3D-Swinging Atwood machine and related problems, *Physics Letters A*, **380**, 9, 989-991

8. Manafian J., Allahverdiyeva N., 2022, An analytical analysis to solve the fractional differential equations, *Advanced Mathematical Models and Applications*, **6**, 2, 128-161

9. Nayfeh A.H., 2005, Resolving controversies in the application of the method of multiple scales and the generalized method of averaging, *Nonlinear Dynamics*, **40**, 61-102

10. Nunes A., Casasayas J., Tufillaro N.B., 1995, Periodic orbits of the integrable swinging Atwood's machine, *American Journal of Physics*, **63**, 2, 121-126

11. Prokopenya A.N., 2017, Motion of a swinging Atwood's machine: simulation and analysis with Mathematica, *Mathematics in Computer Science*, **11**, 4, 417-425

12. Prokopenya A.N., 2021, Searching for equilibrium states of Atwood's machine with two oscillating bodies by means of computer algebra, *Programming and Computer Software*, **47**, 1, 43-49

13. Pujol O., Pérez J.P., Ramis J.P., Simó C., Simon S., Weil J.A., 2010, Swinging Atwood machine: experimental and numerical results, and a theoretical study, *Physica D: Nonlinear Phenomena*, **239**, 12, 1067-1081

14. Seadawy A.R., Manafian J., 2018, New soliton solution to the longitudinal wave equation in a magnetoelectro-elastic circular rod, *Results in Physics*, **8**, 1158-1167

15. Starosta R., Sypniewska-Kamińska G., Awrejcewicz J., 2017, Quantifying non-linear dynamics of mass-springs in series oscillators via asymptotic approach, *Mechanical Systems and Signal Processing*, **89**, 149-158

16. Tufillaro N.B., 1985, Motions of a swinging Atwood's machine, *Journal de Physique*, **46**, 1495-1500

17. Tufillaro N., 1986, Integrable motion of a swinging Atwood's machine, *American Journal of Physics*, **54**, 142-143

18. Tufillaro N.B., 1988, Teardrop and heart orbits of a swinging Atwood's machine, *American Journal of Physics*, **62**, 3, 231-233

19. Tufillaro N.B., Nunes A., Casasayas J., 1998, Unbounded orbits of a swinging Atwood's machine, *American Journal of Physics*, **56**, 1117-1120

20. Yakubu G., Olejnik P., Awrejcewicz J., 2022, On the modeling and simulation of variable-length pendulum systems: A review, *Archives of Computational Methods in Engineering*, **29**, 4, 2397-2415

21. Yehia H.M., 2006, On the integrability of the motion of a heavy particle on a tilted cone and the swinging Atwood's machine, *Mechanics Research Communications*, **33**, 5, 711-716

Manuscript received November 12, 2023; accepted for print January 29, 2024

JOURNAL OF THEORETICAL AND APPLIED MECHANICS
62, 3, pp. 477-490, Warsaw 2024
https://doi.org/10.15632/jtam-pl/189316

STUDY ON A CONCISE AND UNIFIED UNSTABLE CREEP MODEL FOR ROCKS

Yang Cheng
College of Architectural Engineering, Tongling University, Tongling, China
e-mail: chengytl@163.com

Liangliang Zhang
School of Civil Engineering and Architecture, Anhui University of Science and Technology, Huainan, China
e-mail: zllaust@163.com

The unsteady creep curve of rocks is antisymmetric to the dynamic surface subsidence curve of coal mining. Accordingly, a four-parameter unsteady creep model of rock was established using an analogous reasoning method from the perspective of phenomenology, and a simple method for determining the model parameters was proposed. The test curves of four different types of rocks were in good agreement with the theoretical curves of the model. In particular, the accelerated creep test curves with nonlinear characteristics were consistent with the theoretical curves of the model, verifying the rationality and accuracy of the model.

Keywords: rock mechanics, creep model, antisymmetric, unsteady creep, damage

1. Introduction

The creep behavior of rocks is a key factor affecting the safety and long-term stability of a structure (Wei *et al.*, 2019). When the external load is less than the long-term strength of the rock, the creep that occurs in the rock is steady, which includes instantaneous strain, attenuation, and constant velocity creep stages. This type of creep can be described using classic creep models (the Burgers, Bingham, and Nishihara models) (Song *et al.*, 2023). Theoretical and practical engineering applications of these creep models have been well established. When the external load is greater than the long-term strength of the rock, unsteady creep occurs in the rock, which includes instantaneous strain, attenuation creep, constant-velocity creep, and accelerated creep stages (Jin *et al.*, 2024). The establishment of an unsteady creep model for rock is an important and difficult task in rock mechanics (Taheri *et al.*, 2020).

Existing creep models can be divided into the following categories: empirical creep model (Zhang *et al.*, 2013; Zivaljevic and Tomanovic, 2022), component combination creep model (Zhao *et al.*, 2019; Zhang *et al.*, 2011) and improved component combination creep model based on nonlinear rheology theory (Zhang and Wang, 2020; Yang *et al.*, 2014), creep damage theory (Yang *et al.*, 2015; Song and Li, 2022) and fractional order theory (Zhou *et al.*, 2011; Liu *et al.*, 2021). Empirical creep models establish mathematical expressions for strain and time through curve fitting based on existing creep test data. The creep equations of such models are simple in form, with high precision and few parameters. However, owing to the unclear physical meaning of parameters and the short creep test time compared with the actual creep process of rock mass, the creep characteristics of the rock reflected by this model are quite different from the actual rock mass; therefore, it is only suitable for describing the creep process of specific rocks under specific test conditions. However, it has rarely been applied to the study of creep characteristics in rock engineering. The component-combination creep model combines elastic, plastic, and viscous components through different forms of series and parallel connections to obtain a combination

model that can describe rock elasticity, viscosity, viscoelasticity, and viscoplasticity. The physical meaning of these model parameters is clear, and the creep equation can be derived easily. The component-combination creep model is more widely applicable than the empirical creep model because of its variable combination forms. However, because the model parameters of this type of creep model are constant, this model can only describe the steady creep of rock and cannot describe unsteady creep. Therefore, this model is not suitable for analyzing the actual creep failure in rock mass engineering (Discenza *et al.*, 2020).

The improved component-combination creep model reflects nonlinear characteristics of the accelerated creep process of rocks by concatenating nonlinear damage bodies based on the component-combination model or by replacing the nonlinear creep model parameters with the component-combination creep model parameters, thereby establishing a mechanical model that can describe the unsteady creep process of rocks. Compared with the empirical creep model and component combination creep model, this type of model has been greatly improved in theory and practice; however, it still has the following two shortcomings. (1) The creep equation is too complicated. In the process of constructing the unsteady rock creep model, four different equations are often used to describe the instantaneous strain stage, attenuated creep stage, constant velocity creep stage, and accelerated creep stage in segments (such as using elastic elements to describe the instantaneous strain, Kelvin bodies to describe the attenuated creep stage, viscous bodies to describe the constant-velocity creep stage, and time-dependent deteriorated viscoplastic bodies to describe the accelerated creep stage). Then, according to the superposition principle, these four equations are superimposed to establish a mechanical model that can describe the unsteady creep process of rocks. Although the physical meaning and function of each part of the improved creep model established by this method are clear, and the constitutive and creep equations are easy to deduce, the form of the final creep equation is too long and complicated because of the large number of functions, which is not conducive to numerical simulation analysis and practical engineering applications. In addition, the four equations are independent of each other and there is no unified equation to describe the unsteady creep process in rocks. (2) The creep model has several parameters. The improved creep model improves the accuracy of the model by introducing undetermined parameters, but at the same time, introducing new model parameters increases the difficulty of parameter determination. Moreover, owing to the complexity of the improved creep model, the creep equation contains many undetermined parameters, usually more than 7 (Yan *et al.*, 2020). Such many creep parameters are difficult to determine accurately based on limited test data. Therefore, although the improved component combination creep model can describe the unsteady creep process of an indoor rock test well, owing to the limitation of the number of parameters, it is difficult to effectively analyze the creep mechanical properties of actual engineering rock masses.

In summary, to facilitate finite element software programming and actual creep failure process analysis of rock mass, it is urgent to establish a mechanical model of rock creep with fewer parameters and a unified creep function, which should be able to describe instantaneous strain, attenuated creep, constant velocity creep, and accelerated creep characteristics of rock simultaneously. In view of this, this study establishes a rock unsteady creep model with four model parameters only by an analogy reasoning method from the perspective of phenomenology, and provides a method to determine the model parameters, which provides a reference for the study of rock creep characteristics.

2. Four-parameter unsteady creep model

Many on-site monitoring data and theoretical studies have shown that the subsidence process of a certain point of the surface caused by coal mining is composed of three parts: the initial subsidence stage, the rapid subsidence stage and the decay subsidence stage, and it is approxi-

mately an "S" shaped curve with time, as shown in the red curve in Fig. 1. While the typical unsteady creep curve of rock is approximately an inverse "S" curve, as shown by the blue curve in Fig. 1. Therefore, the dynamic surface subsidence curve exhibits an antisymmetric relationship with the unsteady creep curve. Therefore, the surface dynamic subsidence function is first determined, and then the inverse function of the surface dynamic subsidence function is obtained by considering $\varepsilon(t) = t$ as the symmetry axis, which can yield a unified functional form describing the unsteady creep process of rocks. According to the basic mathematical theory, the functions represented by the red and blue curves are inverse functions of each other. Therefore, if the surface dynamic subsidence function is determined and its inverse function is obtained, the unsteady creep function of the rock can be established.

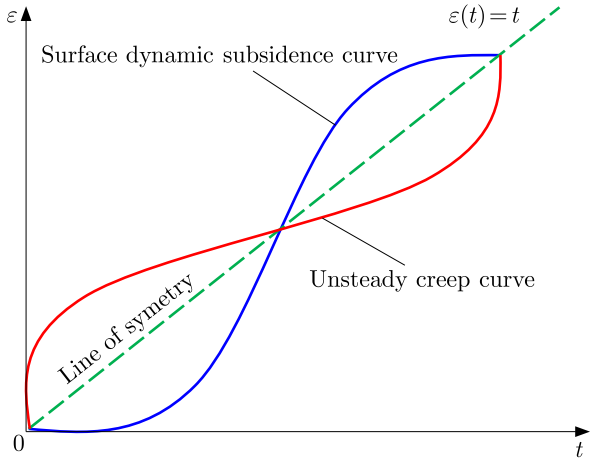

Fig. 1. Demonstration of the unsteady creep curve

The analysis indicates that the key to establishing a mechanical model that can reflect the unsteady creep process of rocks is to determine an "S" type function that can describe the surface dynamic subsidence law with time. Based on the classic Knothe time model (Hejmanowski, 2015), an improved Knothe time model was established by proposing new model assumptions (Zhang *et al.*, 2020) that could accurately describe the surface dynamic subsidence process caused by coal mining. The model function is expressed as follows

$$W(t) = W_0[1 - \exp(-Ct^n)] \tag{2.1}$$

where $W(t)$ is the surface dynamic subsidence, W_0 is the final surface subsidence, C is the time influence coefficient related to the mechanical properties of the overlying strata, t is time, and n is the model order.

The surface dynamic subsidence curves for different model orders n are shown in Fig. 2.

From Fig. 2, under different n conditions, the surface dynamic subsidence curves are all of "S" type, which is antisymmetric with the unsteady creep curves of rocks. Therefore, the unsteady creep models of rocks can be established by determining the inverse function of (2.1).

In Eq. (2.1), time t is the independent variable and $W(t)$ is the dependent variable; its inverse function expression is obtained as follows

$$t = \left[-\frac{1}{C}\ln\left(1 - \frac{W(t)}{W_0}\right)\right]^{\frac{1}{n}} \tag{2.2}$$

In Eq. (2.2), $W(t)$ is the independent variable and time t is the dependent variable. In the creep function, the independent variable is time t and the dependent variable is strain ε. Therefore, the function expression of the unsteady creep model of the rock can be obtained by analogous reasoning as follows

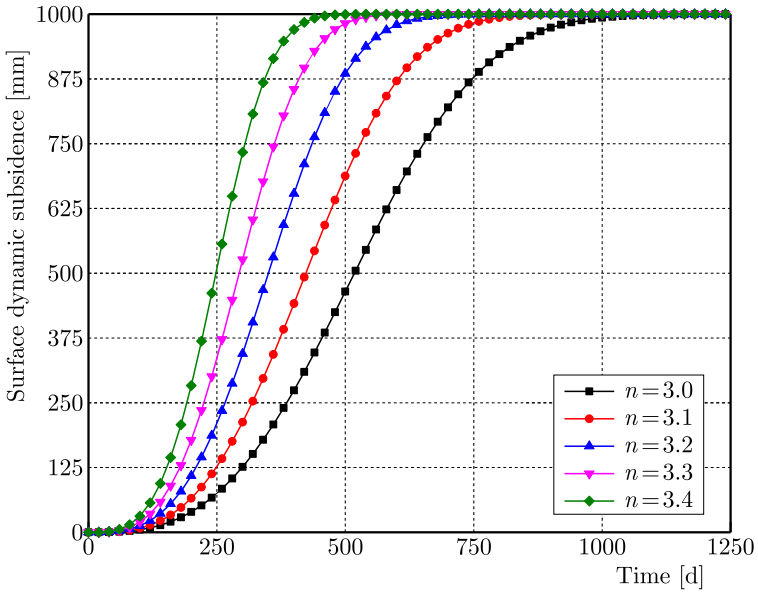

Fig. 2. Surface dynamic subsidence curves

$$\varepsilon = \left[-\frac{1}{C}\ln\left(1-\frac{t}{W_0}\right)\right]^{\frac{1}{n}} \tag{2.3}$$

In Eq. (2.1), W_0 is the final surface subsidence, which is the maximum value of the independent variable $W(t)$, then W_0 in Eq. (2.3), and is the maximum value at time t, that is, the time when the rock undergoes creep failure. Parameter C in Eq. (2.1) is the time influence coefficient related to mechanical properties of the overlying strata. This parameter is related to the physical and mechanical properties of the strata and time, and is expressed as viscosity in the rock creep model. Simultaneously, because the creep characteristics of the rock are closely related to the stress level σ, $\sigma/\eta = 1/C$ can be set, and Eq. (2.3) can be further expressed as

$$\varepsilon = \left[-\frac{\sigma}{\eta}\ln\left(1-\frac{t}{t_f}\right)\right]^{\frac{1}{n}} \tag{2.4}$$

where η is the viscosity coefficient of the rock and t_f is the time when the rock undergoes creep failure.

The creep model function established by Eq. (2.4) represents the variation in the creep strain with time and does not include the instantaneous strain stage in the unsteady creep process of rocks. Therefore, to reflect the entire creep process, it is necessary to add an instantaneous strain that is only related to the stress level but independent of time based on Eq. (2.4), which can be represented by an elastic element. Based on the above analysis, a four-parameter unsteady creep mechanics model is established, as shown in Fig. 3.

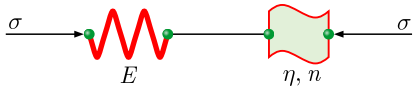

Fig. 3. Four-parameter unsteady rock creep model

According to the stress-strain relationship of the series and parallel connections, the unsteady creep equation of the rock is obtained as follows

$$\varepsilon = \frac{\sigma}{E} + \left[-\frac{\sigma}{\eta}\ln\left(1-\frac{t}{t_f}\right)\right]^{\frac{1}{n}} \tag{2.5}$$

where E is the elastic modulus of the elastic element.

We derived Eq. (2.5) and obtained the creep velocity and acceleration as follows

$$\begin{aligned}\varepsilon' &= \frac{1}{n}\frac{\sigma}{\eta}\frac{1}{t_f - t}\Big[-\frac{\sigma}{\eta}\ln\Big(1-\frac{t}{t_f}\Big)\Big]^{\frac{1-n}{n}} \\ \varepsilon'' &= \frac{1}{(t_f-t)^2}\left\{\Big(\frac{\sigma}{\eta}\Big)^2\frac{1}{n}\Big[\frac{1-n}{n} - \ln\Big(1-\frac{t}{t_f}\Big)\Big]\Big[-\frac{\sigma}{\eta}\ln\Big(1-\frac{t}{t_f}\Big)\Big]^{\frac{1-2n}{n}}\right\}\end{aligned} \tag{2.6}$$

According to Eq. (2.6), the creep rate is always greater than zero, indicating that the creep strain gradually increases with time, which is consistent with the actual situation. The critical moment for rock creep acceleration to be 0 is $\{1-\exp[(1/n)-1]\}t_f$, and when the creep time does not reach this critical value, the creep acceleration is always less than 0, indicating that the rock creep rate gradually decreases during this stage. When the creep time is between this critical value and the time when the rock undergoes creep failure, the creep acceleration is always greater than 0, indicating that the rock rate gradually increases with time at this stage. Therefore, the moment when the creep acceleration is 0 is not only the moment when the rock creep rate is minimum, but also the starting point of the accelerated creep stage. The above analysis indicates that the four parameter rock non-stationary creep model cannot strictly meet the creep deformation laws of the entire rock process, especially the creep rate characteristics during the constant velocity creep process. However, the constant velocity creep does not mean that the creep rate remains strictly unchanged, but the amplitude of change is relatively small (Wang *et al.*, 2018). Therefore, the four parameter rock unsteady creep model is reasonable and feasible for reflecting the complete creep process of rocks.

3. Model parameters determination

From Eq. (2.5), the creep equation contains only four model parameters E, η, t_f, n, which greatly reduces the number of parameters compared to other complex creep models and is beneficial for practical engineering applications. The creep curves of the rocks at different stress levels are shown in Fig. 4. At low stress levels, there was no accelerated creep stage in the creep curve; however, an accelerated creep process occurred at medium and high stress levels. Moreover, the creep failure time at a high stress was significantly shorter than that at a medium stress. Based on the characteristics of rock creep curves under different stress states, as shown in Fig. 4, a simple and feasible method for determining creep model parameters was proposed.

Determination of elastic modulus E

The instantaneous elastic strain ε_e is generated during rock loading and can be described by an elastic element. Based on the elastic constitutive relationship, the elastic modulus E is determined as

$$E = \frac{\sigma}{\varepsilon_e} \tag{3.1}$$

Determination of t_f

Without considering the influence of the rock occurrence environment, the creep failure time of rocks is only a function of stress; therefore, $t_f = f(\sigma)$. As shown in Fig. 4, the creep failure time decreases with an increase in the stress level. According to the Kachanov material creep damage rate theory (Kachanov, 1992), the time at which the rock undergoes creep failure can be determined using the following equation

$$\frac{dD}{dt} = k\Big(\frac{\sigma}{1-D}\Big)^{\upsilon} \tag{3.2}$$

where dD/dt is the damage rate, D is the damage variable, k, υ are rock material constants.

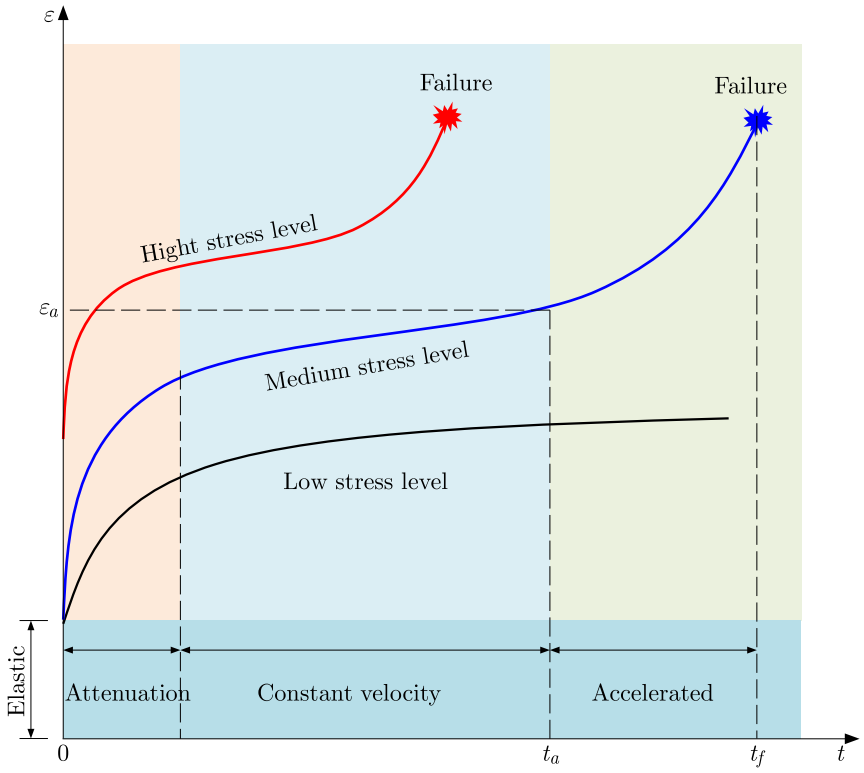

Fig. 4. Creep curves of rocks under different stress levels

Assuming that the damage variable is equal to one when the rock undergoes creep failure, the expression for the rock failure time obtained from Eq. (3.2) is

$$t_f = \frac{1}{C(1+\upsilon)\sigma^{\upsilon}} \tag{3.3}$$

Through the unsteady creep test curve of rock under different stress levels, the material constants k, υ can be determined, and then the functional relationship between rock creep failure time and stress level can be obtained.

Determination of η, n

The corresponding time for the rock to enter the accelerated creep stage from the constant--velocity creep stage in Fig. 4 is t_a, and the corresponding strain is ε_a. Because the creep acceleration of rock is zero when the creep velocity reaches its minimum value

$$t_a = \Big[1 - \exp\Big(\frac{1}{n} - 1\Big)\Big] t_f \tag{3.4}$$

The expression for n obtained from Equation (3.4) is

$$n = \Big[1 + \ln\Big(1 - \frac{t_a}{t_f}\Big)\Big]^{-1} \tag{3.5}$$

When $t = t_a$, $\varepsilon = \varepsilon_a$ according to Eq. (2.4), there is

$$\varepsilon_a = \frac{\sigma}{E} + \Big[-\frac{\sigma}{\eta}\ln\Big(1 - \frac{t_a}{t_f}\Big)\Big]^{\frac{1}{n}} \tag{3.6}$$

The expression for η obtained from Eq. (3.6) is

$$\eta = -(\varepsilon_a - \varepsilon_e)^{-n}\sigma \ln\Big(1 - \frac{t_a}{t_f}\Big) \tag{3.7}$$

In summary, all four parameters of the unsteady creep model of the rock were determined. Meanwhile, the creep model parameters can also be obtained through curve fitting based on rock creep experimental data.

4. Model validation

The rationality and accuracy of the four-parameter rock unsteady creep model established in this study were verified by referring to the uniaxial compression creep test results for four different types of rock. The creep model parameters of the four types of rock under different stress levels were obtained by curve fitting of experimental data. A comparison between the theoretical curve of the four-parameter rock unsteady creep model and the test results is shown in Figs. 5-8.

Table 1. Model parameters of different types of rocks

Rock	σ [MPa]	E [GPa]	t_a [h]	ε_a [10^{-3}]	n	η [GPa h]	t_f [h]	C	υ
Schist (Sterpi	34.30	7.49	169.2	5.38	3.22	$1.67 \cdot 10^{-6}$	338.4	6.12	3.29
and Gioda, 2009)	39.40	7.91	98.5	5.72	2.60	$2.59 \cdot 10^{-4}$	214.3	$\cdot 10^{-9}$	
Changshan salt rock	14.41	40.14	538.0	0.49	4.36	$7.21 \cdot 10^{-11}$	1030	9.56	44.32
(Cao *et al.*, 2020)	14.72	33.38	215.5	0.58	3.83	$1.26 \cdot 10^{-13}$	401	$\cdot 10^{-57}$	
Qiaohou salt rock	7.77	2.69	114.8	1.18	2.20	0.76	273	1.71	0.26
(Zhong & Ma, 1987)	11.3	1.71	86.4	1.70	1.75	0.14	248	$\cdot 10^{-3}$	
	52.82	28.40	8.5	2.27	5.42	$1.23 \cdot 10^{-14}$	15.30		
Sandy shale rock	55.37	28.69	4.6	2.32	5.11	$1.21 \cdot 10^{-13}$	8.34	1.69	15.30
(Zhong & Ma, 1987)	56.64	27.23	3.2	2.37	4.37	$1.46 \cdot 10^{-11}$	5.96	$\cdot 10^{-25}$	
	58.31	27.50	1.9	2.45	4.32	$9.7 \cdot 10^{-12}$	3.56		

As can be seen from the comparison results in Figs. 5-8, the four-parameter rock unsteady creep model can not only describe the instantaneous strain stage, attenuation creep stage, and constant velocity creep stage of different types of rocks under different stress levels but also reflects the accelerated creep stage with particularly obvious nonlinear characteristics, and its rationality has been verified. The theoretical curve of the model is in good agreement with the test results, indicating that the model can accurately predict the creep strain trends of different types of rocks under different stress levels over time, effectively design support forms, and determine the support construction time. In addition, Eq. (2.4) shows that the model can describe the unsteady creep process of rocks in a simple and unified expression, overcoming the shortcomings of complex creep equations and numerous model parameters in component combination models, which are more conducive to engineering applications.

To further verify the accuracy of the four-parameter rock unsteady creep model, the relative standard deviation between the test and theoretical creep values for the four types of rocks was calculated without considering the error of the test data. The calculation formula is shown in Eq. (4.1) (Zhao *et al.*, 2020). The calculation results show that the relative standard deviations between the test and theoretical values of schist under stress levels of 34.3 MPa and 39.4 MPa are 0.83% and 0.55%, respectively, which are basically negligible. The relative standard deviations between the test values and theoretical values of Changshan salt rock under stress levels of 14.41 MPa and 14.72 MPa are 2.87% and 1.55%, respectively. The relative standard deviations

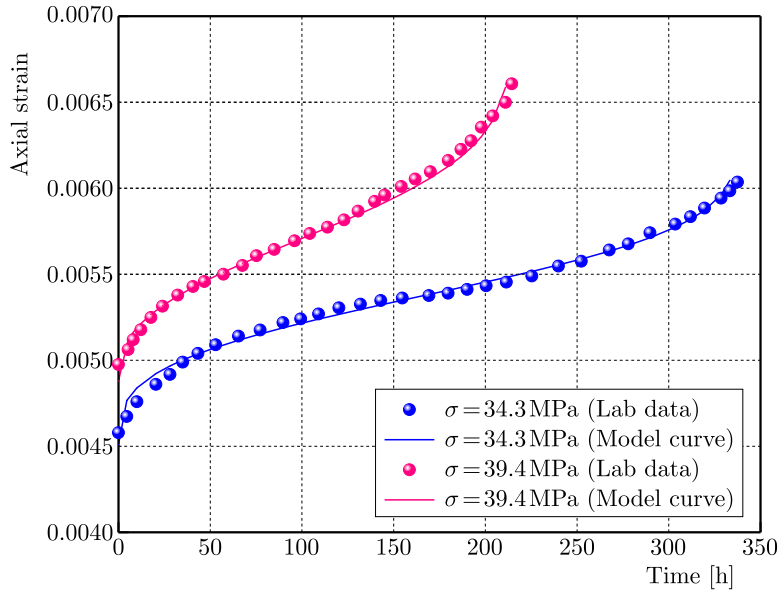

Fig. 5. Comparison between test and theoretical curves for schist

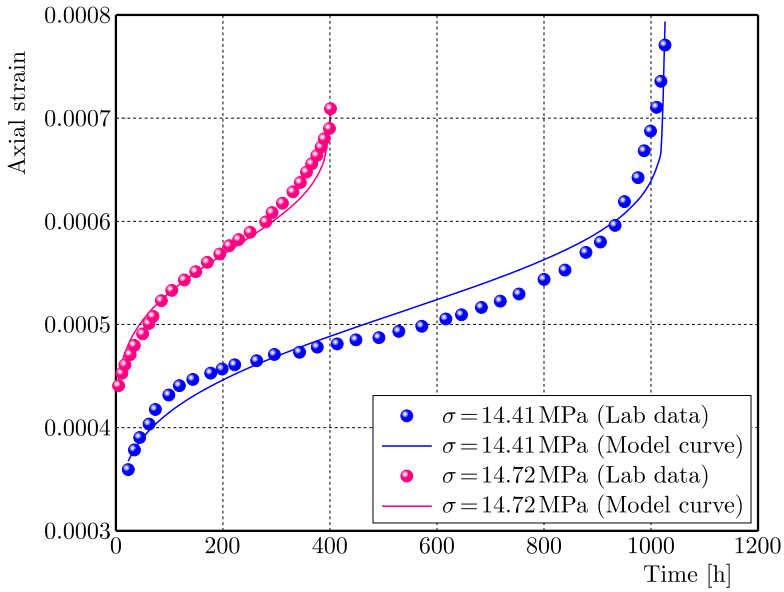

Fig. 6. Comparison between the test and theoretical curves for the Changshan salt rock

between the test values and model theoretical values of Qiaohou salt rock under stress levels of 14.41 MPa and 14.72 MPa are 4.83% and 4.94%, respectively. The error of Qiaohou salt rock is slightly larger than that of Changshan salt rock, but it is still within the allowable range. The relative standard deviations between the test and theoretical values of sandy shale at stress levels of 52.82, 55.37, 56.64 and 58.31 MPa are 1.15%, 1.05%, 0.80%, and 0.82%, respectively. The relative standard deviations of sandy shale at the four stress levels were small. The above calculations indicate that the relative standard deviation between the creep test values and the theoretical values of the four types of rocks was less than 5%. Error analysis further confirmed the accuracy of the four-parameter rock unsteady creep model

$$m = \sqrt{\frac{1}{N-1}\sum_{i=1}^{N}(\varepsilon_s - \varepsilon_l)^2} \qquad f = \frac{m}{\varepsilon_f} \tag{4.1}$$

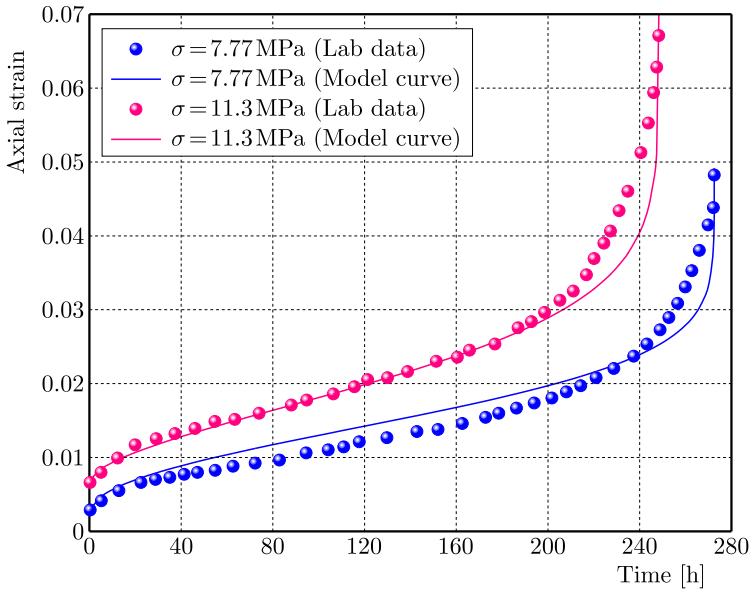

Fig. 7. Comparison between test and theoretical curves for Qiaohou salt rock

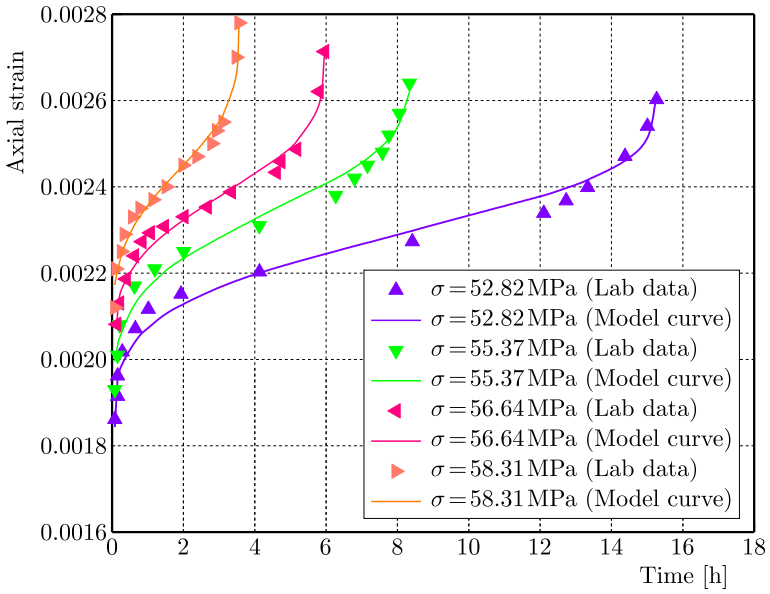

Fig. 8. Comparison between the test and theoretical curves for sandy shale rock

where m is the standard deviation, f is the relative standard deviation, and are the test and theoretical values. ε_f is the strain on the rock during the creep failure. N is the number of samples.

5. Model parameter analysis

The rock unstable creep model established in this paper only contains four model parameters, which has the advantage of few parameters and high accuracy. This Section discusses the local influence of the four model parameters on the rock unstable creep curve.

5.1. The influence of E

Assuming $\sigma = 60\,\text{MPa}$, $\eta = 2.0 \cdot 10^{-12}\,\text{GPa h}$, $t_f = 15\,\text{h}$, $n = 4$, according to Eq, (2.5), the unsteady creep curves of the rocks corresponding to different elastic modulus E were obtained, as shown in Fig. 9.

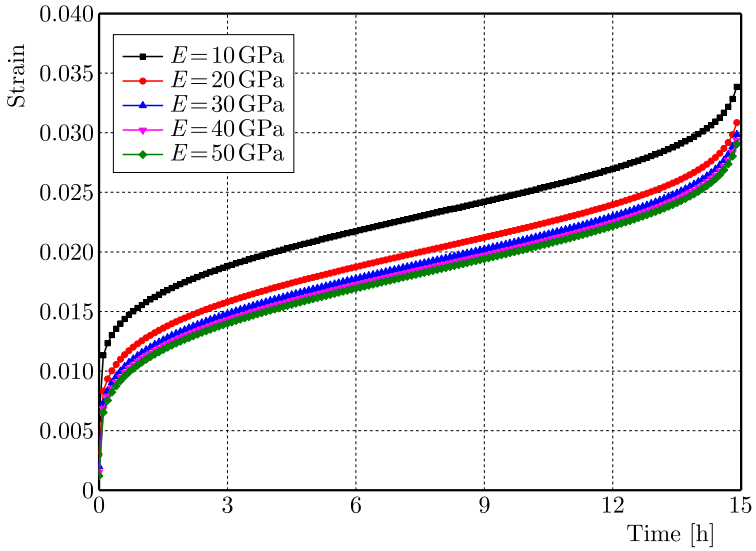

Fig. 9. Influence of E on the creep curve

Figure 9 shows that a change in E does not affect the shape of the model creep curve and creep strain, but only affects the instantaneous elastic strain. With an increase in E, the instantaneous strain at the same time gradually decreases. In addition, Fig. 9 shows that, under the same E value increment, the reduction in instantaneous strain gradually decreases; that is, according to the order from bottom to top, the model creep curve becomes increasingly sparse from dense. This indicates that when the value of E is small, a change in its value significantly influences the instantaneous elastic strain of the model. However, when the value of E was large, a change in its value had little influence on the instantaneous elastic strain.

5.2. The influence of η

Assuming $\sigma = 60\,\text{MPa}$, $E = 30\,\text{GPa}$, $t_f = 15\,\text{h}$, $n = 4$, according to Eq. (2.5), the unsteady creep curves of the rocks corresponding to different viscosity coefficients η were obtained, as shown in Fig. 10.

Figure 10 shows that a change in η has little effect on the shape of the model creep curve; however, with an increase in η, the creep stress variable at the same time gradually increases. In addition, Fig. 10 shows that, under the same η value increment, the creep strain increment simultaneously gradually decreases; that is, according to the order from bottom to top, the model creep curve becomes increasingly dense from sparse. This indicates that when the value of η is small, a change in its value significantly influences the creep strain of the model. However, when the value of η was large, the change in its value had little influence on the creep strain.

5.3. The influence of t_f

Assuming $\sigma = 60\,\text{MPa}$, $E = 30\,\text{GPa}$, $\eta = 2.0 \cdot 10^{-12}\,\text{GPa h}$, $n = 4$, according to Eq. (2.5), the unsteady creep curves of the rocks corresponding to different t_f were obtained, as shown in Fig. 11.

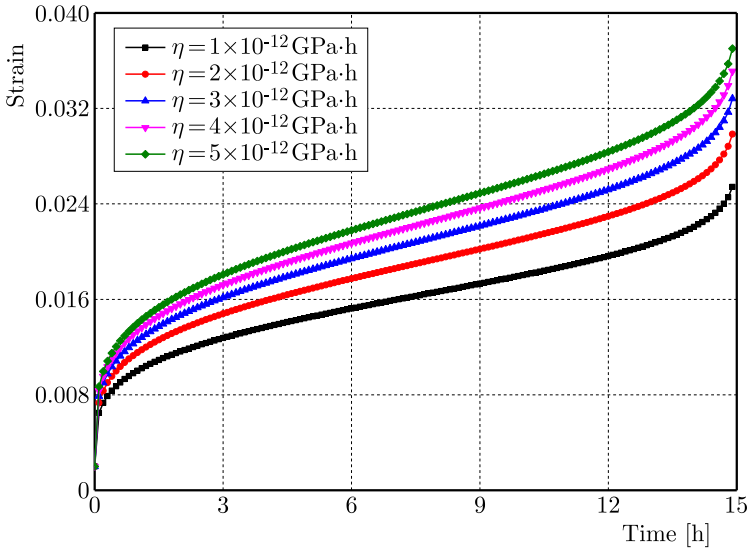

Fig. 10. Influence of η on the creep curve

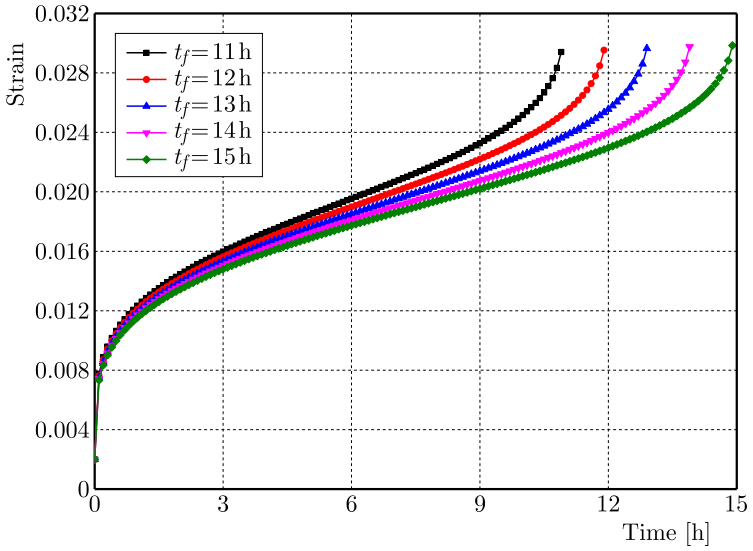

Fig. 11. Influence of t_f on the creep curve

Figure 11 shows that a change in t_f has significantly effect on the shape of the model creep curve. The smaller the value of t_f, the steeper the creep curve, and the faster the rate of increase in creep strain. In addition, t_f represents the time when the rock undergoes creep failure, therefore, the smaller t_f, the shorter the time for the rock to undergo creep failure.

5.4. The influence of n

Assuming $\sigma = 60\,\text{MPa}$, $\eta = 2.0 \cdot 10^{-12}\,\text{GPah}$, $E = 30\,\text{GPa}$, $t_f = 15\,\text{h}$, according to Eq. (2.5), the unsteady creep curves of rocks corresponding to different model orders n were obtained, as shown in Fig. 12.

As shown in Fig. 12, n has a significant influence on the shape of the creep curve of the model. As n increases, the creep strain simultaneously increases nonlinearly; that is, according to the order from bottom to top, the creep curve becomes increasingly sparse. Simultaneously, as the creep rate at the same time increased, the characteristics of accelerated creep became increasingly obvious, and the starting point of accelerated creep appeared earlier.

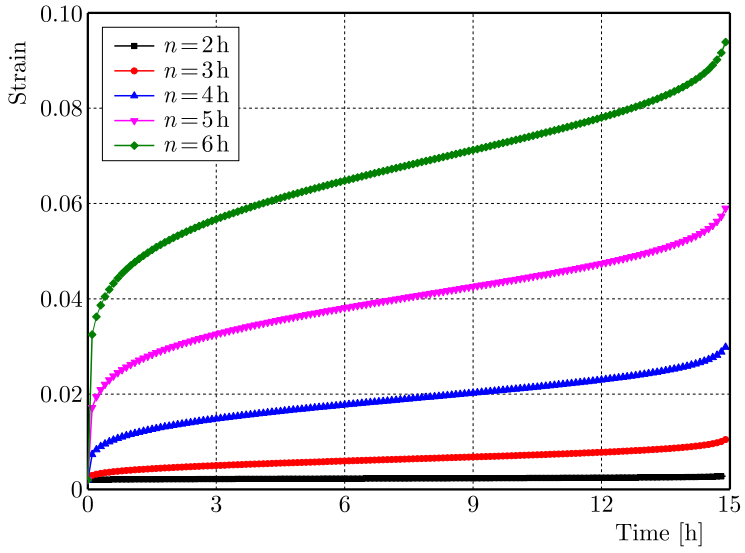

Fig. 12. Influence of n on the creep curve

6. Conclusions

Based on the antisymmetric relationship between the surface dynamic subsidence curve of coal mining and the unsteady creep curve of rocks, a rock unsteady creep model with four model parameters was established from the perspective of phenomenology using analogical reasoning. A simple and feasible method for determining the model parameters is provided based on the characteristics of the rock creep curve.

The rationality and accuracy of the four-parameter unsteady creep model were verified based on the compression creep data of four different rocks at different stress levels. The model not only describes the instantaneous strain stage, attenuation creep stage, and constant velocity creep stage of rocks at different stress levels, but also reflects the accelerated creep stage with particularly obvious nonlinear characteristics.

The unsteady creep strain of the rocks increases with an increases in the viscosity coefficient and model order. Under the same increment in the viscosity coefficient, the creep strain increment at the same time gradually decreases, whereas under the same increment in the model order, the creep strain increment at the same time gradually increases.

Acknowledgements

The authors would like to thank the editors and anonymous referees for detailed and valuable suggestions that helped to improve the original manuscript to its present form.

The research described in this paper was financially supported by Natural Science Research Project in the Universities of Anhui Province (No.KJ2021A1056).

References

1. Cao W.G., Chen K., Tan X., Chen T., 2020, A novel damage-based creep model considering the complete creep process and multiple stress levels, *Computers and Geotechnics*, **124**, 103599

2. Discenza M.E., Martino S., Bretschneider A., Mugnozza G.S., 2020, Influence of joints on creep processes involving rock masses: results from physical-analogue laboratory tests, *International Journal of Rock Mechanics and Mining Sciences*, **128**, 104261

3. Hejmanowski R., 2015, Modeling of time dependent subsidence for coal and ore deposits, *International Journal of Coal Science and Technology*, **2**, 287-292

4. Jin J.C., Yang F.W., Jing L.H., She C.X., Song Z.Y., 2024, New accelerated rock creep model considering nonstationary viscosity coefficient, *International Journal of Non-Linear Mechanics*, **159**, 104628

5. Kachanov M., 1992, Effective elastic properties of cracked solids: critical review of basic concepts, *Applied Mechanics Reviews*, **45**, 8, 304-335

6. Liu X.L., Li D.J., Han C., 2021, Nonlinear damage creep model based on fractional theory for rock materials, *Mechanics of Time-Dependent Materials*, **25**, 341-352

7. Song Y., Fan B., Li Y., Wang H., 2023, Research on creep-fatigue model of anchored jointed rock mass, *Journal of Theoretical and Applied Mechanics*, **61**, 1, 163-173

8. Song Y., Li Y.Q., 2022, Study on the shear creep characteristics of anchored jointed rock masses under creep fatigue loading, *Journal of Theoretical and Applied Mechanics*, **60**, 4, 625-635

9. Sterpi D., Gioda G., 2009, Visco-plastic behaviour around advancing tunnels in squeezing rock, *Rock Mechanics and Rock Engineering*, **42**, 319-339

10. Taheri S.R., Pak A., Shad S., Mehrgini B., Razifar M., 2020, Investigation of rock salt layer creep and its effects on casing collapse, *International Journal of Mining Science and Technology*, **30**, 3, 357-365

11. Wang J.B., Liu X.R., Song Z.P., *et al.*, 2018, A whole process creeping model of salt rock under uniaxial compression based on inverse S function (in Chinese), *Chinese Journal of Rock Mechanics and Engineering*, **37**, 11, 2446-2459

12. Wei F., Chen J., Zou Q.L., 2019, A nonlinear creep damage model for salt rock, *International Journal of Damage Mechanics*, **28**, 5, 758-771

13. Yan B.Q., Guo Q.F., Ren F.H., Cai M.F., 2020, Modified Nishihara model and experimental verification of deep rock mass under the water-rock interaction, *International Journal of Rock Mechanics and Mining Sciences*, **128**, 104250

14. Yang S.Q., Xu P., Ranjith P.G., 2015, Damage model of coal under creep and triaxial compression, *International Journal of Rock Mechanics and Mining Sciences*, **80**, 337-345

15. Yang W.D., Zhang Q.Y., Li S.C., Wang S., 2014, Time-dependent behavior of diabase and a nonlinear creep model, *Rock Mechanics and Rock Engineering*, **47**, 4, 1211-1224

16. Zhang K., Zhou H., Shao J.F., 2013, An experimental investigation and an elastoplastic constitutive model for a porous rock, *Rock Mechanics and Rock Engineering*, **46**, 6, 1499-1511

17. Zhang L.L., Cheng H., Yao Z.S., Wang X., 2020, Application of the improved Knothe time function model in the prediction of ground mining subsidence: A case study from Heze city, Shandong Province, China, *Applied Sciences*, **10**, 3147

18. Zhang L.L., Wang X.J., 2020, Viscoelastic-plastic damage creep model for rock (in Chinese), *Chinese Journal of Geotechnical Engineering*, **42**, 6, 1085-1092

19. Zhang Z.L., Xu W.Y., Wang W., 2011, Study of triaxial creep tests and its nonlinear visco--elastoplastic creep model of rock from compressive zone of dam foundation in Xiangjiaba hydropower station (in Chinese), *Chinese Journal of Rock Mechanics and Engineering*, **30**, 1, 132-140

20. Zhao Y.L., Liu Q., Tang L.M., Xie S.L., 2019, The double Burgers model of fractured rock masses considering creep fracture damage, *Journal of Vibroengineering*, **21**, 4, 974-987

21. Zhao Y., Yan H., Wu P., Zhou D., 2020, Linear correction method for improved atmospheric vertical profile retrieval based on ground-based microwave radiometer, *Atmospheric Research*, **232**, 104678

22. Zhong S.Y., Ma M.J., 1987, An approach to creep failure regularity of weak rock (in Chinese), *Journal of Central South University*, **18**, 5, 495-500

23. Zhou H.W., Wang C.P., Han B.B., Duan Z.Q., 2011, A creep constitutive model for salt rock based on fractional derivatives, *International Journal of Rock Mechanics and Mining Sciences*, **48**, 116-121

24. Zivaljevic S., Tomanovic Z., 2022, Loading history effect on time-dependent deformations after unloading – reversible creep of soft rock (marl), *Mechanics of Time-Dependent Materials*, **26**, 499-530

Manuscript received October 25, 2023; accepted for print February 8, 2024

JOURNAL OF THEORETICAL AND APPLIED MECHANICS
62, 3, pp. 491-505, Warsaw 2024
https://doi.org/10.15632/jtam-pl/189768

DESIGN AND OPTIMIZATION OF DYNAMIC CABLE CONFIGURATION DEVICE FOR INTELLIGENT CABLE RETRACTABLE VEHICLE

Zhanlong Li, Zhizhao Ren

School of Vehicle and Transportation Engineering, Taiyuan University of Science and Technology, Taiyuan, China, and Shanxi Intelligent Transportation Laboratory Co., Ltd., Taiyuan, China

corresponding author Zhanlong Li, Zhizhao Ren, e-mail: lizl@tyust.edu.cn, 1529067216@qq.com

Hui Wang, Zheng Zhang

School of Vehicle and Transportation Engineering, Taiyuan University of Science and Technology, Taiyuan, China, and Smart Transportation Laboratory in Shanxi Province, Taiyuan, China

Beijun Guo

Technology Center, Shanxi Jiacheng Hydraulic Co., Ltd., Yuanping, China

A new mining dynamic cable configuration device has been designed with adjustable cable curvature, full-range guiding restriction, and an anti-dragging warning function to improve the intelligence level and multi-scenario applicability. The digital model of the dynamic cable configuration device is constructed, and a theoretical formula for interactions between its structure parameters, assembly parameters, and the cabling work state is deduced. Strength analysis and topology optimization reconstruction of the side plate of the dynamic cable configuration device are carried out by using Ansys. The intelligent cable retractable device has been successfully applied in engineering. These research results can provide a theoretical basis for cooperative regulation and intelligent upgrading of both mining dynamic cable configuration devices and intelligent cable retractable devices.

Keywords: mechanical engineering, dynamic cable configuration device, mathematic model, topology optimization

1. Introduction

Mining electric shovels are indispensable equipment for large-scale open-pit mines in stripping operations (Topno *et al.*, 2021; Wang *et al.*, 2023). Their workload accounts for more than 50% of the total workload. Due to the requirements of high-power and continuous excavation, electric shovels often operate with high-voltage electricity (6000 V-10000 V) delivered by cables as a real-time power source. The reliability of the cable power supply directly affects the efficiency of excavation and mining operations (Zhao, 2023). Currently, electric shovels mainly use intelligent cable retractable devices to wind and unwind high-voltage cables during stripping operations in large-scale open-pit mines. Given the weight and bending radius of mining high-voltage cables, as well as frequent operation of the cable winding equipment, a dynamic cable configuration device is typically used to assist coordinated take-up and take-down by the reel (Han *et al.*, 2012; Amnuanpol, 2019).

The rationality, intelligence, and lightweight level of the structural design of the dynamic cable configuration device are crucial for ensuring reliable cabling work as an important component of an intelligent cable retractable device. However, there are several issues in the current application process of mining dynamic cable configuration devices on the market. (1) The dynamic cable configuration device lacks accuracy in following the reel assembly, which leads to cable accumulation or disorder (in Fig. 1a), resulting in uneven cable arrangement and heat

buildup, which reduces the capacity and service life of the cables. (2) Unreasonable design parameters of the dynamic cable configuration device can cause wear, bending, or even breakage of cables while also reducing precision in screw drive (in Fig. 1b) (Kevac *et al.*, 2017). (3) There is a lack of effective warning devices; therefore, the cables are susceptible to scraping and pressing by rocks and coal in unstructured pavement environments found in open-pit mines. Additionally, an excessive force from a large reel can lead to safety hazards such as cable breakage and leakage (Sun *et al.*, 2022). Therefore, it is essential to investigate how structural and assembly parameters influence stability within the dynamic cable configuration devices to enhance their applicability across various scenarios while prolonging their service life.

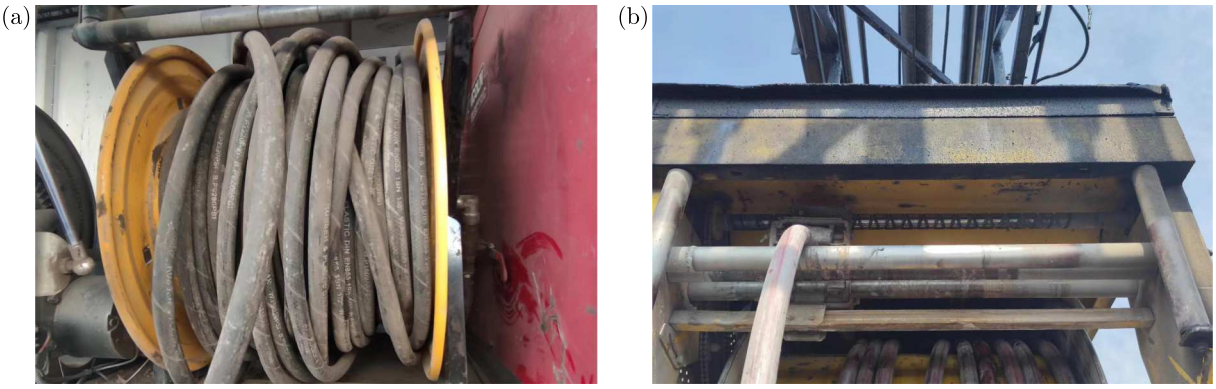

Fig. 1. Application statu: (a) cable accumulation or confusion, (b) local deformation of the screw

Wang (2022) used Ansys to analyze how different positions of guide wheels affect the strength of the dynamic cable configuration device during sailing and towing conditions. The results showed that the maximum force and deformation occurred when the guide wheels were in middle positions under both conditions, providing insights into strength analysis and verification for similar types of dynamic cable configuration devices. Kevac *et al.* (2017) introduced dynamic variables such as winding/unwinding radius and cable length, considering their impact on the dynamic response of cable winding/unwinding systems, and defined a general form for mathematical models of cable winding/unwinding systems. In the same year, Kevac and Filipovic (2017) conducted a comprehensive analysis and characterization of nonlinear and pulsating phenomena associated with the radial multi-layer winding process on winches, extending its applicability to studying rope winding processes in complex systems. These research studies establish a fundamental framework for structural design and parameter optimization of dynamic cable configuration devices under challenging mining conditions. Concurrently, topology optimization based on the variable density approach, which utilizes strain energy as the objective function and volume as the constraint function, has gradually emerged as a pivotal technique for automated design across diverse industries such as automotive, mechanical, and aerospace sectors since its introduction by Bendsøe and Kikuchi (1988). Notably, this approach is extensively employed in lightweight design of structures, offering an effective means for weight reduction and reconstruction design of cable winders (Zhang *et al.*, 2007).

Therefore, to address the aforementioned issues, this study initially proposes the design of a novel mining dynamic cable configuration device featuring adjustable cable curvature, full-range guiding restriction, and an anti-dragging warning function, aimed to enhance the quality and stability of cabling operations. Subsequently, a mathematical model is established to examine the effects of cable arrangement structure and assembly parameters on the device performance, thereby providing a reliable parameter influence law for the structural design and assembly position determination of the device. Finally, based on strength analysis results of the device side plate, the topology optimization module Ansys is employed to reconstruct the side plates

in effort to reduce the influence of device quality on the stability of the screw and the improve unit mass-bearing capacity under various working conditions.

2. Dynamic cable configuration device

The intelligent cable retractable device is positioned at the front of the intelligent cable retractable vehicle, which consists of the frame assembly, reel assembly, power system, transmission system, dynamic cable configuration device, etc. Power is transmitted to the reel and reciprocating screw-screw pair through the transmission device. This enables it to work in conjunction with the chassis system to realize safe and stable operation for functions such as "active cable winding, passive cable discharging and in situ cable winding and discharging", as shown in Fig. 2. One end of the dynamic cable configuration device is placed on the guiding rod by means of a guiding wheel set, and the other end is connected to the reciprocating screw through the screw pair. It serves as a key device for the intelligent cable retractable device to realize an even arrangement and stable unwinding of the cables.

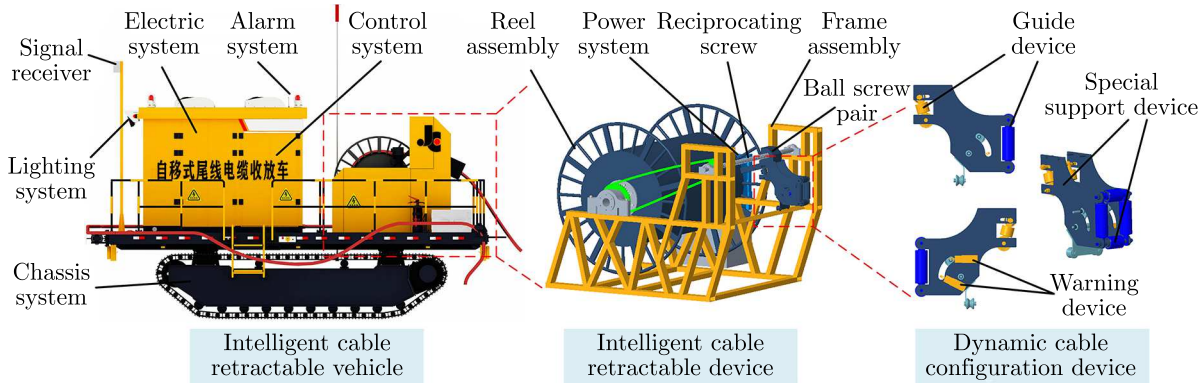

Fig. 2. Intelligent cable retractable device

2.1. Dynamic cable configuration device structure

The dynamic cable configuration device consists of three parts: the guide device, special support device and warning device, as shown in Fig. 3. Among them, the guide device works through

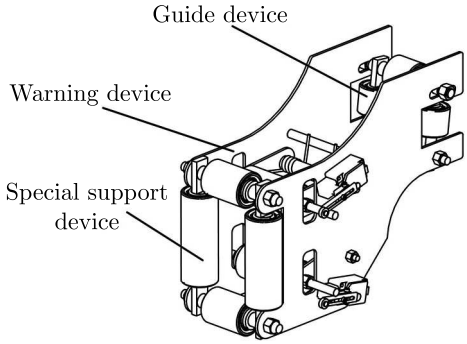

Fig. 3. Dynamic cable configuration device

synergistic cooperation of each roller to provide full-range cable guidance; the special support device has characteristics of strong loading-impact resistance, compatibility with multiple types of cables, and good alignment characteristics, which can realize stable arrangement of cables in the process of winding and releasing. By monitoring cable tension, the warning device can switch

between three working states of the cabling work – warning and emergency shutdown – while providing anti-dragging warnings to prevent cable bending or breaking due to overstretching. Additionally, the dynamic cable configuration device is fixed on the reciprocating screw pair for left-right translation and automatic reversing. The mechanical structure transmission mode of the reciprocating screw-screw pair ensures uniform cable arrangement and improves cabling work stability.

The dynamic cable configuration device possesses characteristics of anti-dragging warning and adjustable cable bending radius. With the addition of a control system, it can achieve intelligent monitoring and warning of the state of the dynamic cable configuration device, as well as adaptive adjustment of the bending radius. This feature allows for excellent adaptability to the intelligent cable retractable device, and is highly significant for construction of intelligent mines.

2.2. Guide device

The guide device is divided into a front guide device and a rear guide device, which are composed of lateral rollers and transverse rollers. The lateral and transverse rollers are in the same plane. During the cable movement process, they can play a role in guiding and protecting the full range of the cable. Each roller consists of a smooth roller and rolling bearings. By cooperating with each roller, the friction coefficient can be reduced to minimize cable wear, as shown in Fig. 4.

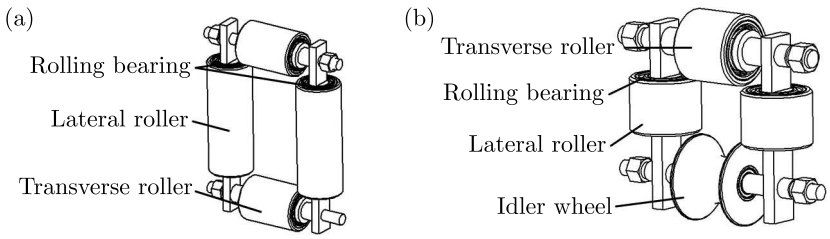

Fig. 4. Guide device: (a) front guide device, (b) rear guide device

By setting up a rotating arm structure, the rear guide device can adjust its angle according to the maximum bending coefficient of different cable specifications, and then adjust the bending radius of the input cable to adapt to different types of cables.

2.3. Special support device

The special support device comprises a front support roller assembly and a rear support roller assembly, which can realize the uniform arrangement of cables during cable installation operation. Moreover, the special support device exhibits robust loading-impact resistance and compatibility with various cable types while ensuring precise alignment. Consequently, it can accommodate diverse cable-supporting needs effectively. Withstanding up to 10 meters of the cable (weighing 6.9 kg/m), its exceptional stability guarantees compliance with overall stiffness and strength requirements, as depicted in Fig. 5.

2.4. Warning device

The warning device consists of the upper and lower stroke switch, rocker, and torsion spring. Through cooperation of the torsion spring with the rocker, the upper and lower stroke switch can be triggered, allowing for feedback on the state signal of the dynamic cable configuration device to be sent back to the controller. This enables obtaining information about cable tautness state

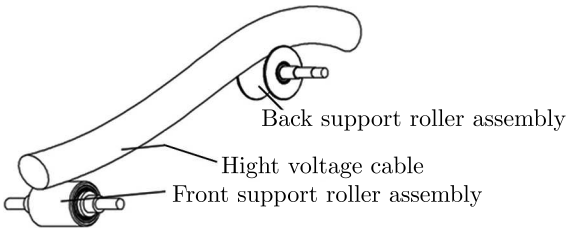

Fig. 5. Special support device

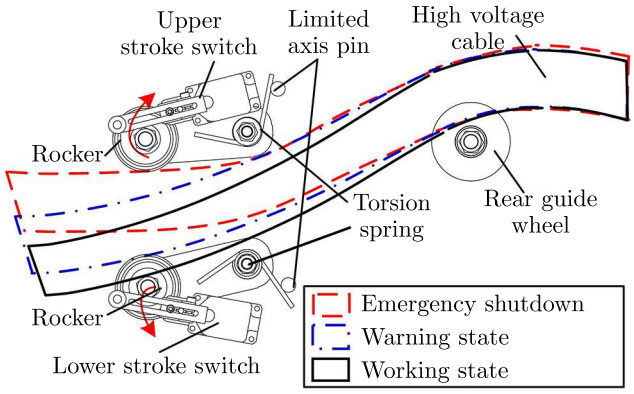

Fig. 6. Warning device

in order to regulate three working states of the cabling work, warning and emergency shutdown, as shown in Fig. 6.

- Working state: the contact between the cable and the rocker triggers the action of the lower stroke switch, and the dynamic cable configuration device runs normally;
- Warning state: the cable is lifted by resistance and separated from the rocker, but the upper and lower stroke switch are not triggered. At this time, the cable is subjected to a large tension, but not more than the maximum permissible tension, and the system gives a warning;
- Emergency shutdown: the resistance of the cable continues to increase, and the cable lifts to contact the upper rocker, triggering the upper stroke switch. At this point, the tension of the cable is greater than the maximum permissible tension, and the system stops in emergency to protect the cable from excessive tension damage.

3. Characteristics of parameter interaction

The structure parameters, assembly parameters, and performance indicators of the dynamic cable configuration device are interconnected. Studying the interaction law of each parameter is a prerequisite for optimizing and transforming the dynamic cable configuration device.

3.1. Design parameters of the dynamic cable configuration device

Figure 7 shows a schematic diagram of the movement principle of the dynamic cable configuration device when the intelligent cable retractable device is used for a high-voltage cable retracting and releasing work. In Fig. 7, α_1 is the angle between the suspended cable and horizontal direction, which can be set according to operating conditions; α_2 is the angle between the horizontal direction and connecting line (between the reel center and the lower roller center of the special support device); α_3 is the angle between the connecting line (between the center of

the reel and lower roller center of the special support device) and tangent line (between the reel and lower roller of the special support device); α_4 is the angle between horizontal direction and connecting line (between the lower roller center of the special support device and guide device roller center); β_1 is the angle between the cable of segment AB and segment BC; β_2 is the angle between the cable of segment AB and suspended cable; γ_1 is the angle between the vertical direction and resultant force on the lower roller of the guide device; γ_2 is the angle between the vertical direction and resultant force on the lower roller of the special support device.

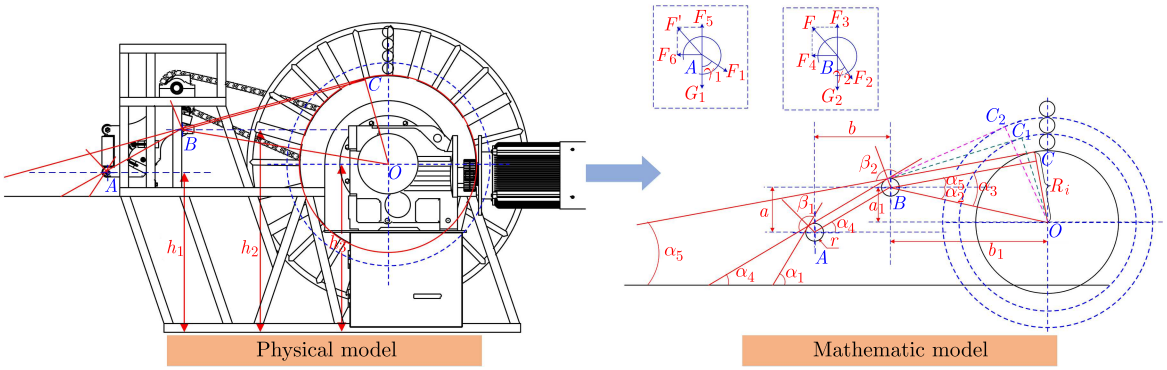

Fig. 7. Working model of the intelligent cable retractable device

Based on the geometric relationship in Fig. 7, when the dynamic cable configuration device is used to arrange a cable, an expression between the structure parameters, assembly parameters, and position parameters of each segment of the cable can be obtained

$$\begin{aligned} \alpha_2 &= \arctan\frac{a_1}{b_1} \qquad & \alpha_3 &= \arcsin\frac{R_i - r}{\sqrt{a_1^2 + b_1^2}} \\ \alpha_4 &= \arctan\frac{a}{b} \qquad & \alpha_5 &= \alpha_3 - \alpha_2 \end{aligned} \tag{3.1}$$

and

$$\beta_1 = \pi - \alpha_1 + \alpha_4 \qquad \beta_2 = \pi - \alpha_4 + \alpha_5 \tag{3.2}$$

and

$$\gamma_1 = \frac{\beta_1}{2} - \left(\frac{\pi}{2} - \alpha_1\right) \qquad \gamma_2 = \frac{\beta_2}{2} - \left(\frac{\pi}{2} - \alpha_4\right) \tag{3.3}$$

where a_1 and b_1 are the vertical and horizontal distances between the lower roller center of the special support device and the center of the reel, a and b are the vertical and horizontal distances between the lower roller center of the special support device and the lower roller center of the guide device, R_i $(i = 1, 2, 3, \ldots)$ is the radius when winding i-layers of the cable on the reel, R_1 is equal to the reel radius, r is the radius of the roller of the dynamic cable configuration device.

When the number of cable layers on the reel changes, the expression for R_i is as follows

$$R_i = R_1 + (i - 1)d \tag{3.4}$$

where d is the diameter of the high-voltage cable.

The cable of segments AB and BC are approximately arranged in a straight line, when a pre-tightening force is applied by the intelligent cable retractable device. Therefore, the cable

bending radius λ can be determined from the length and angle parameters of the cable in segments AB and BC

$$l_{BC} = \frac{R_i - r}{\tan\alpha_3} \qquad l_{AB} = \frac{a}{\sin\alpha_4} \qquad l_{AC} = l_{AB}^2 + l_{BC}^2 - 2l_{BC}l_{AB}\cos\beta_2$$
$$\lambda = \frac{l_{AC}}{2\sin\beta_2} \tag{3.5}$$

where l_{AB} and l_{BC} are the lengths of the cable in segments AB and BC.

At the same time, the warning state of the warning device depends on the structure parameters a and b. When $\alpha_4 = \alpha_1$, the lower stroke switch is disconnected and the warning is activated.

The structure parameters and assembly parameters of the dynamic cable configuration device are designed as listed in Table 1.

Table 1. Structure parameters of the cable arrangement device

Parameter	Value	Parameter	Value
a_1 [mm]	193	α_1 [°]	60
b_1 [mm]	1163.5	d [mm]	65
a [mm]	240.5	d_1 [mm]	40
b [mm]	423	g [m/s^2]	9.8
R_1 [mm]	534	r [mm]	32.5

Substituting the parameter values from Table 1 into Eq. (3.1) to (3.5) onr can obtain.

Table 2. Position parameters of cable arrangement device

Parameters	$i = 1$	$i = 2$	$i = 3$
α_2 [°]	9.42	9.42	9.42
α_3 [°]	25.16	28.71	32.37
α_4 [°]	29.62	29.62	29.62
β_1 [°]	149.62	149.62	149.62
β_2 [°]	166.13	169.67	173.33
γ_1 [°]	44.81	44.81	44.81
γ_2 [°]	22.68	24.45	26.28
λ [mm]	4972410	6404040	9441800

From Table 2, it can be observed that during the operation of the dynamic cable configuration device, α_3, β_2 and γ_2 will vary with the number of cable layers arranged on the reel, primarily affecting the working environment of the lower roller of the special support device. Simultaneously, a bending radius 15 times greater than the diameter of the cable is required for proper functioning. Based on the data in Table 2, increasing the number of cable layers proves to be advantageous in enhancing the high-voltage cables working environment.

3.2. Mechanical characteristics of the dynamic cable configuration device

The force analysis of the guide device roller and the special support roller is shown in Fig. 7, when the cable is arranged on the reel. The equilibrium equations of the two rollers are obtained

$$F_1 = 2F_s\cos\frac{\beta_1}{2} \qquad F_2 = 2F_s\cos\frac{\beta_2}{2} \qquad F_s = \frac{G_s}{\tan\alpha_1} \tag{3.6}$$

and

$$F_5 = G_1 + F_1 \cos\gamma_1 \qquad F_6 = F_1 \sin\gamma_1 \qquad F' = \sqrt{F_5^2 + F_6^2} \tag{3.7}$$

and

$$F_3 = G_2 + F_2 \cos\gamma_2 \qquad F_4 = F_2 \sin\gamma_2 \qquad F = \sqrt{F_3^2 + F_4^2} \tag{3.8}$$

where F_1 and F_2 are the resultant forces acting on the guide device roller and the special support roller, F_4 and F_3 are the vertical and horizontal components of the force F on the reciprocating screw, F_5 and F_6 are the vertical and horizontal components of the force F' on the guiding rod, m is mass of the dynamic cable configuration device, F_s is the tensile force on the cable, G_s is the gravity force acting on the suspended cable, $G_2 = G_1 = mg/2$.

The contact length between the reciprocating screw and the screw pair is much smaller than the length of the reciprocating screw, so the force on the reciprocating screw can be simplified to the concentrated force. Additionally, since the length of the reciprocating screw is much larger than its section diameter, we can neglect the effect of the shear force on bending deformation (Tang *et al.*, 2022). Based on the plane assumption that the cross-section perpendicular to the axis remains perpendicular to the deflection curve after deformation, a force analytical model for the reciprocating screw is established with the axis of the screw before deformation as the x-axis, the vertical direction as the y-axis, and the longitudinal symmetry plane of the screw as the xy plane, as shown in Fig. 8.

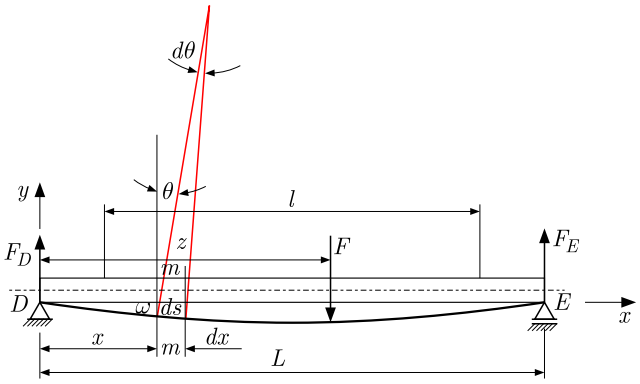

Fig. 8. Force analytical model for the reciprocating screw

Using the static equilibrium equation, the support constraints at the ends D and E of the reciprocating screw are obtained

$$F_D = \frac{F(L-z)}{L} \qquad F_E = \frac{Fz}{L} \tag{3.9}$$

where L is the length of the reciprocating screw, z is the x-axis coordinate value of the screw pair, which varies within the effective length l of the reciprocating screw.

The bending moment equation for any point of the reciprocating screw is obtained in segments

$$M(x) = \begin{cases} \dfrac{F(L-z)}{L}x & \text{for} \quad 0 \leqslant x \leqslant z \\ \dfrac{Fz}{L}(L-x) & \text{for} \quad z \leqslant x \leqslant L \end{cases} \tag{3.10}$$

Due to small deformation of the reciprocating screw, a differential equation for the deflection curve of the reciprocating screw is established (Gere and Timoshenko, 1984)

$$\frac{d^2\omega}{dx^2} = \frac{M}{EI} \tag{3.11}$$

where $I = \pi d_1^4/64$ is the cross-section moment of inertia of the screw relative to the centroid axis, d_1 is the diameter of the reciprocating screw, ω is the displacement of the centroid of the cross-section with coordinates x along the y-direction, which is the deflection, E is the elastic modulus of the reciprocating screw, 210 GPa.

The substitution of Eq. (3.10) into Eq. (3.11) yields

$$EI\omega(x) = \begin{cases} \dfrac{F(L-z)}{6L}x^3 + C_1 x + D_1 & \text{for} \quad 0 \leqslant x \leqslant z \\ \dfrac{Fz}{2}x^2 - \dfrac{Fzx^3}{6L} + C_2 x + D_2 & \text{for} \quad z \leqslant x \leqslant L \end{cases} \tag{3.12}$$

According to the continuity condition, when $x = z$, the first derivative of the deflection with respect to the deflection at the segmental point corresponds to equality. From the boundary conditions, for $x = 0$ or $x = L$, $\omega = 0$, we obtain

$$\omega(x) = \begin{cases} \dfrac{Fx[2L^2 z + z(x^2+z^2) - L(x^2+3z^2)]}{6LEI} & \text{for} \quad 0 \leqslant x \leqslant z \\ \dfrac{Fz[2L^2 x + x(x^2+z^2) - L(z^2+3x^2)]}{6LEI} & \text{for} \quad z \leqslant x \leqslant L \end{cases} \tag{3.13}$$

By using Eqs. (3.8) and (3.13), a sensitivity expression for screw deflection to the mass change of the dynamic cable configuration device is obtained

$$S = \frac{d\omega}{dm}\frac{m}{\omega} = -\frac{gm\left(\frac{mg}{2} + F_2\cos\gamma_2\right)}{2\left[\left(\frac{mg}{2} + F_2\cos\gamma_2\right)^2 + (F_2\sin\gamma_2)^2\right]} \tag{3.14}$$

Based on the measured values ($m = 30$ kg and $G_s = 690$ N), the data in Tables 1 and 2 are substituted into Eq. (3.14) to obtain $S = -0.48$, which means that the mass of the dynamic cable configuration device is reduced by 20%, and the maximum screw deflection is reduced by 9.6%.

At the same time, the number of retracted cable meters is directly proportional to the tension F_s on the cable, when the intelligent cable retractable device retracts the cable in situ. An increase of F_s will change the load-bearing state of the dynamic cable configuration device. In order to comprehensively describe its state under different loads, we define the mass utilization coefficient as the load borne by the unit mass. When this coefficient exceeds a certain limit value, it indicates that the dynamic cable configuration device is in an overloaded working state. When it is lower than a certain limit value (at this time $\alpha_4 = \alpha_1$), it indicates that the dynamic cable configuration device is in a warning working state. Under conditions satisfying strength and stiffness, a higher mass utilization coefficient implies greater utilization per unit mass, making for a more economical and reasonable structure of the dynamic cable configuration device

$$P = \frac{F_f}{m} \tag{3.15}$$

where P is the mass utilization coefficient, F_f is the load of the dynamic cable configuration device. The expression for F_f is obtained

$$F_f = \sqrt{(F_1\cos\gamma_1 + F_2\cos\gamma_2)^2 + (F_1\sin\gamma_1 + F_2\sin\gamma_2)^2} \tag{3.16}$$

By substituting the values from Tables 1 and 2 into Eqs. (3.6), (3.15), and (3.16), it can be concluded that the mass utilization coefficient of the dynamic cable configuration device is 16.58 N/kg, when the intelligent cable retractable device operates in conjunction with the chassis.

4. Strength analysis of side plates of the dynamic cable configuration device

High-voltage cables used in open-pit mines have a high mass per unit length. In order to ensure that the dynamic cable configuration device has sufficient load-bearing capacity under design loads and to guarantee safety and reliability of its structure. Ansys is utilized for static simulation of the side plates of the dynamic cable configuration device based on the 3D model created by Solidworks in this Section (Nie *et al.*, 2011).

The side plates of the dynamic cable configuration device are made of Q235B steel with a Young's modulus of 206GPa, Poisson's coefficient of 0.3, a yield strength of 250 MPa and a tensile strength of 460 MPa. The thickness of the side plates is 5 mm. The vertical upward load is set at 2000 N, and the vertical downward load is set at 700 N. The specific distribution is shown in Fig. 9.

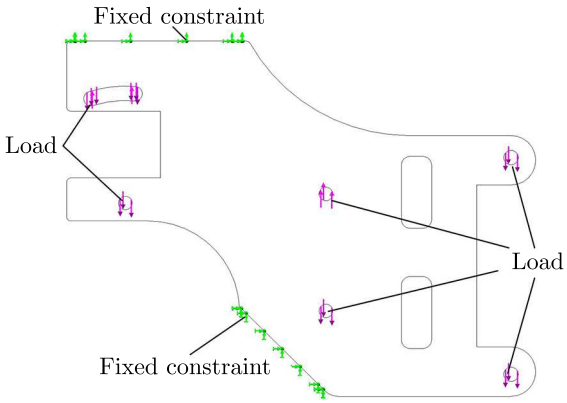

Fig. 9. Schematic of side plates loading

The side plate of the dynamic cable configuration device was statically analyzed to obtain the corresponding stress and strain cloud diagrams, as shown in Fig. 10. Among them, the weight of the side plate is 5.268 kg, and the maximum stress is 30.824 MPa, which is much smaller than the permissible stress of the material and meets both strength and stiffness requirements.

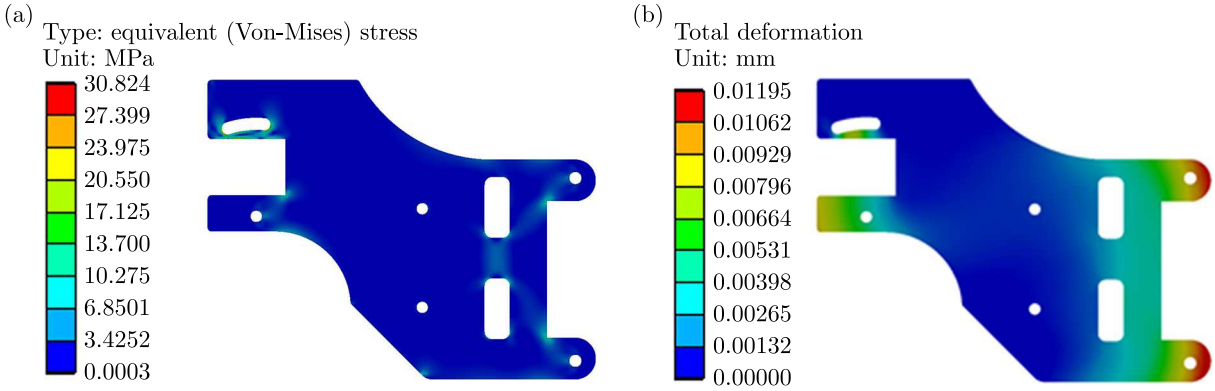

Fig. 10. Stress analysis of the side plates: (a) stress, (b) strain

The safety coefficients are calculated according to

$$N = \frac{[\sigma]}{\sigma} \tag{4.1}$$

where N is the safety coefficient, $[\sigma]$ is the permissible stress, σ is the maximum working stress.

According to Eq. (4.1), $N = 8.11$, the side plates are designed to meet strength requirements.

5. Topology optimization and reconstruction

The accuracy of the reciprocating screw is affected by its stiffness in cabling work. If the deformation is too large, it will affect the precision of the screw and the screw pair, resulting in uneven wear, noise, vibration, and reduced lifespan. The lightweight design of the dynamic cable configuration device is an important method to improve both the precision of cabling work and the mass utilization coefficient of the dynamic cable configuration device. This design also enhances operational efficiency and reduces production costs. In this Section, the topological reconstruction of the side plates for the dynamic cable configuration device is performed based on Ansys.

5.1. Optimization program

Topological optimization can identify the optimal material distribution scheme within the optimization space of a homogeneous material (Song *et al.*, 2017). In this Section, the objective of topology optimization is to minimize strain energy for the overall structure of the side plate, while ensuring that the volume of the optimized side plate does not exceed 40% of its original volume. The mathematical representation of topological optimization is as follows (Radhi *et al.*, 2021)

$$\begin{aligned} &\text{find:} \quad \mathbf{x} = [X_1, X_2, \ldots, X_n]^{\mathrm{T}} \\ &\min: \quad C(x) = \frac{1}{2}\mathbf{U}^{\mathrm{T}}\mathbf{K}\mathbf{U} \\ &\text{s.t.} \quad \left\{\sum_{i=1}^{N} V_i X_i \leqslant V^*;\ \mathbf{F} = \mathbf{K}\mathbf{U};\ X_{min} \leqslant X_i \leqslant 1\ (i = 1, \ldots, n)\right\} \end{aligned} \tag{5.1}$$

where $\mathbf{U}$, $\mathbf{K}$ and $\mathbf{F}$ are the displacement vector, global stiffness matrix and load vector, respectively, for the n element domain. The first constraint is a volume constraint to be below a certain value V^*. The second constraint represent the equilibrium condition, from which $\mathbf{U}$ is calculated. Here, a value X_{min} of 0.001 was found to be suitable for our simulations.

5.2. Analysis of optimization results

The optimization analysis converges after 24 iterations, and the topology optimization results are shown in Fig. 11.

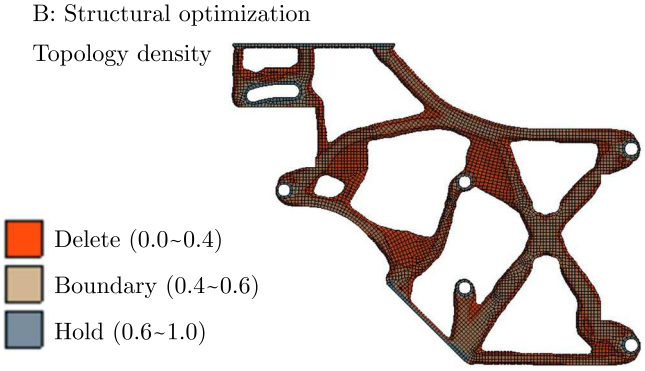

Fig. 11. Topology optimization results

The side plates have been reconstructed based on the topology optimization results, weighing 2.227 kg as depicted in Fig. 12a. By applying the same constraints and loading conditions as the original model for static analysis, the maximum stress is measured at 31.624 MPa with a safety coefficient of 7.9, as shown in Fig. 12b.

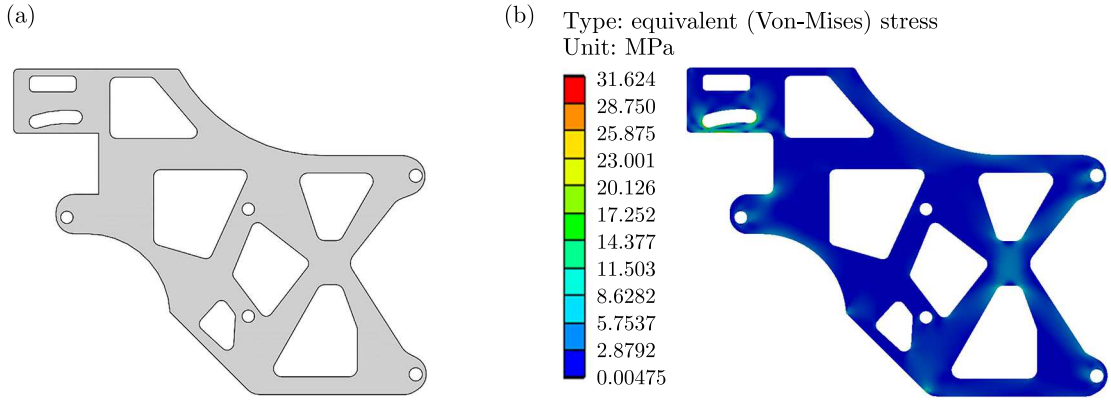

Fig. 12. Reconstructed side plates: (a) side plate model, (b) stress diagram

After reconstruction, the stress on the side plate is much lower than the material yield strength, and the design still has a significant redundancy. Therefore, in the second reconstruction, the thickness of the side plate is reduced to 3 mm. The weight of the side plate after this second reconstruction is 1.670 kg. By applying identical constraints and loading conditions as in the original model for static analysis, we measured a maximum stress of 37.722 MPa with a safety coefficient of 6.62, as shown in Fig. 13.

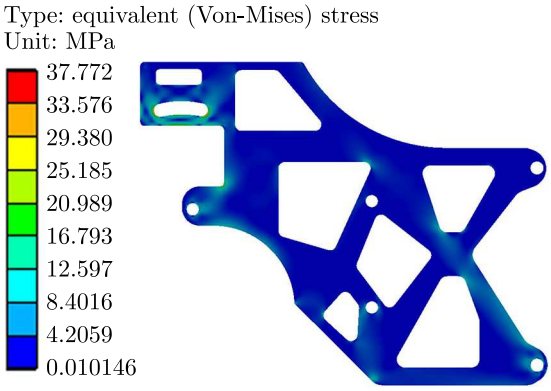

Fig. 13. Stress diagram of the side plates after second reconstruction

5.3. Comparative analysis

As shown in Table 3 and 4, when the thickness of the side plate is taken as 5mm, the weight of the side plate decreases by 57.7% to 2.227 kg, while the maximum stress is reduced to 31.624 MPa. Additionally, the mass of the dynamic cable configuration device decreases by 20.3% to 23.918 kg. When the thickness of the side plate is reduced to 3 mm, its weight decreases by 68.3% down to 1.670 kg and the maximum stress becomes 37.772 MPa. Meanwhile, the mass of the dynamic cable configuration device decreases by 24.0% to 22.804 kg.

To ensure the precision of cabling work and extend equipment service life while reducing operational costs, the weight reduction achieved with a safety coefficient that meets requirements makes the side plate weighing only 1.670kg better fit for lightweight design specifications. The mass utilization coefficient for the dynamic cable configuration device reaches 21.83 N/kg when

Table 3. Comparative advantage

	Deformation	Equivalent (von Mises) stress
Original side plate	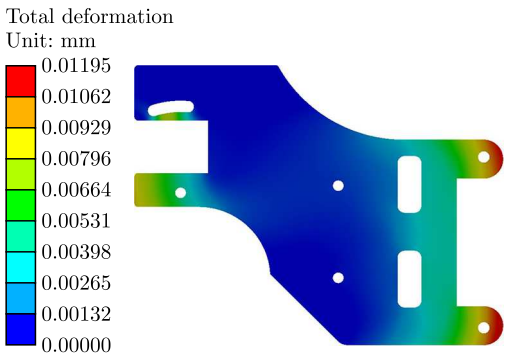	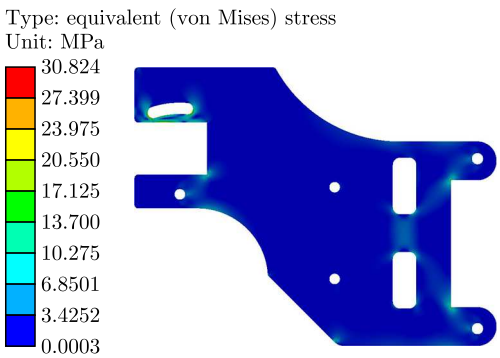
Optimized side plate (5 mm)	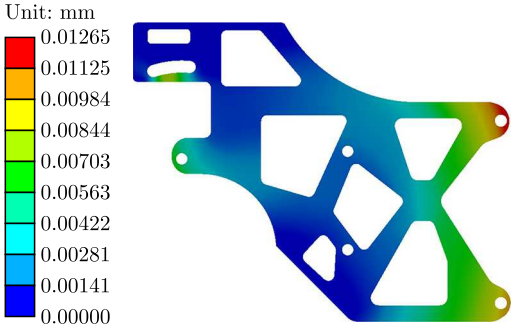	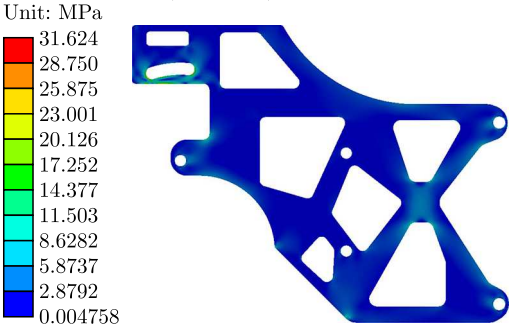
Optimized side plate (3 mm)	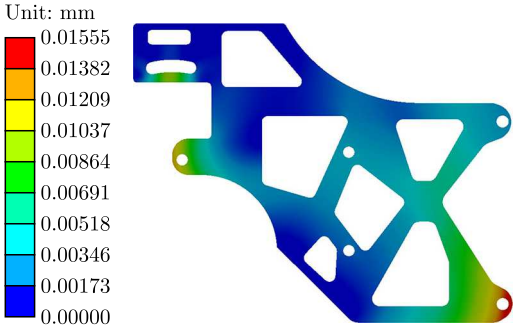	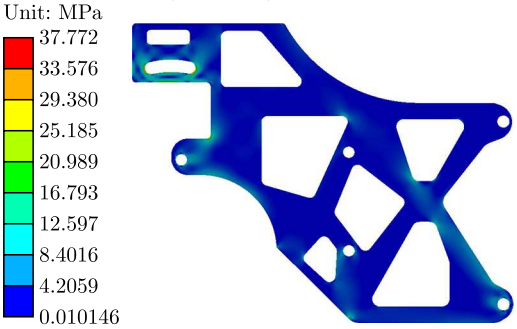

Table 4. Data analysis

Structural element	Weight [kg]	Maximum stress [MPa]	Safety coefficient
Original side plate	5.268	30.824	8.11
Optimized side plate (5 mm)	2.227	31.624	7.9
Optimized side plate (3 mm)	1.670	37.772	6.62

the intelligent cable retractable device works in conjunction with the chassis. This design concept has already been adopted and successfully implemented in large-scale open-pit mine engineering applications, such as showed in Fig. 14.

(a) (b)

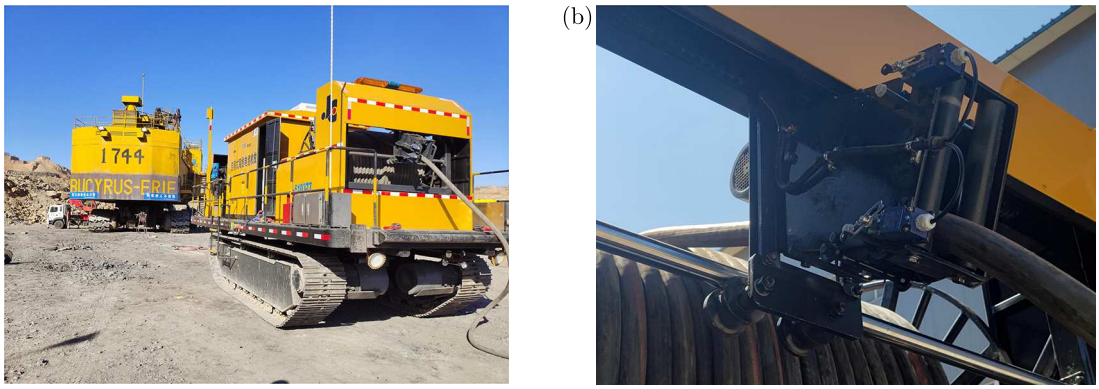

Fig. 14. (a) Intelligent cable retractable vehicle, (b) dynamic cable configuration device

6. Conclusions

This study has developed a novel mining dynamic cable configuration device for mining enterprises, which was designed and optimized based on both the mathematical model of the device and the topological optimization results obtained from Ansys. The engineered application of this mining dynamic cable configuration device has been successfully implemented in a large open-pit mine. During the research process, we have drawn the following conclusions.

- The dynamic cable configuration device is equipped with an adjustable cable bending degree, full-range guiding limit and an anti-dragging warning function, effectively preventing high-voltage cables from being ripped off or bent. This greatly enhances multi-scenario application capability of the intelligent cable retractable vehicle.
- The mathematical expressions and interaction laws of parameters such as cable bending radius and utilization coefficient of the dynamic cable configuration device are theoretically derived, providing a theoretical basis for structural design of this device, determination of assembly positions, and performance optimization.
- After optimization, the weight of the side plate of the dynamic cable configuration device decreased by 68.3%, and the weight of the device decreased by 24.0%. The maximum deflection of the reciprocating screw was reduced by 11.52%. Through actual engineering applications, it has been observed that stability in discharging cables of the device has been significantly enhanced.

Acknowledgements

This research was supported by the Xinzhou City Science and Technology Plan Project – Key Research and Development Plan (Grant No.20220107), the National Natural Science Foundation of China (Grant No. 52272401), the Fundamental Research Program of Shanxi Province (Grant No. 202203021211185), the Shanxi Students' Platform for Innovation and Entrepreneurship Training Program (Grant No. 20230671) and the Guizhou Province Science and Technology Plan Project – Science and Technology Innovation Talent Team (CXTD [2022]015).

References

1. Amnuanpol S., 2019, Shape sequence of rope coiling on a rotating plane, *EPL (Europhysics Letters)*, **125**, 5, 54001
2. Bendsøe M.P., Kikuchi N., 1988, Generating optimal topologies in structural design using a homogenization method, *Computer Methods in Applied Mechanics and Engineering*, **71**, 2, 197-224

3. Gere J.M., Timoshenko S.P., 1984, *Mechanics of Materials*, 2nd SI ed., Van Nostrand Reinhold Co., New York

4. Han Y.Y., Zhang Z.G., Zhu K.G., 2012, The design on the improvement of the electric scooptram's cable arrangement device, *Applied Mechanics and Materials*, **2034**, 229-231

5. Kevac L., Filipovic M.M., 2017, Mathematical model of cable winding/unwinding system, *Journal of Mechanics*, **35**, 1, 1-13

6. Kevac L., Filipovic M., Rakic A., 2017, Dynamics of the process of the rope winding (unwinding) on the winch, *Applied Mathematical Modelling*, **48**, 821-843

7. Nie J.N., Wang H., Xie D.F., 2011, Finite element analysis of drum on the new type self-driven towing machine for cable, *Applied Mechanics and Materials*, **1245**, 55-57, 664-669

8. Radhi A., Iacobellis V., Behdinan K., 2021, Manipulation of topologically optimized structures using graphic statics, *Materials Design*, **198**, 109286

9. Song G.H., Jing S.K., Zhao F.L. Wang Y.D., Xing H., Zhou J.T., 2017, Design optimization of irregular cellular structure for additive manufacturing, *Chinese Journal of Mechanical Engineering*, **30**, 5, 1184-1192

10. Sun L.Q., Zhang X.D., Zeng Q.L., Gao K.D, Jiang K., Zhou J.W., 2022, Application of a screw conveyor with axial tilt blades on a shearer drum and investigation of conveying performance based on DEM, *Particuology*, **61**, 91-102

11. Tang Z., Li S.Q., Huang F., Yang J.W., Yang F., *et al.*, 2022, Optimization of a cable support strategy for roadways in coal mines by using the PSO algorithm, *Geotechnical and Geological Engineering*, **40**, 153-163

12. Topno S.A., Sahoo L.K., Umre B.S., 2021, Energy efficiency assessment of electric shovel operating in opencast mine, *Energy*, **230**, 120703

13. Wang Z.Y., 2022, *Dynamics Analysis of the Cable Arrangement System for Full Ocean Depth Geological Winch* (in Chinese), Harbin Engineering University, Harbin

14. Wang Z.W., Jin Z., Wang J., 2023, Maceral and organic geochemical characteristics of the No. 6 coal seam from the Haerwusu Surface Mine, Inner Mongolia, China, *Energy Exploration and Exploitation*, **41**, 5, 1643-1662

15. Zhang W.H., Dai G.M., Wang F.W., Sun S.P., Bassir H., 2007, Using strain energy-based prediction of effective elastic properties in topology optimization of material microstructures, *Acta Mechanica Sinica*, **23**, 1, 77-89 .

16. Zhao S.X., 2023, *Lightweight and Dynamic Characteristic Research of Walking System for Intelligent Cable Retracting and Releasing Machine* (in Cinese), Taiyuan University of Science and Technology, Taiyuan

Manuscript received November 9, 2024; accepted for print February 19, 2024

JOURNAL OF THEORETICAL AND APPLIED MECHANICS
62, 3, pp. 507-519, Warsaw 2024
https://doi.org/10.15632/jtam-pl/188526

DETERMINATION OF CHABOCHE AND BOUC-WEN PARAMETERS FOR QUENCHED AND TEMPERED STEEL

Ciro Santus, Lorenzo Romanelli, Tommaso Grossi, Paolo Neri
University of Pisa, Department of Civil and Industrial Engineering (DICI), Pisa, Italy
e-mail: ciro.santus@unipi.it; lorenzo.romanelli@phd.unipi.it (corresponding author); tommaso.grossi@phd.unipi.it; paolo.neri@unipi.it

During cyclic loadings, metal alloys can undergo cyclic plasticity, for example, at notches. The Chaboche kinematic hardening model provides a versatile and realistic description of the material stress-strain behaviour under multiaxial cyclic loadings. In this work, the global properties, extracted from stabilized cycles of strain-controlled tests and from a force--controlled test, are employed to calculate the parameters. Alternatively, the Bouc-Wen model can provide a reliable representation of nonlinear hysteretic phenomena, and the classic nonlinear least squares approach is employed to tune its constants. The performances of the two proposed techniques are compared, and a final discussion is provided.

Keywords: cyclic-plasticity, hysteretic behaviour, Chaboche kinematic hardening model, Bouc-Wen model

1. Introduction

The presence of notches in mechanical components can enhance the plastic behaviour, in particular, under cyclic loadings, thus an accurate description of the constitutive behaviour of metal alloys is crucial for structural analysis. For example, in (Bertini *et al.*, 2017; Santus *et al.*, 2023b) the use of a cyclic plastic constitutive law was motivated by the fact that, assuming purely elastic behaviour, the presence of a severe V-notch combined with a high fatigue load ratio R ($R = \sigma_{min}/\sigma_{max}$), resulted in very high and not meaningful values of stress near the notch. The Chaboche kinematic hardening (CKH) model (Chaboche, 1986) is a powerful and recognized model to describe the cyclic plastic behaviour of metals. Given that it is a kinematic model, it accounts for the Bauschinger effect, which generally occurs during the cyclic plastic behaviour of materials. This latter statement, together with the necessity to consider the plastic behaviour of the material near the notches, justifies the widespread use of this model in fatigue analyses such as in (Karolczuk *et al.*, 2019; Hosseini and Seifi, 2020; Santus *et al.*, 2022). The CKH model is also implemented in Ansys finite element (FE) software.

Since its first introduction, the Chaboche model has undergone several proposals of modification. Chaboche himself (Chaboche, 1991) suggested a modification to improve the ratcheting prediction, which was subsequently validated by other researchers (Shafiqul and Tasnim, 2000). Some changes to the classical CKH model were also proposed by (Dafalias *et al.*, 2008), where the parameters of backstress components were assumed variable during cyclic-loading to improve the ratcheting rate prediction. Despite all the modifications of the Chaboche hardening rule, the computation of Chaboche parameters is a challenging task even considering the classical formulation of this model. Typically, only stabilized cycles extracted from strain-controlled tests (SCTs) on plain specimens can be used to calculate the parameters, but force-controlled tests (FCT) can also be used as in (Koo and Lee, 2007; Mahmoudi *et al.*, 2011). Different techniques can be employed to obtain the Chaboche parameters such as genetic algorithms (Badnava *et al.*,

2012; Dvoršek *et al.*, 2023), particle-swarm optimization (Li *et al.*, 2018) and gradient-based optimization algorithm (Chaparro *et al.*, 2008). The latter algorithms typically demand substantial computational resources.

Alternatively, the Bouc-Wen (B-W) model (Bouc, 1967; Wen, 1976) is widely employed to describe the hysteretic behaviour of mechanical systems such as piezo-actuated devices (Cai *et al.*, 2023) or wire rope isolators (Neri and Holzbauer, 2023). Various optimization algorithms can be again employed to obtain B-W parameters such as the Levenberg-Marquardt algorithm (Ni *et al.*, 1998), multi-objective optimization algorithms (Ortiz *et al.*, 2013) or particle-swarm optimization (Charalampakis and Dimou, 2010).

In this research, a novel and physics-based algorithm to calculate the CKH model parameters was employed. The global properties of stabilized cycles of the SCTs, such as the gradient at extreme points of the cycles (EPOC), the hysteresis area (HA), the stress range (SR), the average stress (AS), the average plastic strain (APS) and the plastic strain range (PSR) were employed to compute the parameters. To provide an accurate description of the transient during the FCT, the experimental ratcheting rate was also employed during determination of the parameters. The Bouc-Wen model was also used to replicate the cyclic-plastic behaviour considering the nonlinear hysteretic nature of cyclic plastic phenomena. However, the search of the parameters required a different strategy due to different nature of model equations.

Section 2 is dedicated to show the experimental data and, in Section 3, the utilized procedure to calculate the CKH parameters is explained along with the corresponding obtained results. In Section 4, the Bouc-Wen model is introduced and the corresponding results to model the cyclic plastic behaviour are shown. Finally, in Section 5, a discussion with a comparison between the two engaged algorithms is provided.

2. Materials

The alloy investigated in this research is 42CrMo4 quenched and tempered steel. All tests were performed on plain specimens (i.e. without notches) and under uniaxial loading. The mean values of the yield strength and of the ultimate strength, obtained by a standard tensile test, were equal to $S_Y = 500\,\text{MPa}$ and $S_U = 700\,\text{MPa}$, respectively. Three SCTs and one FCT were employed to calculate the CKH parameters. Two SCTs were performed at $R_\varepsilon = -1$, which means that the minimum imposed total axial strain and the maximum imposed total axial strain were opposite, while one was performed at $R_\varepsilon \neq -1$. The FCT was conducted at $R = -0.66$, and R indicates the ratio between the minimum and the maximum imposed axial stress. The SCTs conducted at $R_\varepsilon = -1$ are shown in Fig. 1, Cycle I (C_I) and Cycle II (C_{II}) indicate the stabilized cycles and ε_p represents the axial plastic strain. The useful quantities extracted from the stabilised cycles are also shown in Fig. 1, and their corresponding numerical values are reported in Table 1.

Table 1. Global properties extracted from C_I and C_{II}

	$\Delta\varepsilon_p$ [–]	$\Delta\sigma$ [MPa]	A [mJ/mm^3]	$d\sigma/d\varepsilon_p$ [GPa]
C_I	1.43%	1030	12.0	5.81
C_{II}	0.50%	918	3.61	20.2

The useful quantities extracted from the FCT in order to apply the procedure are shown in Fig. 2. The ratcheting rate in Fig. 2b presents an initial linear trend, which is used to calculate the Chaboche parameters. It is important to remark that the CKH model is not able to reproduce a variable (increasing) ratcheting rate, unless combining the CKH model with damage mechanics models.

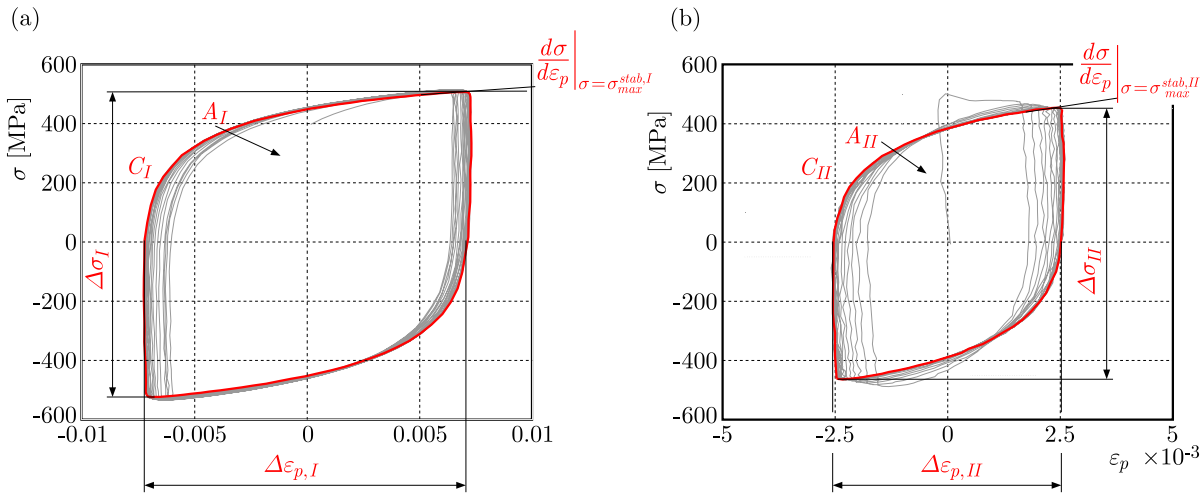

Fig. 1. Strain-controlled tests performed at $R_\varepsilon = -1$, the transient cycles are indicated in grey, while the stabilized cycles are marked in red as (a) C_I and (b) C_{II}

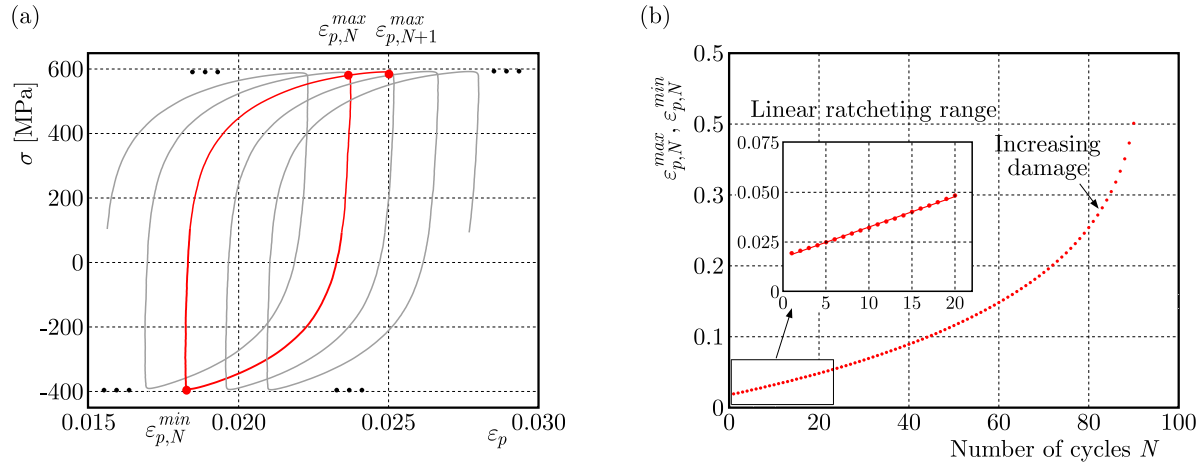

Fig. 2. (a) Few cycles of the force-controlled test involved in the research with significant quantities highlighted; (b) experimental maximum plastic strain per cycle of the force-controlled test employed in this research

From Fig. 2a some useful quantities need to be defined as the plastic strain amplitude (PSA) per cycle and the plastic strain rate per cycle, which are formalized as

$$\Delta\varepsilon^a_{p,N} = \frac{\varepsilon^{max}_{p,N+1} + \varepsilon^{max}_{p,N}}{2} - \varepsilon^{min}_{p,N} \qquad \Delta\varepsilon^r_{p,N} = \varepsilon^{max}_{p,N+1} - \varepsilon^{max}_{p,N} \tag{2.1}$$

These two quantities $\Delta\varepsilon^a_{p,N}$ and $\Delta\varepsilon^r_{p,N}$ are not generally constant. However, FE simulations by involving the Chaboche model showed that, after the initial cycles, a constant ratcheting rate can be obtained as described in (Kreethi *et al.*, 2017; Zhang *et al.*, 2020). Given these latter findings, the two quantities of Eqs. (2.1) can be assumed constant in order to describe the ratcheting rate, and they can be substituted with $\Delta\varepsilon^a_p$ and $\Delta\varepsilon^r_p$ in which there is no dependence on the number of cycles N.

3. Computation of the CKH parameters

For a plain specimen loaded uniaxially, and employing the CKH model, the dependence between the axial stress σ and the backstress components can be described by Eqs. (3.1). In these

equations σ_L is the elastic limit (to be calculated), μ is a coefficient equal to 1 during positive loading ramps, and to -1 during negative loading ramps and χ is the total backstress obtained by the sum of backstress components

$$\sigma = \mu\sigma_L + \chi \qquad \chi = \sum_{i=1}^{n} \chi_i \qquad d\chi_i = C_i d\varepsilon_p - \gamma_i \chi_i |d\varepsilon_p| \tag{3.1}$$

The third of Eqs. (3.1) describes a differential equation which governs the dynamics of the backstress components. C_i and γ_i are the CKH model parameters to be tuned. In this work, the classical CKH model with three backstress components was calibrated, and the fourth backstress was eventually added to improve the prediction of stabilized cycles of the SCTs near the elastic limit zones. The qualitative trends of the three backstress components, according to our procedure and for an ideal plastic strain controlled test with $R_{\varepsilon p} = 0.1$, are reported in Fig. 3. The first backstress has the most rapid dynamics (Fig. 3a), while the second backstress has much slower dynamics than that of the first one (Fig. 3b). Finally, the third backstress was assumed with a linear trend as shown in Fig. 3c that is just obtained by imposing $\gamma_3 = 0$. It is important to highlight that the first backstress leads to a nonzero value of the HA of the stabilized cycle, while the second backstress leads to an almost null value of the HA of the stabilized cycle, which can be approximated as null in the following analysis. The maximum and the minimum values of the first and second backstress components, as concerns the stabilized cycles, are opposite as highlighted in Figs. 3b and 3c. On the contrary, a nonzero mean stress remains for the linear backstress component, despite the loading cycling.

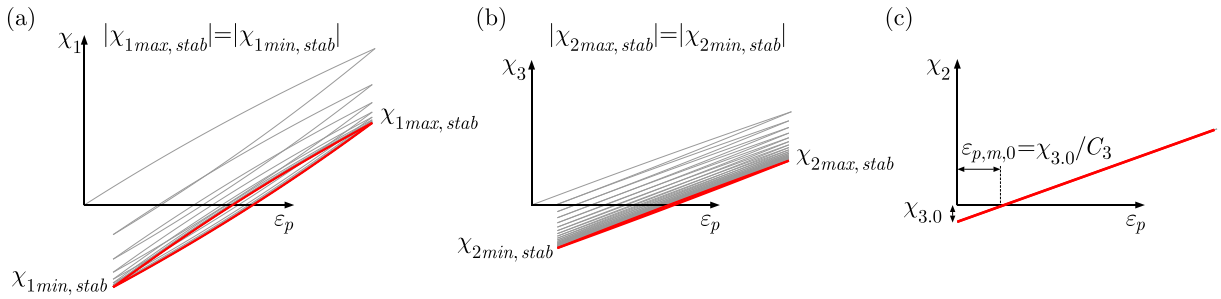

Fig. 3. Trends of the three backstress components for ideal plastic SCT at $R_{\varepsilon p} = 0.1$: (a) first backstress component (fast), (b) second backstress component (slow) and (c) third backstress component (stable)

The CKH parameters to be determined were C_1, γ_1, C_2, γ_2, C_3, $\chi_{3,0}$ and σ_L, and the procedure to calculate them was presented in (Santus *et al.*, 2023a) and is briefly recalled here. Using the average point of the stabilized cycles extracted from the SCTs, the parameters C_3 and $\chi_{3,0}$ were determined by combining C_I and Cycle III (C_{III}), which indicates the stabilized cycle of the strain-controlled test (SCT) performed at $R_\varepsilon \neq -1$. Equations (3.2) provide a 2×2 linear system which relates the AS $\sigma_m = (\sigma_{max} + \sigma_{min})/2$ and the APS $\varepsilon_{p,m} = (\varepsilon_{p,max} + \varepsilon_{p,min})/2$ of the stabilized cycles, which are also the experimental inputs. When the experimental SCT performed at $R_\varepsilon \neq -1$ is almost fully relaxed, the obtained value of C_3 is much lower than the values of C_1 and C_2

$$\chi_{3,0} + C_3 \varepsilon_{p,m,I} = \sigma_{m,I} \qquad \chi_{3,0} + C_3 \varepsilon_{p,m,II} = \sigma_{m,II} \tag{3.2}$$

Once the parameters C_3 and $\chi_{3,0}$ were calculated, Eqs. (3.3)-(3.5) were employed to calculate the other parameters, except for γ_2, which was calculated using the FCT. The experimental inputs of Eqs. (3.3)-(3.5) were all extracted from the stabilized cycles of the SCTs performed at $R_\varepsilon = -1$ (C_I and C_{II}). Assuming the inequality given by $\gamma_2 \Delta\varepsilon_p \ll 1$, which is meaningful considering the low value of γ_2 and which was employed in all the following equations, Eqs. (3.3)

can be obtained to model the gradient at the EPOC in the $\sigma - \varepsilon_{pl}$ plane. In Eqs. (3.3), the PSR $\Delta\varepsilon_p = (\varepsilon_{p,max} - \varepsilon_{p,min})$ and the gradient at the EPOC, $d\sigma/d\varepsilon_p$ calculated at σ_{max}^{stab}, are the experimental inputs, and the nonlinear system can be solved to obtain the expressions for C_1 and C_2 depending on γ_1

$$\begin{aligned} C_1\Big(1 - \tanh\frac{\gamma_1\Delta\varepsilon_{p,I}}{2}\Big) + C_2 &= -C_3 + \left.\frac{d\sigma}{d\varepsilon_p}\right|_{\sigma=\sigma_{max}^{stab,I}} \\ C_1\Big(1 - \tanh(\frac{\gamma_1\Delta\varepsilon_{p,II}}{2}\Big) + C_2 &= -C_3 + \left.\frac{d\sigma}{d\varepsilon_p}\right|_{\sigma=\sigma_{max}^{stab,II}} \end{aligned} \tag{3.3}$$

The expressions to calculate the values of the elastic limit for C_I and C_{II} were obtained as functions depending on γ_1 only, as shown in Eqs. (3.4). In these latter equations, the PSR and the SR $\Delta\sigma = (\sigma_{max} - \sigma_{min})$ are, in turn, the experimental inputs. The expressions of $\sigma_{L,I}$ and $\sigma_{L,II}$ obtained from Eqs. (3.4) should lead to the same value considering that the elastic limit is obviously a unique material property. Given that this assumption is not satisfied, in general, an averaged function was defined as $\sigma_L = (\sigma_{L,I} + \sigma_{L,II})/2$

$$\begin{aligned} \sigma_{L,I} &= \frac{\Delta\sigma_I}{2} - \frac{C_1}{\gamma_1}\tanh\frac{\gamma_1\Delta\varepsilon_{p,I}}{2} - \frac{C_2 + C_3}{2}\Delta\varepsilon_{p,I} \\ \sigma_{L,II} &= \frac{\Delta\sigma_{II}}{2} - \frac{C_1}{\gamma_1}\tanh\frac{\gamma_1\Delta\varepsilon_{p,II}}{2} - \frac{C_2 + C_3}{2}\Delta\varepsilon_{p,II} \end{aligned} \tag{3.4}$$

The last property to be considered during the determination of the parameters is the HA of the stabilized cycle, which is described for C_I and C_{II}, by A_I^{mod} and A_{II}^{mod}, respectively. It is important to highlight that Eqs. (3.2)-(3.5) were obtained in (Santus *et al.*, 2023a) by supposing plastic SCTs, but they were extended to total SCTs without any loss of generality

$$\begin{aligned} A_I^{mod} &= 2\sigma_L\Delta\varepsilon_{p,I} + 2\Big(\frac{C_1}{\gamma_1}\Delta\varepsilon_{p.I} - 2\frac{C_1}{\gamma_1^2}\tanh\frac{\gamma_1\Delta\varepsilon_{p,I}}{2}\Big) \\ A_{II}^{mod} &= 2\sigma_L\Delta\varepsilon_{p,II} + 2\Big(\frac{C_1}{\gamma_1}\Delta\varepsilon_{p.II} - 2\frac{C_1}{\gamma_1^2}\tanh\frac{\gamma_1\Delta\varepsilon_{p,II}}{2}\Big) \end{aligned} \tag{3.5}$$

Three error functions, all depending on γ_1 only, were then defined:

- An error function to quantify the difference between the values obtained by the expression of $\sigma_{L,I}$ and those obtained by the expression of $\sigma_{L,II}$

$$\Sigma = \Big|\frac{\sigma_{L,I} - \sigma_{L,II}}{\sigma_L}\Big|$$

- A relative error function about the HA of C_I

$$\Lambda_I = \frac{A_I^{mod} - A_I}{A_I}$$

- A relative error function about the HA of C_{II}

$$\Lambda_{II} = \frac{A_{II}^{mod} - A_{II}}{A_{II}}$$

The three introduced error functions were then included into a global error function, which is presented in

$$\psi(\gamma_1) = (1 - \alpha)\Sigma^2 + \alpha(\Lambda_I^2 + \Lambda_{II}^2) \tag{3.6}$$

The weight parameter α can balance between the importance of considering the relative error of the HA and the error about the cycle amplitude. The parameter α is considered in the range $[0, 1]$. The searched value of γ_1 was just found by minimizing the global error function presented in Eq. (3.6). A qualitative trend of the global error function $\psi(\gamma_1)$, obtained with $\alpha = 0.5$, is shown in Fig. 4. Once the value of γ_1 was obtained, the parameters C_1, C_2 and σ_L were then easily numerically calculated by following the expression proposed in Eqs. (3.3)-(3.5). The last parameter to be calculated was γ_2 by involving the FCT. Considering the CKH model with only two nonlinear backstress components, the relationship between the AS, the PSA per cycle and the plastic strain rate per cycle for a FCT on a plain specimen is provided by

$$\sigma_m = \sum_{i=1}^{2} \frac{C_i}{\gamma_i} \frac{\sinh(\gamma_i \Delta\varepsilon_p^r/2)}{\sinh(\gamma_i \Delta\varepsilon_p^a)} \tag{3.7}$$

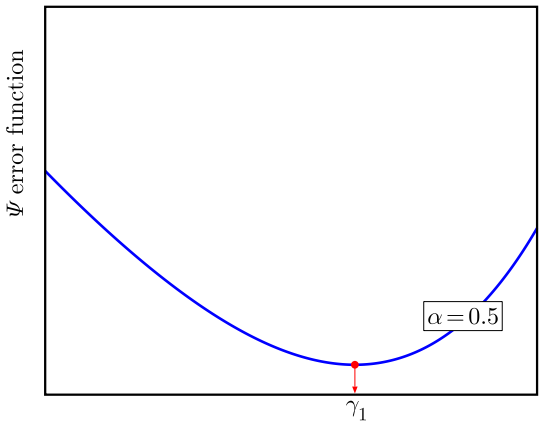

Fig. 4. An example of the trend of the global error function $\psi(\gamma_1)$ with $\alpha = 0.5$

Considering that, generally, $\gamma_i \Delta\varepsilon_p^r \ll 1$ for each backstress component giving a small plastic strain increment per cycle, Eq. (3.7) can be simplified into Eq. (3.8). This latter equation can be easily inverted, and the value of γ_2 can thus be obtained

$$\sigma_m = \sum_{i=1}^{2} \frac{C_i}{\sinh(\gamma_i \Delta\varepsilon_p^a)} \tag{3.8}$$

When the third linear backstress is also considered, the maximum value of this backstress component evolves cycle per cycle according to

$$\chi_{3,i+1}^{max} = \chi_{3,i}^{max} + C_3 \Delta\varepsilon_p^r \tag{3.9}$$

This latter equation highlights that the only achievable equilibrium, when the third linear backstress component is considered, occurs for $\Delta\varepsilon_p^r = 0$, i.e. for a plastic shakedown. According to this latter statement, the quantities $\Delta\varepsilon_{p,N}^a$ and $\Delta\varepsilon_{p,N}^r$ cannot be considered constant. The relationships shown by Eqs. (3.2), which were used for SCTs, are also valid to describe the average point of the stabilized cycle of a FCT as remarked in (Santus, Grossi *et al.*, 2023). Therefore, the relationship to describe the APS of the stabilized cycle can be obtained by inverting Eqs. (3.2), thus obtaining

$$\varepsilon_{p,m} = \frac{\sigma_m - \chi_{3,0}}{C_3} \tag{3.10}$$

This equation highlights that the APS of the stabilized cycle of a FCT is relatively high for low values of C_3, thus it is reached after a quite big number of cycles. Therefore, the PSA per cycle

and the plastic strain rate per cycle can be considered constant without any loss of accuracy, and Eq. (3.8) can be finally employed to obtain the value of γ_2. In Fig. 5, some of the obtained results are reported, more specifically, in Fig. 5a, the blue line predicts the mean points of the stabilized cycles as described in Eqs. (3.2), and in Fig. 5b, differences between the experimental stabilized cycles C_I and C_{II} and the corresponding modelled cycles are shown.

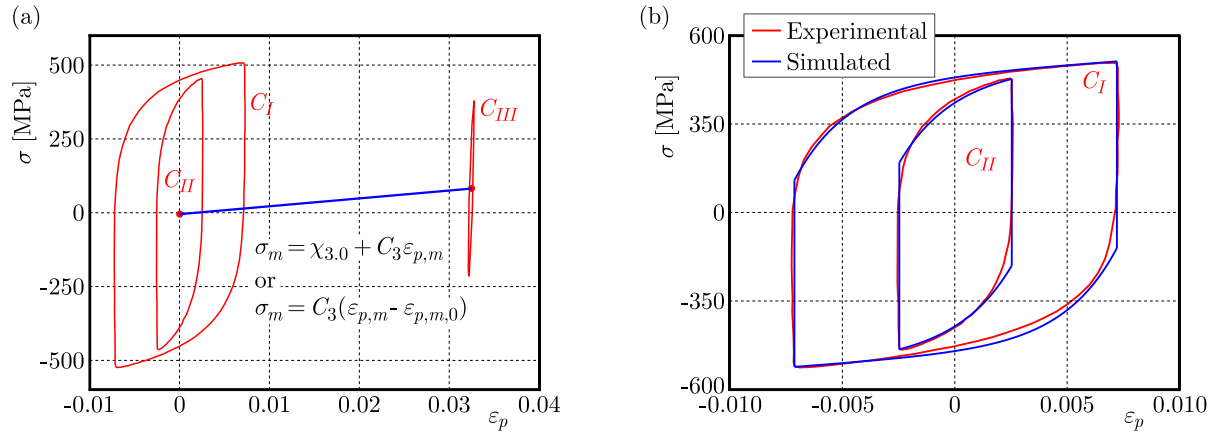

Fig. 5. (a) Average points of the stabilized cycles of the SCTs, (b) small differences between experimental and reproduced C_I and C_{II} cycles by using the proposed procedure with three backstress components

The ratcheting rate was also modelled, and the obtained results are reported in Fig. 6. The comparison between the experimental and the modelled ratcheting rates is reported in Fig. 6a. Clearly, this latter comparison was carried out in the region where the ratcheting rate could be considered constant according to Fig. 2. In Fig. 6b, a comparison between the experimental and the modelled FCT is shown in the same ratcheting cycle range.

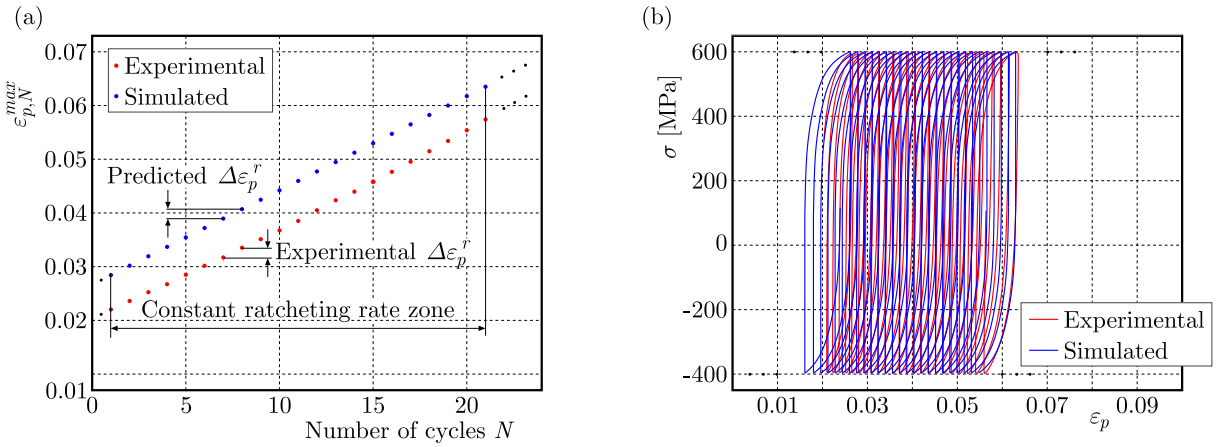

Fig. 6. (a) Differences between experimental and modelled ratcheting rates in the constant ratcheting rate region and (b) differences among experimental and modelled fully reproduced cycles of the force-controlled test in the same constant ratcheting region

The fourth backstress, with an imposed high value of γ_4, thus quickly saturating, was added to improve the prediction of the stabilized cycles of the SCTs near the elastic limit region. The searched ratio between C_4 and γ_4 was aimed at minimizing the further error function described by

$$\varphi\left(\frac{C_4}{\gamma_4}\right) = |\sigma_A - \sigma_B|^2 + |\sigma_C - \sigma_D|^2 \tag{3.11}$$

A graphical and qualitative explanation of the error function described by this latter equation is provided in Fig. 7a. The superimposition of the fourth backstress, with a high value of γ_4, modifies Eqs. (3.4). In fact, the elastic limit can be modelled as $\sigma'_L = \sigma_L - C_4/\gamma_4$, where σ'_L is the updated (and lower) value of the elastic limit provided that σ_L is the value of the elastic limit previously obtained with the CKH model with three backstress components. The updated expression of the elastic limit can be then substituted into Eqs. (3.5) leading to a clear decrease in the value of the modelled HA. Finally, the comparisons between the experimental and simulated stabilized cycles, considering the fourth backstress component and for C_I, C_{II} and C_{III}, are reported in Fig. 7b. The numerical values of the obtained CKH parameters are shown in Table 2.

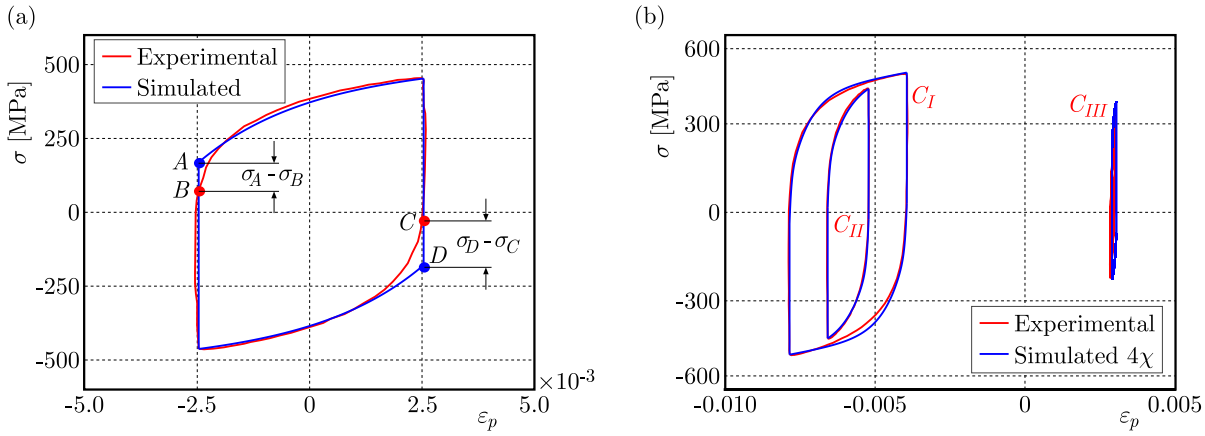

Fig. 7. (a) Inaccuracy of the simulated stabilized cycle, which can be corrected by introducing the fourth backstress component, (b) differences among experimental and modelled C_I, C_{II} and C_{III} considering the additional fourth backstress component

Table 2. Obtained parameters for the CKH model with four backstress components

σ_L [MPa	C_1 [MPa]	γ_1 [–]	C_2 [MPa]	γ_2 [–]	C_3 [MPa]	γ_3 [–]	$\chi_{3,0}$ [MPa]	C_4 [MPa]	γ_4 [–]
240	69200	426	2840	4.63	2670	0	−4.86	38200	5000

4. Use of the Bouc-Wen model to describe the cyclic-plastic behaviour

The B-W model is widely used to describe the hysteretic behaviour of mechanical systems, and its general form is described as

$$\begin{aligned} &Y = Y_2(z + Y_1) \qquad Y_1 = k_1 x + k_2 \operatorname{sgn}(x) x^2 + k_3 x^3 \qquad Y_2 = b^{cx} \\ &\dot{z} = \dot{x}\Big(\alpha + \delta x - [\gamma + \beta \operatorname{sgn}(\dot{x}) \operatorname{sgn}(z)] z^n\Big) \end{aligned} \tag{4.1}$$

In these equations, the variable x and its derivative with respect to time $\dot{x}$ are the input variables, while Y is the output variable. It is important to highlight, by considering the last expression of Eqs. (4.1), that the time variable could be simplified, thus leading to a not time-dependent expression. However, the time variable defines the sequence of the loading, i.e. the change of sign of the input variable x, but the velocity of change of this variable does not affect the output of the problem. As a consequence, in all performed searches of the Bouc-Wen model parameters presented below, the time was never involved. In the last equation of Eqs. (4.1), the term δx was added with respect to the original formulation of the model, as in (Neri and Holzabuer,

2023). This added term aims to reproduce the possible asymmetry between the two EPOC. In this research, the input variables were the axial plastic strain ε_p and its differential $d\varepsilon_p$, while the output variable Y represented the axial stress. The parameters of the B-W model were calculated by the Levenberg-Marquardt algorithm. This algorithm combines the steepest--descent and the Newton-Raphson methods, thus obtaining two different types of behaviour: far from possible singularities, the algorithm tends to enhance Newton-Raphson to improve the convergence rate, while, in order to improve its robustness, it tends to the steepest-descent algorithm near eventual singularities to improve its robustness. This latter characteristic can then balance between the aim of convergence and the robustness to the singularities. The Levenberg--Marquardt algorithm is fully implemented in the MATLAB software, which is widely employed in optimization problems. The results of this algorithm are presented in Fig. 8. The parameters were firstly calibrated by C_I and validated by C_{II} (Fig. 8a) and vice versa (Fig. 8b). The parameters were also calculated for the FCT, as shown in Fig. 9. The obtained B-W parameters are reported in Table 3.

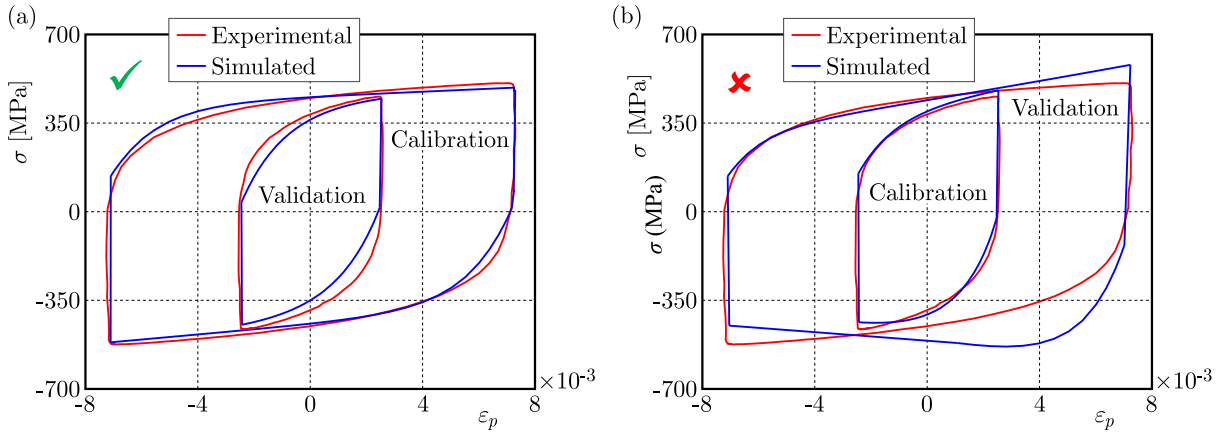

Fig. 8. Differences among experimental and simulated C_I and C_{II} by involving the B-W model: (a) C_I employed to calculate the constants of the B-W model and C_{II} utilized to validate the obtained constants, (b) C_{II} employed to calculate the constants of the B-W model and C_I utilized to validate the obtained constants. This latter approach introduces higher errors

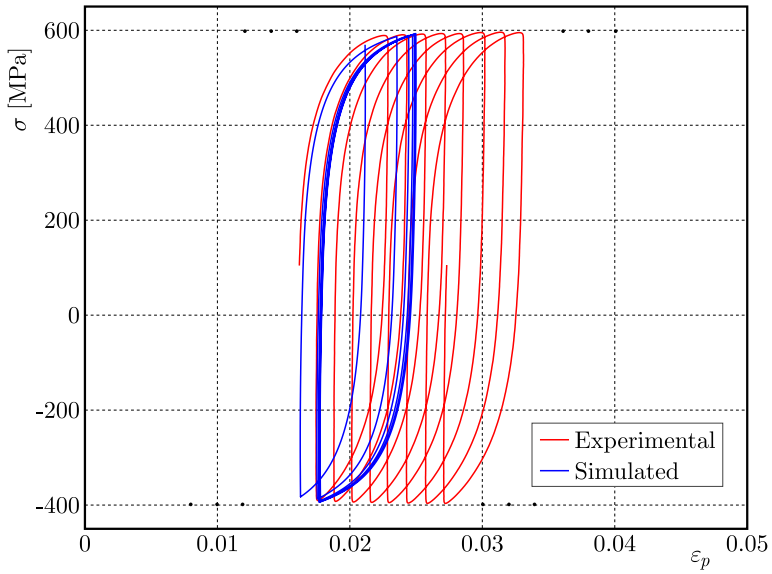

Fig. 9. Comparison between the experimental and the predicted force-controlled test by using the Bouc-Wen model

Table 3. Calculated constants of the B-W model

Extracted from	α [MPa]	β [MPa^{1-n}]	γ [MPa^{1-n}]	n	δ [MPa]	c	k_1 [MPa]	k_2 [MPa]	k_3 [MPa]
C_I	28.7	14.8	−13.7	0.860	−0.139	0	0.738	0	0
C_{II}	40.6	37.7	−34.8	0.681	1.12	0	0	0	0
Force--controlled test	15.5	0.068	0.036	1.290	−0.026	0	0.479	0	0

After critically considering the obtained values of the B-W parameters reported in Table 3, it can be observed that this model collapses for all the investigated cases into equations (4.2), given that from the optimization algorithm it was found out that $k_2 = k_3 = c = 0$, $\delta \approx 0$ and $n \approx 1$. A null value of k_1 was identified only when the optimization was carried out on C_{II}, while it was considerably not null in the other cases. According to Eqs. (4.2), the output variable Y was obtained by the sum of z and Y_1, which resemble nonlinear and linear backstress components, respectively. Therefore, under these circumstances, the B-W model collapsed into the CKH model with two backstress components in which one was nonlinear and the other was linear. In addition to this, the term $\gamma + \operatorname{sgn}(x)\operatorname{sgn}(z)$, which is the equivalent of γ of in the CKH model, varies during the loading due to the sign of x and sign of z, while γ in the CKH model remains constant during the loadings

$$\begin{aligned} &Y = z + Y_1 \qquad Y_1 = k_1 x \qquad Y_2 = 1 \\ &dz = dx\Big(\alpha - [\gamma + \beta \operatorname{sgn}(dx)\operatorname{sgn}(z)]z\Big) \end{aligned} \tag{4.2}$$

5. Conclusions

In this research, the cyclic-plastic behaviour of plain specimens made of 42CrMo4 (Q+T) was analyzed with the Chaboche kinematic hardening model and, for a comparative purpose, also with the Bouc-Wen model. The main findings of this research are reported below:

- The employed novel procedure to identify the Chaboche kinematic hardening model parameters is based on the global properties, such as the gradient at the EPOC, the HA, the AS, the SR, the PSR and the APS of the stabilized cycles obtained from the SCTs and on the ratcheting rate obtained from the FCT.
- The parameters of the Chaboche kinematic hardening model with three backstress components were tuned, and the fourth backstress was eventually added to improve the prediction accuracy near the elastic limit regions. The procedure allowed one to obtain a good prediction accuracy as highlighted in Fig. 5 for the Chaboche model with three backstress components, in Fig. 6 for the ratcheting rate and in Fig. 7 for the Chaboche model with four backstress components. In this latter figure, C_{III} was used as an independent validator given that it was only employed to calculate the values of C_3 and $\chi_{3,0}$. The utilized procedure makes use only of explicit formulas, and it avoids the use of complex optimization algorithms.
- Given that cyclic plasticity introduces a hysteretic phenomenon, the Bouc-Wen model was also engaged to reproduce the cyclic-plastic behaviour of the investigated steel. The Bouc--Wen parameters were tuned by C_I and validated by C_{II} and vice versa. For comparison, the parameters were also calculated from the FCT. In Fig. 8, it is shown that the Bouc--Wen model can accurately reproduce the stabilized cycle from which the parameters were obtained, but a lack of accuracy was observed when they were employed to reproduce

the stabilized cycle of the SCT not accounted for calibration. More precisely, the model if calibrated by C_I and validated by C_{II}, see Fig. 8a, provided a better prediction accuracy than in, vice versa, Fig. 8b. This latter behaviour can be explained just considering that the strain range of C_I was wider than that of C_{II}.

- By observing the obtained numerical results for the Bouc-Wen parameters reported in Table 3, it can be noted that this model collapsed for the investigated data into something very similar to the Chaboche kinematic hardening model with nonlinear and linear backstress components. It is reasonable to obtain $k_2 = k_3 = 0$, given that these two parameters can change the sign of concavity of the quantity Y during the tensile loading phase or during the compressive loading phase, as shown in (Neri and Holzbauer, 2023). This mentioned change of concavity makes no sense if contextualized for cyclic-plastic phenomena where the concavity has a positive sign during the entire compressive loading phase, and it has a negative sign during the entire tensile loading phase. It is also reasonable to obtain a low value of δ, if compared to the obtained value of α, given that generally there is not an evident asymmetry between the two EPOC in the cyclic plastic behaviour. However, rather than the Chaboche, the Bouc-Wen model misses the equivalent of the term σ_L, which allows one to model the elastic limit stress of the material.
- The Bouc-Wen model did not provide an accurate description of the ratcheting rate even if the model parameters search were optimized in a force-controlled test, as shown in Fig. 9. As explained in (Santus *et al.*, 2023a), the relationship between the SR and the PSA per cycle $\Delta\varepsilon_p^a$ in a force-controlled test is equal to the relationship between the SR and the PSA for a stabilized cycle obtained from a SCT test (Eqs. (3.4)). During determination of the Chaboche model parameters, according to our procedure, the SCTs are primarily employed to calculate the parameters and then the FCT is employed to calculate just the value of γ_2 of the slightly nonlinear backstress component. Following this approach, when calculating the value of γ_2, the relationship between the SR and the PSA per cycle is generally satisfied due to the previous tuning of the backstress with the most rapid dynamics. Reconsidering the equivalent CKH model, if only a slightly nonlinear backstress component is employed, Eq. (3.8) can be used to calculate the value of γ_2, but Eqs. (3.4) cannot be satisfied in general, since another nonlinear backstress component is required to provide an accurate reproduction of the FCT.

Acknowledgement

This paper was presented at WECM'23 – 2nd Workshop on Experimental and Computational Mechanics (Pisa, Italy, 20-22 September, 2023). Based on the evaluation by Selection Committee chaired by Prof. Jerzy Warmiński, Lublin University of Technology, Poland, and composed of Prof. Simone Camarri and Prof. Luigi Lazzeri, University of Pisa, Italy, this work was awarded the "WECM'23 Best Paper Award in Experimental Mechanics". Authors gratefully acknowledge the University of Pisa for the organisation of the workshop and for the payment of the publication fee.

References

1. Badnava H., Pezeshki S.M., Fallah Nejad K., Farhoudi H.R., 2012, Determination of combined hardening material parameters under strain controlled cyclic loading by using the genetic algorithm method, *Journal of Mechanical Science and Technology*, **26**, 3067-3072

2. Bertini L., Le Bone L., Santus C., Chiesi F., Tognarelli L., 2017, High load ratio fatigue strength and mean stress evolution of quenched and tempered 42CrMo4 Steel, *Journal of Materials Engineering and Performance*, **26**, 3784-3793

3. Bouc R., 1967, Forced vibrations of mechanical systems with hysteresis, *Proceedings of the Fourth Conference on Nonlinear Oscillations*, Prague, Czech Republic, **10**, 142-149
4. Cai J., Dong W., Nagamune R., 2023, A survey of Bouc-Wen hysteretic models applied to piezo-actuated mechanical systems: Modeling, identification, and control, *Journal of Intelligent Material Systems and Structures*, **34**, 16, 1843-1863
5. Chaboche J.L., 1986, Time-independent constitutive theories for cyclic plasticity. *International Journal of Plasticity*, **2**, 149-188
6. Chaboche J.L., 1991, On some modifications of kinematic hardening to improve the description of ratchetting effects, *International Journal of Plasticity*, **7**, 661-678
7. Chaparro B.M., Thuillier S., Menezes L.F., Manach P.Y., Fernandes J.V., 2008, Material parameters identification: Gradient-based, genetic and hybrid optimization algorithms, *Computational Materials Science*, **44**, 339-346
8. Charalampakis A.E., Dimou C.K., 2010, Identification of Bouc-Wen hysteretic systems using particle swarm optimization, *Computers and Structures*, **88**, 21-22
9. Dafalias Y.F., Kourousis K.I., Saridis G.J., 2008, Multiplicative AF kinematic hardening in plasticity, *International Journal of Solids and Structures*, **45**, 2861-2880
10. Dvoršek N., Stopeinig I., Klančnik S., 2023, Optimization of Chaboche material parameters with a genetic algorithm, *Materials*, **16**, 1821
11. Hosseini R, Seifi R., 2020, Fatigue crack growth determination based on cyclic plastic zone and cyclic J-integral in kinematic–isotropic hardening materials with considering Chaboche model, *Fatigue and Fracture of Engineering Materials and Structures*, **43**, 2668-2682
12. Karolczuk A, Skibicki D, Pejkowski Ł., 2019, Evaluation of the Fatemi-Socie damage parameter for the fatigue life calculation with application of the Chaboche plasticity model, *Fatigue and Fracture of Engineering Materials and Structures*, **42**, 197-208
13. Koo G.-H., Lee J.-H., 2007, Investigation of ratcheting characteristics of modified 9Cr-1Mo steel by using the Chaboche constitutive model, *International Journal of Pressure Vessels and Piping*, **84**, 284-292
14. Kreethi R., Mondal A.K., Dutta K., 2017, Ratcheting fatigue behaviour of 42CrMo4 steel under different heat treatment conditions, *Materials Science and Engineering*, **679**, 66-74
15. Li J., Li Q., Jiang J., Dai J., 2018, Particle swarm optimization procedure in determining parameters in Chaboche kinematic hardening model to assess ratcheting under uniaxial and biaxial loading cycles, *Fatigue and Fracture of Engineering Materials and Structures*, **41**, 1637-1645
16. Mahmoudi A.H., Badnava H., Pezeshki-Najafabadi S.M., 2011, An application of Chaboche model to predict uniaxial and multiaxial ratcheting, *Procedia Engineering*, **10**, 1924-1929
17. Neri P., Holzbauer J., 2023, Experimental characterization and numerical modeling of wire rope isolators, *Proceedings of the Nodycon: Third International Nonlinear Dynamics Conference*, Rome, Italy
18. Ni Y.Q., Ko J.M., Wong C.W., 1998, Identification of non-linear hysteretic isolators from periodic vibration tests, *Journal of Sound and Vibration*, **217**, 737-756
19. Ortiz G.A., Alvarez D.A., Bedoya-Ruíz D., 2013, Identification of Bouc-Wen type models using multi-objective optimization algorithms, *Computers and Structures*, **114-115**, 121-132
20. Santus C., Grossi T., Romanelli L., Pedranz M., Benedetti M., 2023a, A computationally fast and accurate procedure for the identification of the Chaboche isotropic-kinematic hardening model parameters based on strain-controlled cycles and asymptotic ratcheting rate, *International Journal of Plasticity*, **160**, 103503
21. Santus C., Romanelli L., Grossi T., Neri P., Romoli L., *et al.*, 2022, Torsional-loaded notched specimen fatigue strength prediction based on mode I and mode III critical distances and fracture surface investigations with a 3D optical profilometer, *International Journal of Fatigue*, **161**, 106913

22. Santus C., Romanelli L., Grossi T., Bertini L., Le Bone L., *et al.*, 2023b, Elastic-plastic analysis of high load ratio fatigue tests on a shot-peened quenched and tempered steel, combining the Chaboche model and the Theory of Critical Distances, *International Journal of Fatigue*, **174**, 107713

23. Shafiqul B., Tasnim H., 2000, Anatomy of coupled constitutive models for ratcheting simulation, *International Journal of Plasticity*, **16**, 381-409

24. Wen Y.K., 1976, Method for random vibration of hysteretic systems, *Journal of Engineering Mechanics, ASCE*, **102**, 249-263

25. Zhang B., Wang R., Hu D., Jiang K., Hao X., *et al.*, 2020, Constitutive modelling of ratcheting behaviour for nickel-based single crystal superalloy under thermomechanical fatigue loading considering microstructure evolution, *International Journal of Fatigue*, **139**, 105786

Manuscript received November 22, 2023; accepted for print January 13, 2024

JOURNAL OF THEORETICAL AND APPLIED MECHANICS
62, 3, pp. 521-534, Warsaw 2024
https://doi.org/10.15632/jtam-pl/189805

FEED-FORWARD ARTIFICIAL NEURAL NETWORK AS SURROGATE MODEL TO PREDICT LIFT AND DRAG COEFFICIENT OF NACA AIRFOIL AND SEARCHING OF MAXIMUM LIFT-TO-DRAG RATIO

Rafał Kieszek, Maciej Majcher, Borys Syta, Adam Kozakiewicz
Military University of Technology, Faculty of Mechatronics, Armament and Aerospace, Warsaw, Poland
e-mail: borys.syta@wat.edu.pl

The problem of computation time in numerical calculations of aerodynamics has been studied by many research centres. In this work, a feed forward artificial neural network (FF-ANN) was used to determine the dependence of lift and drag coefficients on the angle of attack for NACA four-digit families. A panel method was used to generate the data needed to train the FF-ANNs. Optimisation using a genetic algorithm and a neural metamodel resulted in a non-standard NACA aerofoil for which the optimal angle of attack was determined with a maximum L/D ratio. The optimisation results were validated using the finite volume method.

Keywords: Artificial Neural Network (ANN), NACA airfoil, optimization, surrogate model, model reduction

List of designations

α – angle of attack
C_l, C_d – lift and drag coefficient, respectively
K – lift-to-drag ratio, L/D ratio
m – maximum camber in tenths of chord
p – position of the maximum camber along chord in tenths of chord
R – regression
R^2 – coefficient of determination
t – maximum airfoil thickness in tenths of chord
x_U, x_L, y_U, y_L – coordinates of point for upper (U) and lower (L) edge of airfoil
y_t, y_c – thickness and camber coordinates, respectively
θ – angle of inclination of tangent to chamber of airfoil at point
Ma_H – Mach number of undisturbed flow

1. State of the art

The use of artificial intelligence in engineering is becoming increasingly popular. The main task of artificial intelligence research is to construct machines and computer programs capable of performing selected functions of the mind and human senses, not amenable to numerical algorithmization. Such problems are sometimes called AI-complete and include decision-making in the absence of all data. This paper uses AI to predict behavior of a system for intermediate values not present in the results of numerical simulations.

The applications of Artificial Neural Networks (ANNs) is becoming increasingly popular, especially in areas that require time-consuming numerical calculations. One such an area is aerodynamic analysis. Costly wind tunnel tests or time-consuming CFD (computational fluid dynamics) analyses are required to determine aerodynamic characteristics of aerofoils. In this paper, the authors propose an alternative approach by replacing hard calculations (like CFD) with ANNs. The objective of this work was to demonstrate that this approach could enable rapid analysis of aerofoils and determine their aerodynamic characteristics without the need to perform numerical analyses for each aerofoil in a selected family of NACA aerofoils.

The problem of computation time for numerical calculations of aerodynamics has been studied by many research centres all over the world, demonstrating its complexity and the need for novel solutions. A variety of methods have been used to reduce the running time of algorithms. For example, Proper Orthogonal Decomposition (POD) (Berkooz *et al.*, 1992) is a method that reduces complexity of numerical simulations, such as CFD. Typically, it is used in CFD analyses (including turbulence analyses) to replace the Navier-Stokes equations with models that are simpler to solve. This method has been used by Bakewell and Lumley (1967), among others. Various methods based on machine learning tied to CFD are used to reduce computation time (San and Maulik, 2018), usually combined with neural networks. However, an ANN requires a large volume of training data and thus significant computational time. This problem was presented by Fukami *et al.* (2021). Buterweck and Głuch (2014) used ANNs to analyse the effect of Mach number on the prediction of turbine blade degradation. Prediction of aerodynamic characteristics using an artificial neural network for a wind turbine was performed by Verma and Baloni (2021). Sekar *et al.* (2010) presents an approach based on analysis of data produced with a CFD solver to predict the incompressible laminar flow field around aerofoils. The approach was based on a combination of a deep convolutional neural network (CNN) and a deep multilayer perceptron (MLP). Aramendia *et al.* (2019) used ANNs to predict the aerodynamic efficiency of Gurney flaps. A CFD-based drag coefficient analysis was also carried out in (Viquerat and Hachem, 2020), where a set of random geometries based on Bézier curves was prepared to train the neural network. Pressure distributions were calculated for several representative cases. In addition, a lift and drag coefficient was predicted based on CFD approximation calculations (Kharal and Saleem, 2012). Kharal and Saleem (2012) described an aerofoil using Bézier curves, developed their aerodynamic characteristics and then proceeded with FF-ANN training. The inverted ANNs were then used to determine aerofoil geometry for a given drag coefficient. Similarly, inverted ANNs were used in (Sun *et al.*, 2015), where geometry of the aerofoil was described as shown in Fig. 1. The pressure distribution on the aerofoil and then on the wing was determined by the proposed ANN algorithm. Thirumalainambi and Bardina (2003) also analysed the optimal ANN structure for predicting aerodynamic coefficients of an aircraft.

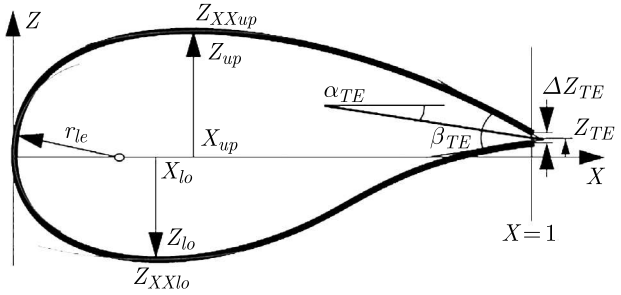

Fig. 1. Airfoil geometry (Sobieczky, 1999)

A frequently used method for optimising aerodynamics is genetic algorithms. Porta Ko *et al.* (2023) describes the process of optimising kinked aerofoils using the NSGA-II (Non-dominated

Sorting Genetic Algorithm). Optimisation to minimise the aerodynamic forces generated was carried out in (Khan *et al.*, 2022) where solar panels were studied.

The most common method used in computer fluid mechanics is the finite volume method (FVM) used for CFD analyses, which takes place in conjunction with ANNs. One example of less commonly used methods would be a combination of the vortex method and a neural network (Sessarego *et al.*, 2020).

The use of surrogate models is relatively infrequently used in practice due to errors arising from the surrogate model approximations. The main purpose of the article is to demonstrate that it is possible to prepare a surrogate model based on AI or, more precisely, SSN. The accuracy of such a model should be sufficient and the optimization results should be no worse than the available solutions.

2. NACA four-digit family

In this work, an artificial neural network was used to determine the dependence of lift and drag coefficients on the angle of attack for NACA four-digit aerofoils. First, the data was generated from an open database of aerodynamic diagrams to train the ANN. The data generation was described by Drela (1989).

An asymmetric NACA four-digit aerofoil (NACA – National Advisory Committee for Aeronautics, NACAmpt) is defined by three parameters: m, p, t. Equations (2.1) and (2.2) were used to describe the aerofoil geometry mathematically, based on the work [12]

$$\begin{aligned} x_U &= x - y_t \sin\theta \qquad & y_U &= y_c + y_t \cos\theta \\ x_L &= x + y_t \sin\theta \qquad & y_L &= y_c - y_t \cos\theta \end{aligned} \tag{2.1}$$

and

$$\begin{aligned} y_t &= \pm\frac{t}{0.2}(a_1\sqrt{x} - a_2 x - a_3 x^2 + a_4 x^3 - a_5 x^4) \\ \theta &= \arctan\frac{dy_c}{dx} \\ y_c &= \begin{cases} \dfrac{m}{p^2}(2px - x^2) & \text{for} \quad 0 \leqslant x \leqslant p \\ \dfrac{m}{(1-p)^2}[(1-2p) + 2px - x^2] & \text{for} \quad p \leqslant x \leqslant 1 \end{cases} \end{aligned} \tag{2.2}$$

where: $a_1 = 0.2969$, $a_2 = 0.1260$, $a_3 = 0.3516$, $a_4 = 0.2843$, $a_5 = 0.1015$ – coefficients defined by NACA.

In the remainder of this work, only asymmetrical aerofoils were analysed. The database of aerodynamic coefficients acting on the aerofoil was determined with reference to (Oliveira, 2021), where after a simple parameterisation of the code, the lift C_l and drag C_d versus the angle of attack α was calculated by Xfoil. Xfoil is a panel-based software that enables analysis of aerofoils and wings operating at low Reynolds numbers.

3. Artificial neural network

This paper uses a feed-forward artificial neural network (FF-ANN). The input (training) parameters for the NACA aerofoil number were: $m, p \in \langle 2; 8\rangle$, $t \in \langle 8; 24\rangle$, as well as angles of attack α within $\pm 24°$. The output (training) data was determined using the Xfoil software; the lift and drag coefficients corresponding to the cases in the input database. The Reynolds number $\mathrm{Re} = 5.7 \cdot 10^6$ and Mach number $\mathrm{Ma}_H = 0.1439$ were set as constant values. This corresponded

to velocity of 49.39 m/s for an average aerodynamic chord of length 1.738 m. The database containing the characteristics of 441 profiles was needed to train the artificial neural network. Due to the lack of availability of such a large database of NACA four-digit profiles, it was decided to use Xfoil to prepare it.

As a result of numerical analyses, it was decided to develop separate ANNs (trained in parallel) for the prediction of lift and drag coefficients for selected angles of attack from the range $\pm 24^\circ$ with an increment of $\Delta\alpha = 2^\circ$.

The MATLAB Neural Network Toolbox was used as the ANN environment. The ANNs were trained using the SCG (Scaled Conjugate Gradient) backpropagation algorithm. The objective of the training was to minimise the mean squared error (MSE) of the data fit. The ANN architecture was optimised, where the mean absolute error (MAE) was the objective function. An optimisation of the ANN structure using a genetic algorithm was done for two and three hidden layers. A feed-forward ANN (3-65-8-1) was chosen as the optimal ANN structure. A diagram of the ANN used is shown in Fig. 2. The optimisation was run until MAE was no greater than 3%. During the ANN optimisation, the size of the ANN was not increased beyond 500 neurons to prevent "learning by heart".

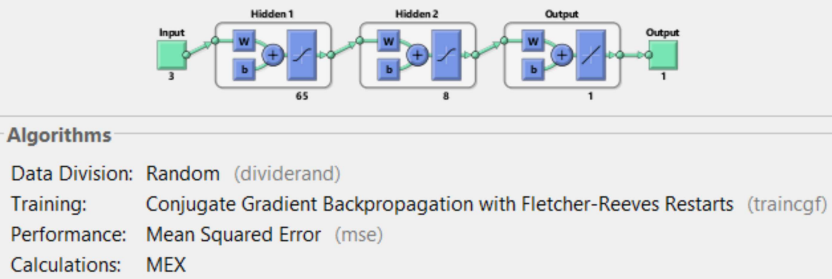

Fig. 2. Scheme of the used artificial neural network, where: w – weights, b – bias

Figure 3 shows the regression results for the ANNs used, trained for the zero angle of attack and the predicted values of the drag coefficient C_d. A high regression coefficient of $R = 0.9858$ was obtained for all the data.

A separate ANN was used for each angle of attack. This reduced the duration of the learning process and increased the accuracy of the ANN learning. The learning time for all optimised ANNs was less than 130 seconds with an approximation error less than 1%. Figure 4 shows the coefficient of lift C_l and drag C_d predicted by the trained ANNs, as a function of the angle of attack for the NACA 2412 aerofoil. The neural model achieved a high coefficient of determination for both lift (0.9984) and drag coefficient prediction (0.9911), compared to the data generated with Xfoil. It also presents the lift and drag coefficients obtained in experimental tests, based on a NACA report (Abbott *et al.*, 1945). For angles of attack from -10° to 16°, the analysis performed with Xfoil and ANN were consistent with experimental tests. For larger angles, the differences were significant. This could be due to the choice of the Reynolds number in the Xfoil software, as confirmed by the conclusions from (Günel *et al.*, 2016) or a tendency towards numerical errors for angles of attack: $\alpha > 8^\circ$ (Saad *et al.*, 2017). However, in order to determine the aerofoil L/D ratio, the accuracy of the ANN was sufficient, as usually the maximum L/D ratio corresponds to an angle of attack in the range from 2° to 8°.

In order to test the adopted research concept, the lift coefficient as a function of angle of attack was calculated for a non-standard NACA four-digit aerofoil in Xfoil. This aerofoil was not present in the ANN teaching database. This aerofoil was NACA model (2.4)(3.6)12, where $m = 2.4$, $p = 3.6$ and $t = 12$ are shown in Fig. 5, which was numerically analysed using the panel method. Comparative results for the Xfoil and ANN are shown in Fig. 6.

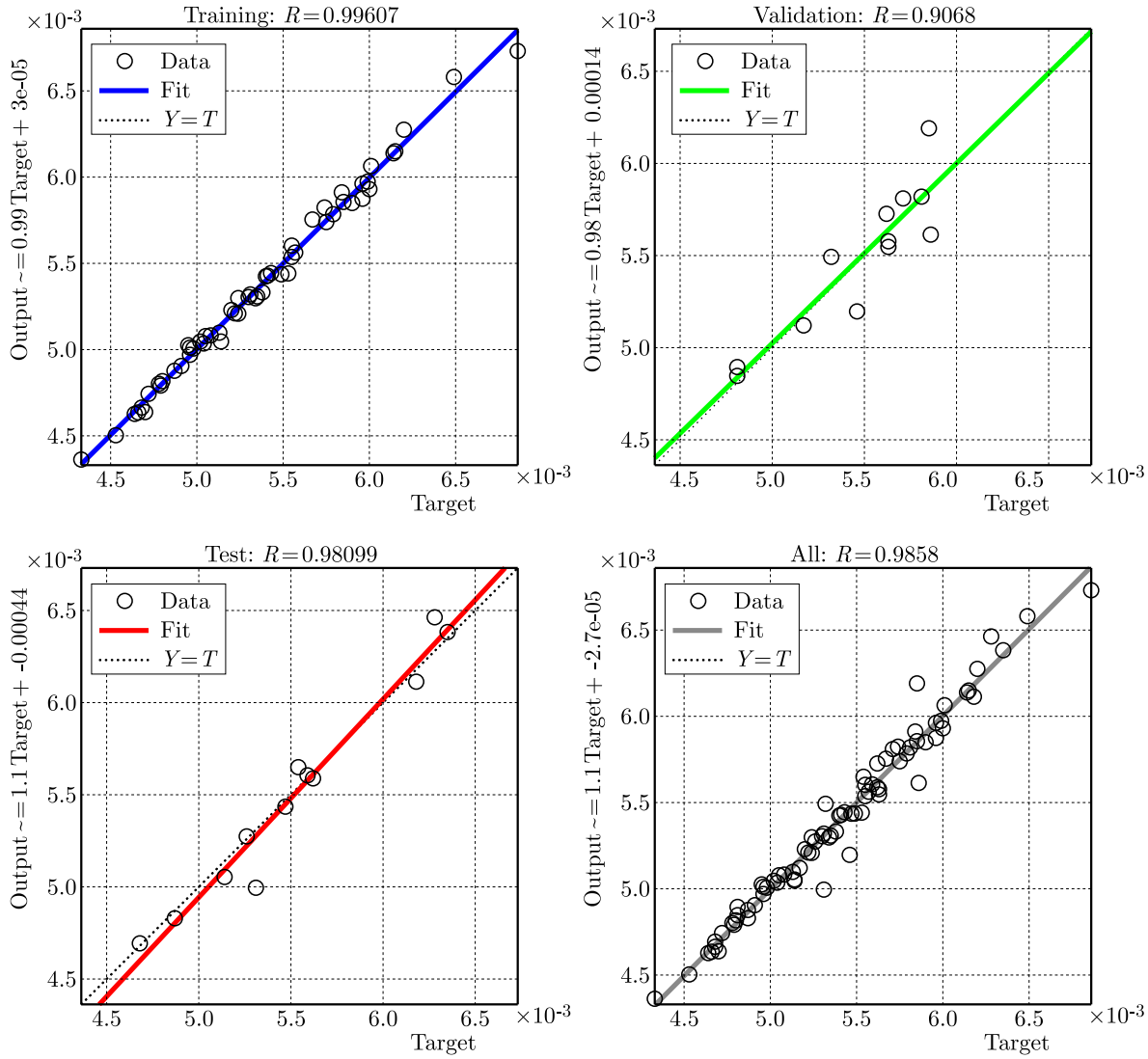

Fig. 3. Regression of used ANN

For the NACA (2.4)(3.6)12 aerofoil, the coefficient of determination (R^2) of the lift coefficient was 0.998. However, the ANN was not able to correctly predict the distribution of the drag coefficient for larger angles of attack (above 16° and below −10°). For angles of attack between −10° and 16°, the accuracy was higher, and the corresponding coefficient of determination was 0.9942, as shown in Fig. 7.

4. Optimization

In this work, an attempt at optimisation was made using the presented neural metamodel to maximise the L/D ratio, $K = C_l/C_x$. Both the lift and drag coefficients were determined using ANNs. The default genetic algorithm (GA) in Matlab was used for optimisation, the working principle of which was based on (Conn *et al.*, 1991). In the algorithm used, the decision variables were parameters m, p and t, which described geometry of the aerofoil. Restrictive conditions related to the span of the database that were used to teach the ANN were imposed, assuming that m = 2-6, p = 2-6 and t = 12-24. The angle of attack α was a discrete variable within ±24° with an increment of 2°. The algorithm with the objective function determined the aerofoil L/D ratio K for all angles of attack α and returned its largest value, the corresponding angle

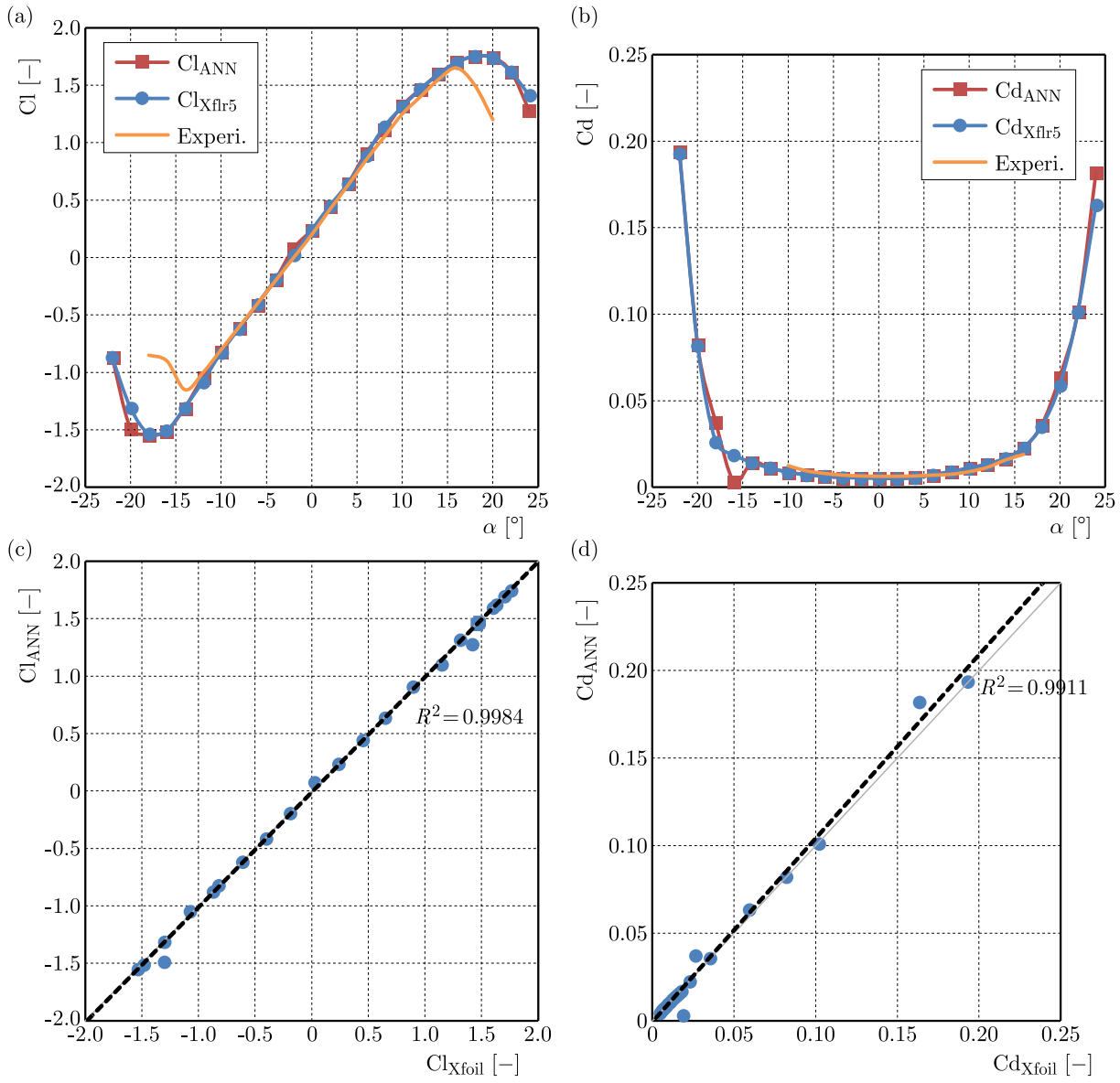

Fig. 4. Predicted, computed and by Xfoil experimental lift (a) and drag (b) coefficients vs. the angle of attack, and the coefficient of determination of lift (c) and drag (d) coefficients for NACA 2412

of attack and the values of the decision variables defining the aerofoil geometries. The NACA 12(5.18)(4.18) aerofoil resulting from the optimisation is shown in Fig. 8.

According to the ANN, the maximum L/D ratio of the tested aerofoil corresponded to the angle of attack $\alpha = 4°$, and after optimisation it was $K = 194.4$ for the ANN and $K = 197.4$ for Xfoil. This provided the difference of relative error of L/D ratio $RE(K) = 1.53\%$. Figure 9 shows the relationship $RE(K) = f(\alpha)$. For angles of attack below $\alpha = -12°$, the calculations diverged.

Thinner aerofoils achieved higher L/D ratios, so the algorithm naturally brought the aerofoil thickness down to a lower limit $t = 12$. Due to simplifications made for the drag coefficient confounded in the Xfoil software, a comparative analysis of the prediction results from the ANN, the Xfoil programme and the Ansys Fluent software were applied.

For further numerical tests of the aerofoil after the optimisation process, a suitable geometrical model of the aerofoil was developed, together with the computational domain in the Ansys Workbench DesignModeler software (Fig. 10).

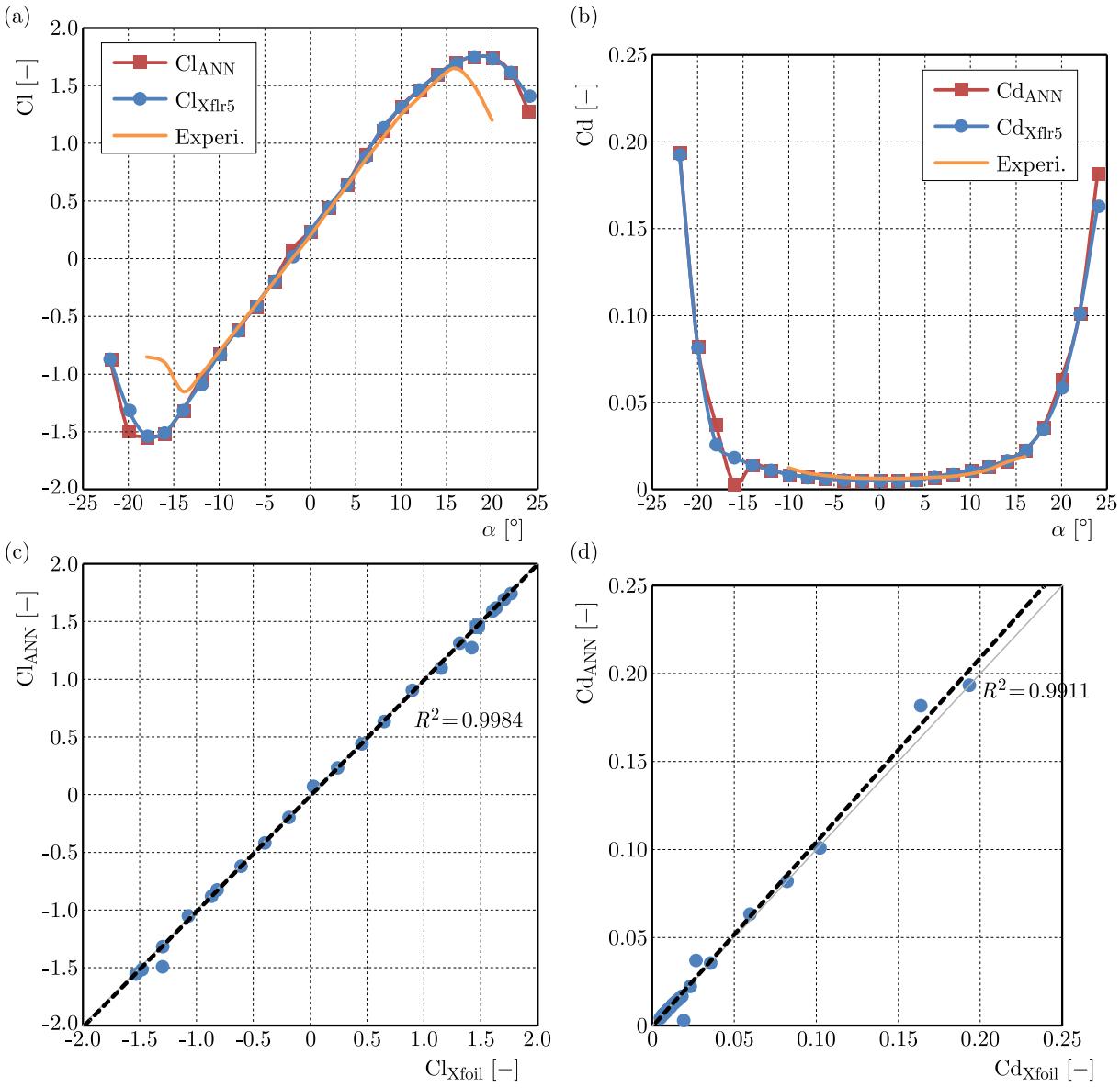

Fig. 5. Example of geometry of a non-standard NACA aerofoil (2.4)(3.6)12

At the stage of developing the domain for digitisation, the relevant edges were assigned with appropriate names representing the boundary conditions. The outer edges of the calculation area were assigned with a pressure-far-field condition, while the edges representing the aerofoil outline were assigned with a wall condition. The computational area was then digitised. The developed computational domain was digitised using a structured grid (Fig. 10a). The grid was appropriately compacted towards the aerofoil (Fig. 10b). The total number of grid elements was 306 000. The numerical grid thus developed was exported in .msh format to Ansys Fluent for numerical simulations of the flow around the aerofoil.

Numerical flow simulations were performed for the Mach number $\mathrm{Ma}_H = 0.1439$ and a reference pressure of 101325 Pa, with Double Precision and Density-Based solver settings (the "Implicit" method). Numerical simulations of the flow around the aerofoil were done over a range of angles of attack $\alpha = \pm 24°$ with an increment of $\Delta\alpha = 2°$. The determinant of convergence of the calculations, and thus the termination of simulation for a given angle of attack, was the obtained value – which was constant in the iteration function of the lift and drag coefficients referenced to the value of the chord, 1.738 m.

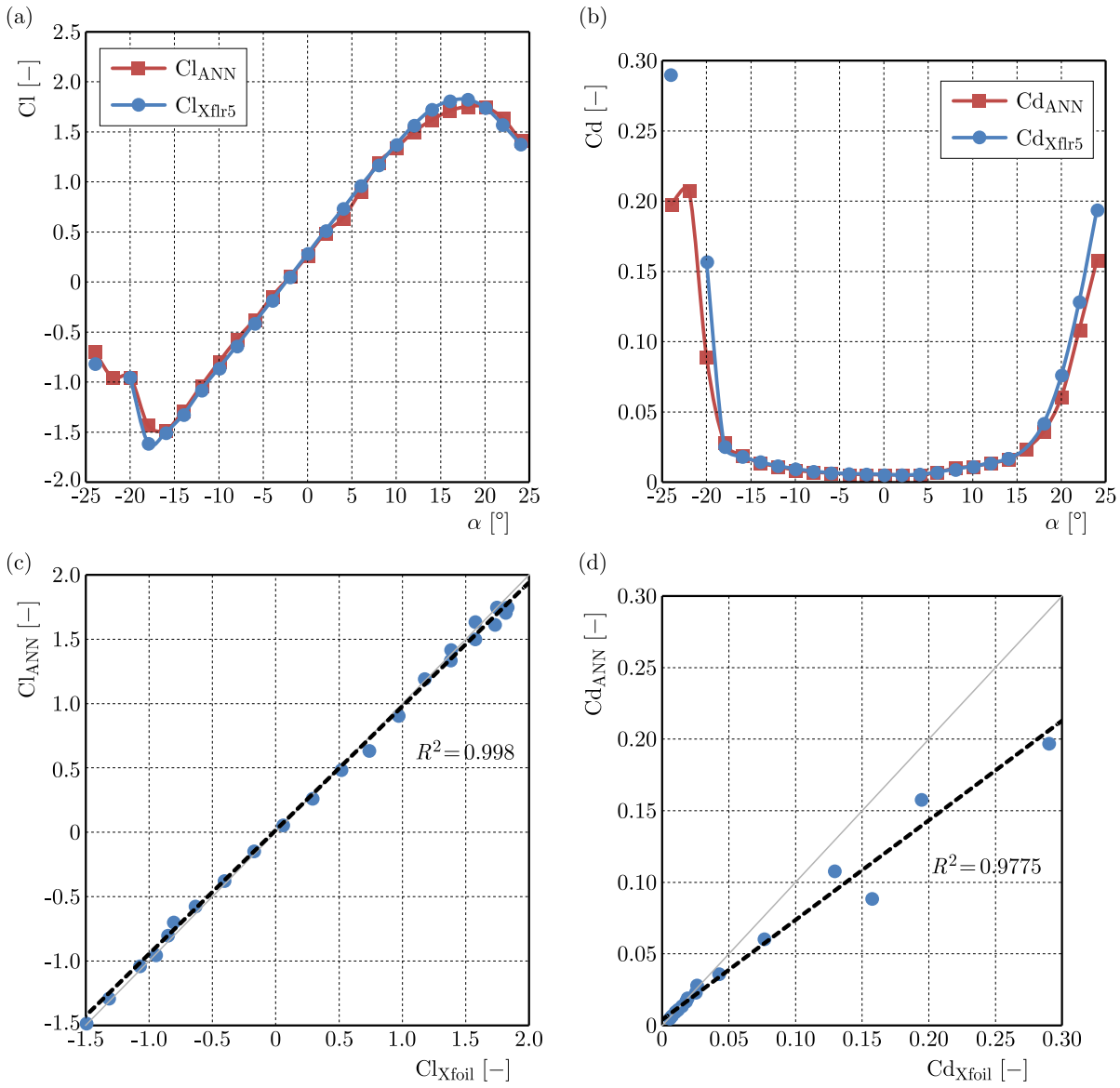

Fig. 6. Predicted by SSN and computed by Xfoil (Xflr5) lift (a) and drag (b) coefficients vs. the angle of attack, and the coefficient of determination of lift (c) and drag (d) coefficients for NACA (2.4)(3.6)12

The results of analyses comparing the aerodynamic characteristics of the optimised aerofoil obtained with the ANN, Xfoil and Ansys Fluent are shown in Fig. 11.

Based on the obtained characteristics, it can be concluded that a satisfactory agreement was achieved, especially in the linear range $C_l = f(\alpha)$. Over the range of critical angles of attack, the lift coefficients obtained from the calculations performed in Ansys Fluent and Xfoil were very close to each other, and partly differed from the values obtained based on the ANN prediction. A similar situation occurred with large negative angles of attack $-15°$ to $-24°$. In the case of the $C_d = f(\alpha)$ characteristics, the drag force coefficients obtained from the numerical analyses run in the Ansys Fluent software were higher than the values obtained from the ANN prediction and Xfoil calculations. This is because for each angle of attack, the Ansys Fluent software determined the drag as the sum of the pressure drag and friction drag. In the case of SSN and Xfoil, the drag calculations run with the assumption of constant freestream velocity and the steady flow which resulted in increased inaccuracies at higher angles of attack. As with the previous profile, the ANN prediction for the drag coefficient over the full range of angles of attack was inadequate. However, for the angles of attack in the range from $-10°$ to $14°$, it was already higher, and the coefficient of determination was $R^2 = 0.9983$, as shown in Fig. 12.

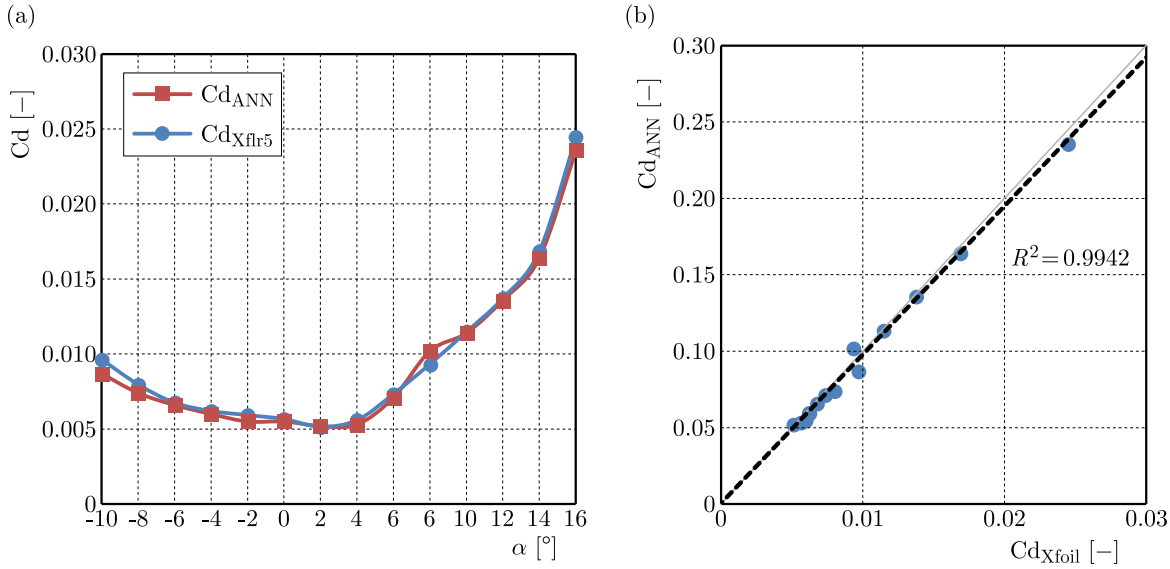

Fig. 7. Predicted by SSN and computed by Xfoil drag coefficients vs. the angle of attack (a) and the coefficient of determination of the drag coefficient (b) for small angles of attacks ($-10 \leqslant \alpha \leqslant 16°$) for NACA (2.4)(3.6)12

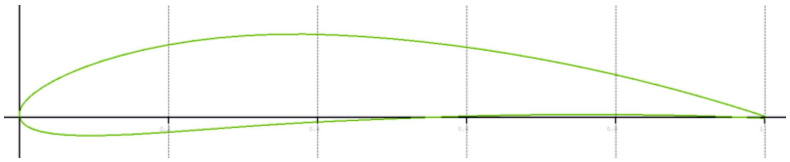

Fig. 8. NACA 12(5.18)(4.18) aerofoil, a result of the optimisation algorithm

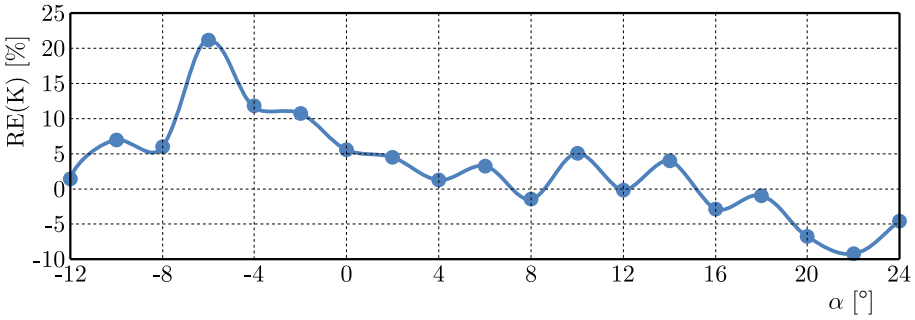

Fig. 9. Relative difference in the L/D ratio determined by ANN and Xfoil

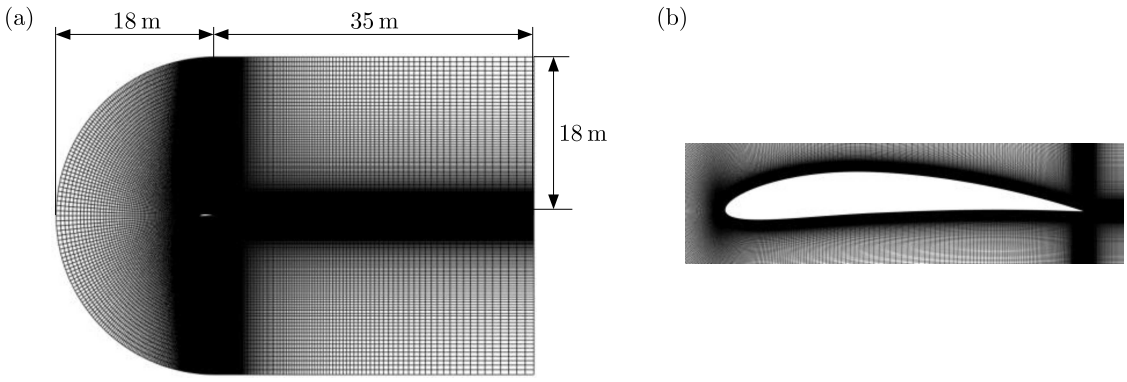

Fig. 10. Discretized computational domain (a), discretized airfoil area (b)

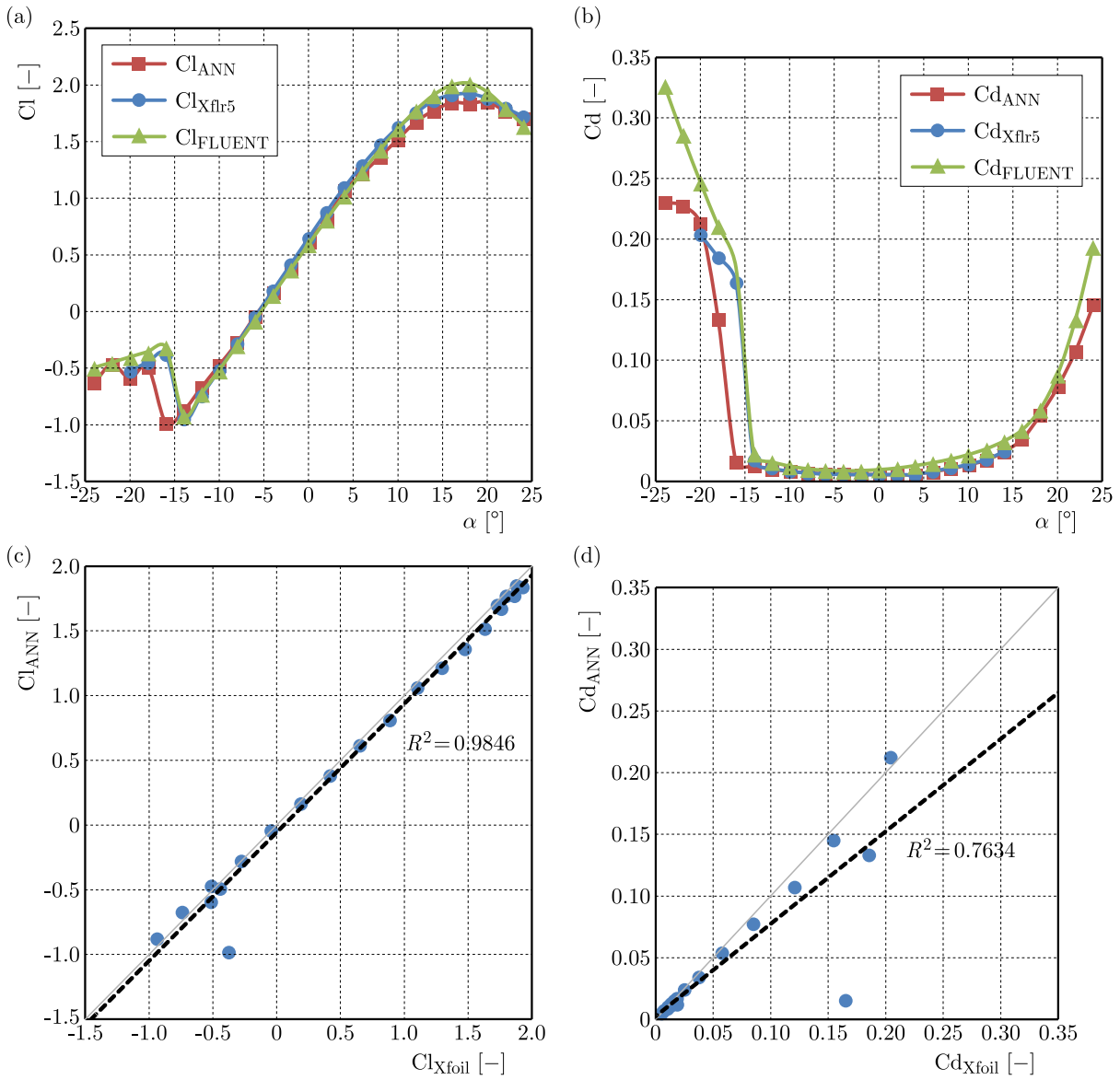

Fig. 11. Predicted by ANN and computed by Xfoil (Xflr5) lift (a) and drag (b) coefficients vs. the angle of attack, and the coefficient of determination of lift (c) and drag (d) coefficients for NACA (5.18)(4.18)12

A comparative analysis of the coefficient of determination of the lift and drag coefficients for all algorithms used was also performed. This comparison is shown in Fig. 13 with $\alpha = \pm 10°$.

The ANNs were trained on the data produced in Xfoil, which was the computational kernel of Xflr5, and therefore the predictions of the aerodynamic coefficients were consistent with the results calculated by Xfoil (Figs. 13a and 13b), and were characterised by $R^2 = 0.9995$ for C_l and $R^2 = 0.9983$ for C_d, respectively. In contrast, the coefficient of determination for the data predicted by the ANN and calculated in Ansys Fluent were $R^2 = 0.9980$ for C_l and $R^2 = 0.9657$ for C_d (Figs. 13e and 13f), respectively.

According to the references reviewed (Hsiao *et al.*, 2013; López-Briones *et al.*, 2020; Dhileep *et al.*, 2020) the lift coefficient calculated with Xfoil and Ansys Fluent were in agreement. This was confirmed by numerical tests, characterised by a coefficient of determination $R^2 = 0.9974$ (Fig. 13c). On the other hand, the frictional drag component was omitted from the Xfoil software and the aerodynamic drag coefficient was underestimated, with a coefficient of determination of $R^2 = 0.9652$ (Fig. 13d).

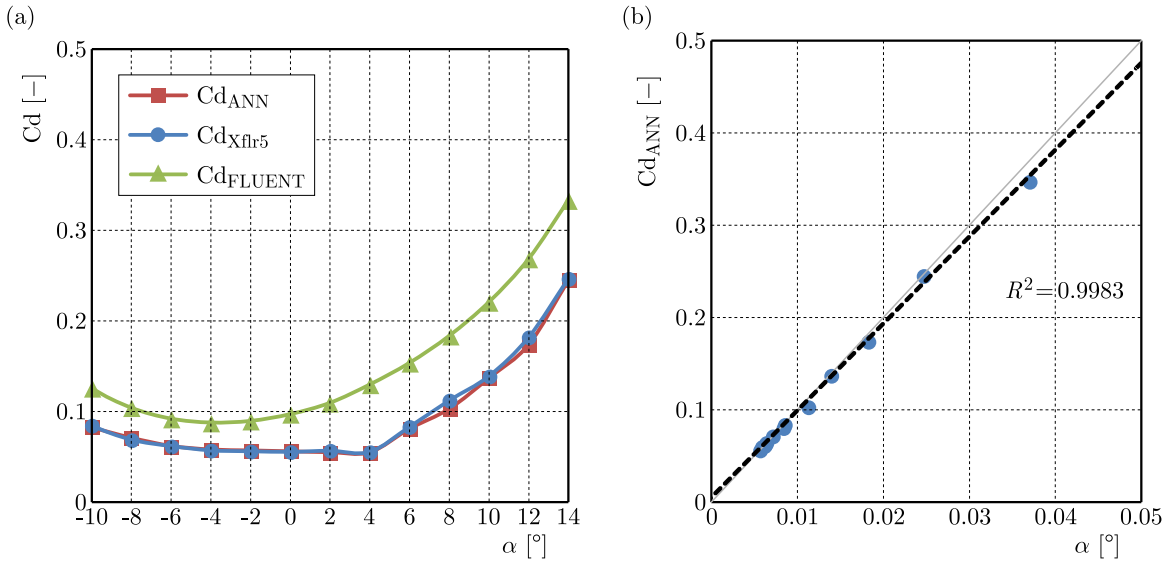

Fig. 12. Predicted by SSN and computed by Xfoil and FLUENT drag coefficient vs. the angle of attack (a) and coefficient of determination of the drag coefficient (b) for small angles of attacks ($-10 \leqslant \alpha \leqslant 16°$) for NACA (5.18)(4.18)12

The analyses were complemented by a comparison of the L/D ratio determined using the methods previously referred to (Fig. 14). The maximum L/D ratios determined by Xfoil and by ANN were $K_{max} = 197$ and $K_{max} = 195$, respectively, for the angle of attack $\alpha = 4°$. In contrast, due to inclusion of the frictional drag component in Ansys Fluent, the L/D ratio for the angle of attack $\alpha = 4°$ was much lower, $K = 78$. The maximum L/D ratio corresponded to the angle of attack $\alpha = 6°$ and was $K_{max} = 80$. The predicted excellence of the aerofoil calculated using Ansys Fluent decreased, as given in (Dhileep *et al.*, 2020).

5. Conclusion

This work demonstrates that the feed-forward artificial neural networks (FF-ANN) used to determine the lift and drag coefficients for a non-standard NACA four-digit aerofoil obtained the change in the lift coefficient as a function of the angle of attack, at a selected interval, with a coefficient of determination of $R^2 = 0.9846$, while for the drag coefficient, the change was a function of the angle of attack and $R^2 = 0.7634$ for the entire range of angles of attack tested. If the interval was narrowed to a range of $-10°$ to $+16°$, the coefficient increased to $R^2 = 0.9983$. The results obtained were compared to the experimental tests (Figs. 4a and 4b) for verification. The coefficient of determination for the lift coefficient, for angles of attack ranging from $-10°$ to $+16°$ was $R^2 = 0.9695$, which can be considered a good result. According to the knowledge from reference literature, the predicted aerofoil L/D ratio calculated using finite volumes decreased, relative to the panel method, but the nature of the L/D ratio change remained the same.

The disadvantages of the presented method are related to the disadvantages of metamodeling and machine learning. There are always errors in the metamodel due to interpolation of functions. In addition, when analyzing a different problem, or even the same problem but for a different Reynolds number, it is necessary to re-generate training data and train the SSN. Generalizing the algorithm for any Reynolds number would require a significant expansion of the database of training cases. In addition, the growth of the database would likely reduce the accuracy of prediction even for the Reynolds number found in the training case database. In further studies,

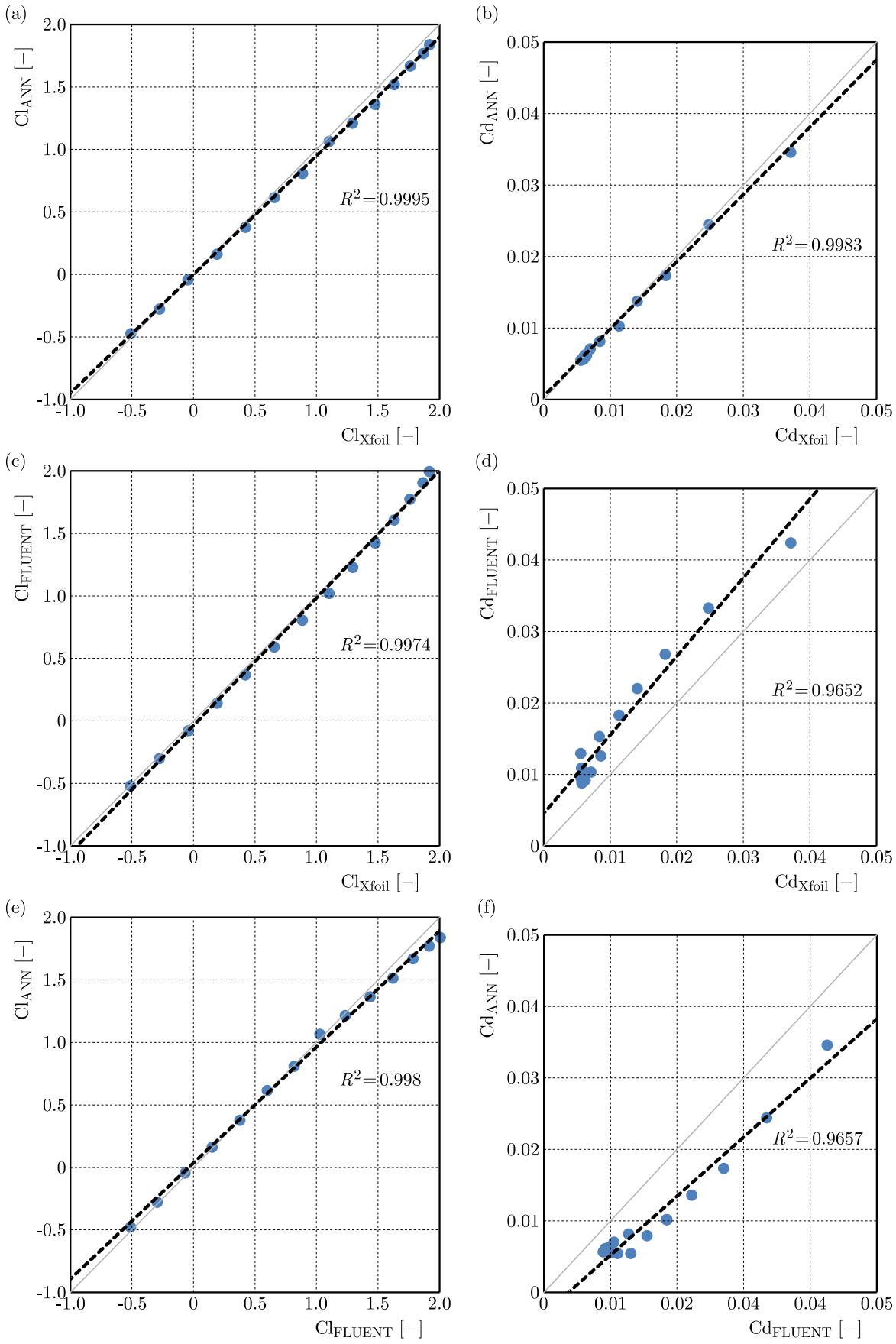

Fig. 13. Cross validation of coefficient of determination for lift (1st column) and drag (2nd column) coefficients (for $\alpha = \pm 10°$) for NACA (5.18)(4.18)12 calculated by ANN and Xfoil (a) and (b), FLUENT and Xfoil (c) and (d), ANN and FLUENT (e) and (f)

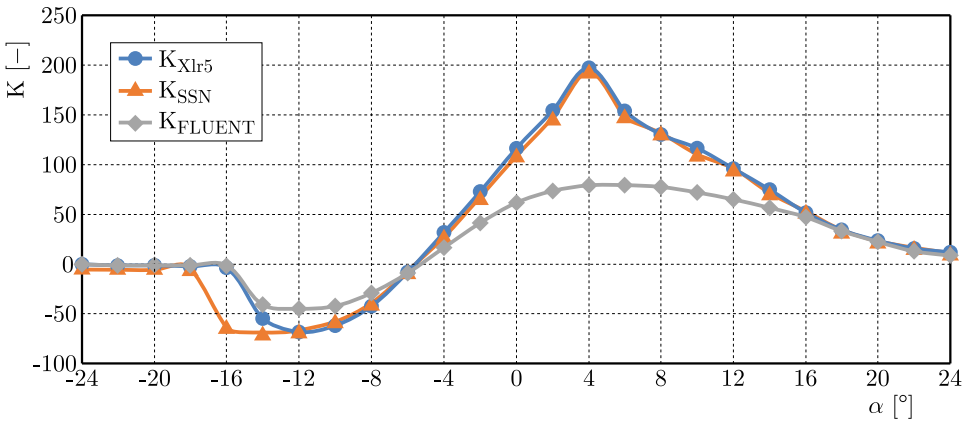

Fig. 14. Comparison of the L/D ratio determined with ANN, Xflr and Fluent

we intend to use finite volume methods (FVM) to obtain more accurate results by, among other things, taking into account frictional resistance, which Xfoil does not.

The proposed algorithm can be used as a metamodel for optimisation. The FF-ANNs reduced the execution time of the algorithm by replacing the solution of computer fluid mechanics equations (in the panel method), while retaining high accuracy for a properly selected range.

The optimised aerofoil will be used on the wing of an unmanned aerial platform designed under Project SZAFIR – Competition No. 4/SZAFIR/2021.

Acknowledgement

This paper was created as part of the project: Unmanned water surface/air platform using ground effect to support offshore Special Forces operations, funded by the NCBiR (National Centre for Research and Development), "SZAFIR" – Competition No. 4/SZAFIR/2021, Contract No. DOB-SZAFIR/01/B/036/04/2021 dated 20/12/2022.

References

1. Abbott H., Doenhoff E., Lous S., Stivers J., 1945, Summary of airfoil data, *National Advisory Commitee for Aeronautics Report*, **824**
2. Aramendia I., Fernandez-Gamiz U., Zulueta E., Saenz-Aguirre A., Teso-Fz-Betoño D., 2019, Parametric study of a Gurney flap implementation in a DU91W (2) 250 airfoil, *Energies*, **12**, 2, 294
3. Bakewell H.P., Lumley J.L., 1967, Viscous sublayer and adjacent wall region in turbulent pipe flow, *Physics Fluids*, **10**, 1880-1889
4. Berkooz G., Holmes P., Lumley J.L., 1993, The proper orthogonal decomposition in the analysis of turbulent flows, *Annual Review of Fluid Mechanics*, **25**, 539-575
5. Butterweck A., Głuch J., 2014, Neural network simulator's application to reference performance determination of turbine blading in the heat-flow diagnostics, [In:] *Intelligent Systems in Technical and Medical Diagnostics*, Springer, Berlin, Heidelberg
6. Conn A.R., Gould N.I. Toint P., 1991, A globally convergent augmented Lagrangian algorithm for optimization with general constraints and simple bounds, *SIAM Journal on Numerical Analysis*, **28**, 2, 545-572
7. Dhileep K., Kumar D., Ghosh S., Ali S.F., Arockiarajan A., 2020, Numerical study of camber morphing in NACA0012 airfoil, *Conference: AIAA AVIATION 2020 Forum*, 2781

8. Drela M., 1989, XFOIL: An analysis and design system for low Reynolds number airfoils, [In:] *Low Reynolds Number Aerodynamics. Proceedings of the Conference Noire Dame*, Indiana, USA, Springer Berlin Heidelberg, 1-12
9. Fukami K., Fukagata K., Taira K., 2021, Machine-learning-based spatio-temporal super resolution reconstruction of turbulent flows, *Journal of Fluid Mechanics*, **909**
10. Günel O., Ko E. Yavuz T. 2016, CFD vs. XFOIL of airfoil analysis at low Reynolds numbers, *IEEE International Conference on Renewable Energy Research and Applications (ICRERA)*, 628-632
11. Hsiao F.B., Bai C.J., Chong W.T., 2013, The performance test of three different horizontal axis wind turbine (HAWT) blade shapes using experimental and numerical methods, *Energies*, **6**, 6, 2784-2803
12. https://web.stanford.edu/ cantwell/AA200_Course_Material/The%20NACA%20airfoil %20series.pdf, [Online 2021.10.25]
13. Khan A.Y., Ahmad Z., Sultan T., Alshahrani S., Hayat K., Imran M., 2022, Optimization of photovoltaic panel array configurations to reduce lift force using genetic algorithm and CFD, *Energies*, **15**, 24, 9580
14. Kharal A., Saleem A., 2012, Neural networks based airfoil generation for a given Cp using Bezier-PARSEC parameterization, *Aerospace Science and Technology*, **23**, 1, 330-344
15. López-Briones Y.F., Sánchez-Rivera L.M., Arias-Montano A., 2020, Aerodynamic analysis for the mathematical model of a dual-system UAV, *17th International Conference on Electrical Engineering, Computing Science and Automatic Control (CCE)*
16. Oliveira R.F. de, 2021, https://github.com/theolivenbaum/XFOILinterface [Online 2021.12.02]
17. Porta Ko A., Smidt S., Schmehl R., Mandru M., 2023, Optimisation of a multi-element airfoil for a fixed-wing airborne wind energy system, *Energies*, **16**, 8, 3521
18. Saad M.M.M., Mohd S.B., Zulkafli M.F., Shibani W.M,, 2017, Numerical analysis for comparison of aerodynamic characteristics of six airfoils, *AIP Conference Proceedings*, AIP Publishing
19. San O., Maulik R., 2018, Neural network closures for nonlinear model order reduction, *Advances in Computational Mathematics*, **44**, 1717-1750
20. Sessarego M., Feng J., Ramos-García N., Horcas S.G., 2020, Design optimization of a curved wind turbine blade using neural networks and an aero-elastic vortex method under turbulent inflow, *Renewable Energy*, **146**, 1524-1535
21. Sekar V., Jiang Q., Shu, C., Khoo B.C., 2019, Fast flow field prediction over airfoils using deep learning approach, *Physics of Fluids*, **31**, 5, 057103
22. Sobieczky H., 1999, Parametric airfoils and wings, [In:] *Recent Development of Aerodynamic Design Methodologies*, Fujii K., Dulikravich G.S. (Edit.), Notes on Numerical Fluid Mechanics (NNFM), vol 65, Vieweg+Teubner Verlag
23. Sun G., Sun Y., Wang S., 2015, Artificial neural network based inverse design: Airfoils and wings, *Aerospace Science and Technology*, **42**, 415-428
24. Thirumalainambi R., Bardina J., 2003, Training data requirement for a neural network to predict aerodynamic coefficients, [In:] *Independent Component Analyses, Wavelets, and Neural Networks*, International Society for Optics and Photonics, 92-103
25. Verma N., Baloni B.D., 2021, Artificial neural network-based meta-models for predicting the aerodynamic characteristics of two-dimensional airfoils for small horizontal axis wind turbine, *Clean Technologies and Environmental Policy*, **24**, 2, 563-577
26. Viquerat J., Hachem E., 2020, A supervised neural network for drag prediction of arbitrary 2D shapes in laminar flows at low Reynolds number, *Computers and Fluids*, **210**, 104645

Manuscript received October 31, 2023; accepted for print January 13, 2024

JOURNAL OF THEORETICAL AND APPLIED MECHANICS
62, 3, pp. 535-545, Warsaw 2024
https://doi.org/10.15632/jtam-pl/189814

NUMERICAL INVESTIGATION OF THE ASYMPTOTIC BEHAVIOR OF TAPE SPRINGS

Michele Coppedè, Roberto Paroni, Marco Picchi Scardaoni
University of Pisa, Department of Civil and Industrial Engineering, Pisa, Italy
e-mail: m.coppede1@studenti.unipi.it; roberto.paroni@unipi.it; marco.picchiscardaoni@ing.unipi.it

Here, we investigate the behavior of the energy of a tape spring as its thickness becomes smaller and smaller. We consider the case of pure bending, i.e., we impose opposite rotations at both ends of the device. First, tape springs are introduced and their peculiar mechanical behavior is explained, and the details of the numerical model are carefully introduced. Then, a parametric study of the device is conducted for increasing end rotations and decreasing values of the thickness. Thus, we obtain parametric diagrams of reaction moments, energy per unit thickness, and energy densities. Finally, energy estimates are obtained.

Keywords: tape spring energy density, bending, elastic hinge, asymptotic behavior

1. Introduction

Tape springs are thin structures with transverse curvature (shells) used in many fields of engineering, for example in the aerospace engineering (CRTS reflector Seffen *et al.*, (2000)). These devices can be used as real deployment organs, thanks to their ability to form localized elastic hinges. This effect is entirely due to presence of the initial transverse curvature. An example of a daily use of these tapes is in carpenter's meters.

In their simplest form they are longitudinally straight, but they can also be provided with a non-zero initial longitudinal curvature. A fundamental characteristic common to all types of tape springs is the ability to concentrate the curvature even if there are no mechanical hinges, i.e., they are capable to form elastic hinges. The geometrical characteristics of straight tape spring devices are: length L, transverse radius of curvature R, angle subtended by the cross-section curve α and thickness t. The characteristics of an isotropic material are Young's modulus E and Poisson's ratio ν. The geometrical parameters are shown in Fig. 1. In general, the relation between the geometrical parameters can be summarized as follows: $t \ll a \ll L$, so these devices can be classified as shells.

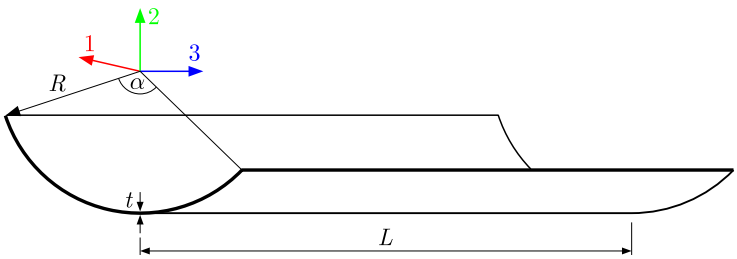

Fig. 1. Geometrical parameters of a straight tape spring

Many studies have been conducted on these devices in the past, mainly on the mechanical behavior under pure bending. In the work of Seffen and Pellegrino (1999), an introduction to the mechanical behavior of tape springs subjected to pure bending and an investigation about the

dynamic deployment of these devices is presented. In the article of Seffen *et al.* (2000), a study about curved tape springs is presented, showing that they have much in common with straight tape spring devices. A dissertation about the formation of elastic folds and an investigation of the mechanical behavior during pure bending is proposed in Seffen's PhD thesis (1997), where the author presents an estimate of key parameters of the moment-rotation relationship. A work about static and dynamic properties of three dimensional tape spring folds, using both experimental and theoretical methods, is presented in Walker's PhD thesis (2004). In the works of Guinot *et al.* (2012), Picault *et al.* (2013, 2014) and Martin *et al.* (2020) different beam models of tape springs are proposed in the case of pure bending, and in the one of Picault *et al.* (2016) there is an extension to 3D motions. In Kumar *et al.* (2023), the authors derive a one-dimensional model for tape springs that accounts for bending and twisting.

As shown in the literature, the moment-rotation relationship of tape spring devices undergoing pure bending is almost linear until a peak moment is reached, then it becomes highly non-linear as the elastic hinge forms. Due to this high non-linearity, the numerical modeling of these devices must be carefully addressed. A schematic example of the moment-rotation relationship is shown in Fig. 2.

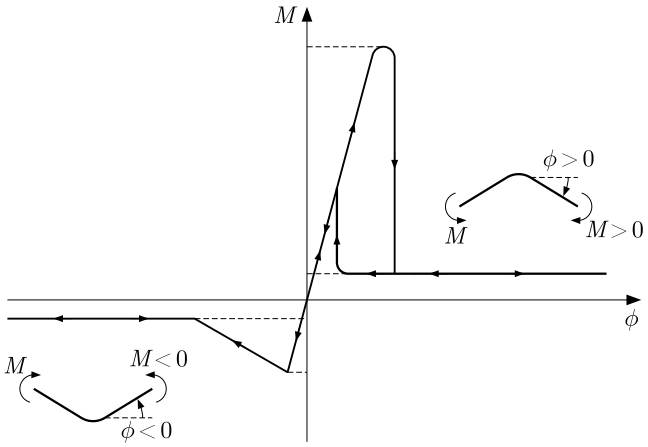

Fig. 2. Qualitative moment-rotation relationship, and lateral views of the deformed centerline in the post-critical regime (once the elastic hinge has taken place). For small rotations, the device deforms smoothly and follows a linear trend in the moment-rotation plane. When rotation increases, the behavior becomes highly non-linear and deeply different in the two cases of bending. This Figure is an adaptation of Fig. 2.4 of Walker's PhD thesis (2004)

It is observed that for small rotations the device deforms smoothly and follows a linear trend in the moment-rotation plane. When rotation increases, the behavior becomes highly non-linear and strongly dependent on the sign of rotation.

The purpose of this article is to highlight the behavior of tape springs as their thickness become smaller and smaller. The main novelty of this paper is to propose very simple formulas to obtain a good estimation of energy per unit thickness in the pre-critical and post-critical regime, in the case of pure bending.

2. Numerical model

Hereafter, we shall always refer to a straight cylindrical shell as shown in Fig. 1.

The characteristics of the examined specimen are those specified in Walker's PhD thesis (2004). The mechanical and geometrical parameters of the sample are: length $L = 267\,\text{mm}$, cross section radius $R = 15.37\,\text{mm}$, thickness $t = 0.1225\,\text{mm}$, angle subtended by the cross section $\alpha = 1.719\,\text{rad}$, Young's modulus 195300 MPa, Poisson's ratio 0.3.

The modeling and analysis challenges have been addressed with the Abaqus software (Smith, 2014).

The tape was simulated as a portion of a cylindrical surface, first modeling the cross section as a circumferential arc of radius R subtending an angle α.

In *Interaction* section two *Reference Points* located at the end cross sections were defined, then all the end nodes were constrained to the *Reference Point*, as shown in Fig. 3. The constraints were applied to the *Reference Points*. With reference to Fig. 1, the degrees of freedom constrained at the *Reference Point* at $x_3 = L$ are: translations in the three directions x_1, x_2 and x_3, rotations around the x_2 and x_3 axes. Instead, at the *Reference Point* at $x_3 = 0$, the degrees of freedom constrained are: translations in the directions x_1 and x_2, rotations about x_2 and x_3 axes.

Rotations at the end cross sections are imposed: at the end $x_3 = 0$, rotation $\phi\mathbf{e}_1$ and at $x_3 = L$, rotation $\phi\mathbf{e}_1$, as shown in Fig. 3.

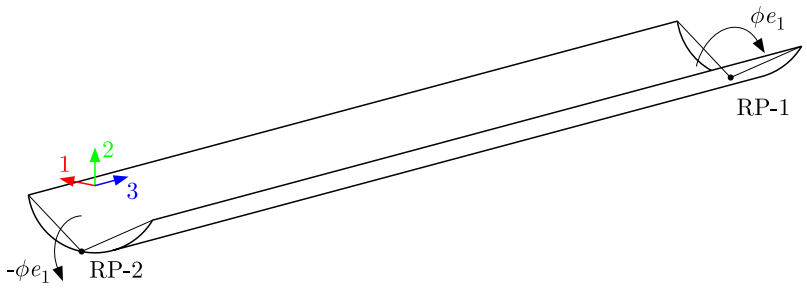

Fig. 3. Schematic view of the sample implemented in Abaqus. In this figure, there are reference points, RP-1 and RP-2 constrained, the segment from RP-1 and RP-2 represent constraints applied to the nodes of the end cross sections and the load condition

The size of the mesh was set up to 2.0 mm, for a total of about 1800 elements. *S8R5* elements were chosen, as in the works of Martin *et al.* (2020) and Picault *et al.* (2016), i.e., eight-node thin--shell elements with five degrees of freedom for each node with quadratic interpolation functions.

Static-Riks analysis was chosen, activating geometric non linearities and imposing the end of analysis when $\phi = \pi/2$. The settings of the step are: maximum number of increments 1000, initial arc length increment 0.01, minimum arc length increment 1E-10, the maximum arc length increment 1.2 and estimated total arc length 1.

The *arc length* method was originally developed by Riks (1972, 1979) and Wempner (1971). This approach is the most used *path following* method in the solution of non-trivial equilibrium paths. The Riks method solves simultaneously for both the load and displacements, and is the ideal method for solving problems of the tape spring devices, characterized by *snap-back* phenomena.

In Fig. 4, there is a view of the Abaqus model.

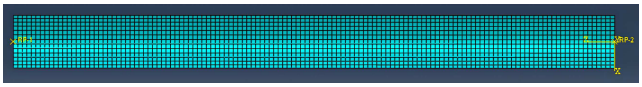

Fig. 4. Orthogonal projection of the Abaqus model on the x_1-x_3 plane, visualized mesh

3. Main results

3.1. M-ϕ diagram

With reference to the characteristics of the tape specified in Section 2, eight different analyses were carried out, for opposite sense bending, varying thickness t of the device and keeping the

other geometrical and material parameters unchanged. The reference thicknesses are shown in Table 1.

Table 1. Thicknesses adopted in the analysis

Thickness t [mm]							
0.1215	0.1225	0.1300	0.1350	0.1400	0.1450	0.1500	0.1550

The thickness $t = 0.1215\,\text{mm}$ is the smallest thickness the convergence of analysis was achieved with.

We made sure that analysis results did not depend on the mesh size. The same analysis were carried out modifying the mesh, setting the mesh size to 1.0 mm for a total of about 3600 elements: the final results were the same.

Figure 5 shows the trends of the positive reactive moment as a function of rotation ϕ (Fig. 3), for the thickness values t shown in Table 1. Referring to the thickness $t = 0.1225\,\text{mm}$, the results obtained here are in good agreement with those of Walker (2004), with an overestimation of the peak moment of about 7%. Instead, the stationary moment was quite close to the reference one.

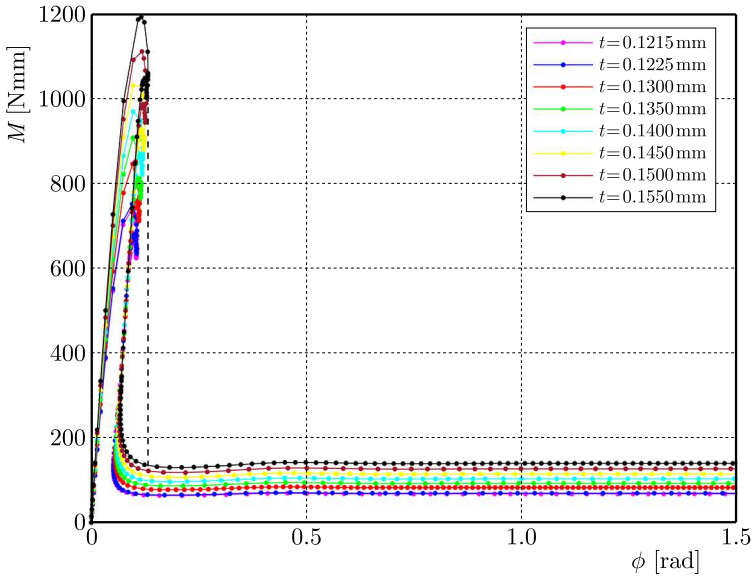

Fig. 5. M-ϕ diagram ($M > 0$)

In Fig. 6, the energy per unit thickness versus rotation ϕ is represented, in the case of opposite sense bending, for the thickness values in Table 1.

From the M-ϕ diagram in Fig. 5, one can observe the typical trend described in previous works, for example Seffen and Pellegrino (1999), for these devices undergoing pure bending: the behavior is almost linear until the peak moment is reached, then the reactive moment M decreases and reaches a stationary value.

From Fig. 6, it can be seen that the trend is initially quadratic, corresponding to the linear behavior in the M-ϕ diagram, Fig. 5. In the post-critical regime, after formation of the elastic hinge, it is linear in ϕ.

For equal sense bending, various analyses were carried out relating to the same thicknesses used for positive bending. However, the convergence of the analysis in this case was much more difficult to achieve. We report just the case $t = 0.1225\,\text{mm}$.

In Fig. 7, the energy per unit thickness versus the rotation ϕ in the case $t = 0.1225\,\text{mm}$, for $M < 0$, is shown. Also, one can see that the energy trend is initially quadratic, then it is linear in ϕ.

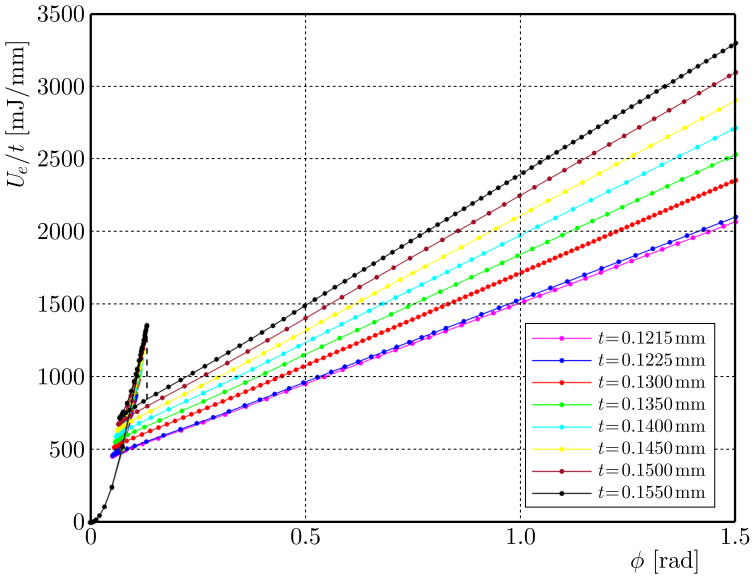

Fig. 6. U_e/t-ϕ diagram ($M > 0$)

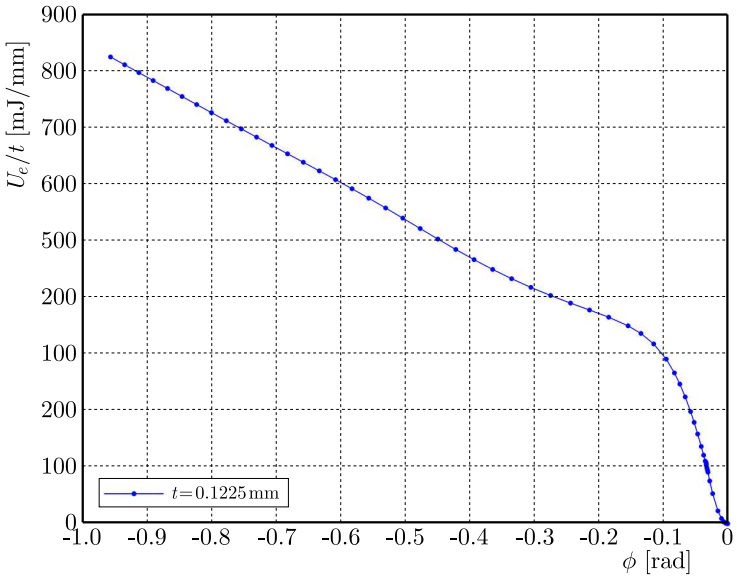

Fig. 7. U_e/t-ϕ diagram ($M < 0$)

To obtain the unloading path of the moment-rotation relationship, as in Fischer (1995), the command and change *restart analysis* was used decreasing the end rotation from $\phi = \pi/2$ to $\phi = 0$. The unloading paths found were the same as the loading ones.

For opposite and equal sense bending, the formation of the localized elastic hinge is due to buckling phenomena. We define the pre-critical regime when the device deforms prior to the elastic hinge has taken place, and post-critical regime when the device deforms after the formation of the localized elastic hinge.

Thanks to the analysis adopted, *Static-Riks* analysis, it is possible to detect *snap-back* phenomena that occur when, for opposite sense bending, the elastic hinge forms and there is a jump in the energy between the two stable solution branches. As shown in Fig. 6, for $t = 0.1550\,\mathrm{mm}$, the analysis captures the branch with a decreasing value of ϕ, but physically there is the *snap-back*, dashed line, that implies a jump in the energy between the two branches. In the same way

there is a jump, dashed line, in the reaction moment diagram M-ϕ, as shown in Fig. 5, from the peak moment to the stationary one.

To estimate the transmission of potential energy distribution between the membrane and the flexural energy densities, which occurs right after the opening, it is enough to calculate the difference between the total energy before and after the formation of the localized elastic hinge.

3.2. Pre-critical regime

The pre-critical regime is before the formation of the localized elastic hinge.

As can be seen from the moment-rotation diagram for opposite sense bending, Fig. 5, for small values of ϕ, the moment is almost linear and the cross section varies its shape smoothly ("opening" of the cross section curve). Here, the energy has a quadratic trend, as represented in Fig. 6.

For the opposite sense bending, it is postulated that for small values of thicknesses t the energy per unit thickness can be represented by a formula of the following type

$$\frac{U_e}{t} = Ct^a\phi^b \tag{3.1}$$

In Eq. (3.1), C is some positive constant depending on the material and geometrical properties of the device, but not on the thickness.

To determine the exponents a and b, the energy per unit thickness is represented in a bi--logarithmic plane, in this way the exponents a and b are actually the slopes of the plotted curves, and the average slope of the curves can be determined. In the pre-critical regime, $a = 0$ and $b = 2$. The energy per unit thickness is independent of the thickness of the tape and quadratic in the rotation ϕ. Therefore, it is membranal regime, and the energy in Eq. (3.1) becomes

$$\frac{U_e}{t} = Ct^0\phi^2 \tag{3.2}$$

The diagrams of energy, normalized with respect to the thickness, are represented in Fig. 8.

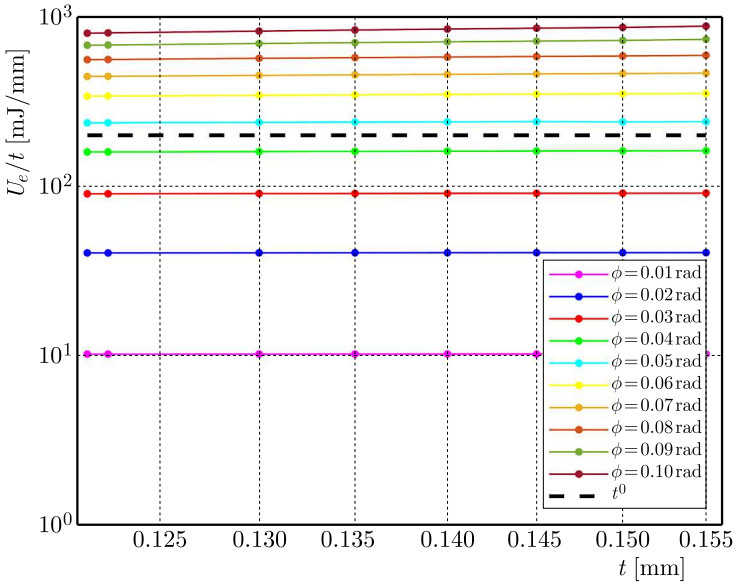

Fig. 8. U_e/t-t diagrams in the pre-critical regime in a bi-logarithmic plane

To obtain the color maps of the energy densities of the shell model, the strain and the stress measures were exported, for every node, from Abaqus. Then, by post processing, we obtained

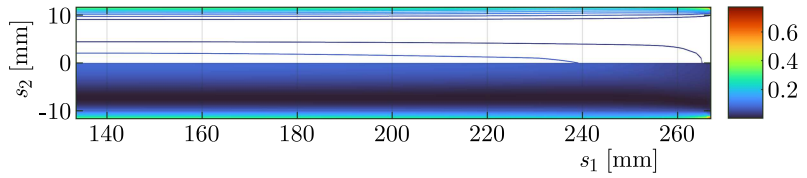

Fig. 9. Membrane energy density u_m/t, pre-critical regime ($M > 0$)

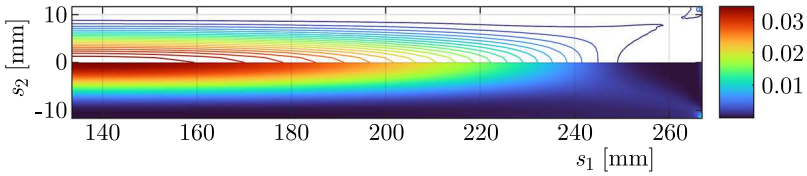

Fig. 10. Flexural energy density u_f/t, pre-critical regime ($M > 0$)

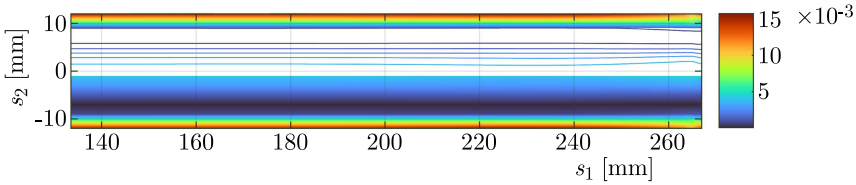

Fig. 11. Membrane energy density u_m/t, pre-critical regime ($M < 0$).

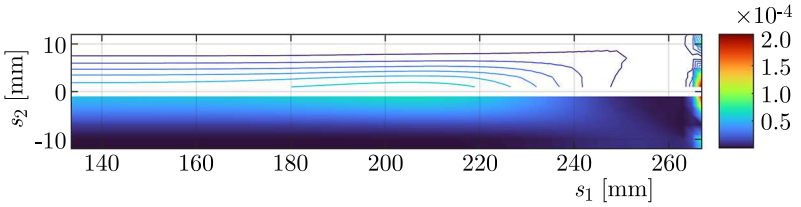

Fig. 12. Flexural energy density u_f/t, pre-critical regime ($M < 0$).

the energy densities by multiplying the membrane and bending strains by the energetically conjugate strains and changes of curvatures. The membrane and the flexural energy densities are represented in Figs. 9 to 12, for the opposite sense ($\phi = 0.1$ rad) and equal sense ($\phi = -0.1$ rad) bending, referring to $t = 0.1225$ mm. In these figures, s_1 represents the longitudinal abscissa of the shell, and s_2 the transversal one. Both the abscissas belong to the middle surface. It is observed that in the pre-critical regime the flexural energy density per unit thickness u_f/t is lower than the membrane energy density u_m/t, for both $M > 0$ and $M < 0$. Furthermore, the maps highlight a concentration of energy in the central area of the tape, close to the area where the elastic hinge will form.

3.3. Post-critical regime

During post-critical regime, i.e., in the case of well formed elastic hinge, the tape is characterized by another behavior in which the energy per unit thickness scales linearly with ϕ, Fig. 6.

For the opposite sense bending, it is postulated that for small values of thicknesses t the energy per unit thickness can be represented by a formula similar to the one used for the pre-critical regime

$$\frac{U_e}{t} = Ct^c\phi \tag{3.3}$$

Analogously, at the pre-critical regime, we got $c = 1.8$. Therefore, in the post-critical regime the normalized energy scales as $t^{1.8}$ and linearly in the rotation ϕ

$$\frac{U_e}{t} = Ct^{1.8}\phi \tag{3.4}$$

This means that in the post-critical regime there is a mixture of membranal and flexural energy, although the main component is flexural. The diagrams of the energy, normalized with respect to the thickness, are represented in Fig. 13.

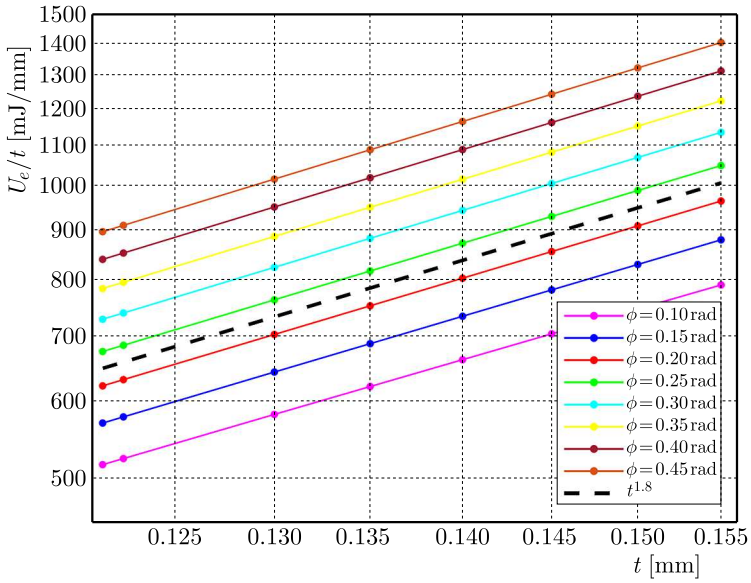

Fig. 13. U_e/t-t diagrams in the post-critical regime in a bi-logarithmic plane

The membrane and flexural energy densities are represented in Figs. 14 to 17 for the opposite sense ($\phi = 1$ rad) and equal sense ($\phi = -1$ rad) bending, referring to $t = 0.1225$ mm. In these figures, s_1 represents the longitudinal abscissa of the shell, and s_2 the transversal one. In the post--critical regime for $M > 0$, it is observed that the membrane energy density per unit thickness u_m/t is approximately zero over the entire tape, with the exception of two areas near the hinge, where there is the transition from the almost constant curvature zone (hinge) and the transition zone. The energy u_f/t represents the largest contribution to the total energy density, and it is most concentrated in the hinge area where it is approximately constant.

Also in the case $M < 0$, the major contribution to the total energy density is given by u_f/t, however there are peaks near the hinge area.

In Figs. 18a and 18b, the trends of variations of longitudinal and transversal curvature are represented for $\phi = 1$ rad in the case $M > 0$.

From Fig. 18a, it can be seen that in the hinge area the longitudinal curvature is close to the initial transversal one, then the curvature increases very rapidly and after the maximum reached at $s_1 \approx 158$ mm becomes very close to zero, and is almost zero from $s_1 \approx 190$ mm. From Fig. 18b, it can be seen that most of the cross section has a constant curvature, while at the edges there is a residual curvature.

In the case $M < 0$, it is observed that the longitudinal curvature has a similar trend to the case $M > 0$. Also the trend of transverse curvature in the hinge area is similar to the case $M > 0$, with a concentration of curvature at the edges of the device.

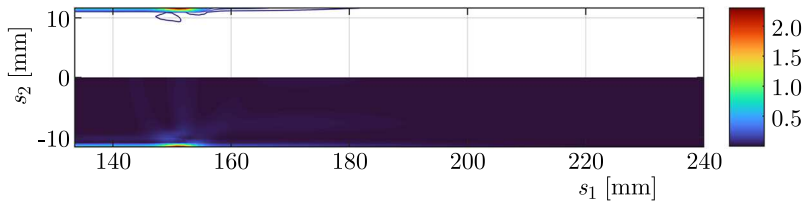

Fig. 14. Membrane energy density u_m/t, post-critical regime ($M > 0$)

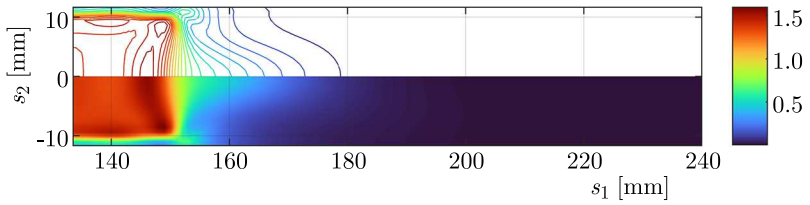

Fig. 15. Flexural energy density u_f/t, post-critical regime ($M > 0$)

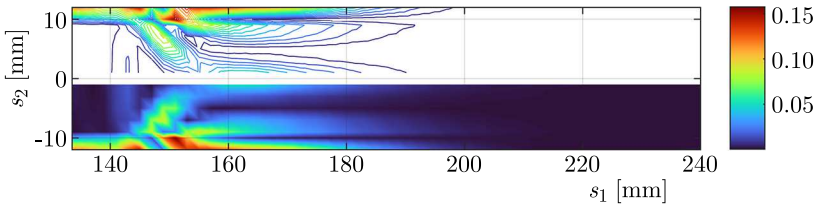

Fig. 16. Membrane energy density u_m/t, post-critical regime ($M < 0$)

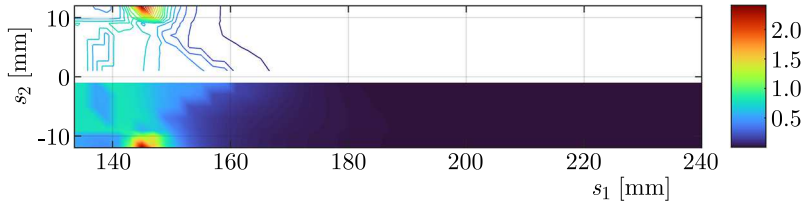

Fig. 17. Flexural energy density u_f/t, post-critical regime ($M < 0$)

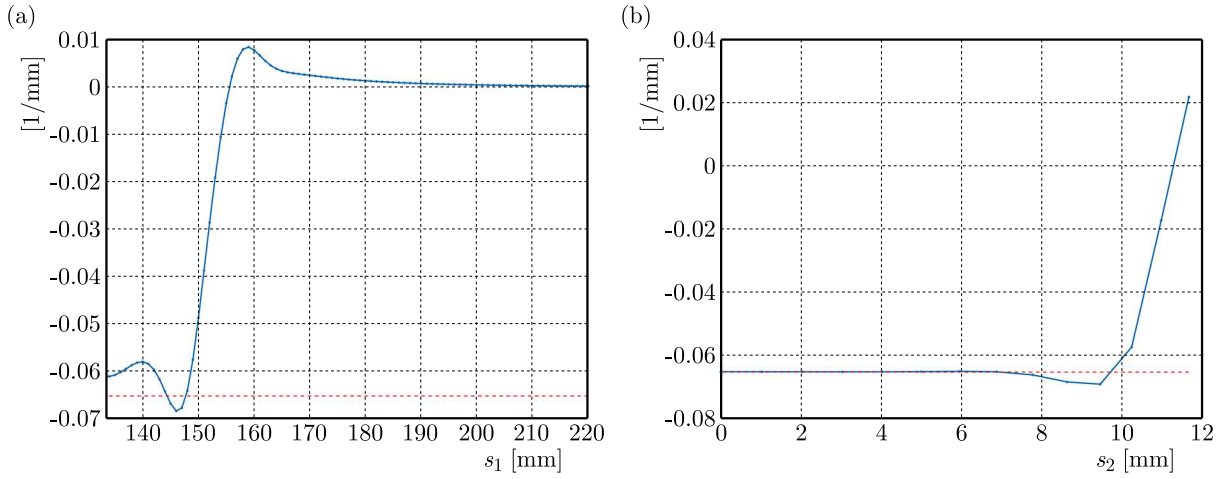

Fig. 18. On the left side, variation of the longitudinal curvature in the center of the tape (on a half of the tape length), on the right side, variation of transverse curvature in the hinge zone. In red dashed line, variation of the transversal curvature from the end configuration, perfectly flat, to the initial one. s_1 and s_2 are shell abscissas belonging to the middle surface. Figures (a) and (b) refer to post-critical regime ($M > 0$)

4. Conclusions

In this paper, a numerical analysis of a tape spring device is carried out. First, tape springs are introduced with a brief description of the particular mechanical behavior under pure bending. Then, the description of the numerical model is presented: mesh, type of mesh elements and the type of analysis conducted. Finally, the main results obtained are: moment-rotation diagrams for opposite sense bending (Fig. 5), energy diagrams per unit thickness for opposite sense and equal sense bending (Figs. 6 and 7), estimates of the energy per unit thickness Eq. (3.2) and Eq. (3.4), obtained from different analyses by varying the thickness of the device, and the color maps of the energies (Figs. 9-12 and 14-17). The moment-rotation diagrams obtained are typical of these devices, characterized by an almost linear trend for small rotations until a peak moment is reached. Then the reactive moment decreases and remains almost constant for further increments of rotation.

As regards the pre-critical regime, it was found that the energy expressed by Eq. (3.2) is typical of a membranal regime, i.e., the device deforms without activating the flexural regime.

For the post-critical regime, after formation of the localized elastic hinge, the energy expressed by Eq. (3.4) suggests the coexistence of the membrane and flexural regime, even if the major energy contribution is flexural.

Possible future developments could be: energy estimates for equal sense bending, development of beam models that are in agreement with these estimates for both opposite sense and equal sense bending.

Acknowledgement

This paper was presented at WECM'23 – 2nd Workshop on Experimental and Computational Mechanics (Pisa, Italy, 20-22 September 2023). Based on the evaluation by a Selection Committee chaired by Prof. Jerzy Warmiński, Lublin University of Technology, Poland, and composed of Prof. Simone Camarri and Prof. Luigi Lazzeri, University of Pisa, Italy, this work was awarded the "WECM'23 Best Paper Award in Computational Mechanics". The authors gratefully acknowledge the University of Pisa for organization of the workshop and for payment of the publication fee.

RP and MPS acknowledge the support from the University of Pisa through project PRA2022-69 "Advanced modeling of ultra-lightweight materials and structures".

This work has been written within the activities of INdAM-GNFM.

References

1. Fischer A., 1995. Bending instabilities of thin-walled transversely curved metallic strips, Report cued/d-struct/tr 154

2. Guinot F., Bourgeois S., Cochelin B., Blanchard L., 2012, A planar rod model with flexible thin-walled cross-sections. Application to the folding of tape springs, *International Journal of Solids and Structures*, **49**, 1, 73-86

3. Kumar A., Audoly B., Lestringant C., 2023, Asymptotic derivation of a higher-order one--dimensional model for tape springs, *Philosophical Transactions of the Royal Society A, Mathematical, Physical and Engineering Sciences*, **381**, 2244, 20220028

4. Martin M., Bourgeois S., Cochelin B., Guinot F., 2020, Planar folding of shallow tape springs: the rod model with flexible cross-section revisited as a regularized Ericksen bar model, *International Journal of Solids and Structures*, **188**, 189-209

5. Picault E., Bourgeois S., Cochelin B., Guinot F., 2013, Un modèle de poutre à section mince flexible pour l'étude du comportement 3d des mètres rubans, *Conference: 11e Colloque National en Calcul des Structures*, Giens, France

6. Picault E., Bourgeois S., Cochelin B., Guinot F., 2016, A rod model with thin-walled flexible cross-section: Extension to 3D motions and application to 3D foldings of tape springs, *International Journal of Solids and Structures*, **84**, 64-81

7. Picault E., Marone-Hitz P., Bourgeois S., Cochelin B., Guinot F., 2014, A planar rod model with flexible cross-section for the folding and the dynamic deployment of tape springs. Improvements and comparisons with experiments, *International Journal of Solids and Structures*, **51**, 18, 3226-3238

8. Riks E., 1972, The application of Newton's method to the problem of elastic stability, *Journal of Applied Mechanics*, **39**, 4, 1060-1065

9. Riks E., 1979, An incremental approach to the solution of snapping and buckling problems, *International Journal of Solids and Structures*, **15**, 7, 529-551

10. Seffen K., 1997, *Analysis of Structures Deployed by Tape-Springs*, PhD Thesis, University of Cambridge

11. Seffen K., Pellegrino S., 1999, Deployment dynamics of tape springs, *Proceedings of the Royal Society of London. Series A: Mathematical, Physical and Engineering Sciences*, **455**, 1983, 1003-1048

12. Seffen K., You Z., Pellegrino S., 2000, Folding and deployment of curved tape springs, *International Journal of Mechanical Sciences*, **42**, 10, 2055-2073

13. Smith M., 2014, Abaqus/standard users manual, version 6.14-5, Simulia, Providence, RI

14. Walker S.J., 2004, *A Study of Three Dimensional Tape Spring Folds for Space Applications*, PhD Thesis, University of Southampton

15. Wempner G.A., 1971, Discrete approximations related to nonlinear theories of solids, *International Journal of Solids and Structures*, **7**, 11, 1581-1599

Manuscript received December 14, 2023; accepted for print February 20, 2024

JOURNAL OF THEORETICAL AND APPLIED MECHANICS
62, 3, pp. 547-560, Warsaw 2024
https://doi.org/10.15632/jtam-pl/188855

USE OF THE BIAXIAL COEFFICIENT IN DETERMINING LIFE FOR A COMBINATION OF CYCLIC BENDING AND TORSION OF BRONZE RG7

Joanna Małecka, Tadeusz Łagoda
Opole University of Technology, Opole, Poland
e-mail: j.malecka@po.edu.pl; t.lagoda@po.opole.pl

The paper proposes a new multiaxiality coefficient that can characterize fatigue tests for various combinations of bending and torsion. This coefficient can be defined depending on the criterion used. The factor is 1 for cyclic bending and 2 for pure torsion. Based on the fatigue tests of the RG7 bronze, analysis of calculation dispersion of the fatigue life was carried out concerning test results obtained through an experiment. This analysis was performed separately for individual tested combinations and for selected multiaxial fatigue criteria. The selected criteria are Huber-Mises, Gough-Pollard, maximum normal stress, maximum shear stress, and maximum normal and shear stress in the plane defined by shear stresses. The average values of the obtained durability were compared to the newly defined multiaxial coefficient distinguishing different combinations of bending and torsion. Fractographic analysis was also performed for selected samples for all four combinations of fatigue tests. It was found that the failure planes and design critical planes do not coincide.

Keywords: biaxial loading, life-time, bending and torsion, cyclic loading

More important nomenclatures

A_σ, m_σ – coefficients in fatigue characteristic for bending
A_τ, m_τ – coefficients in fatigue characteristics for torsion
cal, exp – calculated and experimental
E – elastic modulus
N_f – number of cycles to failure
r, r_{BF} – loading ratio and biaxial factor
$\Delta\tau$ – range of shear stresses
σ_a – amplitude of normal stress from bending
σ_u, σ_y – ultimate and yield stress
τ_a – amplitude of shear stress from torsion

1. Introduction

In the literature, we find numerous works on fatigue tests of cyclic bending with torsion of samples with a solid cross-section, i.e., in which stress and strain gradients for both bending and torsion are important. Less frequently, these are fatigue tests with cyclic tension-compression with torsion. In this case, thin-walled hollow samples are often used. In the case of torsion of thin-walled hollow samples, it does not give an additional effect of a stress gradient or strain. Then, the distribution of stresses and strains can be assumed to be homogeneous. These tests are described as cyclic bending or tension-compression $\tau_a = 0$, cyclic torsion $\sigma_a = 0$, and a combination of cyclic bending and torsion $\tau_a = k_{\tau/\sigma}\sigma_a$, where $k_{\tau/\sigma}$ is the ratio of shear to normal stresses. However, this does not describe the possible combinations uniformly. For this

purpose, a loading ratio has been proposed, which is defined in various ways. In the paper (Slamečka *et al.*, 2016), it was defined as

$$r = \frac{\sqrt{3}\tau_a}{\sigma_a + \sqrt{3}\tau_a} \tag{1.1}$$

But in the works (Slámečka *et al.*, 2010, 2013), it was defined as

$$r = \frac{\tau_a}{\sigma_a + \tau_a} \tag{1.2}$$

It can be seen that in the first case, the correction factor before the shear stress amplitude τ_a is $\sqrt{3}$, which is related to the Huber-Mises hypothesis, and in the second case, it is 1, which is related to the Galileo hypothesis. However, the defined loading ratio always ranges from 0 for cyclic bending (extension-compression) to 1 for cyclic torsion.

Another approach is also conceivable. Expressions can be written according to Tresca's hypothesis as

$$r = \frac{2\tau_a}{\sigma_a + 2\tau_a} \tag{1.3}$$

or the Gough-Pollard (Gough *et al.*, 1951) criterion, which is the most commonly used criterion for a proportional combination of cyclic bending and torsion in the form

$$r = \frac{1}{\sigma_a + \frac{\sigma_{a-1}}{\tau_{a-1}}\tau_a}\frac{\sigma_{a-1}}{\tau_{a-1}}\tau_q \tag{1.4}$$

However, we always get a result in the interval $(0, 1)$, and the final equation can be written as general equation

$$r_{LR} = \frac{k\tau_a}{\sigma_a + k\tau_a} \tag{1.5}$$

where k can be defined as $\sqrt{3}$ – Eq. (1.1), 1 – Eq. (1.2), 2 – Eq. (1.3), and σ_{a-1}/τ_{a-1} – Eq. (1.4) which is the fatigue strength ratio (Papuga *et al.*, 2021; Wächter *et al.*, 2022). If we are dealing with a brittle material, the value of this factor is 1.25, and if we are dealing with an extra ductile material, the value of this factor is > 1.75. However, it can be noticed that the proposed parameter has no physical significance, according to formulas (1.1)-(1.5), although it is very convenient to describe fatigue tests.

A slightly different approach can be found in (Susmel and Lazzarin, 2002) and later used, for example, in (Gan *et al.*, 2021), where a coefficient was introduced to modified fatigue characteristics, which, according to the authors, takes into account both multiaxiality and non-proportionality in the form

$$\rho = \frac{\sigma_{max}}{2\Delta\tau} \tag{1.6}$$

In this case, coefficient (1.6) becomes 0 for torsion and 1 for the axial load. This is opposite to coefficient r_{LR} (1.5). A completely different approach can be found in (Wang *et al.*, 2023) based on (Wang *et al.*, 2001). These papers propose a principal stress coefficient defined as

$$\gamma = \frac{\sigma_2 - \sigma_3}{\sigma_1 - \sigma_3} \tag{1.7}$$

The value of this coefficient determined on the basis of the principal stresses range from 0 to 1.

However, the fatigue life itself is determined using selected multiaxial fatigue criteria. Here, an appropriate criterion should (for example, presented in works (Kardas *et al.*, 2008; Karolczuk *et al.*, 2015; Carpinteri *et al.*, 2018; Łagoda and Macha, 1994; Niesłony *et al.*, 2014) be used to reduce a complex state of stress to an equivalent uniaxial one. Then, the fatigue life is determined based on the specified equivalent amplitude and fatigue characteristics for the uniaxial state of stress. Then, the computational durability is compared with the experimental one. Most often, both calculated and experimental lifetime are presented in a logarithmic system. The diagonal reflects perfect agreement of the calculation results with the experiment. The logarithmic system of axes corresponds to fatigue characteristics written as the logarithm of fatigue life. This approach can be found in many works. The first such an approach is most likely found in (Łagoda and Macha, 1994). It seems, however, that it would be possible to determine the average values of fatigue life dispersion for individual load combinations. Then, such a distribution can be compared with the dispersion for the uniaxial state of stress for particular combinations defined by Eq. (1.5) depending on the criterion used.

This work aims to propose such a biaxiality coefficient using the presented loading factor, which will be adequate to the selected applied criterion, taking into account the complex state of stress and especially various combinations of proportional bending and torsion. The verification of the proposal will be presented based on fatigue tests of bronze RG7 (Małecka and Łagoda, 2023a; Małecka *et al.*, 2023) performed by the authors of this paper. In addition, the work explains in detail the results, which may be used by other authors, of fatigue tests for this material, which have yet to be done before.

2. Biaxiality coefficient

The introduction presents proposals for different definitions of the loading ratio depending on a combination of bending and torsion. In the case of bending or tension-compression, we are dealing with a uniaxial state of stress. However, the matter could be more evident in the case of shear stresses. In this case, the shear stress can be applied by a torque for solid samples (Fig. 1a) or thin-walled hollow samples (Fig. 1b) to eliminate the stress and strain gradient effect. In both cases, we can talk about torsion about one axis. Shear stress can also be caused by technical shear, as shown in Fig. 1c. In this case, the axial force causes shear stress. Pure shear, on the other hand, is defined as simultaneous compression in one direction and tension in the other with the same force values as shown in Fig. 1d. Such fatigue tests have been presented, among others, on cross samples. The results of such tests for the 10HNAP material have been presented, among others, in work (Łagoda *et al.*, 2020). In this case, biaxial cyclic and random fatigue tests with a correlation coefficient of -1 result in pure shear fatigue. Therefore, switching from forces to stresses.

Figure 2a shows uniaxial fatigue tests, and Fig. 2c presents a pure shear stress state caused by a biaxial state of stress, where

$$\sigma_x = -\sigma_y \tag{2.1}$$

and in Fig. 2b, where we have an intermediate situation, i.e

$$\sigma_x = k_{x/y}\sigma_y \tag{2.2}$$

where $-1 < k_{x/y} < 0$. The loading factor known in the literature, presented in the general form by formula (1.5), apart from the fact that it distinguishes various combinations of normal and tangential loads with values from 0 to 1, has no other meaning. Since the uniaxial state is

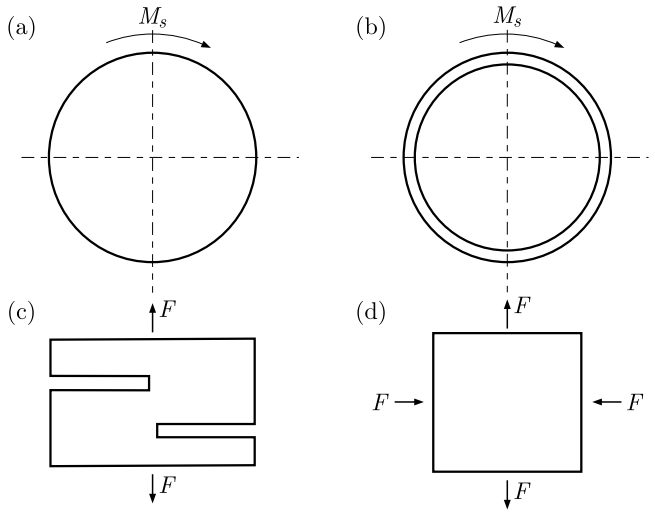

Fig. 1. Different ways to obtain shear stresses: (a) solid bar torsion, (b) tube torsion, (c) technical shear, (d) pure shear

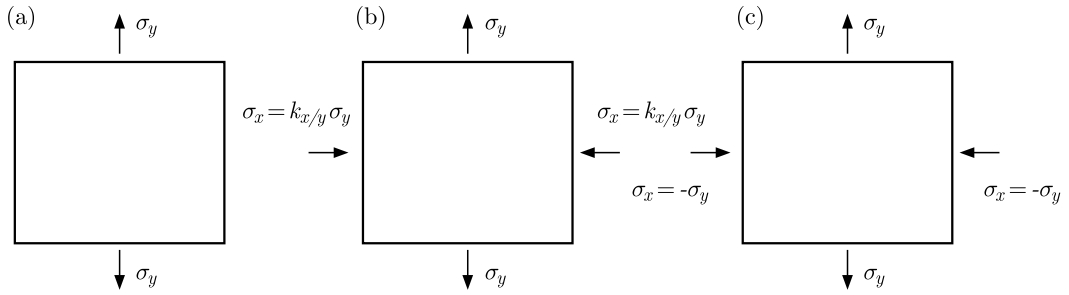

Fig. 2. Stress distribution for: (a) tension, (b) tension with shear, (c) pure shear

associated with the value 1, and the biaxial state with 2, it seems more logical to reformulate general formula (1.5) presented in this work with a new biaxial factor in the form

$$r_{BF} = 1 + \frac{k\tau_a}{\sigma_a + k\tau_a} \tag{2.3}$$

The value of this parameter r_{BF} reaches the minimum value for tension-compression (bending in the plane) equal to 1 (uniaxial load) and for maximum cyclic shear (two-sided torsion) equal to 2 (biaxial state). This means that pure bending reaches 1, and pure torsion values 2. However, the combination of bending and torsion is an intermediate value. The closer this value is to 2, it means that there is a more significant share of torsion. The k coefficient in Eq. (2.3) can be defined here depending on the criterion proposed by the researcher adopted for further calculations.

3. Experimental research and analysis

The fatigue tests concern the RG7 bronze alloy, also known as CuSn7Zn4Pb6. Its basic static properties are $E = 92.14\,\text{GPa}$, $\sigma_u = 270\,\text{MPa}$, $\sigma_y = 120\,\text{MPa}$. The basic chemical composition is Cu: 81%-86%, Sn: 5.2%-8%, Zn: 2%-5%, Pb: 5%-8% (Slamečka *et al.*, 2016; Susmel and Lazzarin, 2002). Tables 1-5 present the results of cyclical experiments in simple load conditions – tension-compression (Table 1), bending in a plane, and torsion on both sides (Table 2), and two combinations of proportional bending and torsion (Table 3). In the case of bending or torsion, nominal stress values are given, i.e., those that result from the given bending or torsion moment and the appropriate elastic section modulus for bending and torsion, respectively.

Table 1. Experimental results of RG7 copper alloy under axial tension-compression conditions

ε_a [‰]	σ_a [MPa]	N_{exp} [cycles]
3.0	192	5954
2.5	167	22556
2.2	162	73986
2.0	156	42000
1.8	136	137849
1.5	140	357851
1.3	–	$>$ 2000000

Table 2. Experimental results of RG7 copper alloy in the conditions of in-plane cyclic

Bending		Torsion	
σ_{an} [MPa]	N_{exp} [cycles]	σ_{an} [MPa]	N_{exp} [cycles]
254	25850	163	17271
254	37723	158	35902
244	27766	158	3215
244	40511	153	171275
233	58327	153	93219
233	85021	143	19122
218	75647	143	70400
218	58069	143	86055
203	229748	135	289812
203	106173	135	785924
188	888016	127	650800
188	596720	127	481710
172	1592848	125	2499155
172	1135442	125	742896
152	1361954	117	3021316
152	571257	117	1349697
142	2011739	115	3215695
142	5827190	102	¿10000000
131	$>$ 10000000		

Based on cyclical tests of the analyzed material, fatigue characteristics were determined according to the Basquin model, the double-logarithmic model, and the formulas according to (ASTM Standard 2003) – for in-plane bending and combinations of bending and torsion and two-sided torsion, respectively

$$\log N_f = A_\sigma - m_\sigma \log \sigma_a \qquad \log N_f = A_\tau - m_\tau \log \tau_a \tag{3.1}$$

The coefficients obtained according to equations (3.1) are summarized in Table 4.

The verification will be presented for several selected multiaxial fatigue criteria:

— Huber-Mises hypothesis

$$\sigma_{a\,eq} = \sqrt{\sigma_a^2 + 3\tau_a^2} \tag{3.2}$$

— Gough-Pollard hypothesis (Gough *et al.*, 1951)

$$\sigma_{a\,eq} = \sqrt{\sigma_a^2 + \left(\frac{\sigma_{a-1}}{\tau_{a-1}}\right)^2 \tau_a^2} \tag{3.3}$$

Table 3. Experimental results of RG7 copper alloy for the combination of cyclic bending and torsion

$\tau_{an} = 0.5\sigma_{an}$			$\tau_{an} = \sigma_{an}$		
σ_{an} [MPa]	τ_{an} [MPa]	N_{exp} [cycles]	σ_{an} [MPa]	τ_{an} [MPa]	N_{exp} [cycles]
177	88	42488	125	125	45085
177	88	59187	125	125	28808
166	83	89283	118	118	110665
166	83	88376	118	118	79988
144	72	136893	112	112	88149
144	72	136991	112	112	104546
133	67	776838	105	105	400352
133	67	424789	105	105	334607
122	61	919070	98	98	522700
122	61	1393731	98	98	896867
112	56	929541	91	91	435266
112	56	5691131	91	91	508131
102	51	> 5400000	84	84	> 10000000
101	50	5851778			
94	47	6058621			

Table 4. Coefficients according to the Basquin model according to formulas (3.1) for particular combinations of bending and torsion (Susmel and Lazzarin, 2002; Wächter *et al.*, 2022)

Bending		Torsion		$\tau_a = 0.5\sigma_a$		$\tau_a = \sigma_a$	
A_σ	m_σ	A_τ	m_τ	A_σ	m_σ	A_σ	m_σ
26.26	9.09	38.34	15.38	24.47	8.85	26.85	10.64

Hypothesis (3.2) and (3.3) have a similar formula, and in a particular case, when $\sigma_{a-1}/\tau_{a-1} = \sqrt{3}$, they are the same:

— maximum normal stress

$$\sigma_{a\,eq} = \sigma_{an,max} \tag{3.4}$$

— maximum shear stress

$$\sigma_{a\,eq} = 2\tau_{ans,max} \tag{3.5}$$

— maximum shear stress and normal stress in the critical plane defined by the maximum shear stress

$$\sigma_{a\,eq} = \Big(2 - \frac{\sigma_{a-1}}{\tau_{a-1}}\Big)\sigma_{an,max} + \frac{\sigma_{a-1}}{\tau_{a-1}}\tau_{ans,max} \tag{3.6}$$

Here, it should be noted that hypotheses (3.4)-(3.6), unlike (3.2) and (3.3), are linear criteria due to components of the stress state, and such criteria can also be dedicated to random or non-proportional loads (Mamiya *et al.*, 2011). Normal and shear stress for a combination of normal (from bending) and shear (from torsion) stresses at an angle α can be determined according to the formulas

$$\sigma_{an}(\alpha) = \cos(2\alpha)\sigma_a + \sin(2\alpha)\tau_a \qquad \tau_{ans}(\alpha) = -\frac{1}{2}\sin(2\alpha)\sigma_a + \cos(2\alpha)\tau_a \tag{3.7}$$

Critical planes for criteria (3.4)-(3.6) were determined for individual combinations of bending and torsion in accordance with formulas (3.7). The critical planes are defined by the angle α for

which the value of the amplitude, according to expressions (3.7), reaches its maximum value. The values of these angles are listed in Table 5, depending on the type of load. Table 5 also shows the positions of critical fatigue planes and experimental positions of the critical planes, which are presented in Figs. 3-6, and shows that the experimental failure planes coincide with the direction determined by the maximum normal stress.

Table 5. Setting the location of the critical planes and the macro-split plane of destruction [°]

	Bending	$\tau_a = 0.5\sigma_a$	$\tau_a = \sigma_a$	Torsion
$\sigma_{an,max}\alpha$	0	22.50	31.45	45
$\tau_{ans,max}\alpha$	45	67.50	76.45	90
Experiment	1.43	20.15	33.30	44.60

In connection with the proposed introduction of the biaxiality factor r_{BF}, it is possible to analyze how this coefficient translates into fracture fractography. Figures 3-6 shows photos of fracture surfaces for durability in the medium durability range, i.e. for durability of about 100 000 cycles. For in-plane bending (Fig. 3), i.e. with the biaxial fatigue factor $r_{BF} = 1$, the development of fatigue cracks can be seen from the two most distant points from the bending plane. In the case of two-sided torsion, i.e. when the biaxial fatigue factor reaches the value $r_{BF} = 2$, the fatigue crack (Fig. 4) may initiate on the entire external surface. In the intermediate case, i.e., a combination of bending and torsion, the proposed factor is within $(1, 2)$. Its exact value depends on the adopted methodology for determining this coefficient. In this case (Fig. 5), fatigue cracks begin to develop where the maximum normal stress occurs. The additional shear stress from torsion amplifies the fatigue cracking effect. A detailed analysis of fatigue cracks leads to the following conclusions. In the case of in-plane bending (Fig. 3), it is effortless to distinguish the fatigue zone and the residual zone, which are characteristic for fatigue fractures.

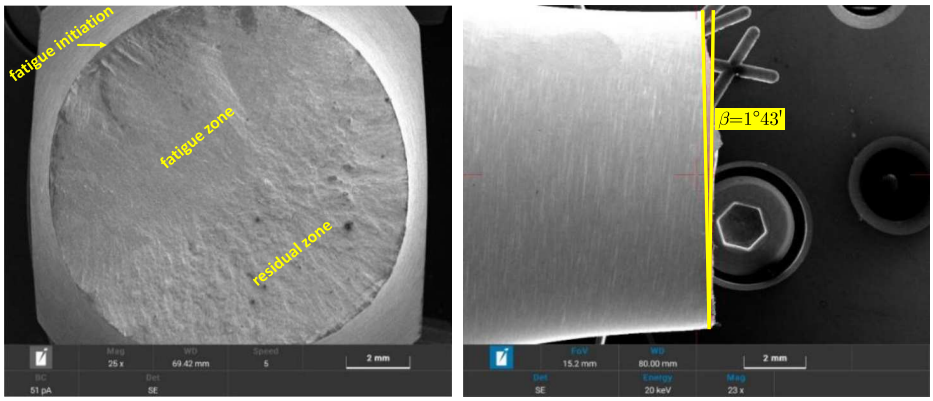

Fig. 3. Cyclic bending in a plane

However, a greater share of the fatigue zone concerning the residual zone is observed. At the fracture, a significant near-focal area is visible, along the edge of which a fatigue focus is visible in the form of characteristic fatigue lines, the distribution of which is not uniform. The surface of the fatigue zone at a low magnification seems smooth, which may indicate that the sample was subjected to a load with a low stress amplitude. In the case of cyclic torsion (Fig. 4), near--focus faults can be observed, which are already visible with the unaided eye. Parallel fatigue lines are observed in relation to the faults, and the morphology of the fracture surface indicates cleavage cracking along the grain sliding planes, as evidenced by the very finely developed surface topography. The branching of the faults, which a load change may have caused, is also clearly visible. For both bending and torsion combinations (Figs. 5-6), the fractures are characterized by a similar microrelief of the fatigue area topography throughout the area. Minor irregularities

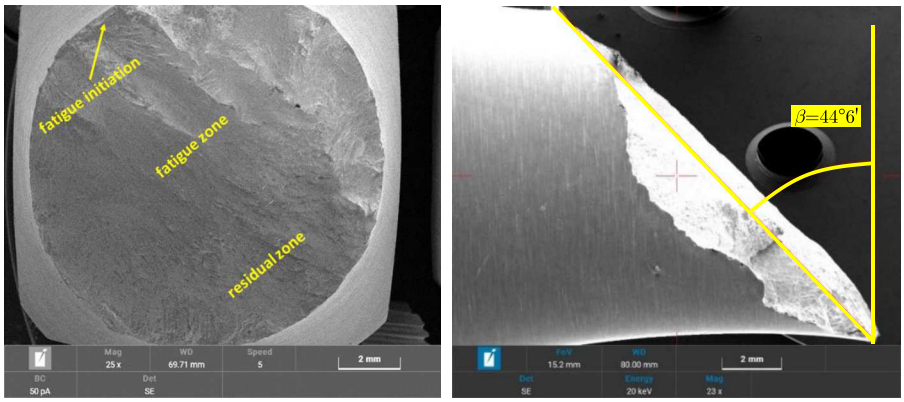

Fig. 4. Double-sided torsion

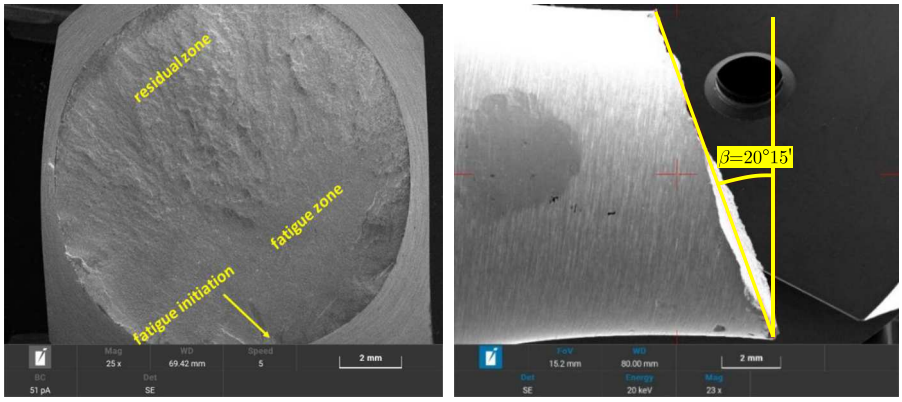

Fig. 5. Combination of cyclic bending with torsion $\tau_a = 0.5\sigma_a$

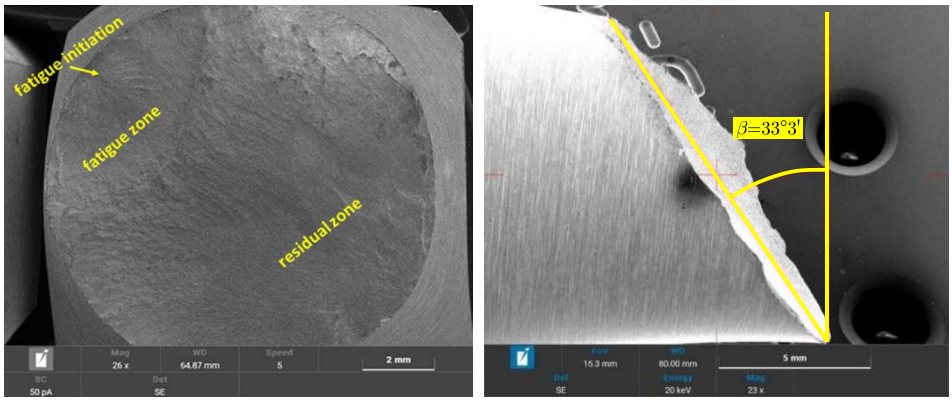

Fig. 6. Combination of cyclic bending with torsion $\tau_a = \sigma_a$

running deep into the fracture surface in the residual zone are noticeable. On the surface of both fractures, it is easy to locate the crack initiation site (fatigue focus visible in the fatigue zone), and it is also easy to identify mutually demarcating zones separating the fatigue zone band from the residual zone band. The surface of the residual zone is an area of a secondary scrap created by friction of the material during bending with torsion. The revealed properties of the scrap form the basis for considerations about the mechanism of initiation and development of fatigue cracks. From the analysis of the obtained images of fracture surfaces, it can be concluded that for each of the analyzed cases, the fatigue zone was formed in a long-term process of fatigue change growth as a result of crack propagation and spreading, and the residual zone was formed as a result of rapid destruction of the already weakened element.

4. Fatigue life according to multiaxial fatigue criteria

Table 6 lists the calculated multiaxial factors. These factors were derived depending on the multiaxiality criterion applied to the combination of proportional bending and torsion. The analysis of these coefficients shows that each time, in the case of cyclic bending, the multiaxiality factor is 1, and for cyclic torsion, it is 2. In the case of a combination of bending and torsion, this coefficient is between 1 and 2. In the case of criterion (3.6), the multiaxial coefficient can be defined in two ways. Both criteria (3.3) and (3.5) can be used here. A detailed analysis showed that for the combination of bending and torsion $\tau_a = 0.5\sigma + a$, this coefficient varies for the analyzed models within (1.33 and 1.50, and for the combination $\tau_a = \sigma_a$ within 1.50 and 1.63). Lower values are for criterion (3.5) – the criterion of maximum shear stresses, and greater for criterion (3.2) – Huber-Mises hypothesis.

Table 6. Multiaxial factors depending on the criterion and combination of bending and torsion

Criterion	Bending	$\tau_a = 0.5\sigma_a$	$\tau + a = \sigma_a$	Torsion
(3.2)	1	1.46	1.63	2
(3.3), (3.6)	1	1.43	1.60	2
(3.4)	1	1.33	1.50	2
(3.5), (3.6)	1	1.50	1.67	2

Then, analysis of the relationship between the obtained computational durability and those obtained as a result of the experiment was performed. Depending on the adopted criterion of multiaxial fatigue (3.2)-(3.6), the equivalent amplitude of normal stress was determined for all the obtained test results. This equivalent amplitude can be thought of as the stress amplitude from bending. Therefore, on the basis of fatigue characteristics $(3.1)_1$, the amplitude of cycles can be determined, where the design life is $N_{cal} - N_f$, based on the transformed characteristics in the form

$$N_{cal} = 10^{A_\sigma - m_\sigma \log \sigma_{aeq}} \tag{4.1}$$

For each of the analyzed characteristics, depending on the adopted criterion, the ratio of computational to experimental durability was determined for all experimental results. A linear approach can be found in the literature (Mamiya *et al.*, 2011) or a logarithmic one (Ma *et al.*, 2001)

$$d = \frac{N_{cal}}{N_{exp}} \qquad d = \log \frac{N_{exp}}{N_{cal}} \tag{4.2}$$

This paper used a linear relationship to analyze the dispersion given by formula (4.2). Then, the spreads mean values $\overline{d}$ and median d_m were determined. Table 7 shows the average values and median of fatigue life dispersion using selected multiaxial fatigue criteria (3.2)-(3.6). A scatter value of 1 means that the calculations perfectly agree with the experimental results. In the case of bending, the average error is close to 1. For the arithmetic mean value, it is slightly more (1.25), and for the median, it is less than 0.884. It follows that neither the mean nor the median value is a parameter that describes the mean value well in this case. Based on other studies, a parameter that would describe this phenomenon should be sought in the future. It may be a prime parameter combining these two average values. Coefficients close to 1 were obtained for torsion for criteria (3.3) and (3.6). This is because these criteria were derived from tests for cyclic bending and cyclic torsion.

For individual criteria, the results of calculating the mean values and the median are also presented in Figs. 7-12. In these figures, full points indicate average values. In these graphs, the

Table 7. Average/median life dispersion depending on the criterion used and the combination of bending and torsion

Criterion	Bending	$\tau_a = 0.5\sigma_a$	$\tau + a = \sigma_a$	Torsion
(3.2)	1.25/0.884	1.062/1.381	0.678/0.612	0.233/0.183
(3.3)	1.25/0.884	3.101/2.576	2.151/1.941	0.976/0.766
(3.4)	1.25/0.884	3.821/3.175	4.054/4.200	34.383/21.018
(3.5)	1.25/0.884	0.902/0.752	0.246/0.222	0.063/0.050
(3.6)	1.25/0.884	3.105/2.579	1.122/1.013	0.974/0.766

scatter band of 95% confidence, taking into account the 95% confidence interval for the mean value based on the standard error of the mean, is additionally marked by blank points. The horizontal line in each figure indicates compliance with the average value for cyclic bending. The analysis of the dispersion obtained in appropriate bands, depending on the criterion used and the multiaxiality coefficient, shows that none of the analyzed multiaxial fatigue criteria was consistent for all tested combinations of proportional cyclic bending with torsion in the 95% confidential interval band. It does not matter whether the arithmetic mean value or the median was taken as the mean value. In any case Gough-Pollard Criterion (3.3) and Maximum Normal Stresses (3.4) did not give satisfactory results. In the case of a small shear stress division, Huber-Mises criterion (3.2) and shear stress criterion (3.5) were effective. However, in the case of a large share of shear stresses, the criterion of shear and normal stresses determined by the maximum normal stress turned out to be effective (3.6). Therefore, it is proposed to use a hybrid criterion: shear stresses and shear and normal stresses determined by the maximum normal stress dependent on the multiaxiality factor in the form

$$\sigma_{aeq} = \begin{cases} 2\tau_{ans,max} & \text{for} \quad 1 \leqslant r_{BF} < \dfrac{3}{2} \\ \left(2 - \dfrac{\sigma_{a-1}}{\tau_{a-1}}\right)\sigma_{an,max} + \dfrac{\sigma_{a-1}}{\tau_{a-1}}\tau_{ans,max} & \text{for} \quad \dfrac{3}{2} \leqslant r_{BF} \leqslant 2 \end{cases} \tag{4.3}$$

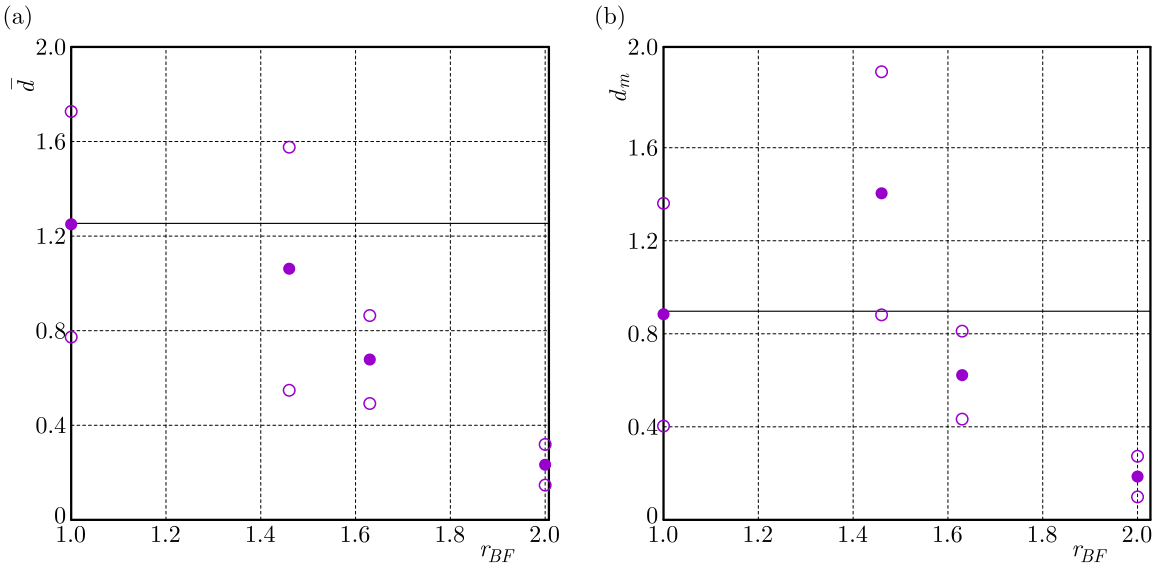

Fig. 7. Dispersion of the computational and experimental durability ratio for Huber-Mises criterion (3.2) with a probability coefficient of 95% depending on the multiaxiality factor: (a) mean value, (b) median value

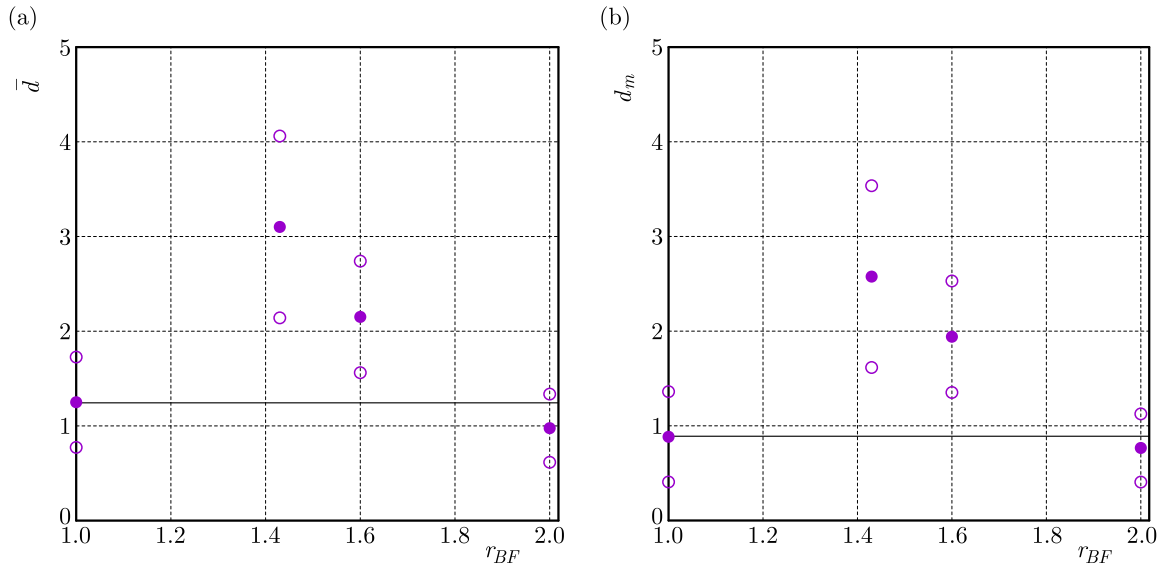

Fig. 8. Scatters of the computational and experimental durability ratio for Gough-Pollard criterion (3.3) with a probability coefficient of 95% depending on the multiaxiality factor: (a) mean value, (b) median value

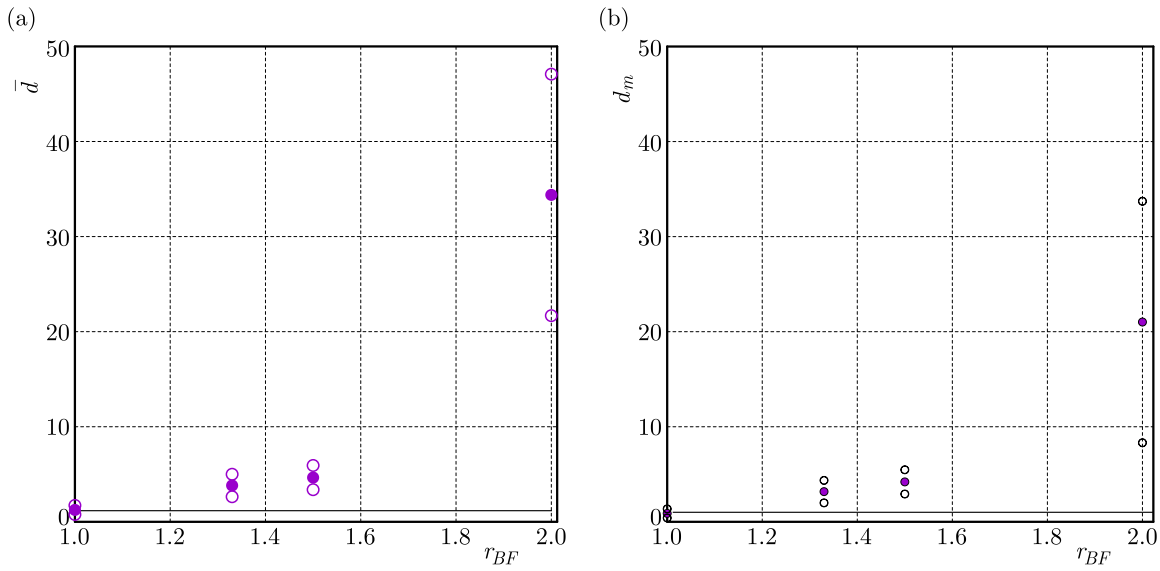

Fig. 9. Dispersion of the computational and experimental life ratio for criterion of maximum normal stresses (3.4) with a probability factor of 95% depending on the multiaxiality factor: (a) mean value, (b) median value

Analyzing the calculations in which critical planes were used, it turns out that the concepts of a critical plane and a crack plane are different. These concepts are not the same and mean completely other things. The values do not have to be the same either.

From the analysis of Table 7 and Figs, 7-12, it can be seen that in the case of mean values defined as average and median, the average value is always higher than that of the median value, except for one case. Additionally, it should be noted that the same situation applies to cyclic bending. Cyclic bending is the reference point in defining the multiaxial fatigue criterion. This value should be 1 for perfect compliance.

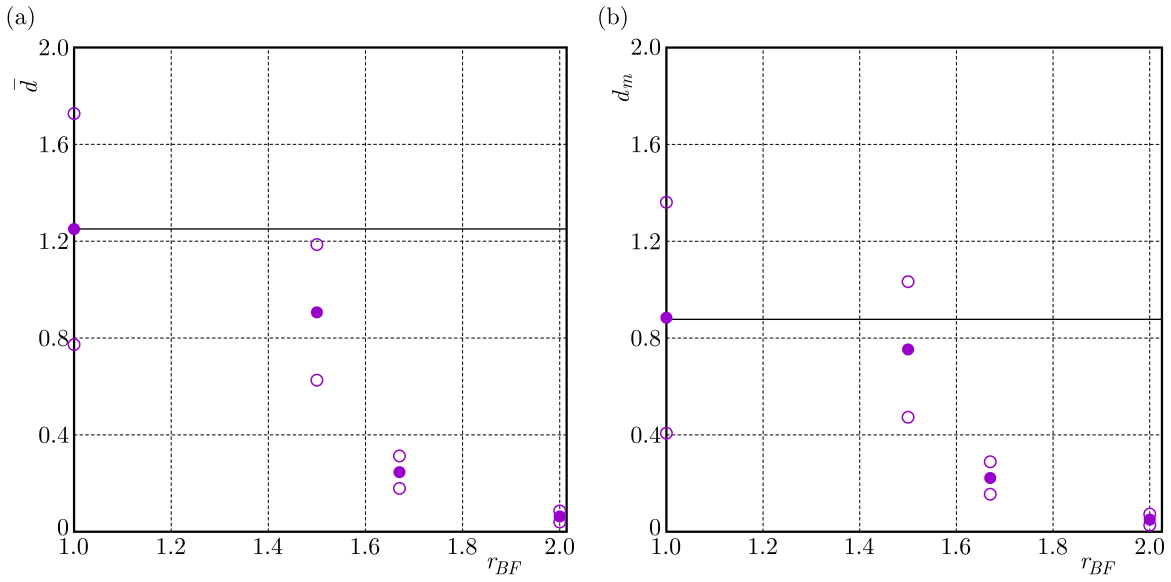

Fig. 10. Dispersion of the ratio of design and experimental life for criterion of maximum shear stresses (3.5) with a probability factor of 95% depending on the multiaxiality factor: (a) mean value, (b) median value

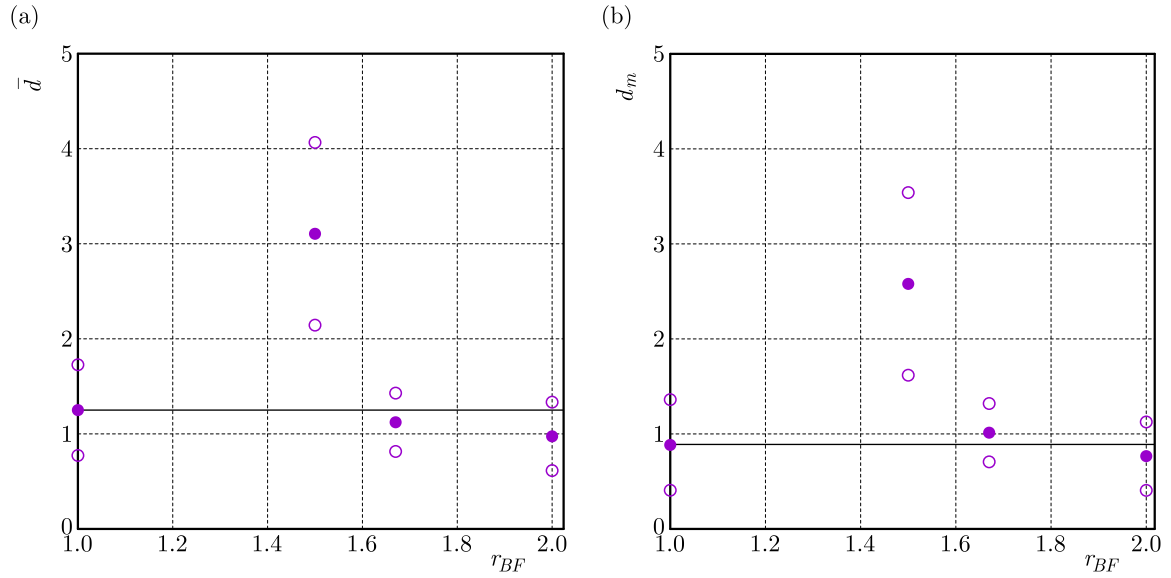

Fig. 11. Dispersion of the ratio of the design and experimental life for the criterion of maximum shear and normal stresses in the critical plane determined by maximum shear stresses (3.6) with a probability factor of 95% depending on the multiaxiality factor according to Tresca: (a) mean value, (b) median value

5. Conclusions

Based on the presented research results, the proposed models and presented analysis, it was found that:

- The new multiaxiality factor r_{BF} proposed in the paper, which can characterize fatigue tests for various combinations of bending and torsion, well characterizes multiaxiality.
- The proposed multiaxiality coefficient r_{BF} is a generalization of various coefficients found in the literature and can be selected depending on the criterion used.

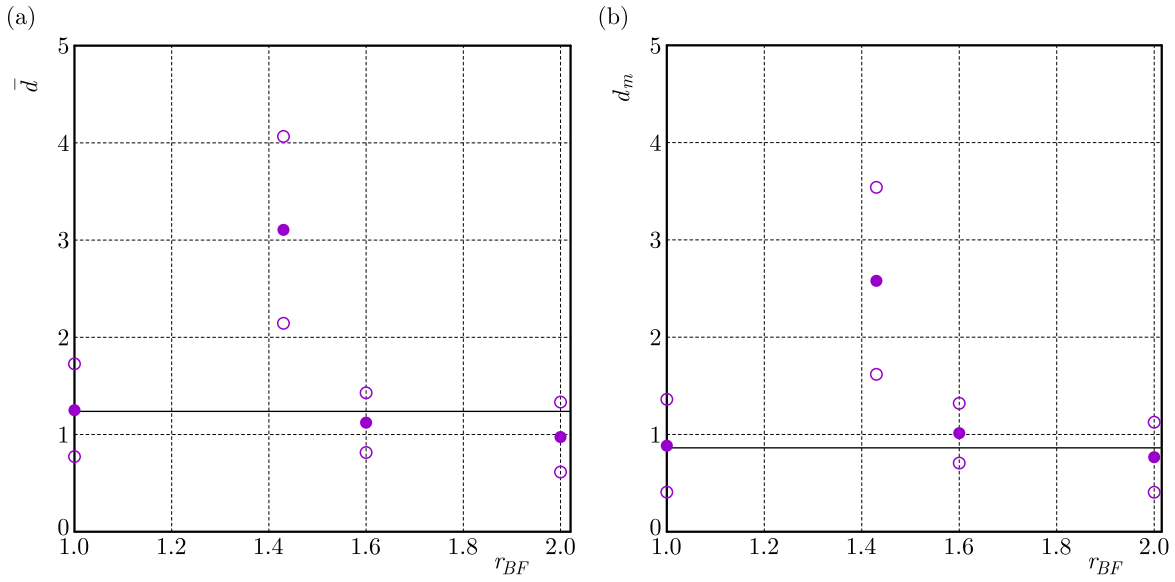

Fig. 12. Dispersion of the ratio of the design and experimental life for the criterion (maximum shear and normal stresses in the critical plane determined by maximum shear stresses (3.6) with a probability factor of 95% depending on the polyaxiality coefficient according to Gough-Pollard: (a) mean value, (b) median value

- The multiaxiality factor r_{BF} is 1 for cyclic bending and 2 for pure torsion. In the case of a combination of bending and torsion, the value of this factor is in the range $(1, 2)$.
- The analysis of the dispersion obtained in appropriate bands, depending on the criterion used and the multiaxiality factor, shows that none of the analyzed multiaxial fatigue criteria was consistent for all tested combinations of proportional cyclic bending with torsion in the 95% confidental interval band. It does not matter whether the arithmetic mean value or the median was taken as the mean value.
- In no case the Gough-Pollard criterion and the maximum normal stresses gave satisfactory results.
- In the case of a small branch of shear stresses, the Huber-Mises criterion and the shear stresses proved effective.
- In the case of a large share of shear stresses, the criterion of shear and normal stresses determined by the maximum normal stress turned out to be effective.
- It was proposed to use a hybrid criterion: shear and shear and normal stresses determined by the maximum normal stress dependent on the multiaxiality factor r_{BF}.
- The fractographic analysis of selected samples for all four combinations of fatigue tests showed that the occurrence of a fatigue center conditions the formation of the fatigue zone, the source of which is the concentration of stresses or an inhomogeneous structure of the material.
- The experimental failure planes are not coincident with the critical planes that are used first to determine the equivalent stresses and, consequently, the design life.

References

1. ASTM E1049-85, 2003, *Standard Practices for Cycle Counting in Fatigue Analysis*, The American Society for Testing and Materials, West Conshohocken, PA
2. Carpinteri A., Vantadori S., Łagoda T., Karolczuk A., Kurek M., Ronchei C., 2018, Fatigue assessment of metallic components under uniaxial and multiaxial variable amplitude loading, *Fatigue and Fracture Engineering Materials and Structures*, **41**, 1306-1317

3. Gan L., Wu, H., Zhong Z., 2021, Multiaxial fatigue life prediction based on simplified energy--based model, *International Journal of Fatigue*, **144**, 106036
4. Gough H.J., Pollard H.V., Clenshaw W.J., 1951, Some experiments on the resistance of metals to fatigue under combined stresses, *Aero Research Council*, **2522**, London: H.M.S.O
5. Kardas D., Kluger K., Łagoda T., Ogonowski P., 2008, Fatigue life of 2017(A) aluminum alloy under proportional constant-amplitude bending with torsion in the energy approach, *Materials Science*, **44**, 541-549
6. Karolczuk A., Kurek M., Łagoda T., 2015, Fatigue life of aluminium alloy 6082 T6 under constant and variable amplitude bending with torsion, *Journal of Theoretical and Applied Mechanics*, **53**, 421-430
7. Łagoda T., Kurek M., Głowacka K., 2020, A formulation of the criterion for multiaxial fatigue in terms of complex number as proposed by Macha, *International Journal of Fatigue*, **133**, 105430
8. Łagoda T., Macha E., 1994, Estimated and experimental fatigue lives of 30CrNiMo8 steel under in- and out-of-phase combined bending and torsion with variable amplitudes, *Fatigue and Fracture Engineering Materials and Structures*, **17**, 1307-1318
9. Ma S., Markert B., Yuan H., 2001, Multiaxial fatigue life assessment of sitered porous iron under proportional and non-proportional loading, *International Journal of Fatigue*, **97**, 214-226
10. Małecka J., Łagoda T., 2023, Fatigue and fractures of RG7 bronze after cyclic torsion and bending, *International Journal of Fatigue*, **168**, 107475
11. Małecka J., Żak K., Łagoda T., 2023b, Fatigue fracture surface of bronze RG7 under proportional cyclic torsion and bending, *Measurement*, **218**, 113126
12. Mamiya E.N., Castro F.C., Algarte R.D., Araújo J.A., 2011, Multiaxial fatigue life estimation based on a piecewise ruled S-N surface, *International Journal of Fatigue*, **33**, 529-540
13. Niesłony A., Łagoda T., Walat K., Kurek M., 2014, Multiaxial fatigue behaviour of AA6068 and AA2017A aluminium alloys under in-phase bending with torsion loading condition, *Materialwissenschaft und Werkstofftechnik*, **45**, 947-952.
14. Papuga J., Margetin M., Chmelko V., 2021, Various parameters of the multiaxial variable amplitude loading and their effect on fatigue life and fatigue life computation, *Fatigue and Fracture Engineering Materials and Structures*, **44**, 2890-2912
15. Slamečka K., Pokluda J., Kianicová M., Horniková M., Major S., Dvorák I., 2010, Quantitative fractography of fish-eye crack formation under bending-torsion fatigue, *International Journal of Fatigue*, **32**, 921-928
16. Slamečka K., Pokluda J., Kianicová M., Horniková J., Obrtlik K., 2013, Fatigue life of cast Inconel 713LC with/without protective diffusion coating under bending, torsion and their combination, *Engineering Fracture Mechanics*, **110**, 459-467
17. Slámečka K., Šesták P., Vojtek T., Kianicová M., Hornková J., Šandera P., Pokluda J., 2016, A Fractographic study of bending/torsion fatigue failure in metallic materials with protective surface layers, *Advances in Materials Science and Engineering*, ID8952657
18. Susmel L, Lazzarin P., 2002, A bi-parametric Wohler curve for high cycle multiaxial fatigue assessment, *Fatigue and Fracture Engineering Materials and Structures*, **25**, 63-78
19. Wächter M., Linn A., Wuthenow R., Esderts A., Gaier Ch., Kraft J., Fllgren C., Vormwald M., 2022, On scaled normal stresses in multiaxial fatigue and their exemplary application to ductile cast iron, *Applied Mechanics*, **3**, 259-295
20. Wang Q., Lade P.V., 2001, Shear banding in true triaxial tests and its effect on failure in sand, *Journal of Engineering Mechanics*, **127**, 754-761
21. Wang Z., Pan P., Zuo J., Gao Y., 2023, A generalized nonlinear three-dimensional failure criterion based on fracture mechanics, *Journal of Rock Mechanics and Geotechnical Engineering*, **15**, 630-640

Manuscript received August 29, 2024; accepted for print January 29, 2024

JOURNAL OF THEORETICAL AND APPLIED MECHANICS
62, 3, pp. 561-571, Warsaw 2024
https://doi.org/10.15632/jtam-pl/188373

PREDICTING THE TRAJECTORY OF A SPINNING PING PONG BALL DURING FLIGHT USING THREE-DIMENSIONAL COORDINATES

Xinyue Li
Nanjing Forestry University, Department of Physical Education, Nanjing, Jiangsu, China
e-mail: y3z411@yeah.net

Predicting the trajectory of a spinning ping pong ball can improve the effectiveness of a ping pong robot in daily training. In this study, the Vicon system was used to capture three-dimensional coordinates of the spinning ping pong ball during flight. Then, a long short-term memory (LSTM) neural network algorithm was improved by combining an adaptive particle swarm optimization (APSO) algorithm and the attention mechanism, and the APSO-LSTM-attention method was obtained for predicting the trajectory of the spinning ping pong ball. It was found through experiments that the APSO-LSTM-attention method had average displacement errors of 6.01 mm, 11.26 mm, and 8.97 mm in the X, Y and Z axes, respectively, and the final point displacement errors were 15.64 mm, 17.93 mm, and 11.26 mm, respectively, indicating that the method outperformed methods such as recurrent neural networks. The time required to predict the complete trajectory by the APSO-LSTM--attention method was also short, only 0.0186 s. The results demonstrate reliability of the proposed method in predicting the trajectory of the spinning ping pong ball and its potential application in practical scenarios.

Keywords: three-dimensional coordinates, ping pong ball, trajectory prediction

1. Introduction

Ping pong, the national game of China, is popular with the public. China has won many medals in various international competitions. For athletes, burying their heads in training can often lead to a bottleneck in technique. How to breakthrough their skills is quite concerned by athletes. With the development of intelligent algorithms and artificial intelligence, ping pong ball robots have become a new tool for daily training players (Gomez-Gonzalez *et al.*, 2019). In the field of ping pong, predicting the trajectory of a ball can help athletes practice better, which effectively reduces manpower costs and improves training efficiency. In other fields, the prediction of missile trajectories in military operations (Mir, 2018), aircraft trajectories (Huang *et al.*, 2021), trajectories of human body motion during transport driving (Bertugli *et al.*, 2021), driving trajectories (Amirloo *et al.*, 2022), and trajectories of athletes during sports (Hauri *et al.*, 2021) can greatly improve research efficiency. With the advancement of intelligent algorithms, research on trajectory prediction has become increasingly widespread worldwide. Kalatian and Farooq (2022) developed a new multi-input network based on long short-term memory (LSTM) and fully connected dense layers for predicting future pedestrian trajectories. The experimental results showed small prediction errors with this method. Xi *et al.* (2021) designed a prediction model for a target maneuvering trajectory, introducing the Levenberg-Marquardt and improved particle swarm optimization (IPSO) algorithms mixed with k-means for optimizing parameters of the radial basis function. Simulation experiments demonstrated high accuracy of this model. Mirmohammad *et al.* (2021) investigated trajectory prediction of soccer balls on a soccer field, proposed a method based on the K-nearest neighbor regression and autoregressive model, and proved high accuracy of the method through simulation and practical testing. Chen *et al.*

(2021) developed an end-to-end fully convolutional coding and decoding attention model based on convolutional LSTM, which was found to have excellent performance in predicting future trajectories of pedestrians through experiments on five crowded video sequences. Song *et al.* (2022) proposed a bidirectional gated recurrent unit with an attention mechanism for prediction of tropical cyclone trajectories. Experimental results on the best path data of Northwest Pacific tropical cyclones from 1988 to 2017 demonstrated excellent performance of this model in predicting future trajectories. Chen *et al.* (2020) introduced a method that utilized a genetic algorithm to optimize the number of neurons and weights in a backpropagation neural network (BPNN) for ship trajectory prediction. The experimental findings indicated that this approach significantly enhanced the accuracy of predictions. Song *et al.* (2022) proposed a radar track prediction method based on the BPNN, compared its result with the Kalman filter track, and found that this method was highly accurate to forecast tracks. Rajini Selvaraj and Gurusamy (2023) integrated an independent recursive neural network, Harris Hawk optimization algorithm, and one-dimensional convolutional neural network autoencoder to forecast tropical cyclone trajectories. Comparison with the existing methods revealed that the method had higher prediction accuracy and efficiency. The trajectory prediction of spinning ping pong balls is the research focus of this paper. By collecting three-dimensional coordinates, a method based on an LSTM neural network was developed, and its performance was analyzed through experiments. This paper provides some theoretical support for promoting the development of intelligent robots, which is conducive to promoting the performance of table tennis robots and their application in practical sports training.

2. Collection of three-dimensional coordinates for a ping pong ball

This paper used a Vicon motion capture system with functions of motion capture and position tracking to measure the trajectory of ping pong balls (Rodrigues *et al.*, 2019; Goldfarb *et al.*, 2021). In a space formed by six cameras, data was captured by attaching reflective markers on ping pong balls, and the Vicon system was utilized to collect and calculate the three-dimensional coordinate data of the reflective markers in real time. The collected data was processed using the accompanying Tracker software to obtain information such as the velocity of the ping pong ball. The Vicon system consisted of the following components.

(1) Vicon cameras: These cameras had a resolution of 2432 × 3048 pixels and a maximum capture frequency of 420 Hz. The capture range was 12 m.
(2) PoE switch: It was used to connect with the host personal computer for data analysis.
(3) Host personal computer: The Tracker software was installed in the host personal computer for data capture, processing, and visualization.
(4) Calibration bar: It has applied to calibrate the Vicon cameras and establish the origin of the coordinate system.
(5) Other accessories: Cables to connect the cameras with the switch, reflective markers for capturing coordinates, and so on.

In the experiment, the environment for collecting the three-dimensional coordinates of the ping pong ball is illustrated in Fig. 1.

During the experiment, the researchers threw the ping pong ball, and the three-dimensional coordinates of the spinning flight of the ping pong ball were collected in real-time using the Vicon system. As the ping pong ball was a sphere with three symmetrical axes, six reflective markers were symmetrically attached to the ping pong ball along its symmetrical axes as reference points. The data was collected at a frequency of 180 Hz. The ping pong ball was thrown 500 times. Each trajectory started from the release and ended when it hit the ground. To further expand the dataset, the collected coordinates of each trajectory were translated and rotated, resulting

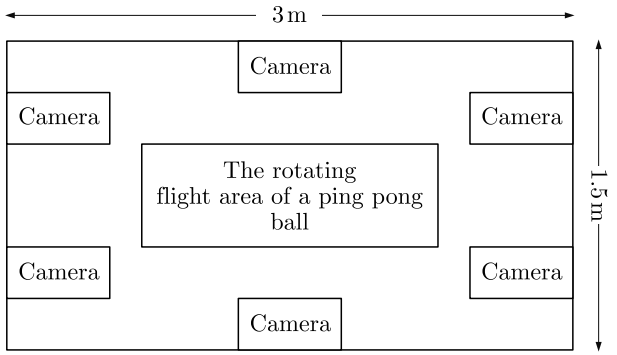

Fig. 1. Three-dimensional coordinate collection environment for a ping pong ball

in a total of 1500 trajectory data. The original three-dimensional coordinates of the ping pong ball are denoted by $L(x, y, z)$. After translating each coordinate by $L(x, y, z)$ units, the new coordinates are obtained as follows

$$L'(x', y', z') = \begin{bmatrix} 1 & 0 & 0 & x_0 \\ 0 & 1 & 0 & y_0 \\ 0 & 0 & 1 & z_0 \\ 0 & 0 & 0 & 1 \end{bmatrix} \begin{bmatrix} x \\ y \\ z \\ 1 \end{bmatrix} \tag{2.1}$$

Assuming that each coordinate rotates by θ° around the Z axis, the following coordinates are obtained

$$L'(x', y', z') = \begin{bmatrix} \cos\theta & -\sin\theta & 0 & 0 \\ \sin\theta & \cos\theta & 0 & 0 \\ 0 & 0 & 1 & 0 \\ 0 & 0 & 0 & 1 \end{bmatrix} \begin{bmatrix} x \\ y \\ z \\ 1 \end{bmatrix} \tag{2.2}$$

Some of the ping pong ball trajectory data is shown in Fig. 2 and Table 1.

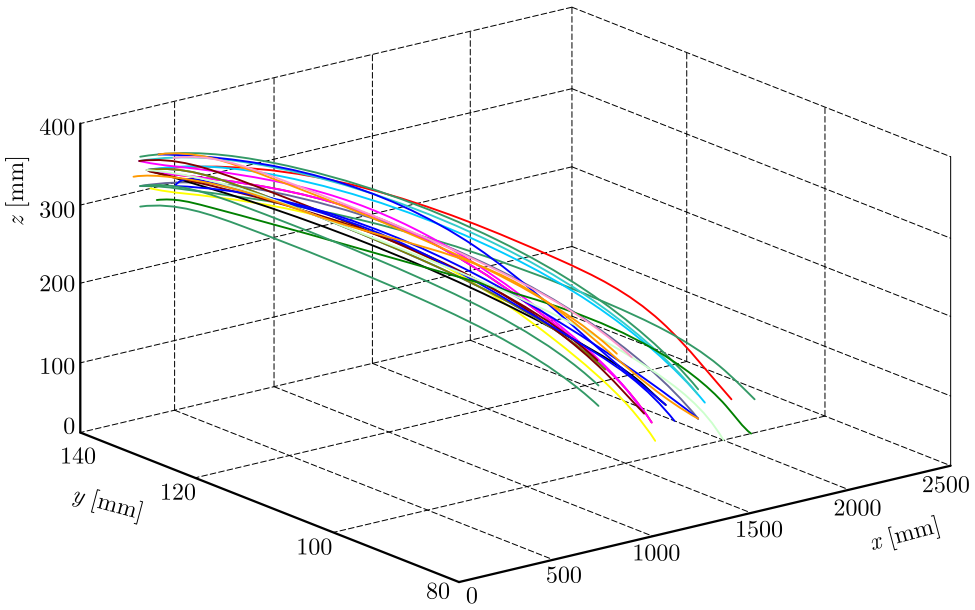

Fig. 2. Ping pong ball rotational flight trajectory data

Table 1. Example of ping pong ball trajectory data

Number	Three-dimensional coordinates [mm]
1	(233.56, 137.88, 354.02)
2	(345.77, 131.25, 341.22)
3	(455.26, 127.36, 322.15)
4	(556.25, 121.26, 311.25)
5	(667.62, 115.33, 296.37)
6	(764.25, 111.25, 256.36)
7	(864.22, 107.36, 241.85)
8	(958.67, 103.22, 222.87)
9	(1065.25, 99.52, 195.74)
10	(1174.52, 97.28, 161.07)

3. Long short-term memory-based trajectory prediction method

3.1. LSTM algorithm

The trajectory of a spinning ping pong ball during flight is a sequence with temporal properties. LSTM has demonstrated excellent performance in predicting time series (Kumar and Gomathi, 2022), and it has been extensively used in various domains such as weather forecasting and stock prediction (Gruet *et al.*, 2018). Therefore, in this study, LSTM is chosen to forecast the trajectory of the spinning ping pong ball during flight.

LSTM predicts data through three gates. First, let σ be the sigmoid activation function. Let W and b be the weight and bias of each gate. In the LSTM, the forgetting gate is used to determine how much information in the unit state value c^{t-1} from the previous moment needs to be forgotten. The input includes input information x^t from the current moment and output h^{t-1} from the previous moment. The output is

$$f_t = \sigma[W_f(h^{t-1}, x^t) + b_f] \tag{3.1}$$

The input gate is used to determine how much information can be input to the cell state. It includes two parts. The first part is to calculate how much information needs to be updated. The output is

$$i_t = \sigma[W_i(h^{t-1}, x^t) + b_i] \tag{3.2}$$

The other part is to calculate a new unit state candidate value $\overline{c}_t$. The calculation formula is

$$\overline{c}_t = \tanh[W_c(h^{t-1}, x^t) + b_c] \tag{3.3}$$

where tanh stands for the tangent function. Finally, the unit state value c^t is updated as

$$c^t = f_t c^{t-1} + i_t \overline{c}_t \tag{3.4}$$

The output calculates how much information can be output first. The corresponding formula is

$$o_t = \sigma[W_o(h^{t-1}, x^t) + b_o] \tag{3.5}$$

Then, the tanh function is combined to control the c^t value between -1 and 1. The final output of the LSTM is obtained after multiplication

$$h_t = o_t \tanh c^t \tag{3.6}$$

The learning process of LSTM is as follows:

- By performing forward calculations on the three gates, the output values of each neuron are obtained.
- The error between the output of each LSTM unit and the actual value is calculated, and all errors are summed up to obtain the total error.
- The weights are continuously updated through backward propagation of the error.
- It is checked whether the total error meets the accuracy requirement. If not, it returns to step one and repeats the calculation until the total error satisfies the accuracy requirement.

3.2. Attention mechanism

To further improve the effectiveness of LSTM on trajectory prediction, the attention mechanism (Zheng *et al.*, 2018) is added to better learn the input three-dimension coordinates of the ping-pong ball. The computational procedure of the attention layer is as follows:
— the attention probability distribution value at the t-th time is calculated using h_t, the output of the LSTM

$$e_t = v \tanh(wh_t + b) \tag{3.7}$$

— the normalized weight coefficient a_t is calculated

$$a_t = \frac{\exp(e_t)}{\sum_{j=1}^{t} e_j} \tag{3.8}$$

— the output of attention at the t-th is calculated

$$s_t = \sum_{t=1}^{i} a_t h_t \tag{3.9}$$

After passing the attention layer, the predictive trajectory value of the ping pong ball output at the t-th time is

$$y_t = \sigma(W_o s_t + b_o) \tag{3.10}$$

3.3. Parameter optimization methods

In LSTM, some parameters are usually determined based on empirical knowledge and require extensive experimentation for validation. This can significantly increase the training time of the algorithm. Therefore, this study employs an adaptive particle swarm optimization algorithm (APSO) to optimize the following parameters of LSTM:

- Learning rate: A value that is too small increases the learning time of the network, while a too large value may cause oscillations around the optimal value.
- Number of iterations: A value that is too small may prevent the network from achieving the best performance, while a value that is too large increases the training time.
- Number of hidden layer nodes: A value that is too small may result in underfitting, while a value that is too large may lead to overfitting.

The PSO algorithm is a method based on the foraging behavior of birds (Amiri *et al.*, 2023). It is known for its few parameters and high precision, and finds extensive applications in multi-objective optimization, industrial system control, and other fields (Bidyanath *et al.*, 2023).

Assuming a particle population $X = (x_1, x_2, \ldots, x_n)$ in a D-dimensional space, with initial positions $X = (X_{i1}, X_{i2}, \ldots, X_{iD})$ and initial velocities $V = (V_{i1}, V_{i2}, \ldots, V_{iD})$, individual and

global best positions are denoted by P_{iD} and P_{gD}, respectively. The PSO algorithm updates the positions and velocities of particles to find the optimal solution. The formulas are as follows

$$\begin{aligned} V_{id}^{k+1} &= wV_{id}^{k} + c_1 r_1 (P_{id}^{k} - X_{id}^{k}) + c_2 r_2 (P_{gd}^{k} - X_{gd}^{k}) \\ X_{id}^{k+1} &= X_{id}^{k} + V_{id}^{k+1} \end{aligned} \tag{3.11}$$

where w stands for the inertia weight, c_1 and c_2 are learning factors, r_1 and r_2 are random numbers in $[0, 1]$, and k denotes the number of iterations.

The value of w will affect the optimization performance of the PSO algorithm. The APSO algorithm makes adaptive improvement on it

$$w = \begin{cases} w_{min} - \dfrac{(w_{max} - w_{min})(f - f_{min})}{f_{avg} - f_{min}} & f \leqslant f_{avg} \\ w_{max} & f > f_{avg} \end{cases} \tag{3.12}$$

where w_{min} and w_{max} represent the maximum and minimum values of w, f is the current particle fitness value, f_{avg} and f_{min} are the average and minimum values of the current particle fitness.

Finally, the flow of the proposed APSO-LSTM-attention method for the ping pong ball trajectory prediction is depicted in Fig. 3.

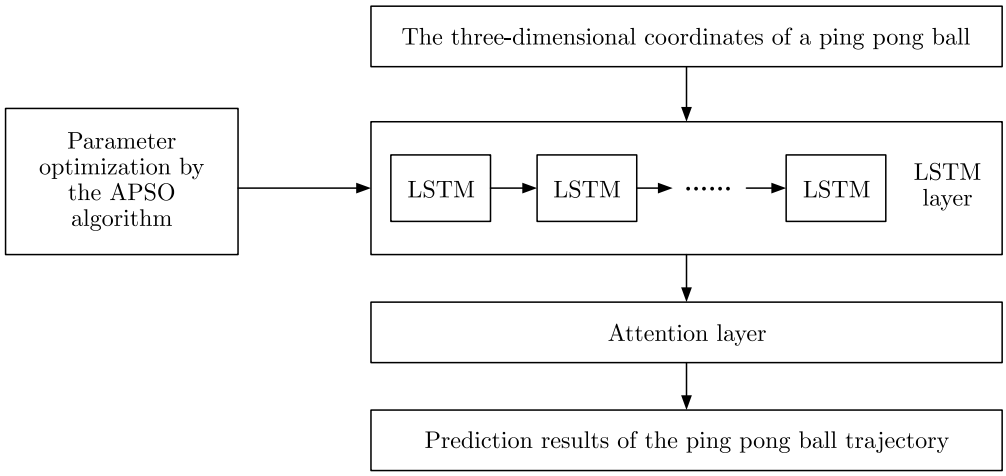

Fig. 3. The APSO-LSTM-attention trajectory prediction method

As shown in Fig. 3, the parameters of the LSTM are first optimized using the APSO algorithm. The optimized parameters are then input to the LSTM to learn from the three-dimensional coordinates of the ping pong ball. Next, the output of the LSTM serves as the input for the attention layer. By integrating the output of the attention layer, the final prediction results for the ping pong ball trajectory are obtained.

4. Results

4.1. Experimental setup

The experiment was conducted in a Windows 10 operating system with an Intel(R) Core(TM) i7-8550U processor and 8 GB of memory. The Python language was used, and the network model was built on the Kears framework based on TensorFlow. In the APSO-LSTM-attention model, the population size for the APSO algorithm was set to 50, the number of iterations was 500, and $c_1 = c_2 = 1.5$. The optimal values of the LSTM parameters obtained by the APSO algorithm were as follows: learning rate 0.001, number of iterations 200, number of nodes in the hidden

layer 64. The three-dimensional coordinates of the i-th ping pong ball trajectory at time t were denoted by $p_t^i(x_t, y_t, z_t)$. A complete trajectory was represented by $(p_1, p_2, \ldots, p_k, \ldots, p_T)$. To predict the three-dimensional coordinates of the ping pong ball at time $k+1$, the trajectory from time 1 to k was used. Then, the trajectory from time 2 to $k+1$ was used to predict the coordinates at time $k+2$. This process was repeated until the entire trajectory was predicted. A total of 1500 trajectories were used in the experiment. The ratio of the training set, the validation set and to and test set was 5:3:2. The data was predicted 100 times for each entry. The final result was obtained by taking the average.

Let $p'_t(x'_t, y'_t, z'_t)$ denote the predicted three-dimensional coordinates of the ping pong ball at time t, and $p_t(x_t, y_t, z_t)$ represents the actual values. Similarly, $p_f(x_f, y_f, z_f)$ represents the predicted three-dimensional coordinates of the endpoint of a trajectory, and $p'_f(x'_f, y'_f, z'_f)$ represents the actual values. The evaluation of trajectory prediction effectiveness was based on the following two indicators:

(1) Average displacement error (ADE), which refers to the error between the predicted result of the three-dimensional coordinates of the ping pong ball and the actual values

$$\text{ADE} = \frac{1}{N}\sum_{t=1}^{k}\sqrt{(x'_t - x_t)^2 + (y'_t - y_t)^2 + (z'_t - z_t)^2} \tag{4.1}$$

(2) Final point displacement error (FDE), which refers to the error between the predicted results of the three-dimensional coordinates of the endpoint of every trajectory and the actual values

$$\text{FDE} = \frac{1}{N}\sum_{t=1}^{k}\sqrt{(x'_f - x_f)^2 + (y'_f - y_f)^2 + (z'_f - z_f)^2} \tag{4.2}$$

4.2. Result analysis

Taking the x-axis coordinate prediction of a trajectory with 20 sample points as an example, the prediction performance of the following methods were compared:

- recurrent neural network (RNN) (Inoue *et al.*, 2018),
- LSTM,
- LSTM-attention,
- APSO-LSTM-attention.

Table 2 presents the percentage error of different methods on the X-axis.

From Table 2, it can be observed that both RNN and LSTM algorithms exhibited relatively large prediction errors on the X-axis, with maximum percentage errors around 3%. In contrast, the LSTM-attention algorithm demonstrated percentage errors below 3% on the X-axis. This confirmed the effectiveness of the attention mechanism. Furthermore, the proposed method achieved a maximum percentage error of only 1.20% and a minimum of 0.03%, showcasing the reliability of optimizing LSTM parameters with the APSO algorithm and its ability to achieve superior results in trajectory prediction.

Taking the 20 sampling points in Table 3 as an example, the results of the proposed method for predicting the three-dimensional coordinates of ping pong ball trajectories are shown in Table 3.

From Table 3, it can be observed that the APSO-LSTM-attention method yielded small errors when compared to the actual values. Among the predictions for the 20 sampling points, the maximum error was found in predicting the X-axis coordinate of sample point 8, with a value of 10.29 mm. The errors for all other sampling points were below 10 mm, which demonstrated the reliability of this method in trajectory prediction.

Table 2. Percentage error of different methods

	Actual value	RNN algorithm	LSTM algorithm	LSTM-attention algorithm	APSO-LSTM--attention method
1	565.38	1.15%	3.08%	1.75%	0.61%
2	662.90	2.85%	3.00%	0.69%	1.13%
3	692.35	3.58%	0.88%	1.84%	0.32%
4	757.02	1.15%	3.54%	1.55%	0.21%
5	810.51	1.11%	−3.18%	0.24%	1.20%
6	826.31	0.57%	1.61%	1.86%	0.86%
7	949.32	−0.16%	1.67%	2.05%	0.43%
8	978.51	3.40%	1.98%	1.98%	1.05%
9	1037.46	3.01%	2.14%	1.97%	0.40%
10	1096.57	2.74%	2.49%	1.25%	0.31%
11	1133.80	1.92%	0.22%	1.38%	0.73%
12	1168.62	−3.38%	1.95%	−0.37%	0.70%
13	1182.20	1.55%	0.81%	0.08%	0.49%
14	1235.44	2.99%	1.42%	0.66%	0.18%
15	1311.63	1.12%	−2.08%	1.35%	0.46%
16	1439.78	−1.24%	1.67%	−1.13%	0.20%
17	1489.86	2.36%	0.90%	0.92%	0.15%
18	1521.97	0.73%	0.76%	1.25%	0.63%
19	1591.20	1.06%	1.55%	0.11%	0.12%
20	1625.60	1.76%	0.48%	0.70%	0.03%

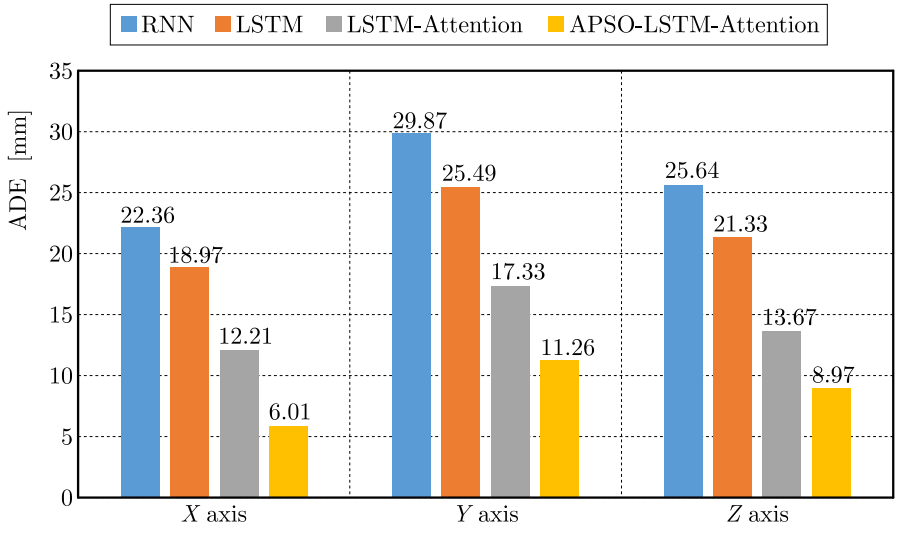

Fig. 4. Comparison of ADE

The comparison results of the ADE among different methods on the test set are presented in Fig. 4.

Firstly, in terms of the prediction in the X-axis, the RNN, LSTM, and LSTM-attention algorithms had ADE values above 10 mm, while the proposed method achieved an ADE of 6.01 mm, reducing the errors by 16.35 mm, 12.96 mm, and 6.2 mm, respectively, compared to the RNN, LSTM, and LSTM-attention algorithms. All methods exhibited high ADE values on the Y-axis. Among them, the RNN algorithm had an ADE of 29.87 mm, while the proposed method showed an ADE of 11.26 mm, significantly lower than the other methods. Finally, in

Table 3. The prediction results of the APSO-LSTM-attention method for three-dimensional coordinates

	Actual value	Prediction result	Error
1	(565.38, 120.33, 321.56)	(568.85, 122.36, 323.55)	(3.47, 2.03, 1.99)
2	(662.90, 116.34, 305.12)	(670.38, 114.25, 303.56)	(7.48, −2.09, −1.56)
3	(692.35, 112.36, 300.12)	(694.58, 114.25, 298.25)	(2.23, 1.89, −1.87)
4	(757.02, 108.26, 297.36)	(758.64, 105.36, 295.62)	(1.62, −2.90, −1.74)
5	(810.51, 106.25, 294.33)	(820.24, 104.22, 291.36)	(9.73, −2.03, −2.94)
6	(826.31, 97.36, 284.26)	(833.39, 100.03, 281.33)	(7.08, 2.67, −2.93)
7	(949.32, 95.36, 281.32)	(953.40, 91.26, 278.65)	(4.07, −4.10, −2.67)
8	(978.51, 93.26, 278.25)	(988.81, 91.26, 275.33)	(10.29, −2.00, −3.79)
9	(1037.46, 89.97, 275.12)	(1041.58, 87.21, 271.33)	(4.12, −2.76, −3.79)
10	(1096.57, 86.25, 271.36)	(1100.00, 84.33, 268.24)	(3.43, −1.92, −3.12)
11	(1133.80, 83.26, 268.45)	(1142.03, 80.26, 264.33)	(8.24, −3.00, −4.12)
12	(1168.62, 81.22, 264.26)	(1176.79, 78.66, 261.36)	(8.17, −2.56, −2.90)
13	(1182.20, 78.64, 261.25)	(1187.98, 75.33, 258.34)	(5.78, −3.31, −5.91)
14	(1235.44, 76.12, 257.26)	(1237.67, 74.21, 255.35)	(2.23, −1.91, −1.91)
15	(1311.63, 74.22, 254.36)	(1317.68, 71.26, 251.33)	(6.05, −2.96, −3.03)
16	(1439.78, 71.15, 251.13)	(1442.68, 68.26, 253.27)	(2.90, −2.89, 2.14)
17	(1489.86, 68.21, 248.61)	(1492.07, 66.33, 245.28)	(2.21, −1.88, −3.33)
18	(1521.97, 65.12, 245.36)	(1531.56, 61.26, 247.36)	(9.59, −3.86, −2.00)
19	(1591.20, 61.42, 241.33)	(1593.18, 59.33, 238.64)	(1.98, −2.09, −2.69)
20	(1625.60, 57.64, 237.52)	(1626.06, 56.97, 235.61)	(0.46, −0.67, 1.91)

the comparison in the Z-axis, the proposed method had an ADE of 8.97 mm, reducing the errors by 16.67 mm, 12.36 mm, and 4.7 mm, respectively, compared to the RNN, LSTM, and LSTM-attention algorithms.

Next, a comparison of the FDE among the different methods is presented in Fig. 5.

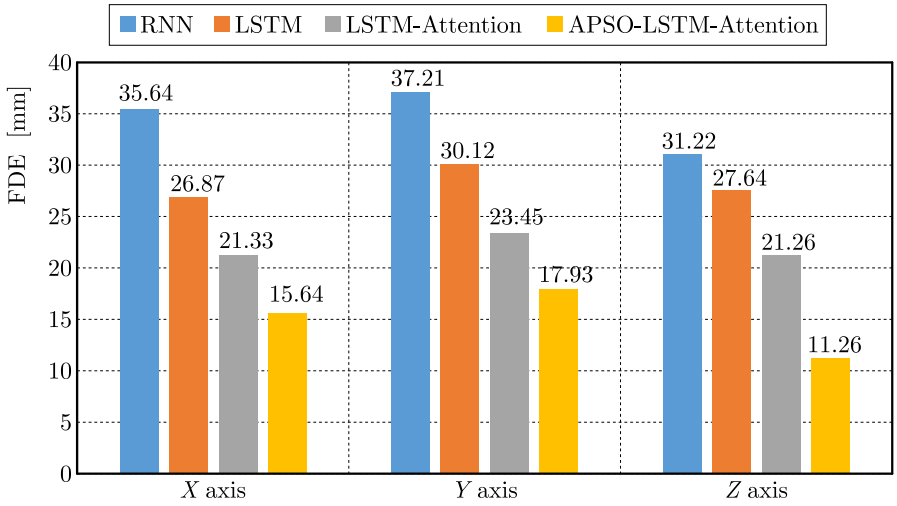

Fig. 5. Comparison of FDE

From Figure 5, it can be seen that the APSO-LSTM-attention method exhibited smaller FDE compared to the RNN, LSTM, and LSTM-attention algorithms. This indicated that the proposed method provided more accurate predictions of the three-dimensional coordinates of the endpoint trajectory of the ping pong ball. This high accuracy is crucial for meeting the

precision requirements in practical applications, such as in human-robot ping pong matches, where accurate prediction of the three-dimensional coordinates is essential for higher training efficiency.

Finally, the prediction time between the different methods was compared. The time required for each method to predict a complete trajectory is presented in Fig. 6.

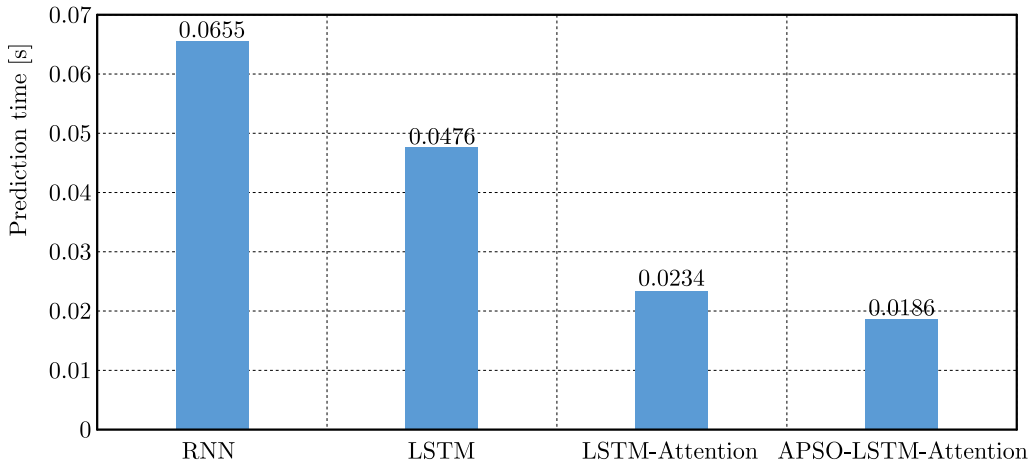

Fig. 6. Comparison of prediction time

From Fig. 6, it can be observed that the prediction time for all the methods was less than 1 s. Comparatively, the RNN algorithm required the longest prediction time, with 0.0655 , while the proposed method had the shortest prediction time of 0.186 s, which was 71.6% less than the RNN algorithm, 60.92% less than the LSTM algorithm, and 20.51% less than the LSTM-attention algorithm. These findings demonstrate that the proposed method does not only exhibit good prediction accuracy but also provides real-time performance.

5. Conclusion

In this study, a trajectory prediction method, the APSO-LSTM-attention algorithm, was designed based on the three-dimensional coordinates of a ping pong ball during rotational flight. The results demonstrated that compared to methods like the RNN and LSTM algorithms, the APSO-LSTM-attention algorithm achieved smaller prediction errors with ADEs of 6.01 mm, 11.26 mm, and 8.97 mm in the X, Y and Z axes, respectively. The FDEs were also smaller, and the time required to predict a complete trajectory was only 0.0186 s, indicating good accuracy and efficiency. These findings support the further application of the proposed method in practical scenarios.

References

1. Amiri A., Salmasnia A., Zarifi M., Maleki M.R., 2023, Adaptive Shewhart control charts under fuzzy parameters with tuned particle swarm optimization algorithm, *Journal of Industrial Integration and Management*, **8**, 2, 241-276

2. Amirloo E., Rasouli A., Lakner P., Rohani M., Luo J., 2022, *Latent Former: Multi-Agent Transformer-Based Interaction Modeling and Trajectory Prediction*, arXiv e-prints

3. Bertugli A., Calderara S., Coscia P., Ballan L., Cucchiara R., 2021, AC-VRNN: Attentive Conditional-VRNN for multi-future trajectory prediction, *Computer Vision and Image Understanding*, **210**, 5, 1-10

4. Bidyanath K., Singh S.D., Adhikari S., 2023, Implementation of genetic and particle swarm optimization algorithm for voltage profile improvement and loss reduction using capacitors in 132 kV Manipur transmission system, *Energy Reports*, **9**, 738-746
5. Chen K., Song X., Ren X., 2021, Modeling social interaction and intention for pedestrian trajectory prediction, *Physica A: Statistical Mechanics and its Applications*, **570**, 9, 1-12.
6. Chen X., Meng X., Zhao Y., 2020, Genetic algorithm to improve Back Propagation Neural Network ship track prediction, *Journal of Physics: Conference Series*, **1650**, 3, 1-9
7. Goldfarb N., Lewis A., Tacescu A., Fischer G.S., 2021, Open source Vicon Toolkit for motion capture and gait analysis, *Computer Methods and Programs in Biomedicine*, **212**, 106414
8. Gomez-Gonzalez S., Nemmour Y., Schölkopf B., Peters J., 2019, Reliable real time ball tracking for robot table tennis, *Robotics*, **8**, 4, 1-13
9. Gruet M.A., Chandorkar M., Sicard A., Camporeale E., 2018, Multiple-hour-ahead forecast of the DST index using a combination of long short-term memory neural network and Gaussian process, *Space Weather*, **16**, 11, 1882-1896
10. Hauri S., Djuric N., Radosavljevic V., Vucetic S., 2021, Multi-modal trajectory prediction of NBA players, *Workshop on Applications of Computer Vision*, 1639-1648
11. Huang M., Ochieng W.Y., Escribano Macias J.J., Ding Y., 2021, Accuracy evaluation of a new generic trajectory prediction model for Unmanned Aerial Vehicles, *Aerospace Science and Technology*, **19**, Dec. Pt. 2, 1-26
12. Inoue M., Inoue S., Nishida T., 2018, Deep recurrent neural network for mobile human activity recognition with high throughput, *Artificial Life and Robotics*, **23**, 2, 173-185
13. Kalatian A., Farooq B., 2022, A context-aware pedestrian trajectory prediction framework for automated vehicles, *Transportation Research Part C: Emerging Technologies*, **134**, 103453
14. Kumar K.S., Gomathi B.R., 2022, Forecasting photovoltaic power output using long short-term memory and neural network models, *International Journal on Engineering Applications*, **10**, 2, 116-125
15. Li S., Wang S., Xie D., 2019, Radar track prediction method based on BP neural network, *The Journal of Engineering*, **21**, 8051-8055
16. Mir M., 2018, *Cruise Missile Target Trajectory Movement Prediction Based on Optimal 3D Kalman Filter with Firefly Algorithm*, arXiv:1807.07006
17. Mirmohammad Y., Khorsandi S., Shahsavari M.N., Yazdankhoo B., Sadeghnejad S., 2021, Ball trajectory prediction for humanoid robots: combination of k-NN regression and autoregression methods, *International RoboCup Symposium*, 1-12
18. Rodrigues T.B., Cathin C.Ó., Devine D., Moran K., O'Connor N.E., Murray N., 2019, An evaluation of a 3D multimodal marker-less motion analysis system, *The 10th ACM Multimedia Systems Conference*, 213-221
19. Rajini Selvaraj A., Gurusamy T., 2023, An optimal model using single-dimensional CAE--IRNN based SPOA for cyclone track prediction, *Expert Systems with Application*, **230**, 1-13
20. Song T., Li Y., Meng F., Xie P., Xu D., 2022, A novel deep learning model by BiGRU with attention mechanism for tropical cyclone track prediction in the Northwest Pacific, *Journal of Applied Meteorology and Climatology*, **61**, 1, 3-12
21. Xi Z., Xu A., Kou Y., Li Z., Yang A., 2021, Target maneuver trajectory prediction based on RBF neural network optimized by hybrid algorithm, *Journal of Systems Engineering and Electronics*, **32**, 2, 498-516
22. Zheng J., Cai F., Shao T., Chen H., 2018, Self-interaction attention mechanism-based text representation for document classification, *Applied Sciences*, **8**, 4, 1-14

Manuscript received August 17, 2023; accepted for print January 3, 2024

JOURNAL OF THEORETICAL AND APPLIED MECHANICS
62, 3, pp. 573-585, Warsaw 2024
https://doi.org/10.15632/jtam-pl/190831

MECHANISMS OF MINING INDUCED INRUSH OF PRESSURIZED WATER IN THE FLOOR CONTAINING FAULTS

Baoliang Zhang, Wei Zhang
School of Architecture and Engineering, Liaocheng University, Liaocheng, China
corresponding author Wei Zhang, e-mail: 1125671372@qq.com

Baotang Shen
The Commonwealth Scientific and Industrial Research Organisation, Queensland, Australia

Yang Gao
School of Architecture and Engineering, Liaocheng University, Liaocheng, China

Mingming Liu
Water-Sediment Regulation and Sand Effective Utilization Special Laboratory of Shandong Provincial Education Department, Liaocheng University, Liaocheng, China

Investigating the propagation of the seepage path of confined water in the floor is an important means to determine the conditions of water inrush from the mine floor for deep mines with high water pressure. In order to better understand the mechanisms of water inrush due to the hidden fault floor above a confined water body, an integrated study including analytical analysis, and similarity simulation experiments were conducted. The study focuses on the distribution of mining induced stress in the floor, the propagation of hidden faults, and the evolution process of water inrush channels during longwall coal seam extraction.

Keywords: floor concealed fault, water inrush mechanism, mining-water pressure action, crack propagation, seepage path

1. Introduction

Mine water inrush has always been a prominent problem that threatens safety of coal production. In recent years, most coal mines in northern China are gradually entering deep mining. The distance between the main coal seam and the aquifer of the lower Ordovician limestone formation is shrinking, and the threat of floor water inrush is becoming increasingly serious (Yin *et al.*, 2021; Zhang *et al.*, 2023a; Cao *et al.*, 2021). Among them, the Han-Xing mining area is one of the typical mining areas with high water inflow in China (Pappalardo *et al.*, 2020). The coal seam is overlaying an Ordovician limestone karst layer with water pressure of over 7.0 MPa, and over 10 large-scale water inrush incidents occurred in the past 20 years, of which 9 occurred in the mining face. Under the disturbance of deep mining and high water pressure, the mining is facing serious water inrush threats. The presence of small hidden faults in the floor further exacerbates the risk of water inrush (Zhao *et al.*, 2018; Zhang *et al.*, 2020a,b,c; Mezza *et al.*, 2022).

The water inrush caused by floor aquifers must have a water inrush path, and formation mechanisms of the water inrush path are the key to control and remediate the water inrush risk. The concealed fault is a natural path for the migration of confined water, which has a profound impact on the stress state of floor and rock permeability, and will significantly increase the original height of water migration (Aguilera *et al.*, 2019; Bhuiyan *et al.*, 2018; Zhang *et al.*, 2020a,b,c). Under specific mining geological conditions, the surrounding rock undergoes periodic

caving with the movement of the working face. Due to the propagation of primary fractures in hidden faults and low mechanical strength, the integrity of water barrier in the floor rock layer is weakened to various degrees. The impact of mining and the propagation of mining fractures in the floor region vary depending on the structural geological conditions (Guerin *et al.*, 2021; Lin *et al.*, 2021). Li *et al.* (2023) established a solid fluid coupling mathematical model and analyzed the relationship between fault elements and water inrush law by using finite element simulation. Yin *et al.* (2022) developed a mechanical model for progressive uplift of faults and derived an analytical formula for the critical mechanics of water inrush from faults, revealing the spatiotemporal evolution of water inrush from the floor through physical simulation. Based on theoretical analysis and numerical simulation, Ren *et al.* (2022) conducted an in-depth study on the characteristics of mining induced floor fault activation and delayed water inrush, and obtained the mechanism of induced fault activation and delayed water inrush under the influence of mining.

Despite the increasing awareness and importance of mine water inrush, floor water inrush accidents still occur from time to time. Based on the investigation and statistics of the causes of multiple large-scale water inrush accidents, Wang *et al.* (2022) pointed out that the reason for the difficulty in containing water inrush accidents in the floor is the concealment and difficulty in detecting hidden small structures. Based on this, the traditional method of preventing and controlling mine water in coal mining faces has been changed, and a regional approach tailored to the mining area has been adopted. The location and scale of hidden structures are determined by injecting a grout slurry and observe its leakage. The method of microseismic monitoring and warning for mine water hazards is adopted by Xiong *et al.* (2023), which describes and predicts the trajectory of water inrush by monitoring the microseismic signals generated during the formation and dynamic development of potential water conducting cracks. The tri-level warning model for mine water inrush established from this can help managing potential water inrush areas, providing a new method for deep hidden structure exploration, dynamic monitoring, and water inrush warning. For the study of the mechanism of coal seam floor damage and water inrush, Tu *et al.* (2022) proposed the concept of "relative water resistance layer of the floor", pointing out that water inrush from the coal seam floor is not only related to thickness of the water resistance layer, but also to water pressure. By analyzing a large amount of on-site measured data, Zhang *et al.* (2020a,b,c) considered the joint control effect of mining stresses and water pressure in the floor rock mass, and proposed the in-situ tensile fracture theory. In view of the spatial relationship between the water conducting fault and the floor plastic slip zone, the shortest distance between the water conducting fault and the floor plastic slip zone is regarded as the critical path of the fault water inrush, and a simplified fracture mechanics model of the floor fault water inrush is established by Zhao *et al.* (2020). Based on the theory of linear elasticity stress propagation in a semi infinite body, the confined water pressure is regarded as an additional stress, and the distribution law of mining induced stress in the floor is obtained by Zhang *et al.* (2022a,b,c), which is used as the basis for judging the risk of water inrush. Based on the stress calculation results of the floor, the Mohr-Coulomb criterion with tensile failure was used to calculate the depth of the floor plate failure, and the effects of water pressure and thickness of the waterproof floor plate on the calculation results were explored by Mineo and Pappalardo (2019).

The present research focuses on the activation of hidden faults and the mechanism of water inrush under the combined action of mining and water pressure. The propagation direction of the seepage path of pressurized water after mining is crucial for determining the scope of key regional governance objectives (Zhang *et al.*, 2022a,bc; Zhang *et al.*, 2023a,b). The water inrush from the coal seam floor is caused by mining disturbances that cause stress field changes, leading to the initiation and propagation of cracks in the floor. Under the impact of high pressure water from the bottom to top, the seepage path gradually evolves into a high-speed water inrush path.

The distribution characteristics of stress field, crack propagation, and seepage behavior of the floor will also vary depending on whether the floor contains hidden structures and the types of hidden structures. Therefore, it is still necessary to further analyze the linkage process between the uplift and migration of mining induced confined water and the development of water path under the combined conditions. This paper adopts an integrated approach combining theoretical analysis, physical simulation, and numerical simulations under the conditions of the existence of hidden faults in the floor. The water inrush mode of hidden faults in the floor is the key research object of this study, and the process of water inrush caused by mining through hidden faults is analyzed to study the mechanism of floor water inrush in deep mining.

2. Simulation experiment on the expansion and activation of hidden faults

2.1. Determination of similarity ratio

The expansion of hidden faults refers to the process of relative opening displacement of the rock layers of the fault under the combined action of external stress and floor support pressure, with the direction of relative displacement determined by the maximum stress direction. Essentially, it is the shear and expansion movement that occurs in the sidewalls of the fault failure zone under the action of mining pressure, causing the material position inside the fault to change from the initial non hydraulic state to a hydraulic state.

The two key factors that can affect water inrush from the floor while maintaining the same hydrological conditions are the mining stress and faults (including size and spatial location). They reduce the effective thickness of the floor waterproof layer. As shown in Fig. 1, water inrush from hidden faults in the coal seam floor is the main form of water inrush from faults. Therefore, the hidden faults in the floor are taken as the main analysis object. When the inclination angle of the hidden faults is α, as the coal seam is mined, if the support pressure on the floor is greater than the maximum deformation strength value, plastic deformation will occur in the rock mass within a certain range of the working face floor, leading to the phenomenon of floor protrusion. The depth of the impact of mining stress on the failure of the bottom plate is L.

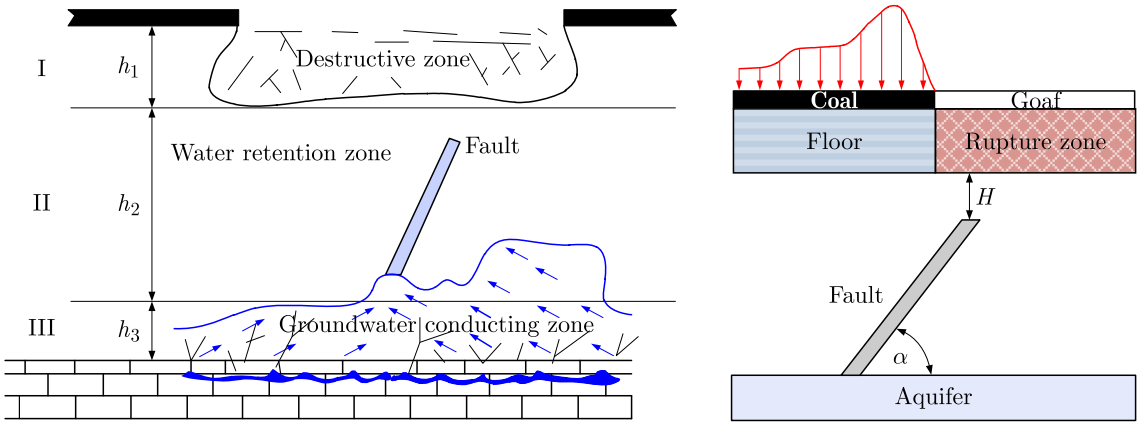

Fig. 1. Structural model of water inrush from floor faults

It is necessary to conduct relevant physical similarity simulation tests to address the above issues. Figure 2 shows the plane stress similarity simulation test independently developed and designed. The bracket has height of 1.5 m, width of 2 m, and thickness of 0.2 m. During the testing process, strain information was collected through the DH3821 static strain analyzer, and stress information was obtained based on the LY-350 soil pressure sensor.

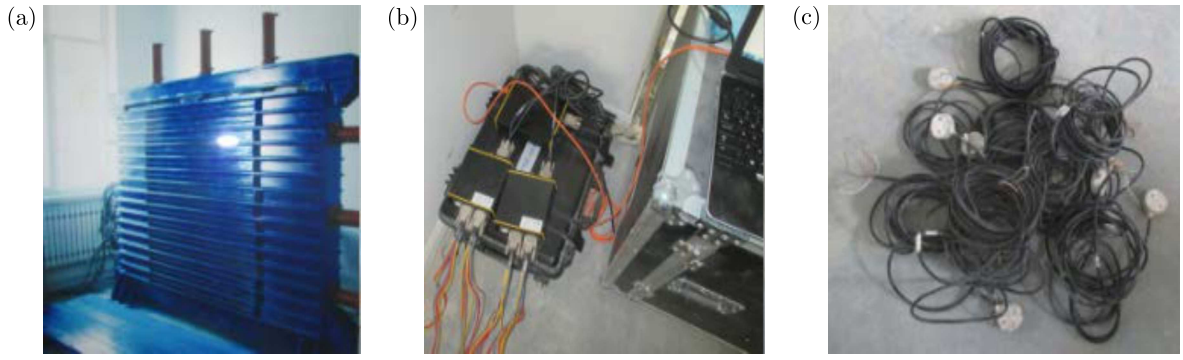

Fig. 2. Schematic diagram of the testing device: (a) test bracket, (b) strain analyzer, (c) pressure cell

The similarity simulation test is based on mining technical conditions, combined with geometric dimensions of the support and based on similarity theory, to determine the simulation similarity ratio:

— geometric similarity ratio

$$C_1 = \frac{x'}{x''} = \frac{y'}{y''} = 100 \tag{2.1}$$

— unit weight similarity ratio

$$C_\gamma = \frac{\gamma'}{\gamma''} = 1.5 \tag{2.2}$$

— time similarity ratio

$$C_\tau = \sqrt{C_1} = 14.1 \tag{2.3}$$

— strength similarity ratio

$$C_p = C_e = C\gamma C_1 \tag{2.4}$$

2.2. Design of the compensated stress measuring point layout

Taking into account the size of the support and the objective impact of boundary coal pillars on the test results, a 20 cm boundary coal pillar is left on both sides of the model. The working face is pushed from left to right, with total length of 150 cm. The model design simulation adopts a long wall full height mining method, and the simulated working face completes mining every 30 min, with parallel operations.

As shown in Fig. 3, due to the height limitation of the test bench, when studying the movement law of the overlying strata in deep mining through experiments, it is not possible to simulate all rock layers. Only a portion of the overlying strata in the mining space can be simulated, and the weight of the remaining overlying strata and the topsoil layer needs to be simplified as a uniformly distributed load applied to the upper boundary of the model. Removing the thickness of the floor, as the actual height of the model laid is 1.09 m, removing the thickness of the floor, calculated in a similarity ratio of 1:100, is equivalent to simulating a 690 m high overburden layer. For a working face with an average mining depth of 1000 m, the remaining 310 m of overlying rock and quaternary clay are simplified as surface loads applied to the top of the model. The vertical stress that the model needs to compensate for can be calculated using the following expression

$$\sigma'' = \frac{C'}{C_p} = \frac{\gamma H}{C_p} \tag{2.5}$$

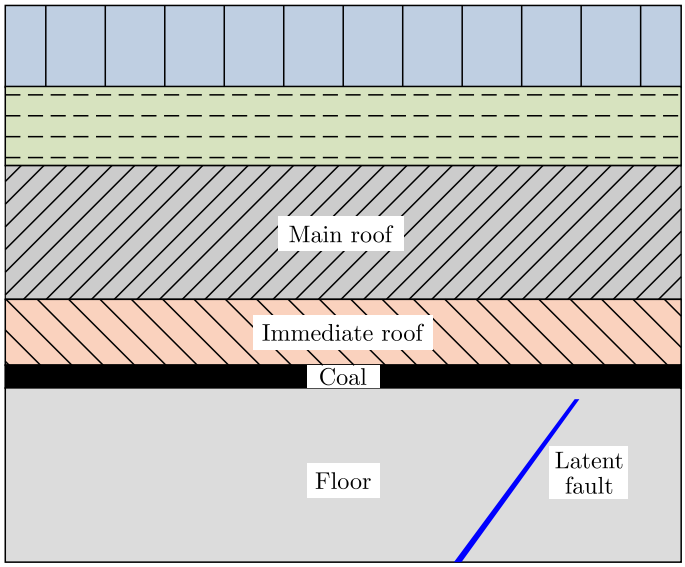

Fig. 3. Similar simulation structural model

2.3. Measuring point layout

As shown in Fig. 4, a total of 10 stress sensors are used in the similar material model to monitor the stress characteristics of the roof and floor in the coal seam during excavation. Among

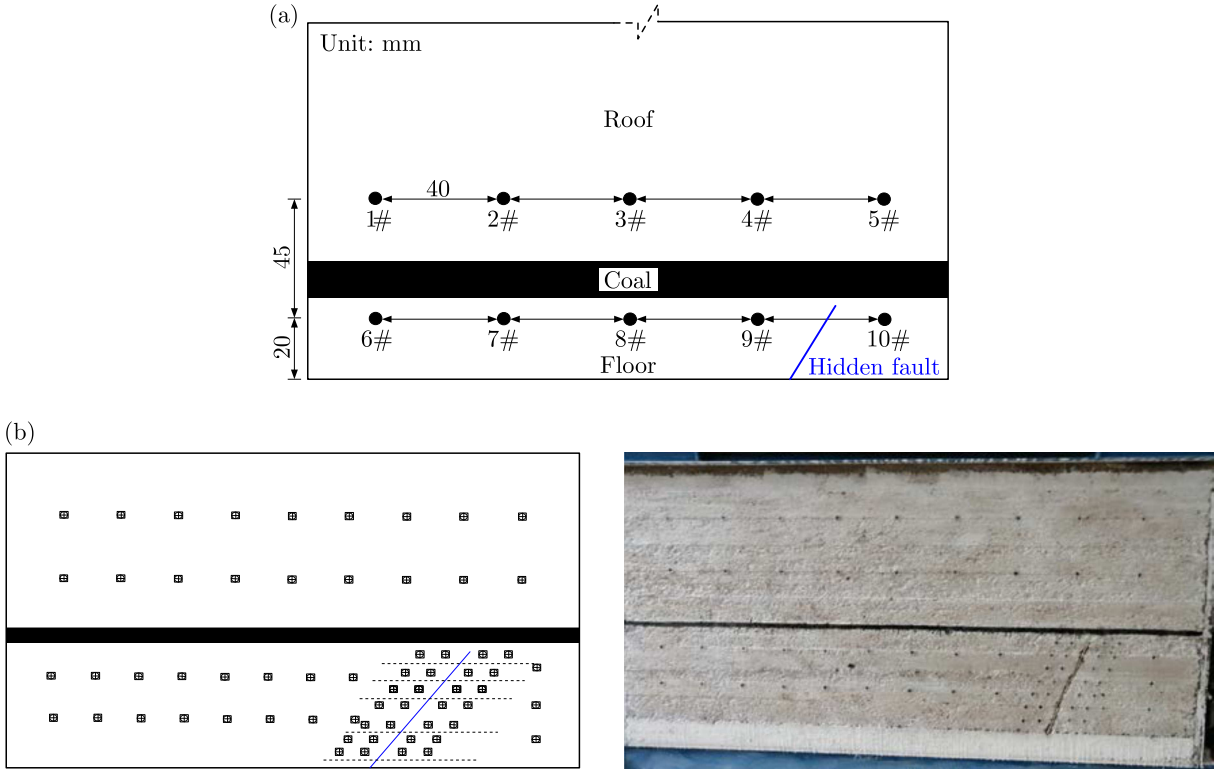

Fig. 4. Schematic diagram of measurement point layout location: (a) of stress gauge layout position, (b) layout of strain gauge

them, the first group has five strain gauges which are uniformly arranged in the medium grained sandstone of the 15th layer of the coal seam roof. The second group consists of five strain gauges which are uniformly arranged in the 19th layer of siltstone. In addition, there are a total of 66

displacement monitoring points for similar material models, and they are arranged in 4 areas. Among them, the distance between the horizontal and vertical displacement monitoring points in the roof is 20 cm. The distance between the horizontal and vertical displacement monitoring points in the left floor of the fault is 15 cm. The vertical distance interval between the monitoring points on the right side of the fault floor is 10 cm. The distance between the displacement monitoring points near the hidden fault and the fault, as well as the horizontal and vertical distances between the two monitoring points are 5 cm.

2.4. Similar material model laying

By combining hydrogeological conditions with experimental methods, a similar material model simulates a 69 m thick roof, a 2 m thick coal seam, and a 38 m thick floor. According to the model parameters and similarity ratio given in Table 1, sand, calcium carbonate, gypsum, and water are used to make the test materials. After the materials are mixed and stirred evenly, they are laid layer by layer. After each layer of rock is laid, mica powder needs to be spread to simulate the layer of the rock, and the laying is carried out step by step until the entire model laying work is completed.

Table 1. Stratification and ratio of rock layers

No.	Lithology	Thickness of stratum [cm]	Accumulated thickness [cm]	Proportion ratio	Coal material usage [kg]			
					sand	calcium carbonate	gypsum	water
1	Sandstone	3	3	7:8:2	19.4	1.7	0.4	2.2
2	Siltstone	10	13	7:5:5	67.2	4.8	4.8	7.7
3	Sandstone	5	18	7:8:2	33.6	3.8	1.0	3.8
4	Mudstone	6	24	9:6:4	37.8	3.2	2.2	4.3
5	Sandstone	10	34	7:7:3	69.1	1.2	6.5	7.7
6	Siltstone	8	42	7:5:5	27.6	1.5	1.5	3.1
7	Sandstone	2	44	7:8:2	12.6	1.4	0.4	1.4
8	Siltstone	2	46	7:5:5	13.4	1.0	1.0	1.5
9	Sandstone	6	52	7:7:3	41.5	3.2	1.3	4.6
10	Mudstone	2	54	9:6:4	13.0	0.9	0.6	1.4
11	Sandstone	2	56	7:8:2	13.8	1.2	0.3	1.5
12	Siltstone	4	60	7:5:5	27.5	1.5	1.5	3.1
13	Sandstone	2	62	7:8:2	13.0	1.2	0.3	1.4
14	Siltstone	1	63	7:5:5	6.9	0.4	0.4	0.8
15	Sandstone	5	68	7:7:3	33.6	3.4	1.4	3.8
16	Mudstone	1	69	9:6:4	6.5	0.4	0.3	0.7
17	Coal	2	71	8:6:4	9.5	0.6	0.4	1.1
18	Mudstone	3	74	9:6:4	18.9	1.6	1.1	2.2
19	Siltstone	5	79	8:6:4	33.6	2.9	1.9	3.8
20	Sandstone	12	91	7:7:3	80.6	8.1	3.5	9.2
21	Mudstone	2	93	9:6:4	13.0	0.9	0.6	1.4
22	Siltstone	1	94	7:5:5	6.7	0.5	0.5	0.8
23	Sandstone	15	109	7:8:2	100.8	11.5	2.9	11.5

As shown in Fig. 5, the laying steps of a similar material simulation model are:

(1) In the early stage, the required quality of each material is calculated in advance based on the size and proportion of the test frame for on-site weighing, the grade of sand and high-

-strength gypsum is determined, and the required frame for the test is checked to ensure its normal use and compliance with performance requirements.

(2) Weigh the material according to the calculated ratio, and when weighing the material, it is necessary to weigh the excess mass. In actual experiments, there may be a decrease in the total amount of the material due to operational reasons (such as material sticking to the mixer, scattering during transportation, etc.), so it is necessary to weigh according to the excess mass.

(3) According to the experimental needs, the template for simulating faults should be placed in advance. Stress sensors should be placed in the rock layers designed for the model, and placed according to the predesigned positions. The stress gauge labels at each position should be recorded to facilitate data processing in the future without confusion.

(4) Weigh each material according to the precalculated material quality and lay it from the bottom to top according to the layer size. During the laying process, sufficient compaction is required to ensure that there will be no significant settlement during the later static process, thereby ensuring the accuracy of the test results.

(5) Spread mica powder between each rock layer (simulating the layered rock layer). After the overall laying is completed, only external loads are applied based on the precalculated loads to simulate the overlying rock that cannot be reflected in the upper part. Place the model for 3 days and maintain it in a room temperature curing state.

Fig. 5. Laying process of a similar material model

3. Analysis of test results

3.1. Analysis of the characteristics of layer deformation

Considering the impact of boundary effects on coal seam mining, the initial mining position is set at a distance of 20 cm from the support boundary. Each excavation distance is 5 cm, the excavation height is 2 cm, and the excavation interval is 30 minutes. In addition, the local and global deformation characteristics of similar material models at intervals of 10 minutes are recorded.

During the entire testing process, a total of 32 excavations were conducted, with total excavation length of 160 cm. As the mining progress increases, the impact of mining stress generated by this disturbance on the roof gradually increases. After the appearance of the initial pressure characteristics, the width and height of fault cracks undergo varying degrees of evolution. A total of 13 push mining cases that met the periodic weighing characteristics were statistically analyzed throughout the entire experiment process. Among them, when the initial pressure is applied at 25 cm during mining, cracks appear on the direct roof, and fracture occurs when the collapse step is reached, with a fracture step of about 25 m (Fig. 6).

As shown in Fig. 7, the curve evolution characteristics illustrate the lateral displacement characteristics of the observation points set on both sides of the fault crack after each compression. When the value in the figure is positive, it indicates that the fault is expanding outward and the failure mode is tensile failure. When the value in the figure is negative, it indicates that

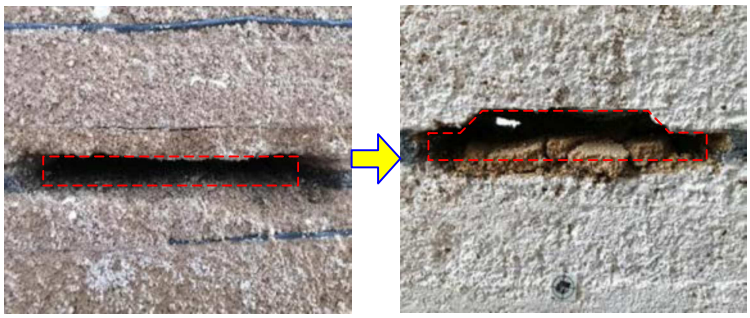

Fig. 6. Initial pressure on the working face

the fault is contracting inward and the failure mode is compression failure. During the testing process, the fault cracks showed overall compression failure, and compression deformation in the middle of the fault was the largest. The X distribution characteristics of deformation on both sides of the fault indicate that the middle part of the fault is in a compression and contraction state, while the two ends of the fault are in an expansion state. After the third pressure application during the experiment, there was no lateral displacement at the bottom of the fault until it continued to grow after the sixth pressure application, indicating that the crack propagation was a process from closure to opening.

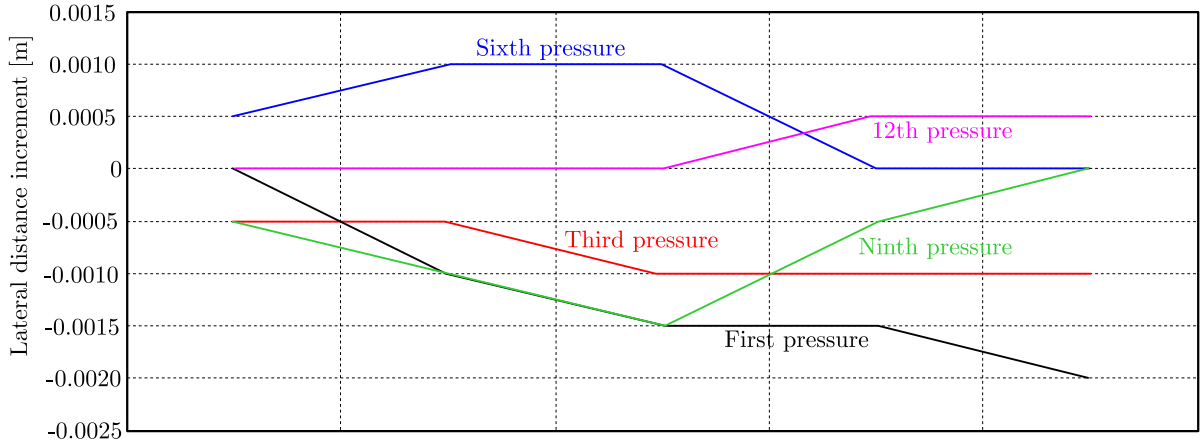

Fig. 7. Characteristics of lateral displacement changes on both sides of faults

When the working face advances 50 cm, the indirect roof collapses. When the working face is advanced to 60 cm, the crack extends to the top plate at 52 cm. When the working face was advanced to 95 cm, the crack had expanded to 67 cm. When the working face is advanced to 140 cm, the crack extends to 109 cm and runs through a similar material model (Fig. 8).

3.2. Analysis of stress evolution characteristics

Sensors 1 and 10 are symmetrically distributed in the direct roof, and are located behind the cutting hole and in front of the stop mining line. As shown in Fig. 9, by comparing and analyzing the distribution characteristics of support stress in the direct roof of the coal wall side, it is found that during the advancing process of the working face, the support stress has always been in an upward state and can be divided into two stages: a slow increase and a rapid increase. It indicates that during the mining process, the overlying rock at the opening has been constantly moving and deformed. During the process of advancing to a distance of 95 cm from the opening off cut, the supporting stress rises slowly. After the working face is advanced to 95 cm, the support stress begins to rapidly increase. When the working face is 60 cm away from

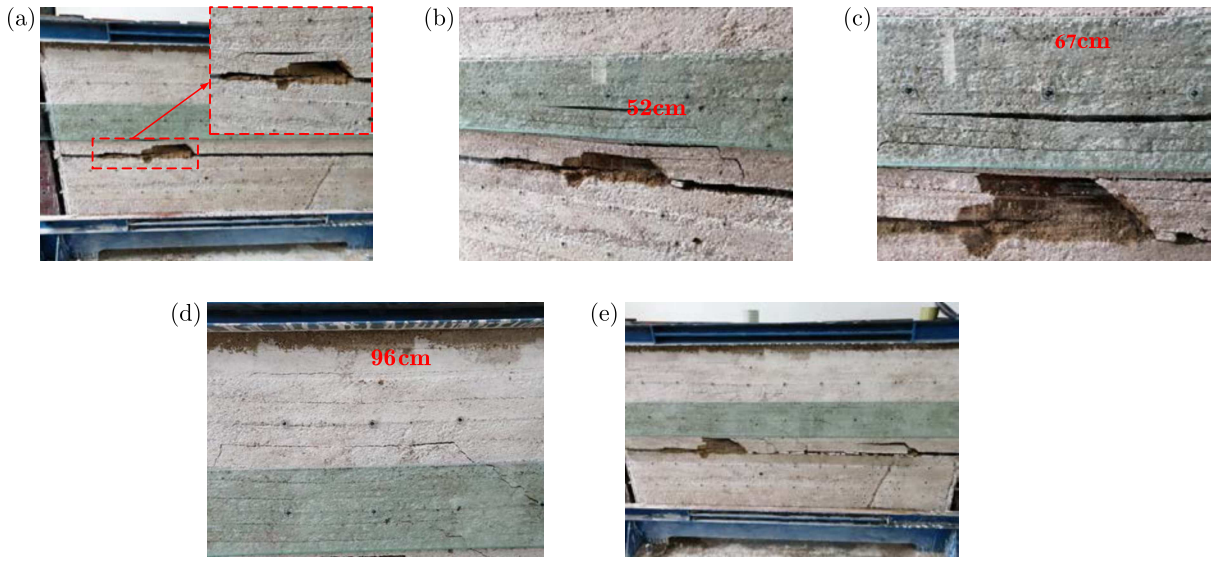

Fig. 8. Deformation characteristics of similar material models: (a) indirect roof collapse, (b) roof crack length is 52 cm, (c) roof crack length is 67 cm, (d) roof crack length is 96 cm, (e) final structure of the model

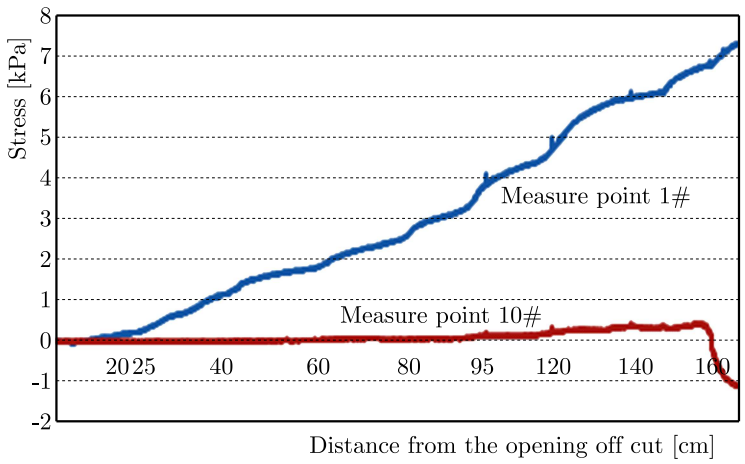

Fig. 9. Stress distribution characteristics of the direct top support

the stopping line, the growth rate of bearing stress decreases. When the working face is 20 cm away from the stopping line, the support stress rapidly decreases. In the process of deep mining, the impact range of mining is relatively large, and within 20 m from the coal wall of the working face, there is a stress rise zone. Moreover, the movement and deformation of the overlying strata at the opening are more severe than at the stopping line.

In the pushing mining process of the working face, the bearing stress in the immediate roof and floor in front of the coal wall experienced a process of rising first and then falling. Due to the large range of advanced influence, the support stress in the top and bottom plates in front of the working face gradually increases, with the maximum value of the top plate support stress being about 5 kPa and the maximum value of the bottom plate support stress being about 8 kPa. After the working face is pushed and mined, the support stress will rapidly decrease. When the distance between the mining line and the goaf is about 30 cm 40 cm, the increment of support stress tends to stabilize, and the final stress values are inconsistent with the position in the goaf. In addition, the stress in the bottom plate gradually changes from a positive value to a negative value, indicating that the bottom plate has undergone a process from compression to expansion (Fig. 10).

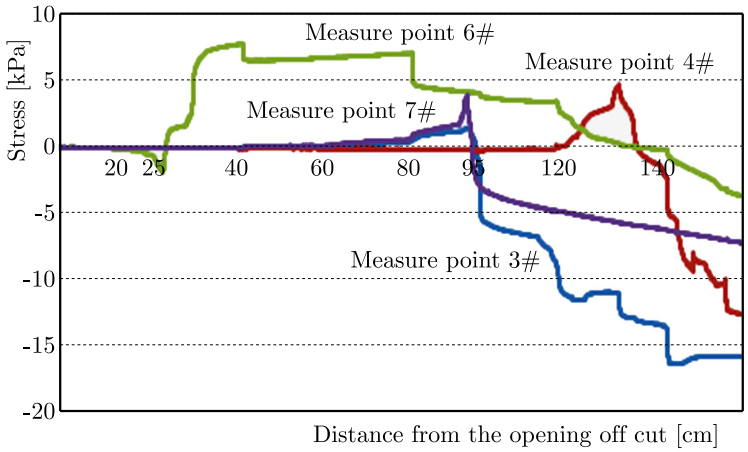

Fig. 10. Distribution characteristics of support stress in the goaf

The maximum decrease in stress increment at the center of the mining area indicates that the place with the maximum deformation caused by the direct roof movement is located near the center of the mining area. The increment of basic top stress shows a trend of first decreasing and then increasing during the process of pushing and mining 35 cm to 40 cm in the working face, indicating that the separation layer between the direct top and the upper rock layer is gradually compacted and closed, so a part of the weight of the upper rock layer is borne by the direct top. After the completion of the working face push mining, the stress increment value of the direct roof in the goaf is basically zero, indicating that the movement and deformation of the direct roof rock in the goaf have become stable. The stress of the floor shows a trend of a rapid increase first and then a slow decrease. The stress of the bottom plate increases with a decrease of the distance from the working face pushing and mining line, and undergoes an evolution process of compression before expansion.

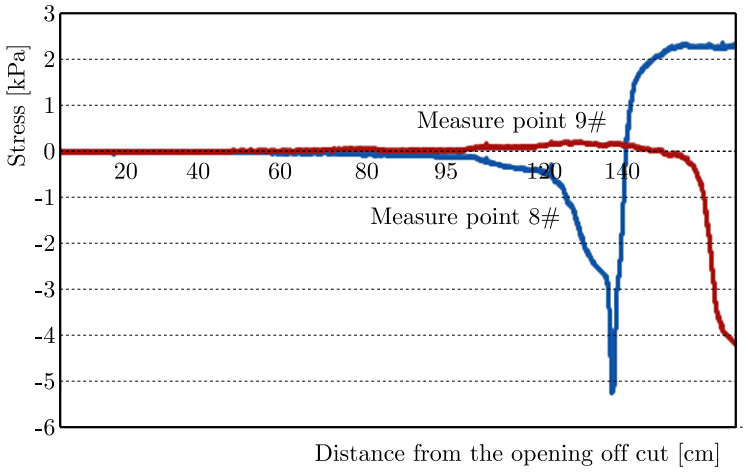

Fig. 11. Characteristics of stress distribution in the fault

The impact of early mining on the stress at the fault is very small, so the stress on both sides of the fault changes slowly, and the overall trend shows a slow increase followed by a rapid decrease. Before the working face is advanced to a distance of 25 cm above the fault, the stress at the fault is basically positive, and then the fault stress rapidly decreases and transforms into a negative value. When the working face is pushed to a distance of 25 cm from the fault, the left side of the fault is pulled and the right side is compressed, and the fault has a tendency to rupture to the upper left. When the working face is pushed to be within 25 cm from the fault,

the left side of the fault is under pressure and the right side is under tension, with a tendency to rupture above the right (Fig. 11).

4. Conclusion

- Under the influence of mining, the edge of macroscopic hidden faults is mainly characterized by oblique shear failure accompanied by overall splitting tensile failure. The shear cracks derived from edge cracks and oblique cracks develop in opposite directions, and the development direction is the shortest path direction required for crack penetration.
- The rock mass near the hidden fault has undergone an evolutionary process of "development of the original separation layer, compaction and sealing of the original separation layer, expansion of the new separation layer, and compaction and sealing of the new separation layer". When the working face advances to a height near three times the fault height, the impact of mining stress on the development of the fault sharply increases.
- When a distance from the working face is greater than 10 times the height of the fault, the vertical stress of the surrounding rock near the macroscopic hidden fault is basically not affected by the mining stress. When the distance from the working face is less than 5 times the height of the fault, the vertical stress of the surrounding rock near the macroscopic hidden fault is gradually affected by the mining stress.

Acknowledgements

The research described in this paper was financially supported by Natural Science Foundation of Shandong Province (No. ZR2022ME165), National Natural Science Foundation of China (No. 52304136), and Liaocheng University Scientific Research Fund (318052263).

References

1. Aguilera M.A., Arias R.M., Manzur T., 2019, Mapping microhabitat thermal patterns in artificial breakwaters: Alteration of intertidal biodiversity by higher rock temperature, Ecology and Evolution, **9**, 22, 12915-12927

2. Bhuiyan M.Y., Lin B., Giurgiutiu V., 2018, Acoustic emission sensor effect and waveform evolution during fatigue crack growth in thin metallic plate, *Journal of Intelligent Material Systems and Structures*, **29**, 7, 1275-1284

3. Cao K.W., Ma L.Q., Wu Y., Khan N.M., Spearing A.J.S., Hussain S., Yang J., 2021, Cyclic fatigue characteristics of rock failure using infrared radiation as precursor to violent failure: Experimental insights from loading and unloading response, *Fatigue and Fracture of Engineering Materials and Structures*, **44**, 2, 584-594

4. Guerin A., Jaboyedoff M., Collins B. D., Stock G. M., Derron M. H., Abellan A., Matasci B., 2021, Remote thermal detection of exfoliation sheet deformation, *Landslides*, **18**, 3, 865-879

5. Li G., Zhu C., He M.C., Zuo Y.J., Gong F.Q., Xue Y.G., Feng G.L., 2023, Intelligent method for parameters optimization of cable in soft rock tunnel base on longitudinal wave velocity, *Tunnelling and Underground Space Technology incorporating Trenchless Technology Research*, **133**, 104905

6. Lin Q.B., Cao P., Liu Y.Z., Cao R.H., Li J.T., 2021, Mechanical behaviour of a jointed rock mass with a circular hole under compression-shear loading: Experimental and numerical studies, *Theoretical and Applied Fracture Mechanics*, **114**, 102998

7. Mezza S., Vazquez P., Ben M'barek Jemai M., Fronteau G., 2022, Infrared thermography for the investigation of physical-chemical properties and thermal durability of Tunisian limestone rocks, *Construction and Building Materials*, **339**, 127470

8. Mineo S., Pappalardo G., 2019, InfraRed Thermography presented as an innovative and non-destructive solution to quantify rock porosity in laboratory, *International Journal of Rock Mechanics and Mining Sciences*, **115**, 99-110

9. Pappalardo G., Mineo S., Imposa S., Grassi S., Leotta A., Rosa F.L., Salerno D., 2020, A quick combined approach for the characterization of a cliff during a post-rockfall emergency, *Landslides*, **17**, 5, 1063-1081

10. Ren F.Q., Zhu C., He M.C., Shang J.L., Feng G.L., Bai J.W., 2022, Characteristics and precursor of static and dynamic triggered rockburst: Insight from multifractal, *Rock Mechanics and Rock Engineering*, **56**, 3, 1945-1967

11. Tu W.F., Li L.P., Zhou Z.Q., Shang C.S., 2022, Thickness calculation of accumulative damaged zone by rock mass blasting based on Hoek-Brown failure criterion, *International Journal of Geomechanics*, **22**, 2, 04021273

12. Wang Q., Xu S., Xin Z.X., He M.C., Wei H.Y., Jiang B., 2022, Mechanical properties and field application of constant resistance energy-absorbing anchor cable, *Tunnelling and Underground Space Technology incorporating Trenchless Technology Research*, **125**, 104526

13. Xiong F., Zhu C., Feng G., Zheng J., Sun H., 2023, A three-dimensional coupled thermo-hydro model for geothermal development in discrete fracture networks of hot dry rock reservoirs, *Gondwana Research*, **122**, 331-347

14. Yin Q., Wu J.Y., Jiang Z., Zhu C., Su H.J., Jing H.W., Gu X.W., 2022, Investigating the effect of water quenching cycles on mechanical behaviors for granites after conventional triaxial compression, *Geomechanics and Geophysics for Geo-Energy and Geo-Resources*, **8**, 2, 77

15. Yin Q., Wu J.Y., Zhu C., He M.C., Meng Q.X., Jing H.W., 2021, Shear mechanical responses of sandstone exposed to high temperature under constant normal stiffness boundary conditions, *Geomechanics and Geophysics for Geo-Energy and Geo-Resources*, **7**, 2, 1-17

16. Zhang C.Q., Cui G.J., Deng L., Zhou H., Lu J.J., Dai F., 2020a, Laboratory investigation on shear behaviors of bolt-grout interface subjected to constant normal stiffness, *Rock Mechanics and Rock Engineering*, **53**, 3, 1333-1347

17. Zhang C.W., Jin Z.X., Feng G.R., Song X.M., Gao R., Zhang Y.J., 2020b, Double peaked stress-strain behavior and progressive failure mechanism of encased coal pillars under uniaxial compression, *Rock Mechanics and Rock Engineering*, **53**, 7, 3253-3266

18. Zhang X.P., Lv G.G., Liu Q.S., Wu S.C., Zhang Q., Ji P.Q., Tang X.H., 2020c, Identifying accurate crack initiation and propagation thresholds in siliceous siltstone and limestone, *Rock Mechanics and Rock Engineering*, **54**, 2, 973-978

19. Zhang W., Guo W.Y., Wang Z.Q., 2022a, Influence of lateral pressure on mechanical behavior of different rock types under biaxial compression, *Journal of Central South University*, **29**, 11, 3695-3705

20. Zhang W., Xing M.L., Guo W.Y., 2023a, Study on fracture characteristics of anchored sandstone with precast crack based on double K criterion, *International Journal of Solids and Structures*, **275**, 112296

21. Zhang W., Zhao T.B., Guo W.Y., Xing M.L., 2022b, Study on mechanical characteristics of rock type I fracture and anchorage strengthening mechanism, *Journal of Theoretical and Applied Mechanics*, **60**, 3, 423-434

22. Zhang W., Zhao T.B., Yin Y.C., 2022c, Prefabricated fractured rock under stepwise loading and unloading, *Journal of Theoretical and Applied Mechanics*, **60**, 1, 167-179

23. Zhang W., Zhang B.L., Zhao T.B., 2023b, Study on the law of failure acoustic-thermal signal of weakly cemented fractured rock with different dip angles, *Rock Mechanics and Rock Engineering*, **56**, 6, 4557-4568

24. Zhao T.B., Guo W.Y., Tan Y.L., Yin Y.C., Cai L.S., Pan J.F., 2018, Case studies of rock bursts under complicated geological conditions during multi-seam mining at a depth of 800 m, *Rock Mechanics and Rock Engineering*, **51**, 5, 1539-1564

25. Zhao T.B., Zhang W., Gu S.T., Lv Y.W., Li Z.H., 2020, Study on fracture mechanics of granite based on digital speckle correlation method, *International Journal of Solids and Structures*, **193**, 192-199

Manuscript received October 10, 2023; accepted for print January 22, 2024

JOURNAL OF THEORETICAL AND APPLIED MECHANICS
62, 3, pp. 587-599, Warsaw 2024
https://doi.org/10.15632/jtam-pl/191444

EVALUATION OF MICROSTRUCTURE AND MECHANICAL PROPERTIES OF FERROMAGNETIC STRUCTURAL STEELS USING BARKHAUSEN NOISE

Katarzyna Makowska

Military University of Technology, Faculty of Mechatronics, Armament and Aerospace, Warsaw, Poland

corresponding author, e-mail: katarzyna.makowska@wat.edu.pl

Zbigniew L. Kowalewski

Institute of Fundamental Technological Research of the Polish Academy of Sciences, Warsaw, Poland

e-mail: zkowalew@ippt.pan.pl

The paper presents an attempt to assess the microstructure and mechanical properties by means of the magnetic Barkhausen noise (MBN) method. The experimental program was supplemented by metallographic examinations and hardness tests. It has been concluded that the MBN method can be used for non-destructive characterization of both single and two-phase steels used in the automotive industry. It was also found that the microstructure of steel can be distinguished using the shape of BN envelope and two magnetic parameters: $U_{b_{pp1}}$ and U_{g1}. On the other hand, the hardness and ultimate tensile strength are described successfully by the $U_{g1}/U_{b_{pp1}}$ parameter.

Keywords: microstructure, mechanical properties, Barkhausen noise, non-destructive method

1. Introduction

Magnetic Barkhausen Noise (MBN) analysis (Jiles, 1998) is regarded as a non-destructive technique of considerable significance in microstructural characterization of ferromagnetic materials. Contemporary industrial requirements enforce research work for effective determination and better assurance of the desired microstructure of steels. In practice, the microstructure is determined by selected metallographic techniques and hardness tests where certain regions of representative specimens can be taken into account. Since application of these methods is time consuming and quite expensive, there is an interest to develop cheap non-destructive techniques capable of rapid inspection of the material state. Performing BN measurements instead of metallographic and hardness tests may reduce the cost of quality control while maintaining its standards.

Among many options, the MBN method can be applied to detect and determine a volume of the sigma phase in duplex stainless steels (Huallpa *et al.*, 2016). Since the sigma phase adversely affects mechanical properties and corrosion resistance of the material, it is necessary to determine its contribution. It has been shown, that a volume of the sigma phase increases as the time of annealing increases (Huallpa *et al.*, 2016). Simultaneously, the BN signal decreases until it equalizes the background level after 24 hours of heat treatment (Huallpa *et al.*, 2016).

Singh *et al.* (2020) showed, that the MBN gets an effective opportunity to distinguish between such thermal treatments as annealing, normalization and quenching. Three variants of heat treatment were carried out. The annealing, normalizing and quenching processes were carried out alternatively at 900°C, 850°C and 800°C. The highest level of the BN signal was obtained for the material annealed at 900°C, and then, successively for the material annealed at 850°C and 800°C. Lower values of BN signal were measured on specimens after normalization. The same tendency of the BN signald variation due to temperature change was observed. The lowest

values of BN were obtained for specimens after quenching, however, an opposite trend was noted, i.e. the highest BN was observed for the specimen thermally treated at 800°C, and the lowest one for 900°C. However, Honkanen *et al.* (2021) stated that based only on the BN amplitude, the ferritic-pearlitic and martensitic microstructure could not be distinguished.

The bainite fraction in 22MnB5 grade steel with 0.23%C was also tested by means of the MBN method (Zhu *et al.*, 2020). Specimens of different bainite and martensite contributions were produced and, subsequently, the peak of MBN and rms value were analysed. A decrease in the BN was observed for the bainite volume lower than 30%. Above this volume, an increase of MBN was noted. The residual internal stresses in the martensite phase were the main reasons of the BN decrease.

According to (Błażewski and Mikoszewski, 1981), an increase of BN due to the bainite fraction increase can be attributed to a lower resistance of the domain walls during the magnetisation cycle in comparison to the small lath structure of martensite with high dislocation density (Kaplan *et al.*, 2007).

A content of the martensitic phase in X70 dual-phase steel after various heat treatments of different inter-critical annealing temperature was tested in (Nebair *et al.*, 2022). It was found that BN decreases if the inter-critical temperature increases. This is due to an increase of the martensite fraction and the number of obstacles as well (Nebair *et al.*, 2022).

In (Tavares *et al.*, 2019) temper embrittlements contributions were detected in the supermartensitic stainless SMSS steel (13%Cr-5%Ni-2%Mo) by MBN. This material belongs to the class of new stainless steels developed in the 1990's. It is commonly used for production of seamless pipes and forged parts for oil and gas installations on land. Conventional martensitic stainless steels become brittle when tempered in the temperature range of 400°C-600°C, as can be verified by impact Charpy tests at room temperature (Pickering, 1976).

Nowadays, the MBN is used as a standard to evaluate the tempering process of steel (Ivanova, 2022). It was found that the time of noise registration could serve as a suitable parameter for analysis of the microstructure. It can be determined on the basis of the zero point of the magnetization sine wave and maximum value of the magnetic noise envelope (Ivanova, 2022). The study found linear relationships between the time of magnetic noise occurrence and the hardness of structures obtained after tempering. The same nature of the relationship was found between the hardness of heat treated structures and the rms signal of BN (Ivanova, 2022).

In (Neslušan *et al.*, 2023), the Barkhausen emission was used to distinguish steels of different yield strengths: 355 MPa, 500 MPa, 700 MPa, 960 MPa and 1100 MPa. It was observed that for specimens investigated non-destructively along the sheet rolling direction, firstly, the BN signal increased up to about 500 MPa, subsequently, it was approximately constant up to about 1000 MPa, and finally decreased. On the contrary, in the case of specimens investigated by means of MBN method in the transverse direction, the BN increased up to 1000 MPa, and then decreased (Neslušan *et al.*, 2023).

Astudillo *et al.* (2022) used the BN to detect presence of martensite induced by deformation. A progressive increase of the rms value of the MBN with an increase of martensite volume was verified (Astudillo *et al.*, 2022). The results showed that the MBN might detect microstructural changes that occurred during the evaluation of initiation and evolution of the austenite–martensite phase transformation (Astudillo *et al.*, 2022). The presented literature examples indicate that the MBN can be useful for identification of the steel microstructure.

Based on this short survey of the BN studies, one can conclude that the method is suitable in many materials science issues. What is lacking, however, is a synthetic description of the microstructure evaluated by means of MBN for a wide range of structural steel grades, commonly used in major industrial branches. Moreover, the available literature data shows that there are no clear answers to rhe question, which parameters determined from the BN envelope allow one

to precisely identify the type of microstructures. This research is an attempt to get closer to answering this question.

2. Experimental procedure

Six structural steels were taken from different automotive or military components (Mars 300 – protective armour fragment – Specimen No. 1), 40NiCrMo7 – ball pin – Specimen No. 2), S700MC – boom toa of a special truck – Specimen No. 3, S355 steel – car trailer – Specimen No. 4, C55 – ball joint housing – Specimen No. 5, and C15 – car stick – Specimen No. 6). Chemical compositions of the tested steels are presented in Table 1.

Table 1. Chemical compositions of the tested steel grades

No.	Steel grade	C	S	P	Si	Mn	Ni	Cr	Mo	V	S	Al	Ti
1	Mars 300	0.49	0.001	0.005	1.01	0.60	1.70	0.30	0.40	–	–	–	–
2	40NiCrMo7	0.38	0.020	0.010	0.26	0.62	1.35	0.82	0.23	–	–	–	–
3	S700MC	0.11	0.013	0.012	0.30	1.87	–	–	0.31	0.10	0.003	0.012	0.21
4	C55	0.56	0.034	0.021	0.23	0.72	0.24	0.38	0.02	–	–	–	–
5	S355	0.09	0.012	0.023	0.47	1.63	–	–	0.40	0.20	0.004	0.013	0.19
6	C15	0.13	0.014	0.022	0.18	0.45	–	–	–	–	–	–	–

Non-destructive Barkhausen tests as well as metallographic and hardness tests were performed on them. Subsequently, a mutual relationship between magnetic properties and the microstructure type of structural steel were found. The surfaces of the elements on which the tests were carried out were polished with a sandpaper with grains of 320 and 1200.

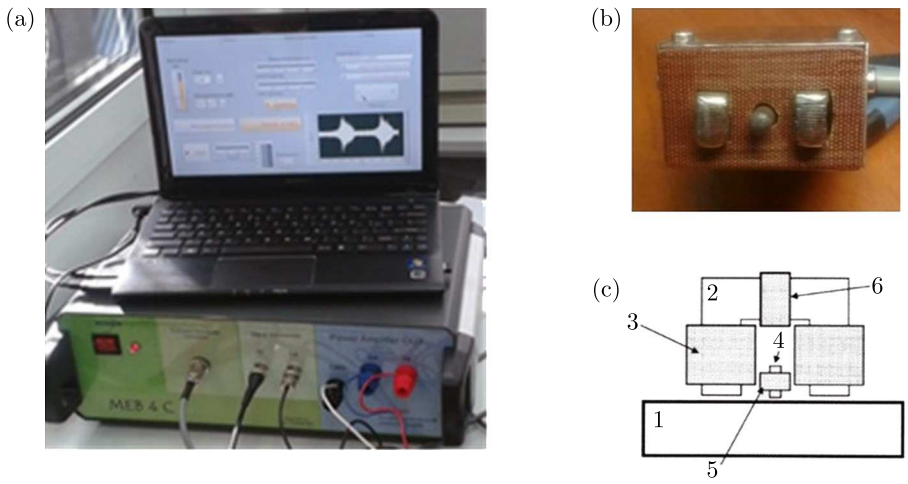

Fig. 1. Barkhausen noise defectoscope: (a) general view, (b) head, (c) diagram of the head (1 – tested specimen, 2 – U-shaped core, 3 – magnetising coil, 4 – core of the measuring coil, 5 – measuring winding, 6 – control winding) (Makowska and Kowalewski, 2020)

Magnetic tests were carried out using the Barkhausen noise defectoscope, Fig. 1. Three measurements were carried out in one area of each specimen. Barkhausen noise envelopes with the highest amplitude are shown. The sensor was set in accordance with the rolling direction of the materials in question. The measuring head consisted of a U-shaped core of electromagnets wrapped in a wound excitation coil. The pick-up coil was built into the sensor that possessed a rounded shape which made it easier to fit the probe to concave and convex surfaces. The control coil was also built into the head. The voltage of the control coil reached its maximum

value when the probe was optimally positioned on the specimen. The voltage signal induced in the coil was proportional to the rate of change of the magnetic flux in the electromagnet core (Makowska and Kowalewski, 2020). The size of the magnetic flux depends on its surface and the magnetic properties of both the core and object tested (Makowska and Kowalewski, 2020). The detailed structure of the sensor is presented on Fig. 1c. A triangular waveform was applied. In the pick-up coil, a voltage signal U_0 was induced. In order to estimate the BN intensity, the fast-variable component of U_0 was measured for the frequency $f = (0 - 500)$ Hz. Analysis of this component provided required data on the material structure of the specimen.

The envelopes of BN were calculated as rms value of U_b according to

$$U_b = \sqrt{\frac{1}{\tau}\int_0^{\tau} U_{tb1}^2(t)\, dt} \tag{2.1}$$

where U_b [V] is the root mean square of the coil output voltage; U_{tb1} [V] is the fast-variable component defining a voltage separated by means of the high-pass filter from induced voltage in the pick-up coil, and τ [s] is the integration time.

In the next step, the amplitude of BN (Ub_{pp}) was used as a parameter defining the voltage difference between the maximum peak value of the MBN (U_b) and the background noise (U_{tb}). The MBN amplitude is able to identify the BN level that depends on microstructural features of the material matrix like the grain boundaries, precipitations or dislocations for example. Also a voltage generator U_g was determined for each Ub_{pp} value. It gives information on the magnetic field strength that is needed to overcome pinning obstacles by the domain walls (Makowska and Kowalewski, 2020).

Also, an integral of the half-period voltage signal of MBN was calculated

$$Int(Ub) = \int_{-U_{g_{max}}}^{+U_{g_{max}}} U_{sb}\, dU_g \tag{2.2}$$

where

$$U_{sb} = \sqrt{U_b^2 - U_{tb}^2} \tag{2.3}$$

and U_{sb} [V] – root mean square of the Barkhausen emission voltage after correction due to background noise, U_b [V] – root mean square of the coil output voltage, U_{tb} [V] – root mean square of background voltage, U_g [V] – generator voltage.

The full width of the half maximum FWHM was also determined. It can be related to the magnetic hardness (Jiles, 1998). In the case of two maxima on the envelope, the amplitude and integral were determined for the following parameters: $U_{b_{pp1}}$, $U_{b_{pp2}}$, $Int(Ub)_1$, $Int(Ub)_2$, $FWHM_1$ and $FWHM_2$. Also, the new $U_{g1}/U_{b_{pp1}}$ parameter was calculated.

The microstructure of the tested materials was analysed using the Olympus PMG 3 light microscope equipped in Zen2Core software. Quantitative analysis of the microstructure was performed using the linear method. The longest chord, also called the Ferret diameter, was proposed as the grain size parameter d_{av} [μm]. The following notations were adopted in this work: $d_{av\,(M)}$ – average grain size of martensite, $d_{av\,(S)}$ – average grain size of high-tempered martensite (sorbite), $d_{av\,(B)}$ – average grain size of bainite, $d_{av\,(F)}$ – average grain size of ferrite, $d_{av\,(P)}$ – average grain size of pearlite, $d_{av\,(C)}$ – average grain size of cementite, V_F – volume fraction of ferrite, V_P – volume fraction of pearlite, V_C – volume fraction of cementite. A relationship between the grain size and amplitude of Barkhausen noise was found.

The Vickers hardness (HV 3) was measured by means of the universal Duramin-500 Struers hardness tester. Five measurements were carried out for each specimen. The Vickers hardness values were converted into the Brinell hardness (Błażewski and Mikoszewski, 1981) in order to assess the ultimate tensile stress, Table 2.

Table 2. Hardness results of the steel grades tested

Steel grade [HV3]	Mars 300	40NiCrMo7	S700MC	C55	S355	C15
Measurement 1	708	306	252	208	165	158
Measurement 2	696	297	258	216	163	156
Measurement 3	705	301	250	212	162	155
Measurement 4	704	308	262	210	168	159
Measurement 5	701	296	260	214	166	157
Average hardness	703	302	256	212	165	157
Standard deviation	±4.07	±4.76	±4.63	±2.83	±2.14	±1.41

3. Results

The envelopes of BN are presented in Fig. 2, whereas the parameters coming from BN envelopes are shown in Figs. 3-6. Microstructures of the tested materials are presented in Fig. 7.

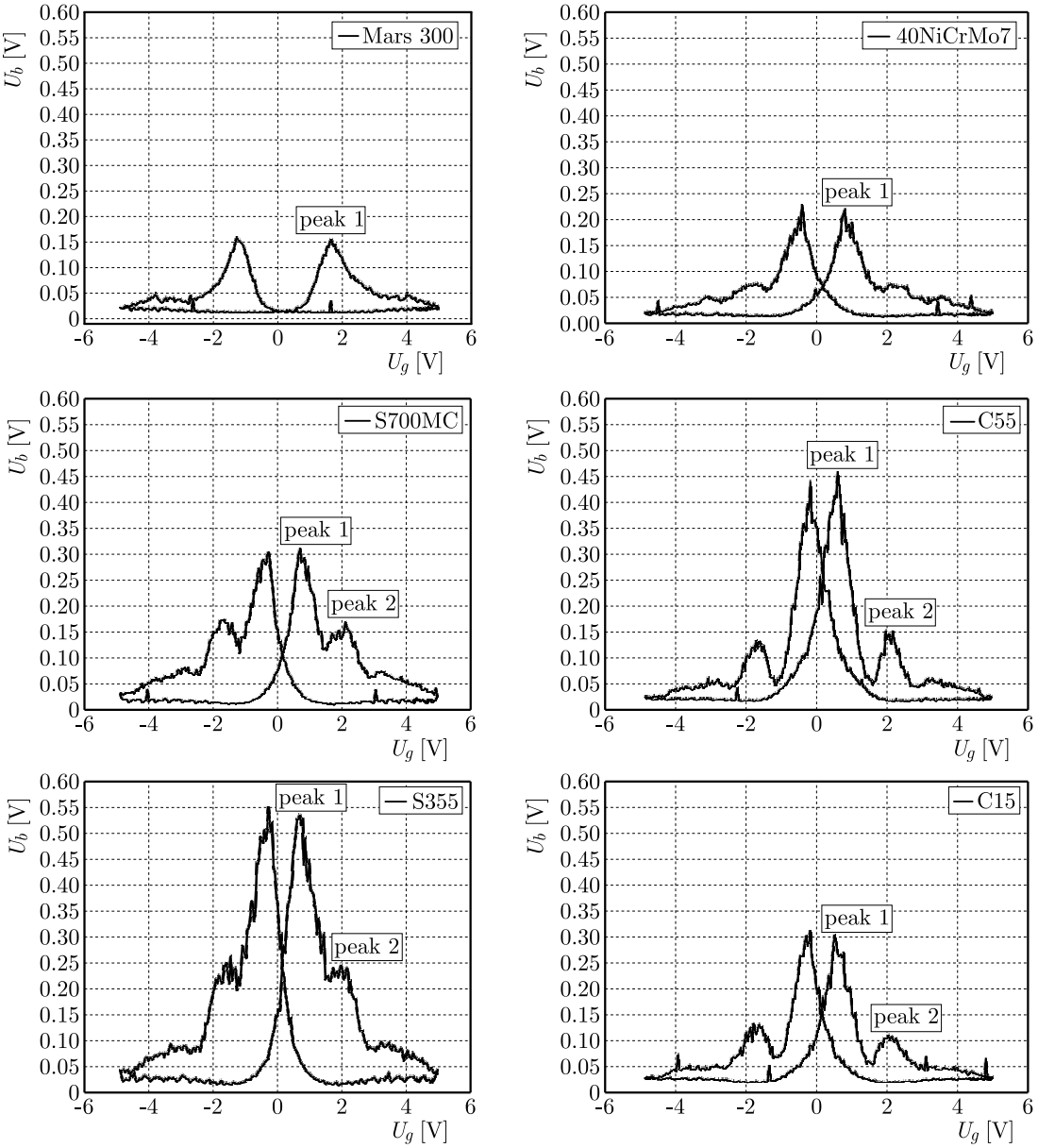

Fig. 2. Barkhausen noise envelopes for different steel grades

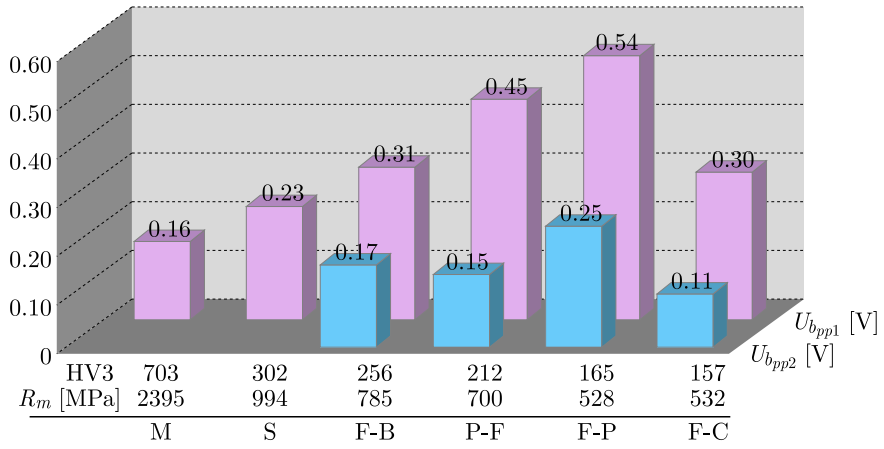

Fig. 3. The first peak $U_{b_{pp1}}$ and the second peak $U_{b_{pp2}}$ of rms Barkhausen envelopes for different steel grades

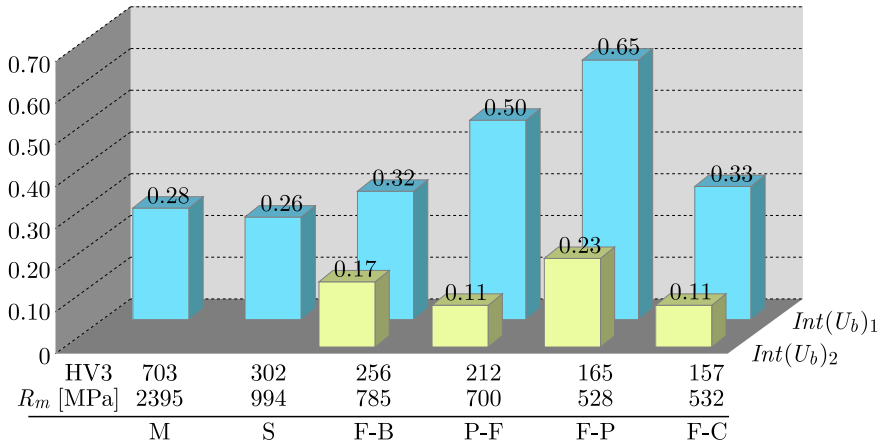

Fig. 4. Integrals of the half-period voltage signal of MBN ($Int(U_b)_1$ and $Int(U_b)_2$)

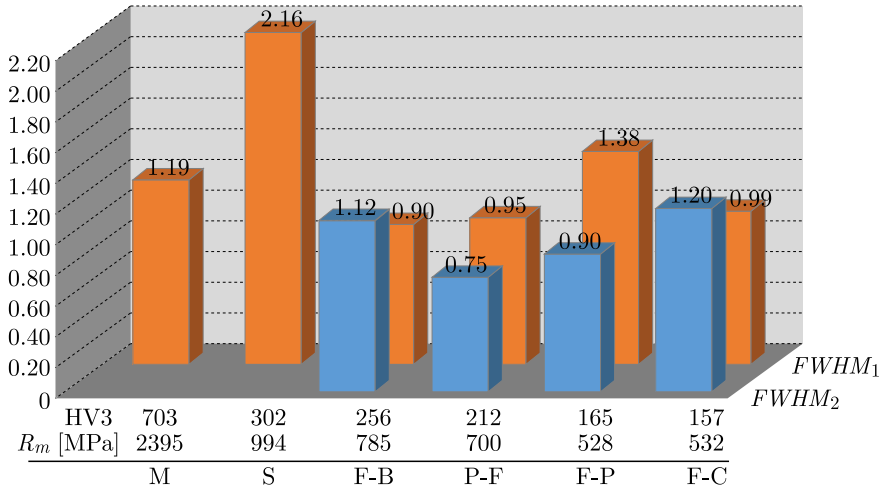

Fig. 5. Width of the first and second peaks determined from the rms envelope of the Barkhausen noise of the tested steel grades ($FWHM_1$ and $FWHM_2$)

Table 2 presents the HV3 hardness results of steel grades, whereas Table 3 shows parameters determined based on the metallographic and mechanical tests: d_{av} – grain size diameter and R_m – ultimate tensile stress. It was observed, that the values of mechanical parameters increase with the reduction of the amplitude and integral value determined from the envelope of BN.

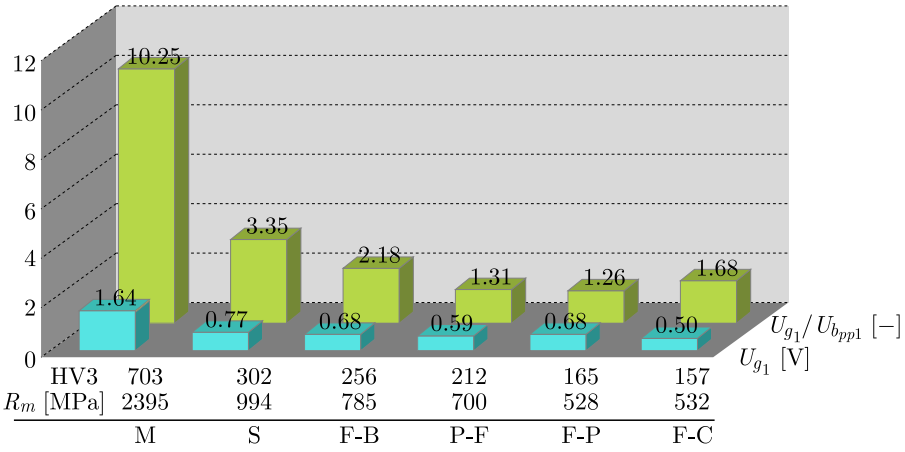

Fig. 6. Graphical representation of U_{g1} and $U_{g1}/U_{b_{pp1}}$ parameters for different steel grades

Table 3. Microstructural and mechanical properties of the steel grades tested

Steel grade	Mars 300	40NiCrMo7	S700MC	C55	S355	C15
Hardness [HV3]	703	302	256	212	165	157
Ultimate tensile stress R_m [MPa]	2396*	994	785	700	528	532
d_{av} [μm]	15.5	10.4	ferrite$_{(F)}$ 2.23 bainite$_{(H)}$ 1.77	pearlite$_{(F)}$ 16.06 ferrite$_{(F)}$ 15.75	ferrite$_{(F)}$ 3.88 pearlite$_{(F)}$ 1.12	22.2

* Fras *et al.* (2018)

As it is shown in Fig. 2, the MBN envelopes are characterized by a varied shape and variable number of peaks. In terms of the mechanical parameters, the Mars 300 has the highest hardness and tensile strength. On the BN envelope, one can indicate a single maximum reflecting the martensitic microstructure (M). The MBN amplitude of this steel has the lowest value due to the high dislocation density in martensite needles, which is typical for this structure (Honkanen *et al.*, 2021). In (Honkanen *et al.*, 2021) it was proved by means of the transmission microscope in the Lorentz mode that the domain walls anchor and bend on dislocations.

Specimen No. 2 has also a high-tempered martensite structure named also as sorbite (S). It contains small cementite particles in the fine grained ferritic matrix. Since the distribution of cementite in the ferritic matrix is practically homogeneous, only a single maximum is observed here. The dense distributed cementite particles can be treated as significant obstacles for movements of the domain walls and, as a consequence, this specimen is characterized by the Ub_{pp} parameter equal to 0.23 V. In (Tavares *et al.*, 2019), the anchorage of domain walls in sorbite steel on carbide precipitates was clearly illustrated. These precipitates were the major obstacles for movement of the domain walls in the microstructure with high-tempered martensite.

The S700MC steel (Specimen No. 3) represented a ferritic-bainitic microstructure. In that case, the MBN envelope had two maxima. The peaks are mainly attributed to nucleation and growth of new domains at various specimen defects and grain boundaries as well as the domain walls annihilation process. It has to be emphasized that the number of peaks depends on the number of phases in the material. The first peak obtained for a lower positive U_g was associated with the presence of ferrite in the microstructure, while the second one, for a higher U_g, was attributed to bainite.

Since the number of dislocations in ferrite grains is relatively low (Honkanen *et al.*, 2019), the domain walls can move more freely and with a higher speed. As a consequence, their anchoring takes place mainly at the boundaries of ferrite grains. Such feature is reflected in magnetic

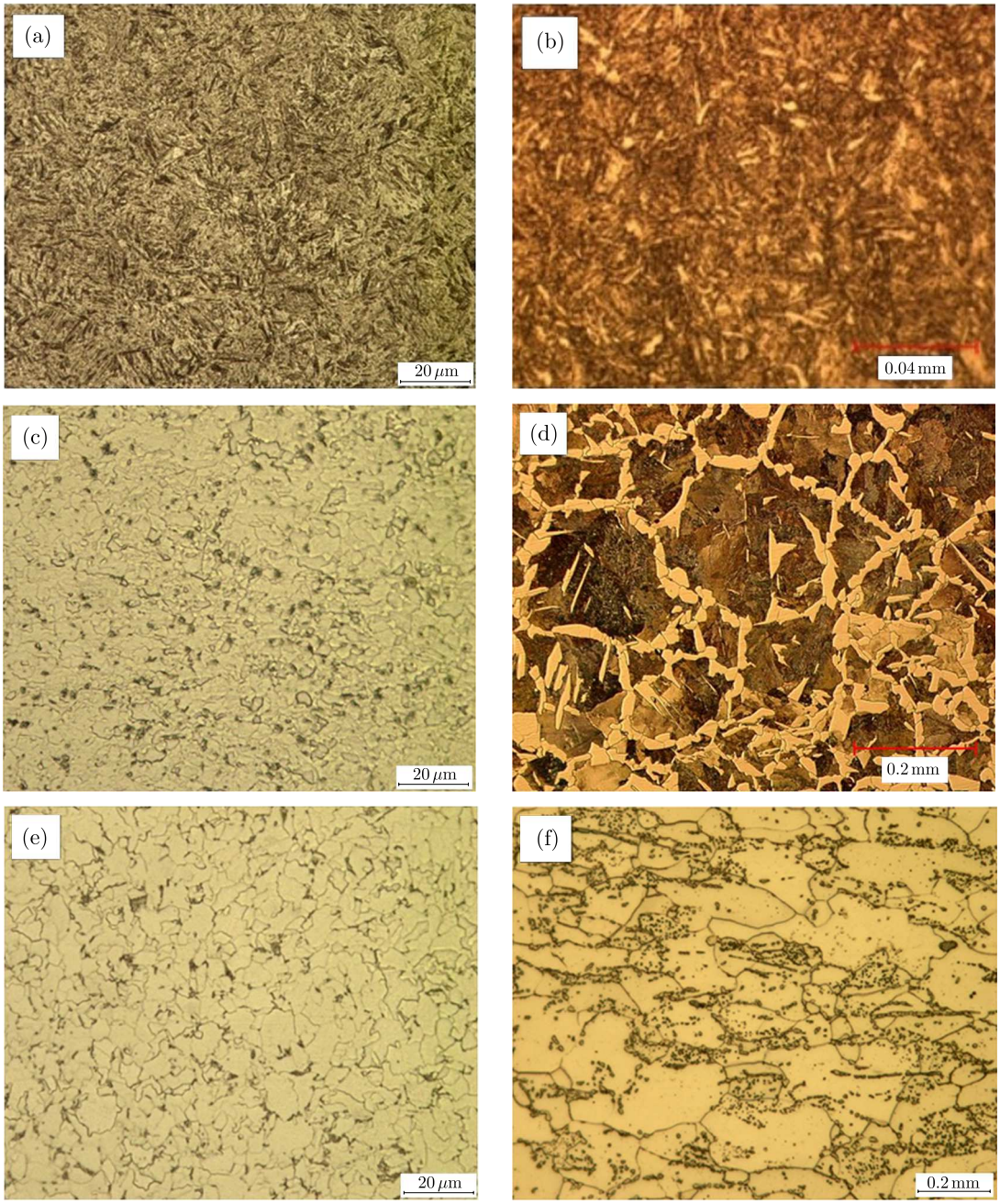

Fig. 7. Microstructures of different steel grades: (a) Mars 300 with the martensitic microstructure, $d_{qv\,M)} = 15.5\,\mu$m, 703 HV3, (b) 40NiCrMo4 with the sorbite microstructure (high-tempered martensite), $d_{av\,(S)} = 10.4\,\mu$m, 302 HV3, (c) S700MC with the ferritic-bainitic microstructure, $d_{av\,(F)} = 2.23\,\mu$m, $d_{av\,(B)} = 1.77\,\mu$m, 256 HV3, (d) C55 with the pearlitic-ferritic microstructure, $d_{av\,(F)} = 15.75\,\mu$m, $d_{av\,(P)} = 16.06\,\mu$m, $V_F = 31.2\%$, $V_P = 68.8\%$, 212 HV3, (e) S355 with the ferritic-pearlitic microstructure, $V_F = 87.9\%$, $V_P = 12.1\%$, $d_{av\,(F)} = 3.88\,\mu$m, 165 HV3, (f) C15 with the ferritic microstructure and secondary cementite precipitates, $d_{av\,(F)} = 22.2\,\mu$m, $d_{av\,(C)} = 0.9 \cdot 10^{-3}\,\mu$m, $V_F = 90.2\%$, $V_C = 9.8\%$, 157 HV3

investigations by a higher maximum than that in the case of Specimen No. 2. By contrast, the peak related to bainite is lower than that from sorbite (high-tempered martensite) in Specimen No. 2 and similar to the peak related to martensite in Specimen No. 1. The domain walls in bainite move more freely and their speed is greater due to the ferritic matrix of bainite, in which,

on the other hand, there are carbides that increase the number of Barkhausen jumps (anchor and disanchor domain walls).

Envelopes determined for Specimens 4 and 5 represent the pearlitic-ferritic and ferritic--pearlitic microstructure, respectively. These specimens differ in the phase volume and grain size. Honkanen *et al.* (2021) studied how domain walls moved in ferrite and pearlite. A movement of the domain walls in steels containing such phases begins in ferrite due to a not sufficient number of pinning sites in its grains. However, there are some hindering elements for domain walls movements in the form of ferrite-ferrite grain boundaries. The generator voltage responsible for the domain walls movement across the ferrite-ferrite grain boundaries is not sufficient to unlock the anchored domain walls at the ferrite-perlite grain boundaries. Only an increase in strength of the magnetic field causes a displacement of the domain walls located perpendicularly to the alternately arranged ferrite and cementite plates. It has been observed that the domain walls anchor or disanchor on the cementite plates during their movement (Honkanen *et al.*, 2021).

Specimen 6 has a lower amplitude than Specimen 5. According to (Gür, 2017), the presence of spheroidite in the ferrite matrix should increase the BN level due to pearlite areas in the ferrite matrix. However, the grain size serves as the main factor affecting the BN level. Based on the relation $Ub_{pp} \sim d^{\sim 0.43}$, it was found by Ng *et al.* (2003) that the BN amplitude decreases as the grain size increases. This is due to a less number of grain boundaries acting as the pinning sites. Ranjan *et al.* (1987) found for technical nickel, that the amount of grain boundaries could be treated as the dominant microstructural parameter affecting the magnetic properties. They discovered that the Barkhausen signal decreased with a grain size increase. Such results were confirmed by tests carried out on a low carbon steel (Anglada-Rivera *et al.*, 2001). Cumulative diagrams of grain size variation as a function of the BN level $U_{b_{pp1}}$ for metastable and stable phases are shown in Figs. 8-9. The metastable phases that represent non-diffusive/semi-diffusion products create dislocation clusters and, moreover, serve as a source of stress concentration during rapid cooling. The just mentioned factors, besides grain boundaries and precipitations, have an additional impact on the level of the BN signal. Figure 8a shows that if the level of the BN signal decreases, then the grain size-increases. A similar effect can be observed in Fig. 8b for cooled steels with phases being products of diffusion transformations, according to the Fe-C system. In the case of the ferritic-bainitic S700MC steel, the value for bainitic (metastable) phase was substituted for $U_{b_{pp1}}$. The results of stereological analysis are given in Table 2.

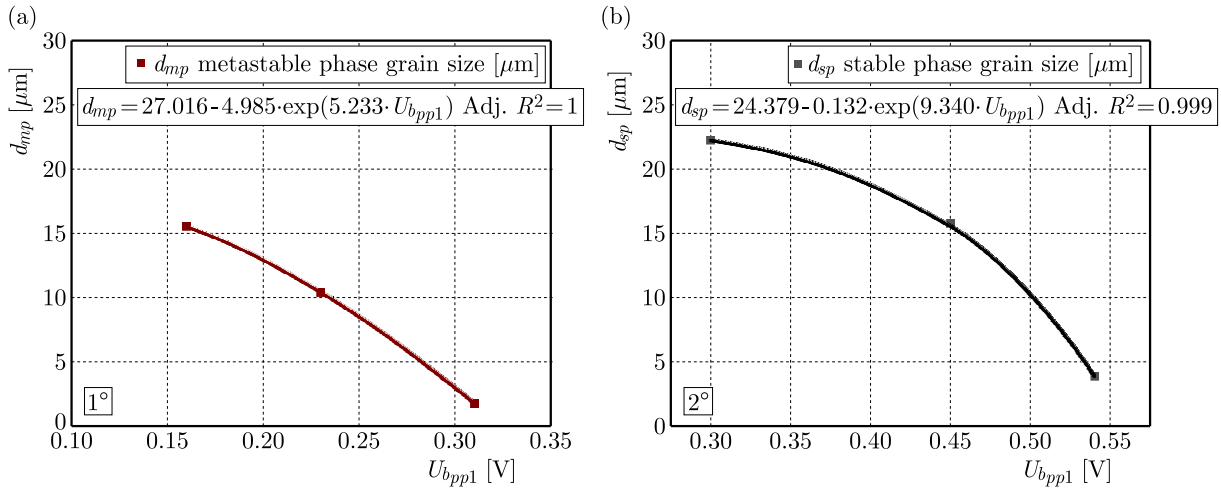

Fig. 8. Grain size as a function of the BN signal level $U_{b_{pp1}}$ for steels with phases being products of: (a) non-diffusion and semi-diffusion transformations, (b) diffusion transformations, according to the Fe-C system

It was observed that the background level of Barkhausen noise also changes depending on the microstructure of steel. It was noted that the background level of Barkhausen noise is lower when more pinning sites hindering movement of the domain walls in the tested material occur.

It was also found that high values of the $U_{g1}/U_{b_{pp1}}$ parameter indicates a very high hardness and tensile strength. In contrary to that result, a lower values of $U_{g1}/U_{b_{pp1}}$ parameters indicate lower values of the hardness and tensile strength, see Fig. 6. Changes in the parameter U_{g1} are not so clear, Fig. 6. However, similarly to the parameter $U_{g1}/U_{b_{pp1}}$, the highest U_{g1} values were observed for the highest hardness and tensile strength and, oppositely, the lowest U_{g1} values were obtained for the lowest hardness and tensile strength.

The results obtained from tests carried out on Specimens No. 1-6 meet the technical requirements for selected automotive and military structural elements. The microstructure and hardness values are in agreement with those recommended by the standards "T-ITS/5/13-CBM Technical condition. Steering rods, wishbones, torque rods and stabilizer rods as well as connectors of the suspension system of motor vehicles. Safety requirements and tests" (in Polish) and "T-ITS/63/13-CBM Technical condition. Ball joints of the steering and suspension systems of motor vehicles. Safety requirements and tests" (in Polish).

The parameters selected from Figs. 3, 5 and 6 created the basis for determination of a new parameter called the Modified Barkhausen Signal (MBS). It is characterized by the equation: $\text{MBS} = (U_{g1}/U_{b_{pp1}}) + U_{g2} - FWHM_2$.

It was observed that the material hardness varied linearly as a function of the MBS parameter, see Fig. 9. This relationship became the basis for a model development enabling determination of mechanical properties, microstructure and grain size of the material. Since the hardness can also be treated as a measure of a microstructure that enables distinction between microstructures tested, it is possible to simultaneously assess either microstructure or mechanical properties using the MBS parameter.

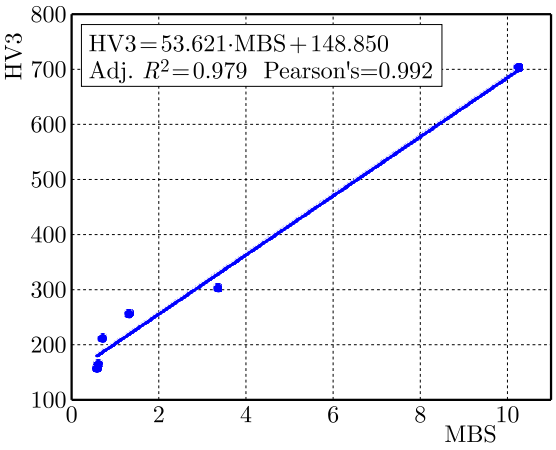

Fig. 9. Relationship between the hardness and MBS parameter

Moreover, if the value of the MBS parameter is greater than 1.3, the grain size of the material is determined using the $U_{b_{pp1}}$ parameter based on the relationship presented in Fig. 8a, whereas if the value of the MBS parameter is less than 1.3, the grain size can be evaluated based on the relationship presented in Fig. 8b, see Fig. 10.

4. Conclusion remarks

In this paper, a non-destructive method is proposed as an optional method for identification of the microstructure and mechanical properties of steel, based on BN measurements. The rms

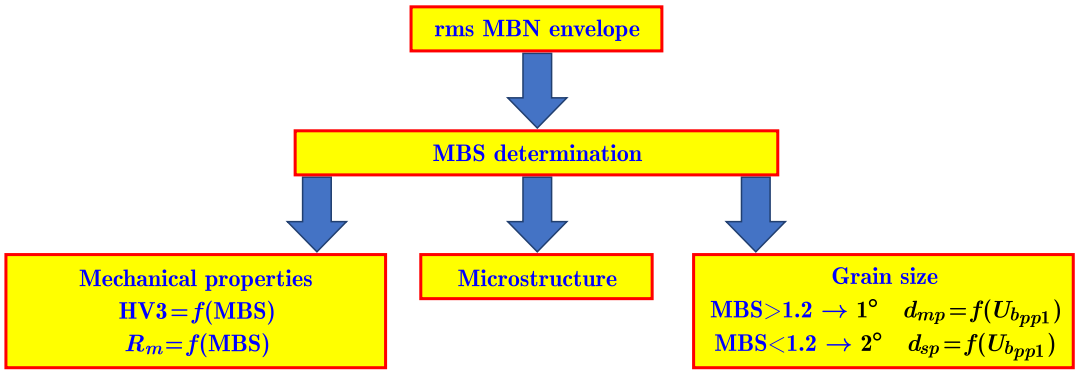

Fig. 10. Barkhausen noise procedure for predicting mechanical properties, microstructure and grain size of structural steels

amplitude of BN enables one to identify the number of phases in the material in question. The MBN double peak reveals two magnetic features and two phases in the specimen. A level of the BN signal depends on the microstructure and material grain size. Evaluation of the material microstructure can be done on the basis of the shape of MBN envelope as well as two parameters determined from the envelope: $U_{b_{pp1}}$ and U_{g1}. Based on the results for Specimen No. 6 representing ferritic structure with cementite precipitations, one can conclude that both parameters better describe the matrix of the material. This due to the fact that in ferrite, a displacement of the domain walls takes place between the adjacent grain boundaries. The parameter $U_{b_{pp1}}$ depends not only on the grain boundaries, but also on precipitations and dislocations. As a consequence, it expresses the microstructural features in the material matrix, whereas the parameter U_{g1} refers to strength of the magnetic field that is needed to overcome pinning obstacles by domain walls. The U_{g1} parameter can be applied to identify coexisting phases with the ferritic structure, i.e.: bainite, cementite or perlite.

The tests carried out can be treated as preliminary studies, and there is no doubt that the further research should be extended to a wider group of steels with an even more diverse structure and grain size. It was also observed that the increase of grain size reduced the level of Barkhausen noise for steels with structures that were products of both diffusion/semi-diffusion and diffusion transformation. Attention is also paid to the $U_{g1}/U_{b_{pp1}}$ parameter whose variation describes changes in the hardness and tensile strength.

A simple Barkhausen noise model is proposed using new magnetic parameters. It enables simultaneous assessment of mechanical properties, microstructure and grain size of the steel tested.

One can indicate BN as a method with a wide application potential in material investigations, especially after their production processes realised.

Acknowledgment

This work was co-financed by Military University of Technology under research project UGB 22-742/2024.

References

1. Anglada-Rivera L.R., Padovese L.R., Capó-Sánchez J., 2001, Magnetic Barkhausen noise and hysteresis loop in commercial carbon steel: influence of applied tensile stress and grain size, *Journal of Magnetism and Magnetic Materials*, **231**, 299-306

2. Astudillo M.R.C., Núñez N.M., Pumarega M.I.L., Ferrari G., Ruzzante J., Gómez M., 2022, Study of martensite induced by deformation with Magnetic Barkhausen Noise technique, *Journal of Magnetism and Magnetic Materials*, **556**, 1-12

3. Augustyniak B., 2003, *Magnetoelastic Phenomena and their Use in Non-Destructive Testing of Materials* (in Polish), Wydawnictwo Politechniki Gdańskiej

4. Blaow M., Evans J.T., Shaw B.A., 2005, Magnetic Barkhausen noise: influence of microstructure and deformation in bending, *Acta Materialia*, **53**, 2, 279-287

5. Błażewski S., Mikoszewski J., 1981, *Measurements of Metal Hardness* (in Polish), WNT

6. Cullity B.D., Graham C.D., 2009, *Introduction to Magnetic Materials*, Wiley

7. Fras T., Roth C.C., Mohr D., 2018, Fracture of high-strength armour steel under impact loading, *International —Journal of Impact Engineering*, **111**, 147-164

8. Gür C.H., 2017, Nondestructive monitoring of pearlite degradation in medium carbon steels, *The 14th International Conference of the Slovenian Society for Non-Destructive Testing*, Bernardin, Slovenia

9. Honkanen M., Santa-Aho S., Laurson L., Eslahi N., Foi A., Vippola M., 2021, Mimicking Barkhausen noise measurement by in-situ transmission electron microscopy – effect of microstructural on Barkhausen noise, *Acta Materialia*, **221**, 1-11

10. Huallpa E., de Montevade E.F., Capó Sánchez J.C., Campos M.A., Padovese L., Goldstein H., 2016, Use of Magnetic Barkhausen Noise (MBN) to follow up the formation of sigma phase in Saf2205 (UNS S31803) Duplex Stainless Steel, *Materials Research*, **19**, 5, 1008-1016

11. Hwang D.G., Kim C.G., Lee K.H., Kim H.C., 1993, The retarding field model of Barkhausen noise and permeability in conventional and highly grain-oriented 3% Si-Fe polycrystals, *Journal of Magnetism and Magnetic Materials*, **125**, 1-2, 129-137

12. Ivanova Y., 2022, Investigation of heat-treated steels using the magnetic noise method, *International Scientific Journal "Machines. Technologies. Materials"*, **16**, 4, 138-141

13. Jiles D., 1998, *Introduction to Magnetism and Magnetic Materials*, Taylor and Francis Group

14. Kaplan M., Gür C.H., Erdogan M., 2007, Characterization of dual-phase steels using magnetic Barkhausen noise technique, *Journal of Nondestructive Evaluation*, **26**, 79-87

15. Kleber X., Vincent A., 2004, On the role of residual internal stresses and dislocations on Barkhausen noise in plastically deformed steel, *NDT and E International*, **37**, 439-445

16. Makowska K., Kowalewski Z.L., 2020, Variation of Barkhausen noise, magnetic and crystal structure of ferromagnetic medium-carbon steel after different loading processes. *The Physics of Metals and Metallography*, **121**, 2, 115-122

17. Nebair H., Helifa B., Bensaid S., Zidelmen S., Lefkaier I.K., 2022, Martensite morphology and volume fraction evaluation of dual-phase X70 steel using magnetic Barkhausen noise technique, *Journal of Magnetism and Magnetic Materials*, **555**, 1-9

18. Neslušan M., Pitoňak M., Minárik P., Tkáč M., Koll ar P., Životský O., 2023, Influence of domain walls thickness, density and alignment on Barkhausen noise emission in low alloyed steels, *Scientific Reports*, **13**, 1-12

19. Ng D.H.L., Cho K.S., Wong M.L., Chan S.L.I., Ma X.-Y., Lo C.C.H., 2003, Study of microstructure, mechanical properties, and magnetization process in low carbon steel bars by Barkhausen emission, *Materials Science and Engineering: A*, **358**, 186-198

20. Pickering F.B., 1976, Physical metallurgy of stainless steel developments, *International Metals Reviews*, **211**, 227-268

21. Ranjan R., Jiles D.C., Buck O., Thompson, R.B., 1987, Grain size measurement using magnetic and acoustic Barkhausen noise, *Journal of Applied Physics*, **61**, 3199-3201

22. Sahebalm A., Kashefi M., Kahrobaee S., 2014, Comparative study of eddy current and Barkhausen noise methods in microstructural assessment of heat treated steel parts, *Nondestructive Testing and Evaluation*, **29**, 3, 208-218

23. Singh S.S., Awale A.S., Chaudhari A., Nahak B., 2020, Monitoring the microstructural changes of heat treated medium carbon steel by Barkhausen noise and hysteresis loop techniques, *Materials Today: Proceedings*, **26**, 1198-1202

24. Tavares S.S.M., Noris L.F., Pardal J.M., Silva da M.R., 2019, Temper embrittlement of supermartensitic stainless steel and non-destructive inspection by magnetic Barkhausen noise, *Engineering Failure Analysis*, **100**, 322-328

25. Zhu B., Xu Z., Wang K., Zhang Y., 2020, Nondestructive evaluation of hot stamping boron steel with martensite/bainite mixed microstructures based on magnetic Barkhausen noise detection, *Journal of Magnetism and Magnetic Materials*, **503**, 53, 1-8

Manuscript received November 7, 2023; accepted for print January 8, 2024

JOURNAL OF THEORETICAL AND APPLIED MECHANICS
62, 3, pp. 601-613, Warsaw 2024
https://doi.org/10.15632/jtam-pl/191178

THE USE OF A GENETIC ALGORITHM IN THE PROCESS OF OPTIMIZING THE SHAPE OF A THREE-DIMENSIONAL PERIODIC BEAM

Lukasz Dolinski, Arkadiusz Zak, Wiktor Waszkowiak
Gdansk University of Technology, Digital Technologies Center, Gdansk, Poland, and
Gdansk University of Technology, Department of Biomechatronics, Gdansk, Poland
corresponding author Lukasz Dolinski, e-mail: lukasz.dolinski@pg.edu.pl

Pawel Kowalski
Gdansk University of Technology, Department of Control Engineering, Gdansk, Poland

Jacek Szkopek
Gdansk University of Technology, Department of Biomechatronics, Gdansk, Poland

Mechanical periodic structures exhibit unusual dynamic behavior thanks to the periodicity of their structures, which can be attributed to their cellular arrangement. The source of this periodicity may result from periodic variations of material properties within their cells and/or variations in the cell geometry. The authors present the results of their studies on the optimization of physical parameters of a three-dimensional axisymetrical periodic beam in order to obtain the desired vibroacoustic properties. The aim of the optimization process of the unit cell shape was to obtain band gaps of a given width and position in the frequency spectrum.

Keywords: periodic beam, shape optimization, genetic algorithm

1. Introduction

Taking into account geometric features of material systems (regardless of the scale at which these structures are built), they can be divided into two separate groups: aperiodic and periodic structures (PS). In the first case, the structures consist of elements forming disordered systems, i.e. without regularity and multiple repetitions of shapes in space. In the second case, the structures consist of basic objects (unit cells) which are repeated at precisely defined intervals in space. Although the subject of systems characterized by periodicity of their structures is extremely wide, structures of this type are invariably associated with the phenomenon of waves and vibrations. This is due to the fact that PS have mechanical properties which are counter-intuitive, especially with regard to vibroacoustic phenomena (Lee *et al.*, 2010). In a similar way to periodic metamaterials, PS exhibit the same unusual dynamic behavior thanks to the periodicity of their structures (Brillouin, 1953). The source of this periodicity may be periodic changes in the material properties within the cells (density or elastic modulus) and/or changes in the cell geometry (cross-section or the presence of certain geometric features) (Yu *et al.*, 2018). The periodicity of is manifested by the presence of the so-called bandgaps which indicate the frequency areas within which the energy cannot be transmitted through these structures (Liu *et al.*, 2011). Although the phenomenon of interaction of with waves is one of the most developed branches of modern physics, this issue is still very popular among researchers, and the range of possible issues to be analyzed is still wide. With the dynamic development and dissemination of numerical methods (especially in the field of modeling methods) and the increase in access to devices with high computing power, a renewed interest can be observed. Thanks to the finite element method, the possibilities of analyzing and designing have significantly increased.

Mechanical metamaterials and mechanical PS have recently become increasingly popular in this field. The difference between them results from scale (actually the ratio: the size of the unit cell to the size of the element), and not from topological differences. It should be noted that, unlike metamaterials, whose unit cells are generally many orders of magnitude smaller than the considered sample of such materials, cell sizes in PS are often comparable to the overall structure. The analysis of the contemporary scientific literature shows that research on metamaterials (micro- or nano-scale structures) predominates, which may be associated with technological constraints on the manufacture of such structures (it is easier to get the required minimum number of elementary cells to obtain specific dynamic properties of structures) and thus potentially greater opportunities for practical applications. Therefore, research (especially experimental) on PS is difficult. On the other hand, reducing the size of the elementary cell directly affects the dynamic properties of periodic systems. The smaller the elementary cell, the more responsive it is to waves and vibrations at higher frequencies. For this reason, there are relatively few projects investigating PS, especially in the context of optimising their shape and topology. The literature lacks comprehensive research aimed at developing and implementing procedures for designing in order to obtain the assumed dynamic properties, including: damping acoustic or elastic waves in specific frequency regimes and/or selected vibration modes. In terms of the design of vibration isolators, there is a lot of research on designs of PS with additional moving elements acting as anti-resonators. The aim of the present study is to look in a different direction at potential practical applications of passive vibroacoustic isolation or filtration of propagating vibroacoustic signals in given frequency bands. It should be noted that the precise design must exist to obtain the desired insulating or filtering properties. This process usually involves some modeling and optimization procedures which lead to predetermined widths as well as positions of individual gaps in the frequency bands. Shape and topology optimization calculations (Halkjær *et al.*, 2006) is a type of computer analysis that is often performed to identify optimal shapes of structures to achieve specific static or dynamic characteristics (e.g. assumed strength with minimum mass or filtered different types of propagation of vibroacoustic signals). Historically, the method of topology optimization in materials design was first used by Sigmund (1994) using the reverse homogenization method. In the following years, many works continued the research in this area (Xia and Breitkopf, 2015). Over the years, attempts have been made to model the dynamics of metamaterials analitically, using methods such as the plane expansion method (PEM) (Yang etal, 2004) or the transfer matrix method (TMM) (Yu *et al.*, 2006), as well as numerically, thanks to the use of sophisticated computational tools based on the classical finite element method (FEM) (Żak *et al.*, 2017; Hsu, 2011) or its variants, as well as experimentally (Xiao *et al.*, 2013). It should be noted that analytical studies were usually limited to one-dimensional (1D) or two-dimensional (2D) structures with simple geometries and boundary conditions. In contrast, FEM seems to overcome these limitations and emerges as a tool capable of solving problems of complex three-dimensional (3D) geometries, arbitrary boundary conditions, as well as material properties.

From the point of view of modern materials science, a constant challenge is to create such artificial structures, whose properties (in particular, dynamic responses) resulting from their periodicity can not only be predictable but, above all, programmed in a purposeful and fully controlled manner. Additionally, it should be mentioned that both the fabrication and testing of such elements in three dimensions are still at a relatively early stage. Therefore, it seems necessary to modify the classic and to develop new methods of optimising the shape and topology of PS, which can not just manage the level of complexity and non-linearity of the models, but can also take into account the issues of manufacturing and experimental verification of such structures. The main idea of the presented research was to develop a novel approach to the design of passive vibration isolators or mechanical vibration filters (without anti-resonators) with optimised dynamic characteristics. It was assumed that a precisely designed shape of a periodic

beam, affecting its dynamic properties, would enable vibration filtering not only in terms of the selected frequency range but above all in terms of the types of vibration to be filtered. Depending on the engineering problem being solved related to vibration isolation, it would be possible to design a vibration-damping filter in a selected frequency band for any combination of mechanical vibration types (longitudinal, transverse, torsional). At the same time, the dimensions of PS enable damping of vibrations at much lower frequencies than metamaterials, with no moving or active elements.

2. Methodology

Analysing the current state of knowledge, it can be seen that the key issue that remains insufficiently explored is the optimisation of topology and shape (Chen *et al.*, 2010). Optimizing the shape of the unit cell of a structure is a challenge because structural analysis of the three-dimensional elasticity problem is computationally intensive. Additionally, external boundary conditions and loads can affect each component differently, making their performance heterogeneous (Tantikom *et al.*, 2005). Algorithms in use today focusing on structural optimization can generally be assigned to one of three basic groups: gradient algorithms, population algorithms and artificial intelligence algorithms (Goldberg and Holland, 1988; Ji *et al.*, 2023). These methods are aimed to achieve the assumed dynamic parameters of designed structural elements (such as damping of mechanical vibrations in specific frequency regimes and/or for selected modes of vibrations). Due to the complexity of numerical models of periodic systems, their non-linear nature and the number and unknown connections of parameters that may affect the dynamic properties of the structure, it seems that the process of designing elements with given dynamic properties should be implemented through a multi-criteria optimization process.

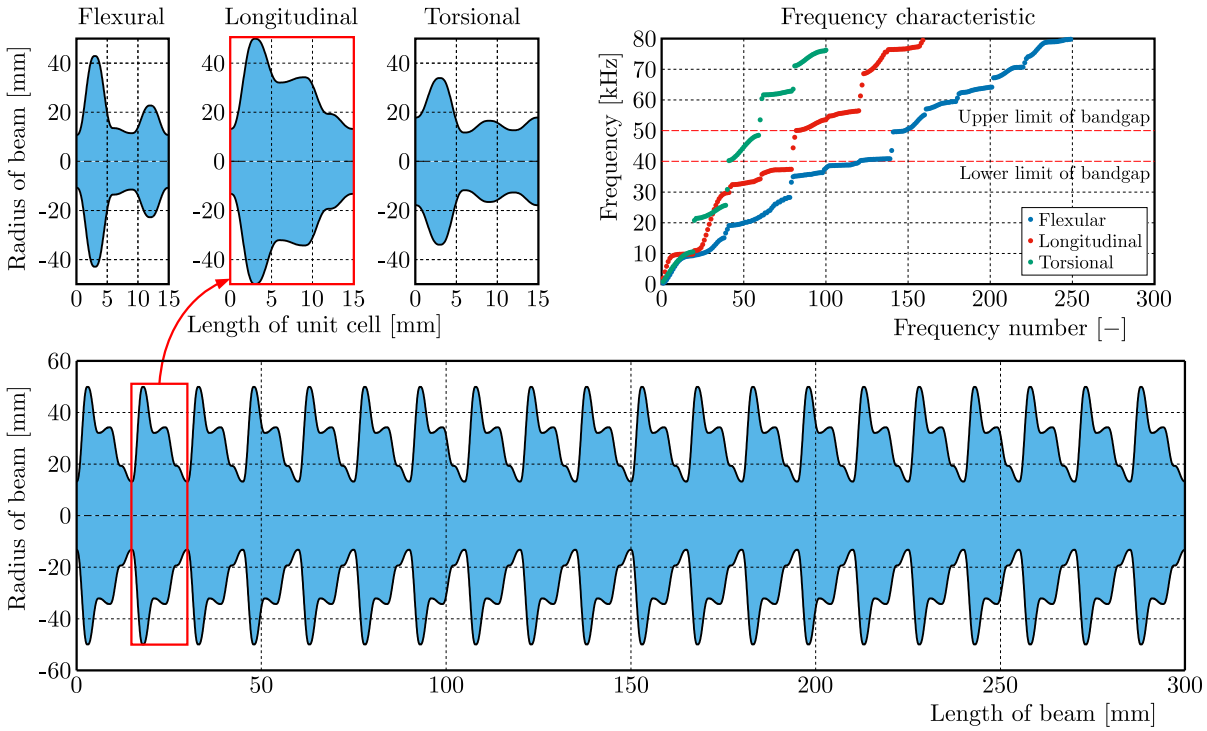

Fig. 1. Periodic beam diagram

The results presented in this paper concern implementation of a genetic algorithm (GA) to optimize the structural parameters (the shape of the unit cell of a tested structure) of a selected axisimmetric isotropic beam representing a periodic mechanical structure. Optimization

calculations were carried out in order to obtain frequency characteristics in which the position and width of the forbidden bands were imposed from above, for each of the three basic types of vibrations (longitudinal, rotational and flexural). Since the dynamic properties of are directly related to the shape of the unit cell, the searched parameters (subject to the optimization process) were the five radii of disks forming the shape of the unit cell, as shown in Fig. 1. The target shape of the cell cross-section is created by a curve passing through subsequent points using interpolating polynomials of the 5th degree. The procedure presented in the authors' earlier research was used here (Żak *et al.*, 2019).

It was assumed that the periodic beam was divided into 20 identical cells of a continuously varying radius in the range between $R_{min} = 10\,\text{mm}$ and $R_{max} = 50\,\text{mm}$. The total length of the beam was $L = 300\,\text{mm}$, therefore the length of a particular cell was $l = 15\,\text{mm}$. Additionally, it was assumed that each cell was subdivided into 5 segments equal in length (3 mm each). Additionally, during the numerical calculation stage, it was necessary to take into account the limitations resulting primarily from the assumption that at the experimental research stage, the samples would be made using 3D printing from PLA material of the following material properties: Young's modulus $E = 2.35\,\text{GPa}$, Poisson's ratio $\mu = 0.36$, mass density $\rho = 1045\,\text{kg/m}^3$ (Witkowski *et al.*, 2021). It should be emphasised that additive manufacturing technologies are characterised by features that should be taken into account both at the stage of developing numerical models and in the optimisation process. For this reason, the length of the beam was determined to be 300 mm (the size of the 3D printer built plate). At this point, the attention should be paid to an extremely important aspect of modelling PS, which is the choice of boundary conditions. In the presented study, the authors assumed that both ends of the beam are free, and the beam has finite length. These parameters were determined primarily in terms of the possibility of manufacturing samples for verification tests. Indeed, the choice of aperiodic boundary conditions with a small number of cells at the same time may affect the dynamic properties of PS (Ashcroft and Mermin, 2022). However, the results of the authors' research (both numerical and experimental) allow the conclusion that certain periodicity features for large PS are already revealed with a smaller number of repeating cells (Żak *et al.*, 2019).

Figure 2 shows the general scheme of the optimization algorithm used in the study. The optimization process can be defined as an iterative mathematical procedure aimed at minimizing the error between actual and predefined parameter values over a discrete range. In order to characterize the optimal shape of the cell within the structure, it is first necessary to build a numerical model of a periodic structure, which can undergo the optimization process. To facilitate the optimisation process, a numerical model of the beam was applied using the spectral finite element method in the time domain (TD-SFEM) combined with a GA. This numerical model has been developed, tested and experimentally verified by the authors for an aluminum beam in earlier studies, the results of which can be found in (Żak *et al.*, 2019).

In the first step of optimization calculations, the algorithm was initialized by creating first--generation individuals. For this purpose, 768 sets of 5 numbers were generated with an accuracy of four decimal places. These numbers represented the successive radii of disks that formed the cross-sectional shape of the unit cell. The population size was dictated by the capabilities of the computing equipment. The calculations were performed on a multi-processor High Power Computer using Matlab software and parallel calculations on 768 processors. In the next step, it was decided to carry out the chromosome generation process according to the value coding scheme, in which the gene is represented by a sequence of values. The chromosome of each individual consisted of 5 pairs of genes (10 genes in total). Each pair defined radii (R_1-R_5) (Fig. 3). The first gene of the given pair determined an integer part of the decimal number (which could take values from 1 to 4), whereas the second gene was its fractional part (accurate to 4 decimal places – the number range from 0 to 9999). Coding the decimal number with division into an integer and a decimal part allowed, first of all, to search for better solutions

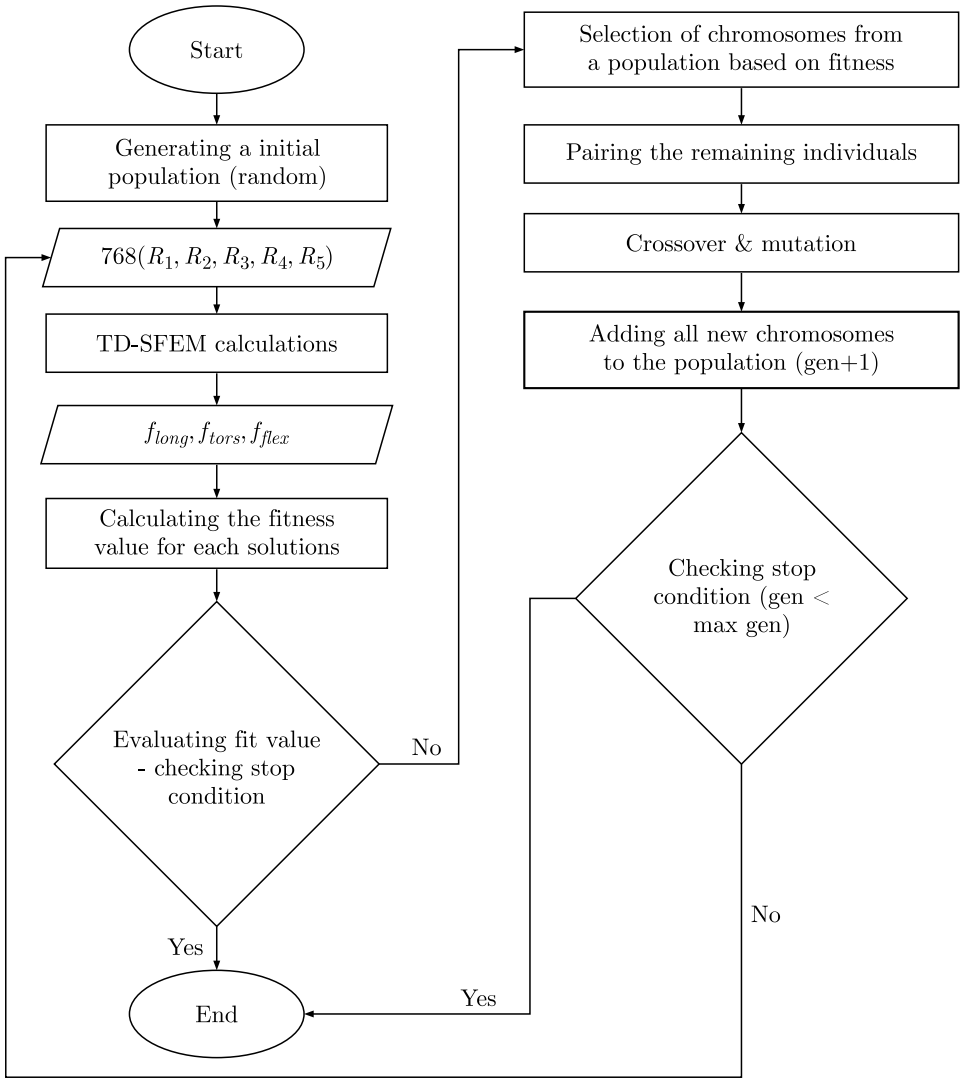

Fig. 2. Scheme of the optimization process using the evolutionary method and the TD-SFEM model

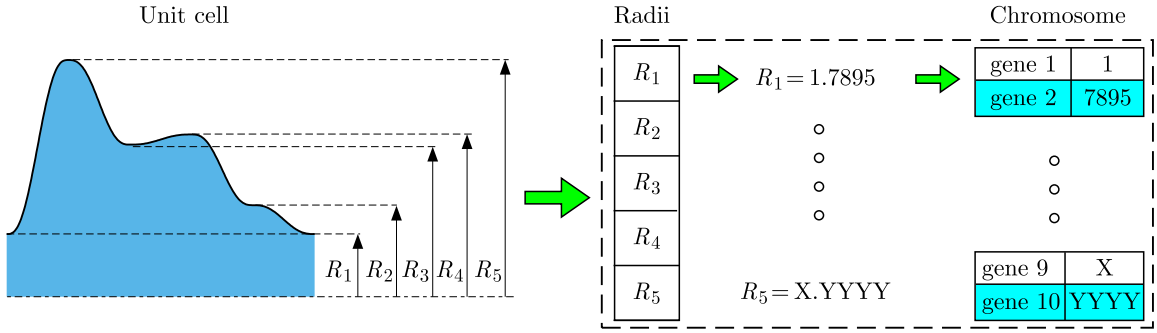

Fig. 3. Scheme for encoding the values of radii creating the shape of the unit cell

around the optimum while maintaining high variability in the first phase of searching for the optimal solution.

The generated population of random solutions was introduced into the FEM numerical model, which generated independent frequency characteristics for each considered type of vibration.

Due to the multi-criteria optimization problem, the basic challenge was to determine the objective function used to evaluate the results of FEM calculations. The aim of the optimization process was to obtain the shape of the unit cell of the periodic beam, which could ensure the appearance of bandgap characteristics in a specific place for all selected types of vibrations.

Table 1. Considered cases of optimization goals

Case No.	Flexural	Longitudinal	Torsional
1	forbiden[1]	allowed[2]	allowed
2	allowed	forbiden	allowed
3	allowed	allowed	forbiden
4	allowed	forbiden	forbiden
5	forbiden	forbiden	allowed
6	forbiden	allowed	forbiden
7	forbiden	forbiden	forbiden

[1] unable to propagate waves in a given frequency range
[2] able to propagate waves in a given frequency range

For mechanical vibration excitations generated in the bandgap range, the beam is a kind of mechanical band-stop filter that does not allow the propagation of waves of selected frequencies. Taking into account 3 basic types of beam vibrations, 7 cases of optimization goals were adopted, the summary of which is presented in Table 1. Since changing one of the radii R_i affects all types of vibrations simultaneously (including the position and width of the frequency bandgaps), the optimization process cannot be carried out by assessing the fit of only one vibration characteristic to the target without simultaneously checking the condition for the other types. Therefore, we can write that the objective function is defined from three separate functions

$$G = \begin{cases} G_{long} = g_1(f_{long}(R_1, R_2, R_3, R_4, R_5)) \\ G_{tors} = g_2(f_{tors}(R_1, R_2, R_3, R_4, R_5)) \\ G_{flex} = g_3(f_{flex}(R_1, R_2, R_3, R_4, R_5)) \end{cases} \tag{2.1}$$

where $f_{(long,tors,flex)}(R_1, R_2, R_3, R_4, R_5)$ is the frequency characteristic of a given type of structure natural vibrations (long – longitudinal, tors – torsional, flex – flexular). The following constrains were imposed

$$R_{min} \leqslant r_i \leqslant R_{max} \qquad (i = 1, 2, ..., 5) \quad \text{and} \quad f_L \leqslant f_i \leqslant f_U \qquad (i = 1, 2, 3) \tag{2.2}$$

where r_i represents the parameter value of the disc radius, and R_{min} and R_{max} represent the lower and upper limit of disc radius, respectively. The value of r_i of the initial generation population is generated randomly. The f_L and f_U represent the lower and upper limit of the bandgap. At the same time, it was assumed that all three types of vibrations have an equal impact on the overall fitting function, and the goal of optimization is to maximize the function G

$$\max(G) = \max\Big(\frac{1}{3}G_{long} + \frac{1}{3}G_{tors} + \frac{1}{3}G_{flex}\Big) \tag{2.3}$$

For each type of vibration, the function can take two forms (G_+ or G_-), depending on the adopted optimization goal (existence of a bandgap in a given range or not). The objective function G takes the form of the G_+ function when the expected result of a perfect match is a full coverage of the given frequency range, which means that the waves can propagate freely. Otherwise (in a given frequency range wave propagation is not allowed) the objective function takes the form of the G_-. The G_+ function (aimed at filling a given band) takes the form of a percentage coverage of the given range by the available natural frequencies, Eq. $(2.4)_1$. Due to

naturally occurring bandgap ranges, the form of the G_+ function is also dependent on the form of currently assessed vibration characteristics of a given type. Figure 4 shows the most common cases of filling the band with natural frequencies of the structure. By modifying the geometric parameters of the unit cell, it is possible to control both the width and position of the bandgaps. If the goal is to fill the entire band with natural frequencies of a given type of vibration, the optimization algorithm can strive to reduce all existing forbidden bands to zero. Hence, the sum of the widths of all frequencies appears in the objective function. The function G_-, Eq. $(2.4)_2$, whose purpose is to remove the frequency from the band, is determined by width of the existing bandgap (or not) in the given frequency band

$$G_+ = \frac{\sum d_i}{\Delta f_{BG}} \qquad G_- = \left(\frac{R}{\Delta f_{BG}}\right)^2 \tag{2.4}$$

where: d_i – natural frequencies of a given type existing in the considered frequency band, R – existing initial bandgap width, Δf_{BG} – bandgap width.

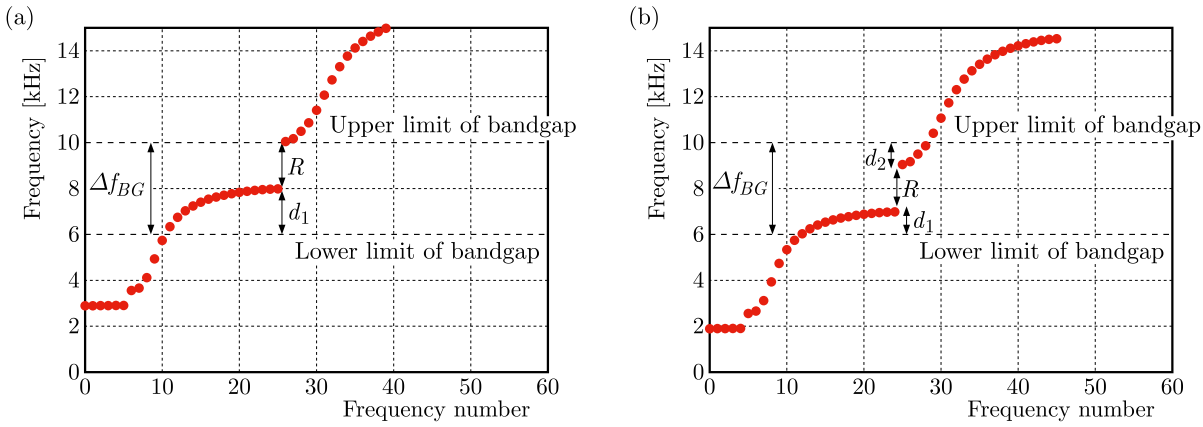

Fig. 4. The width of the existing bandgap R and the width of the natural frequency coverage d_i within the optimization goal: (a) the existing bandgap extends beyond the bandgap limit, (b) the existing bandgap is within the assumed bandgap

After assessing the fit of a given generation, a sorting and selection process takes place. In the selection process, half of the population with the best fit is kept unchanged, while the other half is discarded and new individuals are generated in its place by interbreeding the surviving individuals. For this purpose, pairs of individuals were randomly created and genes were exchanged using the 2-point method. This method involves random crossover points being selected, and the genetic information of parents is swapped as per the segments that have been created. What is important is that in this method the order of genes in the chromosome before and after the crossing operation is preserved. This ensures that there is no possibility of the error of replacing the gene representing the integer part of the number with the decimal part gene.

After replenishing the population with new individuals, a mutation operation was performed, which concerned only new individuals. Taking into account the 60% probability, it was checked whether a given individual would undergo mutation. If so, the gene to be changed was selected at random. The new value of a gene was randomized while maintaining the restrictions for a given gene type (1-4 for an odd gene and 0000 to 9999 for an even gene). In this way, the new population generated was reintroduced to the FEM model, where new frequency characteristics were generated. The process was carried out until a perfect match was achieved or 120 generations were exceeded.

3. Results

As a result of the optimization calculations performed for all assumed cases (Table 1), 7 different shapes of unit cells were obtained. The calculations were divided into three stages depending on the optimization goal. In the first stage, the calculations aimed to obtain the shape of the unit cell for beams in which the wave propagation filtering was assumed for only one form of vibration. The summary of the results is shown in Fig. 5 (a-c: flexural vibrations, d-f: longitudinal vibrations, g-i: torsional vibrations). The first column presents the optimized shapes of the unit cell meeting the optimization condition. The second column shows the resulting frequency characteristics with the marked location of the band gaps for the three vibration types. Analyzing the obtained frequency characteristics, one can notice individual frequencies appearing within the band gaps. These are anti-resonant frequencies, so their occurrence in the assumed frequency band does not affect the result of the optimization process.

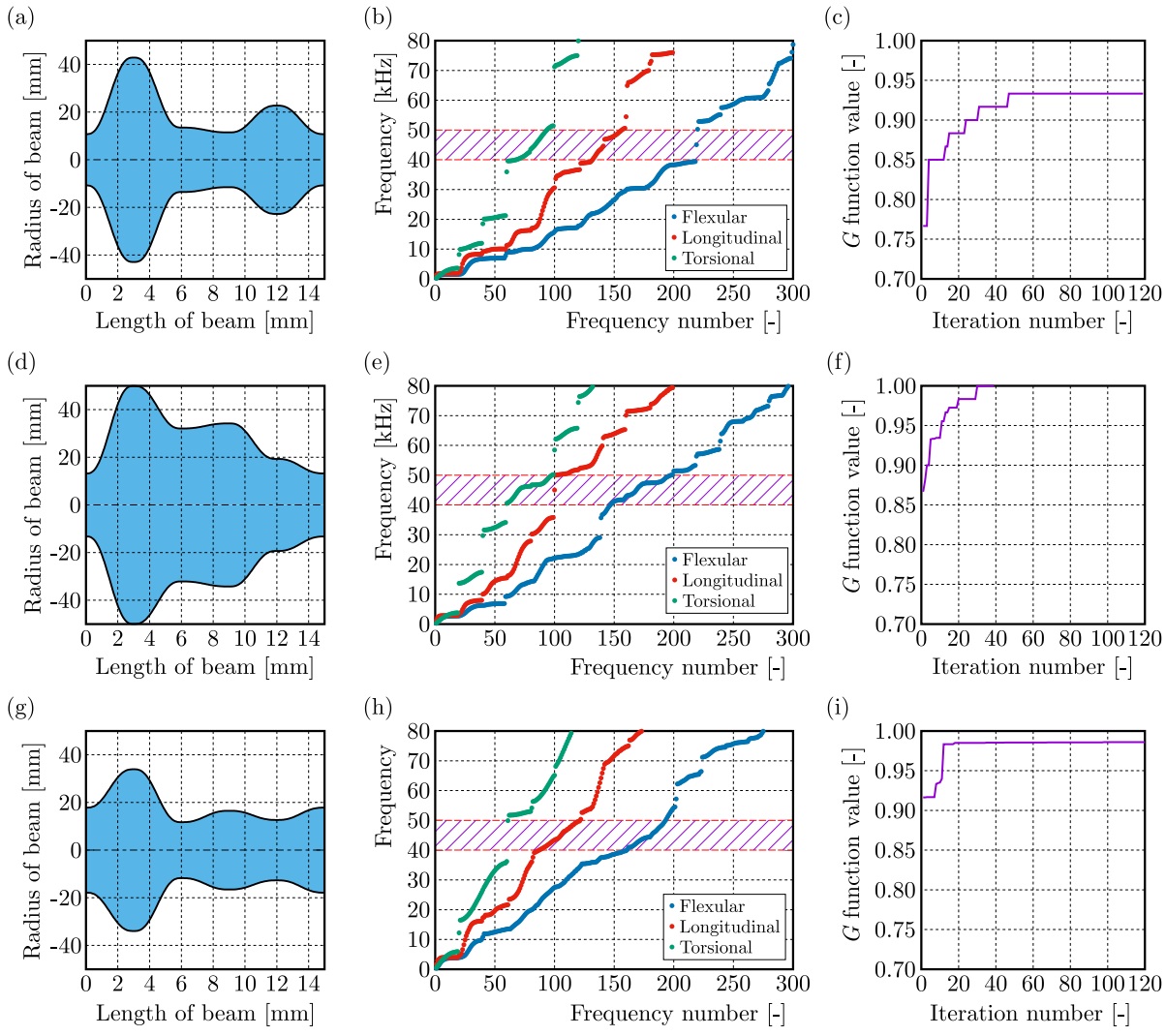

Fig. 5. Results of the optimization process for the first three cases (1st column – the shape of the optimized unit cell, 2nd column – the location of the band gaps for the three modes of vibration, 3rd column – convergence diagram): (a), (b), (c) – filtration of only flexural vibrations; (d), (e), (f) – filtration of only longitudinal vibrations; (g), (h), (i) – filtration of only torsional vibrations

The last column of Fig. 5 contains the convergence graphs obtained during the optimization process. The value of 1 means 100% fulfilment of the objective function. As can be seen, almost

full matching was achieved for longitudinal and torsional vibrations (100% and 98.6%, respectively). Only in the case of flexural vibrations, a convergence of 93.33% was achieved. It should be noted, however, that this is due to the lack of fulfilment of the parallel condition regarding longitudinal vibrations and the full filling of the band gap with natural frequencies (Fig. 5b). The condition of the existence of a band gap in the assumed frequency range for the bending mode of vibrations has been met.

Figure 6 shows the results of the second stage of calculations, in which the cases of attenuation wave propagation in the beam were considered simultaneously for two selected forms of vibration (a-c: bending and longitudinal, d-f: longitudinal and torsional, g-i: bending and torsion). Due to the need to meet the condition of the existence of a bandgap for two types of vibrations simultaneously, the achieved matching levels for all cases are below 100%. The last case of the optimization process considered was damping wave propagation simultaneously for all forms of vibrations in the assumed frequency range.

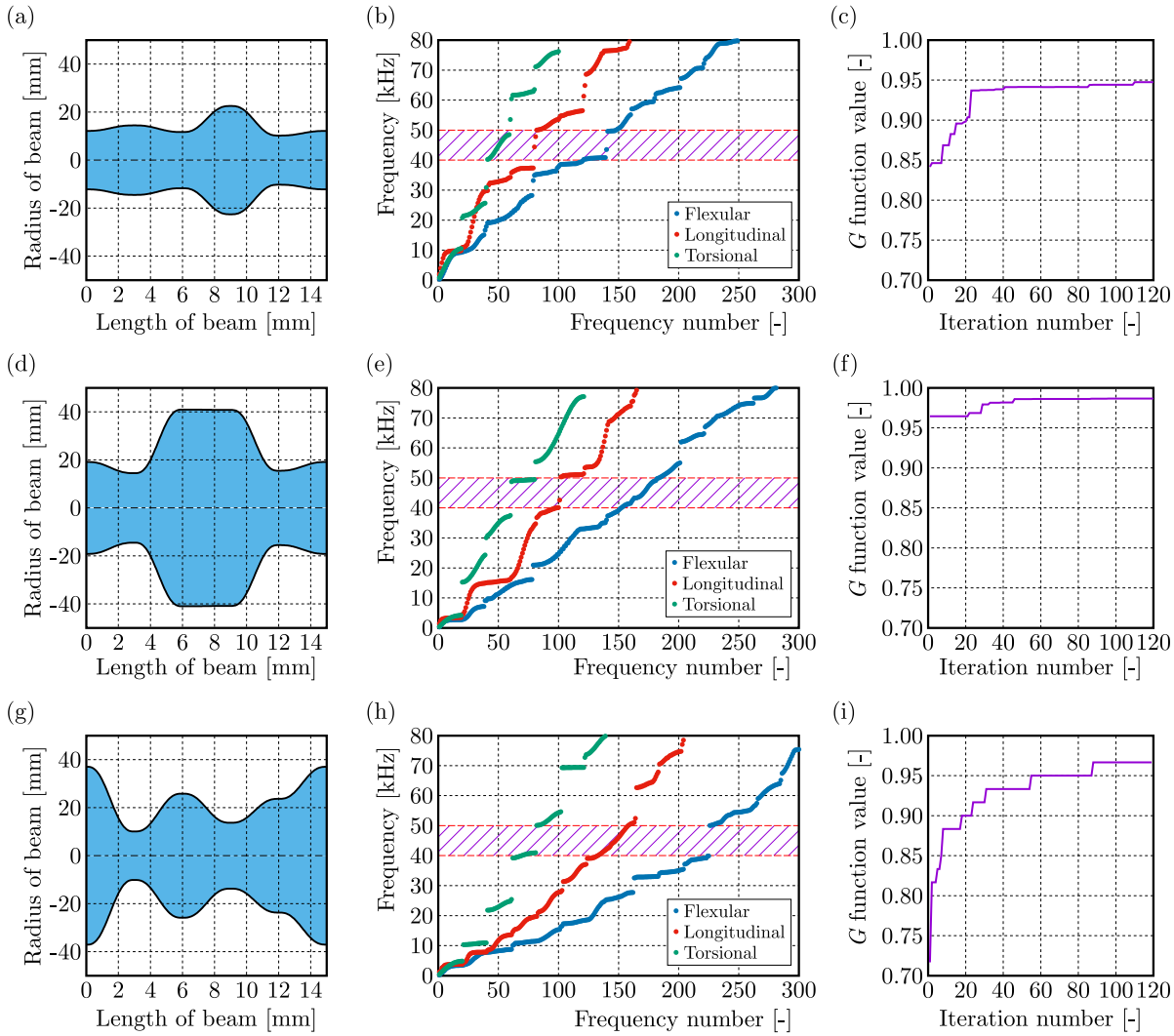

Fig. 6. Results of the optimization process (1st column – the shape of the unit cell, 2nd column – the location of the band gaps, 3rd column – convergence diagram): (a), (b), (c) – filtration of flexural and longitudinal vibrations; (d), (e), (f) – filtration of longitudinal and torsional vibrations; (g), (h), (i) – filtration of flexural and torsional vibrations

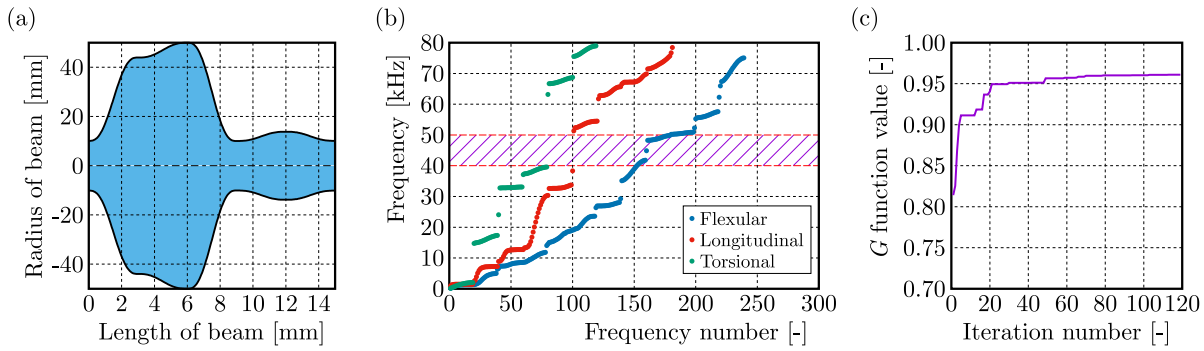

Fig. 7. Results of the optimization process for filtration all types of vibrations: (a) the shape of the optimized unit cell, (b) the location of the band gaps for the three modes of vibration, (c) convergence diagram

The calculation results are shown in Fig. 7. In the case under consideration, despite the need to simultaneously meet the three bandgap conditions, a matching degree of 96.1% was achieved, which is a satisfactory result considering the imposed geometric constraints (minimum and maximum diameter of the unit cell disks).

4. Discussion

The article presents the results of optimization calculations aimed at adjusting geometric parameters of an elementary cell of an axisymmetric mechanical periodic structure. The optimization procedure used by the authors, using a GA and a numerical beam model, made it possible to obtain a structure with the given dynamic properties of the beam in terms of the position and width of the common frequency bandgap. Based on the authors' research described in this article, the following general conclusions can be drawn:

- The GA optimization procedure used by the authors made it possible to adjust the geometric parameters within a single cell defining the periodic beam. Thus, the width and position of the resulting common band gap can be treated aspreconfiguration at the beam modelling stage, allowing the designer to freely select both the position and width of the band gap for longitudinal, bending and torsional vibrations within the natural frequency spectrum of the periodic beam under study. For all cases considered, a level of fit to the objective function in the range of 93.33%-100% was obtained.
- The approach presented by the authors in this work, along with the optimization procedure, can be used in the design of with specific dynamic properties, i.e. widths and positions of the frequency bands in their vibration spectra. Such modelling could complement the inherent properties of high-damping materials such as PLA by extending the frequency range of damped vibrations (vibroacoustic isolators) or designing elements that damp only selected types of vibrations (mechanical filters).
- The main limitation of using the optimization procedures in conjunction with numerical models based on the classical finite element method is their size and complexity (large number of degrees of freedom). The use of the TD-SFEM modelling method, the size of which is tens times smaller than the FEA model, while maintaining the accuracy of the results, allows faster calculations and more robust results, which allows them to be combined with various optimization algorithms.

The growing availability of computers with high computing power has created new paths for the rapid development of optimization methods, including evolutionary methods and machine learning techniques, which enable their application to larger and more complex problems,

including modelling nonlinear problems. The use of advanced numerical methods to predict the physical properties of PS allows one the design and optimization of structures before their experimental implementation, but also the understanding of relationships between physical parameters describing mechanical (topology, shape, size of unit cells, mechanical properties of the material) and their physical properties. The understanding of these relationships is important in relation to the issue of modelling structures characterized by specific mechanical properties. We are convinced that the combination of AI technology and numerical modeling issues may allow us to develop procedures for optimizing mechanical structures to achieve the assumed dynamic properties, including damping mechanical vibrations. At this point, attention should be paid to another aspect related to the complex study of PS. There is no doubt that the interest in the issues of this type of structures is closely related to the possibilities of their production. Taking into account the fact that the authors plan to conduct experimental verification tests in the next stage, it was necessary to take into account the limitations resulting primarily from the assumption that the samples are made using the 3D printing method. The recent advances in additive manufacturing techniques combined with the topological optimization issues enable the design of PS with controlled anisotropy. In other words, 3D printing can be used to produce cellular metamaterials and PS of arbitrary shapes. On the other hand, it should be understood that, despite undeniable advantages, additive technologies have features that should be taken into account both at the stage of developing numerical models and in the optimization process, such as the damping coefficient of the material used, unintended anisotropy and heterogeneity of the material or the limited size of the printed object (the need to combine larger structures with separately printed elements, which introduces additional discontinuities that may affect dynamic properties of the system, in particular wave propagation).

5. Conclusions

This paper presents the results of a study of a 3D axisymmetric periodic beam, which can be used as a vibroacoustic filter due to its precisely defined dynamic properties. The study combines evolutionary optimisation methods with numerical modelling. The use of a spectral finite element method and a GA allowed the behavior of the structure over a wide frequency spectrum to be investigated with a high degree of accuracy at a low computational cost. The optimisation process focused on determining the dimensions and shape of the elemental cell to obtain both the desired width and position of bandgaps present in the frequency spectrum of the beam, for each type of mechanical vibrations (flexural, longitudinal and torsional). The results for all combinations of vibration types were analysed and obtained, resulting in 7 passive mechanical vibration filters allowing the filtering of all or selected types of vibrations in the assumed frequency band (40-50 kHz). In this aspect, the presented method is closer to the topological modelling than to a classical optimisation approach. It is worth noting that the calculations were carried out taking into account the potential technology for making the actual filters, i.e. 3D printing using the PLA material. This was primarily related to limitations on the minimum and maximum dimensions of the specimen. The calculations carried out proved that it is possible to successfully design vibration/vibration isolation elements with precisely tuned dynamic characteristics. This was achieved by combining the properties of periodic structures, mechanical properties of the thermoplastic material and methods for optimising the shape of the elementary cell. At the same time, the challenges and limitations of using such algorithms in the design and shape optimisation of periodic structures were analysed. In conclusion, it can be stated that the design and shape optimisation of periodic structures using GA is a promising research area and has shown great potential in overcoming the limitations of traditional methods to enable the design of periodic structures with improved performance.

Acknowledgments

Financial support of these studies from Gdansk University of Technology by the DEC-40/2021/IDUB/I.3.3 grant under the ARGENTUM – Excellence Initiative – Research University program is gratefully acknowledged.

The authors of this work would like to gratefully acknowledge the support for their research provided by the Academic Computer Centre in Gdansk. All results presented in this paper have been obtained by the use of software available at the Academic Computer Centre in Gdansk.

References

1. Ashcroft N.W., Mermin N.D., 2022, *Solid State Physics*, Cengage Learning
2. Brillouin L., 1953, *Wave Propagation in Periodic Structures: Electric Filters and Crystal Lattices*, **2**, Dover Publications
3. Chen Y., Zhou S., Li Q., 2010, Multiobjective topology optimization for finite periodic structures, *Computers and Structures*, **88**, 11, 806-811
4. Goldberg D.E., Holland J.H., 1988, Genetic algorithms and machine learning, *Machine Learning*, **3**, 95-99
5. Halkjær S., Sigmund O., Jensen J.S., 2006, Maximizing band gaps in plate structures, *Structural and Multidisciplinary Optimization*, **32**, 263-275
6. Hsu J.-C., 2011, Local resonances-induced low-frequency band gaps in two-dimensional phononic crystal slabs with periodic stepped resonators, *Journal of Physics D: Applied Physics*, **44**, 5, 055401
7. Ji W., Chang J., Xu H.-X., Gao J. R., Gröblacher S. *et al.*, 2023, Recent advances in metasurface design and quantum optics applications with machine learning, physics-informed neural networks, and topology optimization methods, *Light: Science and Applications*, **12**, 1
8. Lee S.H., Park C.M., Seo Y.M., Wang Z.G., Kim C.K., 2010, Composite acoustic medium with simultaneously negative density and modulus, *Physical Review Letters*, **104**, 5, 054301
9. Liu X., Hu G., Sun C., Huang G., 2011, Wave propagation characterization and design of two-dimensional elastic chiral metacomposite, *Journal of Sound and Vibration*, **330**, 11, 2536-2553
10. Sigmund O., 1994, Materials with prescribed constitutive parameters: An inverse homogenization problem, *International Journal of Solids and Structures*, **31**, 17, 2313-2329
11. Tantikom K., Aizawa T., Mukai T., 2005, Symmetric and asymmetric deformation transition in the regularly cell-structured materials. Part I: Experimental study, *International Journal of Solids and Structures*, **42**, 8, 2199-2210
12. Witkowski W., Kuik L., Rucka M., Daszkiewicz K., Andrzejewska A., Luczkiewicz P., 2021, Medially positioned plate in first metatarsophalangeal joint arthrodesis, *PLOS ONE*, **16**
13. Xia L., Breitkopf P., 2015, Multiscale structural topology optimization with an approximate constitutive model for local material microstructure, *Computer Methods in Applied Mechanics and Engineering*, **286**, 147-167
14. Xiao Y., Wen J., Wang G., Wen X., 2013, Theoretical and experimental study of locally resonant and Bragg band gaps in flexural beams carrying periodic arrays of beam-like resonators, *Journal of Vibration and Acoustics*, **135**, 4, 041006
15. Yang S., Page J.H., Liu Z., Cowan M.L., Chan C.T., Sheng P., 2004, Focusing of sound in a 3D phononic crystal, *Physical Review Letters*, **93**, 024301
16. Yu D., Liu Y., Zhao H., Wang G., Qiu J., 2006, Flexural vibration band gaps in Euler-Bernoulli beams with locally resonant structures with two degrees of freedom, *Physical Review B*, **73**, 064301
17. Yu X., Zhou J., Liang H., Jiang Z., Wu L., 2018, Mechanical metamaterials associated with stiffness, rigidity and compressibility: A brief review, *Progress in Materials Science*, **94**, 114-173

18. Żak A., Krawczuk M., Palacz M., Doliński L., Waszkowiak W., 2017, High frequency dynamics of an isotropic Timoshenko periodic beam by the use of the time-domain spectral finite element method, *Journal of Sound and Vibration*, **409**, 318-335

19. Żak A., Krawczuk M., Redlarski G., Doliński L., Koziel S., 2019, A three-dimensional periodic beam for vibroacoustic isolation purposes, *Mechanical Systems and Signal Processing*, **130**, 524-544

Manuscript received November 5, 2023; accepted for print March 1, 2024

JOURNAL OF THEORETICAL AND APPLIED MECHANICS
62, 3, pp. 615-629, Warsaw 2024
https://doi.org/10.15632/jtam-pl/190056

MOTION PLANNING FOR TASK-BASED MOTIONS OF MECHANICAL SYSTEMS BASED ON COMPUTATIONALLY GENERATED REFERENCE DYNAMICS

Elżbieta Jarzębowska
Warsaw University of Technology, Warsaw, Poland
corresponding author Elżbieta Jarzębowska, e-mail: elajarz@meil.pw.edu.pl
Krzysztof Augustynek, Andrzej Urbaś
University of Bielsko-Biała, Bielsko-Biała, Poland
e-mail: kaugustynek@ubb.edu.pl; aurbas@ubb.edu.pl

The paper presents a development of a complementary motion planning strategy for task--based motions for mechanicl systems. The key component of the strategy is a computational procedure for generation of constrained dynamical models, where constraints can be material or task-based ones and specify work regime requirements. The procedure provides the constrained dynamics, i.e. reference dynamics, whose solutions satisfy all constraints upon systems and enable motion planning. It is a unified tool for constrained motion analysis, motion planning and controller designs. The procedure effectiveness is demonstrated through constrained dynamics generation and motion planning analysis for a robotic system.

Keywords: task based motion planning, task based constraints, constrained multibody dynamics

1. Introduction

1.1. The paper scope and content

The paper presents a development of a complementary motion planning strategy for mechanical systems, e.g. robotic ones, which are dedicated to deliver work and services, and these can be pre-planned by task based constraints formulated by constraint equations. The key component of the presented motion planning strategy is a computational based procedure for generation of constrained system dynamical models (Jarzębowska *et al.*, 2018a). The constraints imposed upon system models may be holonomic and first order nonholonomic, material or nonmaterial, and the latter ones are referred to as programmed. The programmed constraints, which reflect variety of performance requirements put upon mechanical systems, combined with other constraints imposed upon them, are merged into one constrained dynamics, referred to as a reference dynamics, whose solutions satisfy all constraints put upon them. Then, motion subjected to the desired constraints may be analyzed, refined and planned accordingly. Due to holonomic and nonholonomic constraints of different natures, which are imposed upon various mechanical systems, the paper proposes a novel approach to the motion planning for constrained systems, which is dedicated to task based motions. Also, the approach based upon the reference dynamics aims to support designing of tracking or stabilizing controllers for programmed motions.

1.2. Motion planning strategies developed for mechanical systems

Motion planning is one of the most significant activities for many mechanical systems like robotic systems, either stationary or mobile, car-like vehicles, heavy machine equipment like

cranes and many others. In majority of works, motion planning refers to the planning of motion between the start and final locations and the satisfy constraints. The constraints are mostly collision-avoidance ones. Much of this research and satisfy the constraints has been focused on solving the motion planning problem in a stationary environment where both targets and obstacles are stationary; see e.g. (La Valle, 2006) and references there. A more complex case is for mobile robots and car-like vehicles, where nonholonomic constraints have to be taken into account in the planner as well as overall dynamics. There are many approaches to determine feasible paths for such systems, see e.g. the review in (Lu *et al.*, 2016). Different approaches for motion planning for car-like vehicles and mobile robots operating in dynamic environments are proposed. According to (Chiang *et al.*, 2015), they can be classified as: artificial potential fields-based approaches, state-time space based approaches, velocity obstacles-based motion planning approaches, and probabilistic collision checking based approaches. The approaches which are based on the artificial potential field generate a combined potential field in which the vehicle is attracted to its target position and is kept away from the obstacles The combined potential field moves the vehicle in the work space prespecifying both position and full stop after obstacles velocity (Chiang *et al.*, 2015; Bounini *et al.*, 2017). In this approach, a vehicle is often modelled as a particle and obstacles are convex shaped. Some of the drawbacks of this approach, listed the most often, are possibility of falling into local minima and intensive computation which is required for descriptions of real environment for vehicles. The state-time space approach is an extension of the configuration space and it consists of notation of the vehicle position and time (Chiang *et al.*, 2015). In this approach, the vehicle is modelled as a particle and stationary, and moving obstacles are transformed to static ones. The approaches which are based on the velocity obstacles concept define the velocity obstacles by computing vehicle velocities that would cause a collision with the obstacles assuming that they are moving with constant velocities (Lee *et al.*, 2017). Then, an avoidance maneuver is computed by selecting velocities that are outside of the velocity obstacles and a derived collision-free trajectory consists of a series of avoidance maneuvers (Huang *et al.*, 2018). However, these approaches are restricted to planning decisions to the velocity of the vehicle and they represent each obstacle, including the vehicle, as a disk. These approaches also require strict determination of the time horizon; otherwise the vehicle may skip moving through tight spaces, and then it can be difficult to determine the shortest path. The selection of the proper time horizon is still unresolved. In (van den Berg and Overmars, 2008), probabilistic approaches are used for computing paths in the state-time space. These planners incrementally build a tree of explored configurations for each planning query. Latest research results demonstrate attempts for reducing the complexity of the planning problem by first constructing a path based on the off-line information of the environment, and then planning a collision-free trajectory on this path/roadmap that considers the on-line information (Feyzabadi and Caprin, 2016). There are also approaches which consider uncertainties or imperfections in environment representation performing probabilistic collision detection. Other problems related to finding a path for the vehicle which is safe by construction can be found in, e.g. (Feyzabadi and Caprin, 2016) and references there.

1.3. Methods for dynamics generation for mechanical systems

In our approach to task-based motion planning, the central role plays the constrained dynamics developed by a computational procedure, in which all constraints i.e. holonomic and nonholonomic, material or task-based are merged together. This constrained dynamics, referred to as reference dynamics, can be developed for both stationary and mobile car-like vehicles or robots. Obstacles, fixed or moving, can be treated as constraints and their locations should be specified by the constraints. There are two basic distinctions between the presented computational procedure for reference dynamics development and other constrained motion equations

derivation methods, usually based upon the Lagrange approach and its modifications. The first one is that all constrants upon a system can be considered and merged into one dynamical model and the second should be: that all constraints upon is that the final equations are in the reduced state form, i.e. they are free of constraint reaction forces, which are eliminated at the derivation process. These are essential advantages of our approach, and this computational procedure serves both reference and control oriented dynamics derivation. It works for rigid and flexible system models, for open and closed-loop kinematic chains and enables automation of constrained dynamics generation (Jarzębowska *et al.*, 2018b, 2023). The computational procedure for the reference dynamics development is the one unified method for including any desired trajectory or velocity functions into system dynamics. This distinguishes our method from others developed to obtain dynamics of constrained systems, which are based mostly on Newton-Euler and Lagrange approaches. In many approaches, trajectories are planned separately of the vehicle model by using constraints for position, velocity and acceleration at each time instant like in (Macfarlane and Croft, 2003). Some dynamics modeling approaches exploit the Udwadia-Kalaba derivation method, see, e.g. (Yang *et al.*, 2019; Liu and Liu, 2016) and references there. The so called Udwadia-Kalaba dynamic equations enable including position and first order constraints into the system dynamics and determining the constraint reaction forces. These forces, which ensure that the constraints are satisfied, are referred to as control forces. However, from the control theory point of view, it may be not very convenient to design a control algorithm realizing these forces because they needed to be determined via analytical equations directly from the Udwadia-Kalaba equations and may depend upon higher orders of e.g. velocities. Also, Kane's equations can be used to derive dynamic models of robotic systems, see e.g. (Kane and Lewinson, 1983; Sayers, 1990). They eliminate the nonworking constraint reaction forces in an elegant way but they require a smart choice of generalized speeds, which rely on a modeler experience and may not be straightforward as inputs for control applications. In the case when one wants to select velocities as motion parameters, the use of Boltzmann-Hamel equations written in quasi-velocities can be a good option for dynamics and the use of the Boltzmann-Hamel equations control algorithm generations, see e.g. (Jarzębowska and Cichowski, 2018). Due to complexity of mechanical systems, including robotic systems, intensive computation dedicated to their dynamics derivation, solutions and motion analysis is required. For example, in (Khalil *et al.*, 2017), a recursive approach, based upon Newton-Euler equations, of tree-structure systems with rigid and flexible links with floating bases based upon the Newton-Euler is proposed. It can be applied numerically or using symbolic techniques. An algorithm to generate the inverse dynamics is presented in (Do *et al.*, 2021), and it is based upon the recursive Newton-Euler algorithm, the chain rule of differentiation and the computer algebra.

1.4. The paper motivation and contribution

Our goals are to develop a computationally based procedure for generation constrained dynamical models that would support planning of programmed motions and designing tracking controllers for executing these motions specified by the programmed constraints. These goals are motivated by usually used methods of motion planning and controller designs for constrained dynamical models reported in literature, see e.g. (Dixon *et al.*, 2003) and references there. Usually, system dynamical models without constraints are generated first and next control goals like tracking predefined trajectories or other desired motions, are specified. Next, a controller is designed and quite often, it is dedicated to this dynamics and an associated control goal.

In our approach, the reference dynamics describes the system behavior when the task-based constraints are on, and it may serve two purposes. The first one is analysis and assessment of kinematic parameters needed to be reached by the system to follow the desired motions. It is enabled by solutions of the reference dynamics. If this motion comes from work or service

requirements put upon an existing system, it can be easily verified whether it is feasible and realistic to be accomplished by this system. The second purpose is to provide the complementary motion planner, in which the outputs of the reference dynamics are inputs to the controller. The tracking or stabilizing control architecture can be designed and it uses motions planned by the reference dynamics.

The paper is organized as follows. After the introductory Section, Section 2 provides the details of derivation of the computational procedure of generating constrained system dynamics, which provides motion planning for system models. In Section 3, it is demonstrated how the planned motion can be implemented to a control platform architecture for tracking these desired motions. Section 4 details an example of desired motion of a mechanical system model, e.g. a three-link manipulator model subjected to task-based constraints. Simulation studies about the task-based motion planning are detailed in Section 5. We analyse the planned task-based motion and provide an example of a controller design. Other controllers can be designed in the same way. The paper closes with conclusions, future research prospects and the list of references.

2. The computational procedure of generating constrained system dynamics for mechanical system models

The constraints put on a system are referred to as programmed and they can be combined together with material ones. They are imposed as control goals on system performance or as service tasks, and they all can be presented in a general form (Jarzębowska, 2012, 2008)

$$\mathbf{B}(t,\mathbf{q},\dot{\mathbf{q}},\ldots,\mathbf{q}^{(p-1)})\mathbf{q}^{(p)}+\mathbf{s}(t,\mathbf{q},\dot{\mathbf{q}},\ldots,\mathbf{q}^{(p-1)})=\mathbf{0} \tag{2.1}$$

The constraints can be material for $p=0,1$, or nonmaterial, i.e. programmed for $p\geqslant 1$. The nonmaterial constraints are imposed by a designer or a control engineer to obtain a system desired performance, e.g. they can be imposed upon acceleration $p=2$ or jerk $p=3$, as well as for desired trajectories with $p=1$. Constraints form (2.1) is the generalized constraint formulation and it encompasses the classical analytical constraint concept.

The generalized programmed motion equations (GPME) for rigid body models subjected to constraints (2.1) have the following form (Jarzebowska, 2008)

$$\begin{aligned}&\mathbf{M}(\mathbf{q})\ddot{\mathbf{q}}-\mathbf{h}(\mathbf{q},\dot{\mathbf{q}})+\mathbf{g}(\mathbf{q})=\mathbf{Q}(t,\mathbf{q},\dot{\mathbf{q}})\\&\mathbf{B}(t,\mathbf{q},\dot{\mathbf{q}},\ldots,\mathbf{q}^{(p-1)})\mathbf{q}^{(p)}+\mathbf{s}(t,\mathbf{q},\dot{\mathbf{q}},\ldots,\mathbf{q}^{(p-1)})=\mathbf{0}\end{aligned} \tag{2.2}$$

where: $\mathbf{M}(\mathbf{q})$ is the mass matrix, $\mathbf{h}(\mathbf{q},\dot{\mathbf{q}})$ is a vector of centrifugal forces, $\mathbf{g}(\mathbf{q})$ is a vector of gravity forces, $\mathbf{Q}(t,\mathbf{q},\dot{\mathbf{q}})$ is a vector of external generalized forces which are not controls.

Constrained dynamics model (2.2) is the reference dynamics. The solutions to the reference dynamics satisfy constraints (2.1) imposed upon the model. Equations (2.2) are free of constraint reaction forces, which are eliminated in the derivation process. This is the fundamental advantage of (2.2) which makes them suitable for direct motion analysis, planning task-based motions and for control applications. More details about derivation and application of the GPME method are available in (Jarzębowska, 2012). The derivation of GPME (2.2) requires determination of the system kinetic energy and its derivatives. The derivation algorithm for them is as follows: Assume that constraint equations in (2.2) may be solved, at least locally, with respect to the vector $\mathbf{q}_{\beta}^{(p)}$ of dependent coordinates, i.e.

$$\mathbf{q}_{\beta}^{(p)}=\mathbf{g}_{\beta}^{(p)}(t,q,\dot{q},\ldots,q_{\mu}^{(p)}) \tag{2.3}$$

and $q=(q_{\beta},q_{\mu})$, $q_{\beta}\in\mathbb{R}^{k}$, $q_{\mu}\in\mathbb{R}^{n-k}$. Then do the following:

1. Construct a function P_p such that $P_p = (1/p)[T^{(p)} - (p+1)T_0^{(p)}]$, where T is kinetic energy of an unconstrained system, $T^{(p)}$ is its p-th order time derivative, and $T_0^{(p)}$ is defined by $T_0^{(p)} = \sum_{\sigma=1}^{n}(\partial T)/(\partial q_\sigma)q_\sigma^{(p)}$.
2. Construct a function R_p such that $R_p = P_p - \sum_{\sigma=1}^{n} Q_\sigma q_\sigma^{(p)} = R_p(t, q, \dot{q}, \ldots, q_\mu^{(p)}, q_\beta^{(p)}, q^{(p+1)})$.
3. Construct a function R_p^*, in which $q_\beta^{(p)}$ from R_p are replaced by constraints form (2.3)

$$R_p^* = R_p^*(t, q, \dot{q}, \ldots, q_\mu^{(p)}, g_\beta^{(p)}(t, q, \dot{q}, \ldots, q_\mu^{(p)}), q^{(p+1)}) = R_p^*(t, q, \dot{q}, \ldots, q_\mu^{(p)}, q^{(p+1)})$$

4. Assuming that components of a vector of external forces satisfy $\partial Q_\sigma/\partial q_\sigma^{(p)} = 0$, equations of the generalized programmed motion equations (GPME) for a system with constraints (2.3) have the form

$$\left.\frac{\partial R_p^*}{\partial q_\mu^{(p)}}\right|_{\mu=k+1,\ldots,n} = \frac{\partial R_p}{\partial q_\mu^{(p)}} + \sum_{\beta=1}^{k} \frac{\partial R_p}{\partial q_\beta^{(p)}} \frac{\partial g_\beta^{(p)}}{\partial q_\mu^{(p)}} = 0 \tag{2.4}$$

Resulting equations (2.4) plus constraints (2.3) are equivalent to (2.2).

This derivation procedure can be nicely automated in Matlab or other software environment tools, however, when friction, compliance, flexibility or other phenomena are included into the model, this derivation algorithm may be time consuming. For these reasons, for engineering applications, a computationally efficient approach to the constrained dynamics derivation is needed. To develop the automated and computer oriented procedure for generation of constrained dynamics for rigid body models, reference dynamics (2.2) is rewritten in the form (Jarzębowska *et al.*, 2018)

$$\begin{aligned} &\mathbf{M}(\mathbf{q})\ddot{\mathbf{q}} = \mathbf{h}(\mathbf{q}, \dot{\mathbf{q}}) - \mathbf{g}(\mathbf{q}) + \mathbf{Q}(t, \mathbf{q}, \dot{\mathbf{q}}) \\ &\mathbf{B}(t, \mathbf{q})\dot{\mathbf{q}} = -\mathbf{s}(t, \mathbf{q}) \end{aligned} \tag{2.5}$$

where the matrices and vectors are designed as

$$\mathbf{M}(\mathbf{q}) = \mathbf{M}_i\Big|_{i\in i_{i_c}} + \sum_{j\in i_{d_c}} \mathbf{M}_j \frac{\partial \dot{q}_j}{\partial \dot{q}_i} \qquad \mathbf{M} = \sum_{l=1}^{n_l} \mathbf{M}^{(l)} \qquad \mathbf{M}^{(l)} = (m_{ij}^{(l)})_{i,j=1,\ldots,n_{dof}}$$

$$m_{ij}^{(l)} = \operatorname{tr}(\mathbf{T}_i^{(l)}\mathbf{H}^{(l)}(\mathbf{T}_j^{(l)})^{\mathrm{T}}) \qquad \mathbf{h}(\mathbf{q}, \dot{\mathbf{q}}) = \mathbf{h}_i\Big|_{i\in i_{i_c}} + \sum_{j\in i_{d_c}} \mathbf{h}_j \frac{\partial \dot{q}_j}{\partial \dot{q}_i} \qquad \mathbf{h} = \sum_{l=1}^{n_l} \mathbf{h}^{(l)}$$

$$h_i^{(l)} = \sum_{m=1}^{n_{dof}^{(l)}} \sum_{n=1}^{n_{dof}^{(l)}} \operatorname{tr}(\mathbf{T}_m^{(l)}\mathbf{H}^{(l)}(\mathbf{T}_{m,n}^{(l)})^{\mathrm{T}})\dot{q}_m^{(l)}\dot{q}_n^{(l)} + 2\sum_{m=1}^{n_{dof}^{(l)}} \sum_{n=1}^{n_{dof}^{(l)}} \operatorname{tr}(\mathbf{T}_m^{(l)}\mathbf{H}^{(l)}(\mathbf{T}_{i,n}^{(l)})^{\mathrm{T}})\dot{q}_m^{(l)}\dot{q}_n^{(l)}$$

$$\mathbf{h}^{(l)} = (h_i^{(l)})_{i=1,\ldots,n_{dof}^{(l)}} \qquad \mathbf{g}(\mathbf{q}) = \mathbf{g}_i\Big|_{i\in i_{i_c}} + \sum_{j\in i_{d_c}} \mathbf{g}_j \frac{\partial \dot{q}_j}{\partial \dot{q}_i}$$

$$\mathbf{g} = \sum_{l=1}^{n_l} \mathbf{g}^{(l)} \qquad \mathbf{g}^{(l)} = (g_i^{(l)})_{i=1,\ldots,n_{dof}^{(l)}} \qquad g_i^{(l)} = m^{(l)} g \mathbf{J}_1 \mathbf{T}_i^{(l)} \mathbf{r}_{C^{(l)}}^{(l)}$$

$$\mathbf{Q}(t, \mathbf{q}, \dot{\mathbf{q}}) = \mathbf{Q}_i\Big|_{i\in i_{i_c}} + \sum_{k\in i_{i_c}\cup i_{d_c}} \dot{q}_k \frac{\partial Q_k}{\partial \dot{q}_i} + \sum_{j\in i_{d_c}} \left(\mathbf{Q}_j + \sum_{k\in i_{i_c}\cup i_{d_c}} \dot{q}_k \frac{\partial Q_k}{\partial \dot{q}_j}\right) \frac{\partial \dot{q}_j}{\partial \dot{q}_i}$$

$$\mathbf{Q} = \sum_{l=1}^{n_l} \mathbf{Q}^{(l)} \qquad \mathbf{Q}^{(l)} = (Q_i^{(l)})_{i=1,\ldots,n_{dof}^{(l)}}$$

and $\mathbf{T}^{(l)}$ is a transformation matrix from the local frame of link l to the global reference frame $\{0\}$

$$\mathbf{T}_i^{(l)} = \frac{\partial \mathbf{T}^{(l)}}{\partial q_i^{(l)}} \qquad \mathbf{T}_{i,j}^{(l)} = \frac{\partial^2 \mathbf{T}^{(l)}}{\partial q_i^{(l)} \partial q_j^{(l)}}$$

$\mathbf{H}^{(l)}$ is a pseudo-inertia matrix, $m^{(l)}$ is mass of the link, $\mathbf{r}_{C^{(l)}}^{(l)}$ is the position vector of the center of mass.

In the procedure, it is assumed that constraint Eq. $(2.5)_2$ for $p = 0, 1$ may be solved, at least locally, with respect to the vector $\dot{\mathbf{q}}_{d_c}$ of dependent coordinates

$$\dot{\mathbf{q}}_{d_c} = \dot{\mathbf{q}}_{d_c}(t, \mathbf{q}, \dot{\mathbf{q}}_{i_c}) \tag{2.6}$$

and $\dot{\mathbf{q}} = [\dot{\mathbf{q}}_{i_c}^{\mathrm{T}}, \dot{\mathbf{q}}_{d_c}^{\mathrm{T}}]^{\mathrm{T}}$, $\dot{\mathbf{q}}_{d_c} \in \mathbb{R}^{n_{d_c}}$, $\dot{\mathbf{q}}_{i_c} \in \mathbb{R}^{n_{dof} - n_{d_c}}$.

This partition to independent and dependent coordinate derivatives is equivalent to selection of control inputs at the stage of controller design. Comparing (2.5) derivation to the original GPME derivation reported herein and resulted in (2.4), it can be seen that the computational based procedure for generation of constrained system dynamical models developed in this paper is computer oriented ready to automation. In our derivation, which differs from many schemes based upon the Newton-Euler or Lagrange approaches, we have applied the formalism of joint coordinates and homogeneous transformation matrices together with the matrix trace concept. They enable the effective automatic generation of matrices and vectors for the modification of the GPME algorithm. Also, the selection of independent coordinates which will serve as control inputs conforms to the proactive approach to dynamics and control design for mechanical system models (Banaszuk *et al.*, 2007).

3. Planning and tracking task based motions – an advanced control platform architecture

The reference dynamics, either in general form (2.2) or specialized (2.5) offers advantages from both constrained dynamics motion analyses, planning, and controller design points of view. The constrained dynamics, i.e. the reference dynamics, when solved, shows motion patterns of the planned motion. When they reflect work regime or other engineering related demands, it is easy to analyze kinematic characteristics of a system under the constraint action and other accompanying phenomena like vibration. It enables concluding whether the constraints imposed by a designer or control engineer are realistic for the analyzed system and can be accomplished. They can also be modified accordingly. With the aid of our reference dynamics, i.e. the motion planner for constraint driven motion, a controller can be designed based upon a tracking strategy architecture, presented in Fig. 1. It is dedicated for tracking constrained motions. The key component of the tracking strategy is the computational based procedure for generation constrained system dynamics and constrained motion planning (reference dynamics – motion planning block). Based upon experience with the GPME approach to tracking, various modeling parameters can be selected and the dynamic control model can be developed using any available mechanics based method (dynamic control model block) (Jarzębowska, 2008, 2009). Control laws can be selected from collections of algorithms from linear or nonlinear control theory. It is reflected by the block of "specialized terms to the control law". For example, non--adaptive or adaptive controllers can be used. Both dynamic models, i.e. the reference and control, can be derived in a coordinate system convenient for a designer (Jarzębowska, 2009).

To demonstrate the ease of applying motion planning and then tracking with the strategy architecture presented in Fig. 1, let us adopt feedback linearization to the control dynamics.

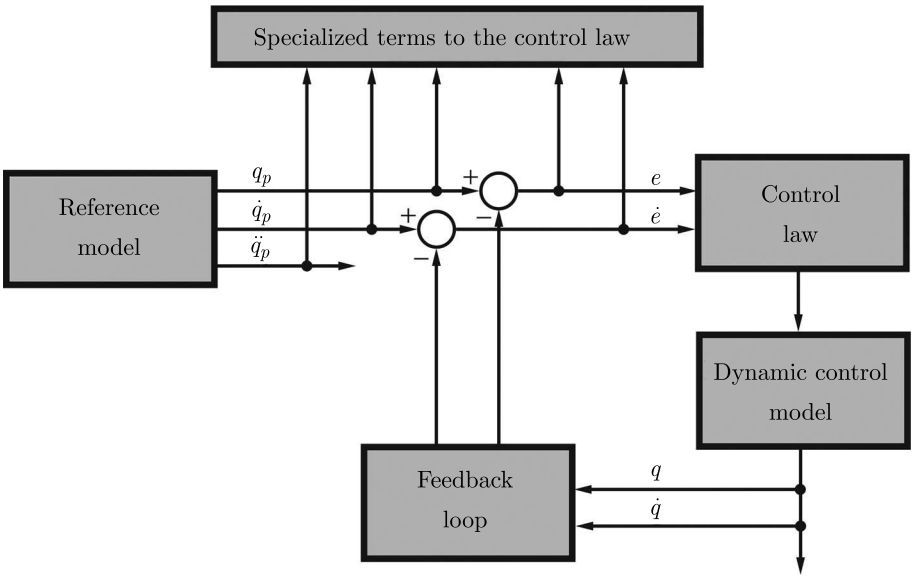

Fig. 1. Tracking strategy architecture

First, generate the reference dynamics (motion planning block), then consider the dynamics with no constraints on the system model (dynamic control model block), i.e.

$$\boldsymbol{\tau} = \mathbf{M}(\mathbf{q})\ddot{\mathbf{q}} + \mathbf{b}(\mathbf{q}, \dot{\mathbf{q}}) + \mathbf{g}(\mathbf{q}) \tag{3.1}$$

Then, apply feedback linearization which enables replacing the controller vector $\boldsymbol{\tau}$ by a virtual controller vector $\mathbf{u}$ as

$$\boldsymbol{\tau} = \mathbf{M}(\mathbf{q})\mathbf{u} + \mathbf{b}(\mathbf{q}, \dot{\mathbf{q}}) + \mathbf{g}(\mathbf{q}) \tag{3.2}$$

where the vector $\mathbf{u} = (u_i)_{i=1,\ldots,n_{dof}}$. For the linearized dynamic control model

$$\ddot{\mathbf{q}} = \mathbf{u} \tag{3.3}$$

the controller $\mathbf{u}$ can be selected. For a purpose of illustration, let us pick the PD controller of the form

$$u_i = \ddot{\widehat{q}}_i - 2\delta_i \dot{e}_i - \delta_i^2 e_i \tag{3.4}$$

where $e_i = q_i - \widehat{q}_i$ is the tracking error, $\widehat{q}_i$ is a value of the i-th coordinate obtained form the motion planner, and δ_i is the control gain.

Notice that within this control architecture, control dynamics (3.1) can be transformed to another control form and another controller can be designed.

4. Example – three-link manipulator task – based motion planning

To demonstrate the process of generation of the reference dynamics, programmed motion planning, its analyses and the controller design, let us examine an example of a three link manipulator whose physical model is presented in Fig. 2a. In Fig. 2b, Denavit-Hartenberg parameters to the manipulator motion description are selected. Motion of the manipulator is described by the vector of generalized coordinates as

$$\mathbf{q} = (q_j)_{j=1,\ldots,3} = [\psi^{(1)}, \psi^{(2)}, z^{(3)}]^{\mathrm{T}} \tag{4.1}$$

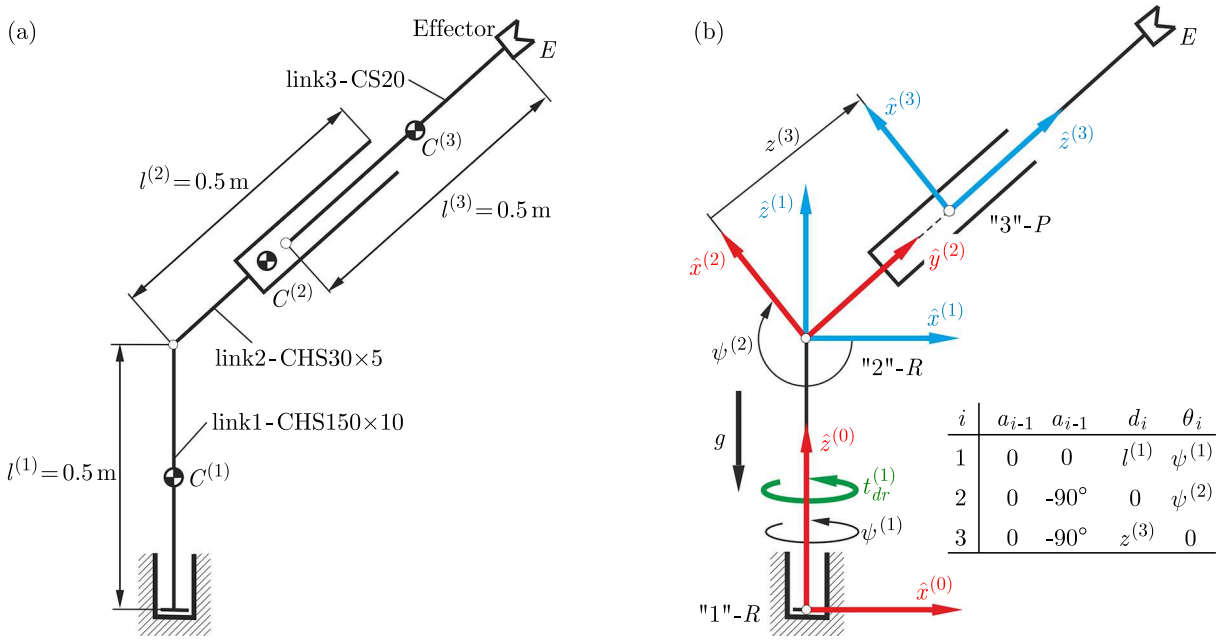

i	a_{i-1}	a_{i-1}	d_i	θ_i
1	0	0	$l^{(1)}$	$\psi^{(1)}$
2	0	-90°	0	$\psi^{(2)}$
3	0	-90°	$z^{(3)}$	0

Fig. 2. (a) Model of a three-link manipulator. (b) The Denavit-Hartenberg notation

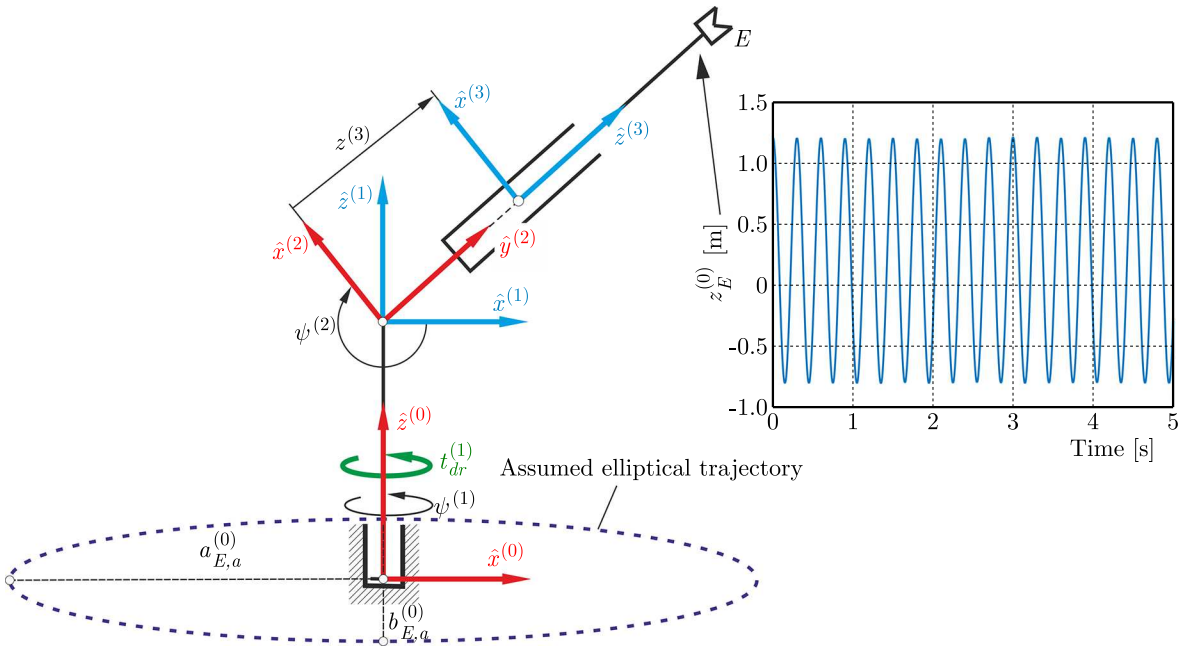

Fig. 3. Assumed programmed constraints

Programmed constraint equations are imposed due to desired motion of the manipulator end-effector. It is illustrated in Fig. 3. The programmed constraints formulation is as follows

$$\begin{aligned} &\Phi_1 \equiv 0 \;\Rightarrow\; \left(\frac{x_E^{(0)}}{a_{E,a}^{(0)}}\right)^2 + \left(\frac{y_E^{(0)}}{b_{E,a}^{(0)}}\right)^2 - 1 = 0 \\ &\Phi_2 \equiv 0 \;\Rightarrow\; z_E^{(0)} - z_{E,a}^{(0)} = 0 \end{aligned} \tag{4.2}$$

where: $x_E^{(0)} = \mathbf{J}_1\mathbf{T}^{(3)}\mathbf{r}_E^{(3)}$, $y_E^{(0)} = \mathbf{J}_2\mathbf{T}^{(3)}\mathbf{r}_E^{(3)}$, $z_E^{(0)} = \mathbf{J}_3\mathbf{T}^{(3)}\mathbf{r}_E^{(3)}$, $a_{E,a}^{(0)}$, $b_{E,a}^{(0)}$ are half-axes of the programmed elliptical trajectory, $z_{E,a}^{(0)}$ is the time assumed function.

It can be seen that this specific kind of the end-effector motion may reflect work regime for the manipulator. Other constraints can be formulated in the same way. The derivation procedure requires differentiation of the programmed constraint equations. The derivatives take the form

$$\begin{aligned} &\dot{\Phi}_1 \equiv 0 \;\Rightarrow\; \mathbf{u}\dot{\mathbf{q}} = \mathbf{0} \qquad \dot{\Phi}_2 \equiv 0 \;\Rightarrow\; \mathbf{C}_3\dot{\mathbf{q}} = 0 \\ &\ddot{\Phi}_1 \equiv 0 \;\Rightarrow\; \mathbf{u}\ddot{\mathbf{q}} + v = 0 \qquad \ddot{\Phi}_2 \equiv 0 \;\Rightarrow\; \mathbf{C}_3\ddot{\mathbf{q}} + d_3 = 0 \end{aligned} \tag{4.3}$$

where

$$\mathbf{C} = \begin{bmatrix} \mathbf{C}_1 \\ \mathbf{C}_2 \\ \mathbf{C}_3 \end{bmatrix} = (c_{ij})_{i=1,2,3,\ j=1,2,3} = \mathbf{J}[\mathbf{T}_1^{(3)}\mathbf{r}_E^{(3)}, \ldots, \mathbf{T}_3^{(3)}\mathbf{r}_E^{(3)}]$$

$$\mathbf{d} = (d_i)_{i=1,2,3} = \mathbf{J}\left(\left(\sum_{i=1}^{n_{dof}}\sum_{j=1}^{n_{dof}} \mathbf{T}_{ij}^{(3)}\dot{q}_i\dot{q}_j\right)\mathbf{r}_E^{(3)}\right)$$

$$\mathbf{u} = (u_j)_{j=1,2,3} = \frac{1}{a_{E,a}^{(0)})^2}\mathbf{J}_1\mathbf{T}^{(3)}\mathbf{r}_E^{(3)}\mathbf{C}_1 + \frac{1}{(b_{E,a}^{(0)})^2}\mathbf{J}_2\mathbf{T}^{(3)}\mathbf{r}_E^{(3)}\mathbf{C}_2$$

$$v = \frac{1}{(a_{E,a}^{(0)})^2}[(\mathbf{C}_1\dot{\mathbf{q}})^2 + \mathbf{J}_1\mathbf{T}^{(3)}\mathbf{r}_E^{(3)}d_1] + \frac{1}{(b_{E,a}^{(0)})^2}[(\mathbf{C}_2\dot{\mathbf{q}})^2 + \mathbf{J}_2\mathbf{T}^{(3)}\mathbf{r}_E^{(3)}d_2]$$

Next, the procedure requires coordinate derivatives partition according to $(2.5)_1$. We need to select independent, i.e. control inputs, and dependent velocities as follows

$$\begin{aligned} &i_{i_c} \in \{1\} \rightarrow \mathbf{q}_{i_c} = [(\psi^{(1)})]^{\mathrm{T}} \\ &i_{d_c} \in \{2,3\} \rightarrow \mathbf{q}_{d_c} = [(\psi^{(2)}, z^{(3)}]^{\mathrm{T}} \end{aligned} \tag{4.4}$$

Relation between dependent and independent velocities can be presented as

$$\dot{\mathbf{q}}_{d_c} = -\mathbf{K}_{d_c}^{-1}\mathbf{K}_{i_c}\dot{\mathbf{q}}_{i_c} \;\Rightarrow\; \frac{\partial\dot{\mathbf{q}}_{d_c}}{\partial\dot{\mathbf{q}}_{i_c}} = -\mathbf{K}_{d_c}^{-1}\mathbf{K}_{i_c} \tag{4.5}$$

where

$$\mathbf{K}_{d_c} = \begin{bmatrix} u_2 & u_3 \\ c_{12} & c_{13} \end{bmatrix} \qquad \mathbf{K}_{i_c} = \begin{bmatrix} u_1 \\ c_{11} \end{bmatrix}$$

Notice, that this partition reflects partition of the coordinates into the control inputs and the controlled ones. As a consequence, in the adopted manipulator model, it is assumed that the column is operated by a flexible drive. The driving torque is determined by the following formula

$$t_{dr}^{(1)} = -s_{dr}^{(1)}(\psi_{dr}^{(1)} - \psi^{(1)}) - d_{dr}^{(1)}(\dot{\psi}_{dr}^{(1)} - \dot{\psi}^{(1)}) \tag{4.6}$$

where $s_{dr}^{(1)}$ and $d_{dr}^{(1)}$ are stiffness and damping coefficients of the flexible drive, respectively.

The displacement of the column $\psi_{dr}^{(1)}$ is a function of time, and it is presented in Fig. 4.

It is assumed that friction is present in manipulator joints. The LuGre friction model (Armstrong-Hélouvry, 1991) is taken into account to calculate the friction coefficients

$$\mu^{(i)} = \sigma_0^{(i)}z^{(i)} + \sigma_1^{(i)}\dot{z}^{(i)} + \sigma_2^{(i)}\dot{q}_i \tag{4.7}$$

where $\sigma_0^{(i)}$, $\sigma_1^{(i)}$, $\sigma_2^{(i)}$ are stiffness, damping and viscous damping coefficients of the bristle, respectively, $z^{(i)}$ is the deflection of the bristle.

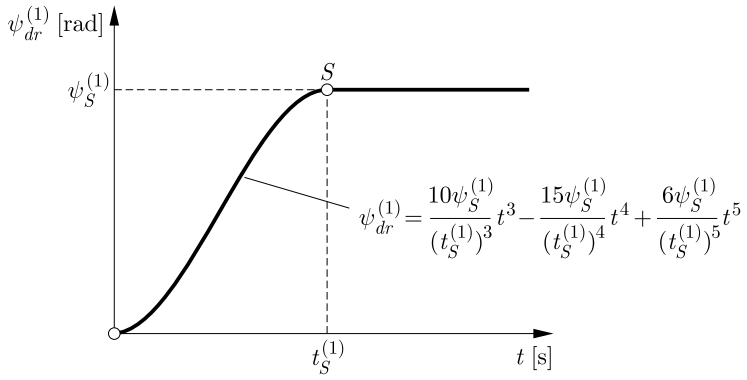

Fig. 4. Assumed displacement of the manipulator column

The deflection velocity $\dot{z}^{(i)}$ is calculated according to the formula

$$\dot{z}^{(i)} = \dot{q}_i - \frac{\sigma_0^{(i)} z^{(i)} \dot{q}_i \operatorname{sgn}(\dot{q}_i)}{\mu_k^{(i)} + (\mu_s^{(i)} - \mu_k^{(i)}) \exp\Big(-\Big(\frac{\dot{q}_i}{\dot{q}_{S,i}}\Big)^2\Big)} \tag{4.8}$$

where $\mu_s^{(i)}$, $\mu_k^{(i)}$ are static and kinetic friction coefficients, respectively, $\dot{q}_{S,i}$ is the Stribeck velocity.

The reference dynamic model of the manipulator is derived based upon modified GPME (2.4), i.e.

$$\begin{bmatrix} \mathbf{M}_i\big|_{i\in i_{i_c}} + \sum\limits_{j\in i_{d_c}} \mathbf{M}_j \dfrac{\partial \dot{q}_j}{\partial \dot{q}_i} \\ \mathbf{u} \\ \mathbf{C}_3 \end{bmatrix} \ddot{\mathbf{q}} = \begin{bmatrix} \mathbf{h}_i - \mathbf{g}_i + \mathbf{Q}_i + \sum\limits_{j\in i_{i_c}\cup i_{d_c}} \dot{q}_j \dfrac{\partial Q_j}{\partial \dot{q}_i} + \sum\limits_{k\in i_{d_c}} \Big(h_k + Q_k - g_k + \sum\limits_{j\in i_{i_c}\cup i_{d_c}} \dot{q}_j \dfrac{\partial Q_j}{\partial \dot{q}_k}\Big) \dfrac{\partial \dot{q}_k}{\partial \dot{q}_i} \\ -v - 2\alpha_1 \mathbf{u}\dot{\mathbf{q}} - \beta_1^2 \Big[\Big(\dfrac{x_E^{(0)}}{a_{E,a}^{(0)}}\Big)^2 + \Big(\dfrac{y_E^{(0)}}{b_{E,a}^{(0)}}\Big)^2 - 1\Big] \\ -d_3 - 2\alpha_2 \mathbf{C}_3 \dot{\mathbf{q}} - \beta_2^2 (z_E^{(0)} - z_{E,a}^{(0)}) \end{bmatrix} \tag{4.9}$$

where α_i, $\beta_i\big|_{i=1,2}$ are coefficients of the Baumgarte numerical solution stabilization method.

5. Numerical studies – simulation results

Manipulator reference dynamic model (4.9) as well as control dynamics (3.2) and (3.3) are analysed in this Section. Specifically, we demonstrate the manipulator model behaviour when the programmed constraints are imposed. Parameters of the manipulator model are presented in Table 1.

Additionally, in the numerical calculations, the following parameters are assumed:

- Flexible drive data: $s_{dr}^{(1)} = 10^4\,\mathrm{Nm/rad}$, $d_{dr}^{(1)} = 70\,\mathrm{Nms/rad}$, $\psi_S^{(1)} = 3600°$, $t_S^{(1)} = 5\,\mathrm{ms}$;
- PD controller data: $\delta_1 = 40$, $\delta_2 = 3$, $\delta_3 = 60$;
- Runge-Kutta IV-order scheme: $h = 10^{-3}\,\mathrm{s}$;
- Baumgarte's coefficients stabilizing numerical solutions: $\alpha = 100$, $\beta = 50$.

Reference dynamics for four initial positions of link 3 with respect to horizontal x asis are analyzed, i.e. 45°, 60°, 70° and 80° are calculated using the GMPE algorithm. The reference

Table 1. Initial manipulator configuration and friction parameters

Parameter	Symbol	Link 1	Link 2	Link 3
Initial configuration	$q_i\big\vert_{t=0}$	0	$270^\circ - \alpha$	0.5 m
Static friction coefficient	$\mu_s^{(i)}$	0.1	0.1	0.1
Kinetic friction coefficient	$\mu_k^{(i)}$	0.2	0.2	0.2
Stiffness coefficient of bristle	$\sigma_0^{(i)}$	5.0 Nm/rad	5.0 Nm/rad	1.0 N/m
Damping coefficient of bristle	$\sigma_1^{(i)}$	0.025 Nm/rad	0.025 Nm/rad	0.02 Ns/m
Viscous damping coefficient	$\sigma_2^{(i)}$	0	0	0
Stribeck velocity	$\dot{q}_{S,i}$	0.175 rad/s	0.175 rad/s	0.001 m/s

time courses thus obtained are applied to the PD controller for the trajectory tracking problem. In numerical simulations, the influence of disturbances of the manipulator initial configuration on the system response and time courses of controls are analyzed. Figure 5a presents the trajectory of the end-effector E in the $x^{(0)}y^{(0)}$ plane of the reference frame $\{0\}$ for different initial configurations. The time course of $z_E^{(0)}$ coordinate is shown in Fig. 5b.

It can be seen that the change of the initial configuration of the manipulator has influence on the position of the effector in the initial moment and on the time after which the given programmed constraints will be achieved. The proposed control algorithm is also effective in the case of disturbances of the initial conditions. In Fig. 6, time courses of the joint coordinates are presented. It can be seen that the motion planner, i.e. the reference motion analysis, enables verification of the programmed motion planned for variety of constraint options. Also, changes in the initial configuration do not have a significant effect on motion of links 1 and 3, while the effect is significantly noticeable in the case of motion of rotary arm 2.

Absolute errors between the reference time courses of displacements and those obtained for the disturbed system, shown in Fig. 7, are determined as

$$\Delta_j^{(\alpha)}(t_i)\Big|_{\alpha\in 60^\circ,70^\circ,80^\circ} = |q_j^{(\alpha)}(t_i) - q_j^{(ref)}(t_i)| \tag{5.1}$$

where $q_j^{(\alpha)}$ are values of the generalized coordinates obtained for angle α, $q_j^{(ref)}$ are reference values of generalized coordinates obtained for angle $\alpha = 45^\circ$.

The results demonstrate that the greatest absolute errors occur in the case of motion of link 2. In the case of other links, they are negligible. It can also be noticed that after 2.5 s, motion of the system is consistent with the assumed constraints. In Fig. 8, time courses of torques and forces obtained from the PD controller are presented.

It can be seen that the torque acting on link 2 has the greatest values up to 1 s, which is related to compensation of disturbances caused by the initial conditions. The time courses of torques and forces have relatively high values, which is caused by the implementation of selected programmed constraints excusively for illustraiting the purposes.

6. Conclusions

Development of a complementary motion planning strategy for task-based motions and a control strategy architecture for tracking these motions based upon a computational procedure for generation of dynamical models with position and first order programmed constraints are presented in the paper. The procedure which was modified comparing to its generic version developed with the aid of the analytical dynamics approach, offers efficient generation of constrained dynamical models which are equivalent to reference dynamic describing motion under the constraints put

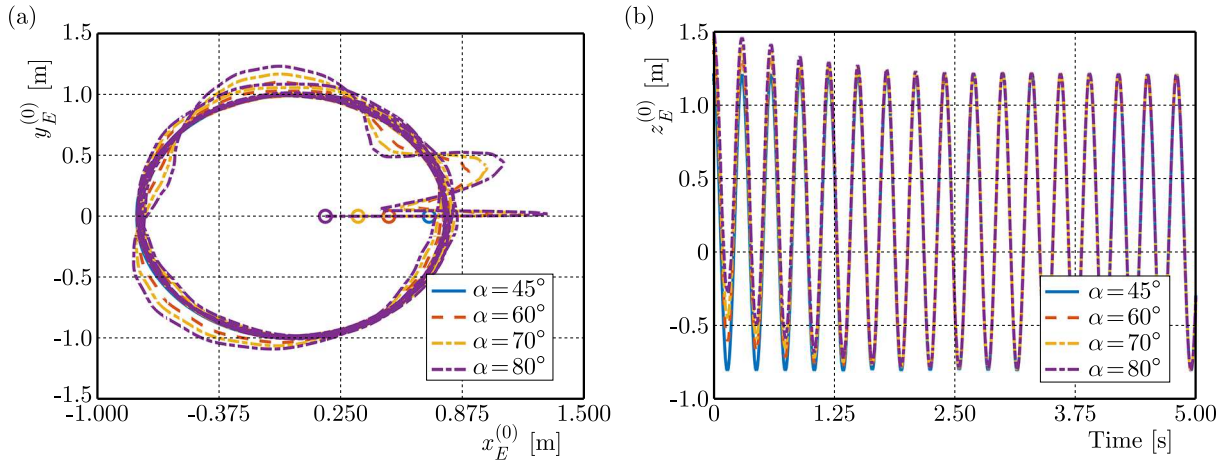

Fig. 5. (a) Trajectory of the end-effector E in the $x^{(0)}y^{(0)}$ plane; (b) time course of $z_E^{(0)}$ coordinate

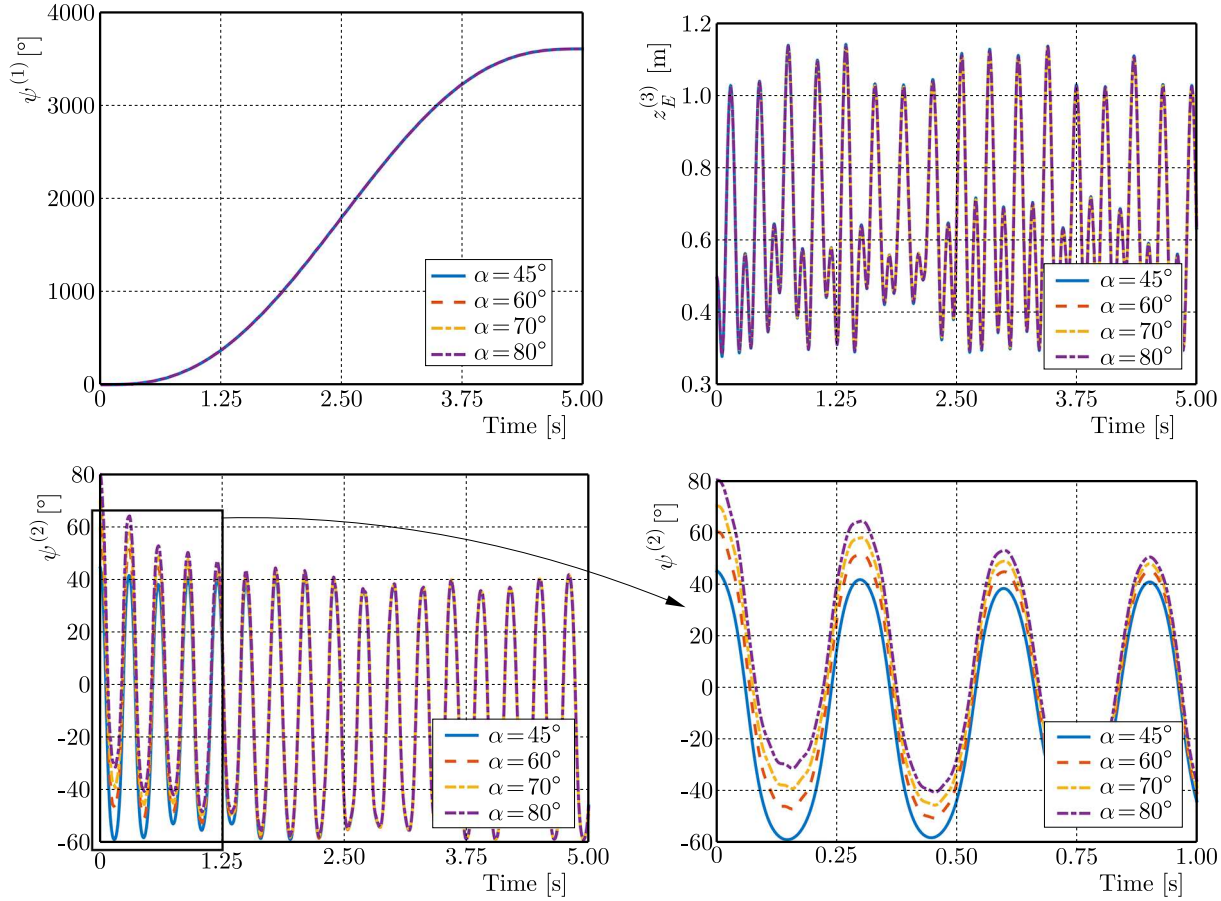

Fig. 6. Time course of joint coordinates

upon the system model. It is not based upon the Newton-Euler or Lagrange approaches but upon the GPME method. It provides reference dynamical models, which may serve as motion planners of constrained motions and enable insight into system performance under the constraints. In the presented procedure, the constraints may be material or nonmaterial, e.g. task-based, and the final equations of motion are derived in the reduced state form, i.e. constraint reaction forces are eliminated at the equations derivation process. This is the essential advantage of our approach comparing to existing dynamical modeling approaches. The effectiveness of this procedure was demonstrated by simulation studies of constrained motion performance of the three link manipulator model.

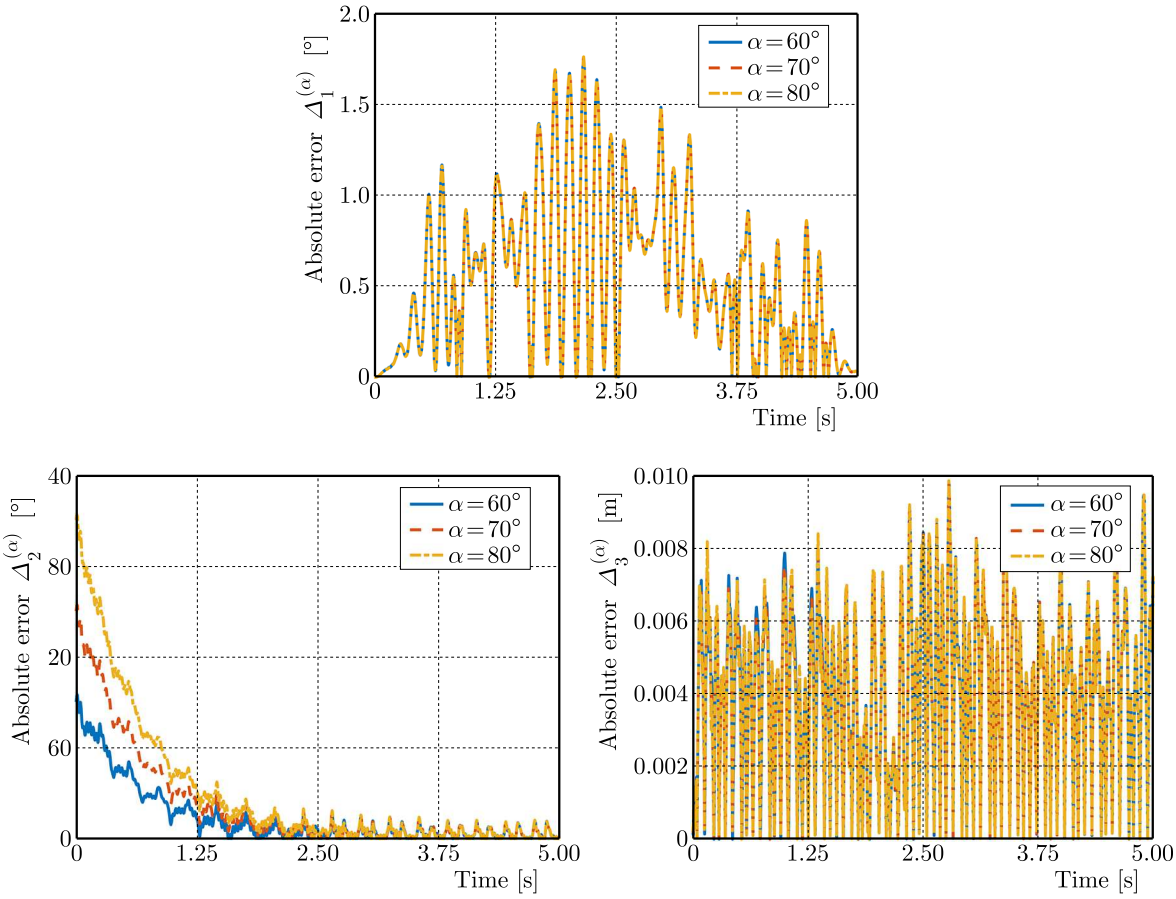

Fig. 7. Time courses of absolute errors for joint coordinates

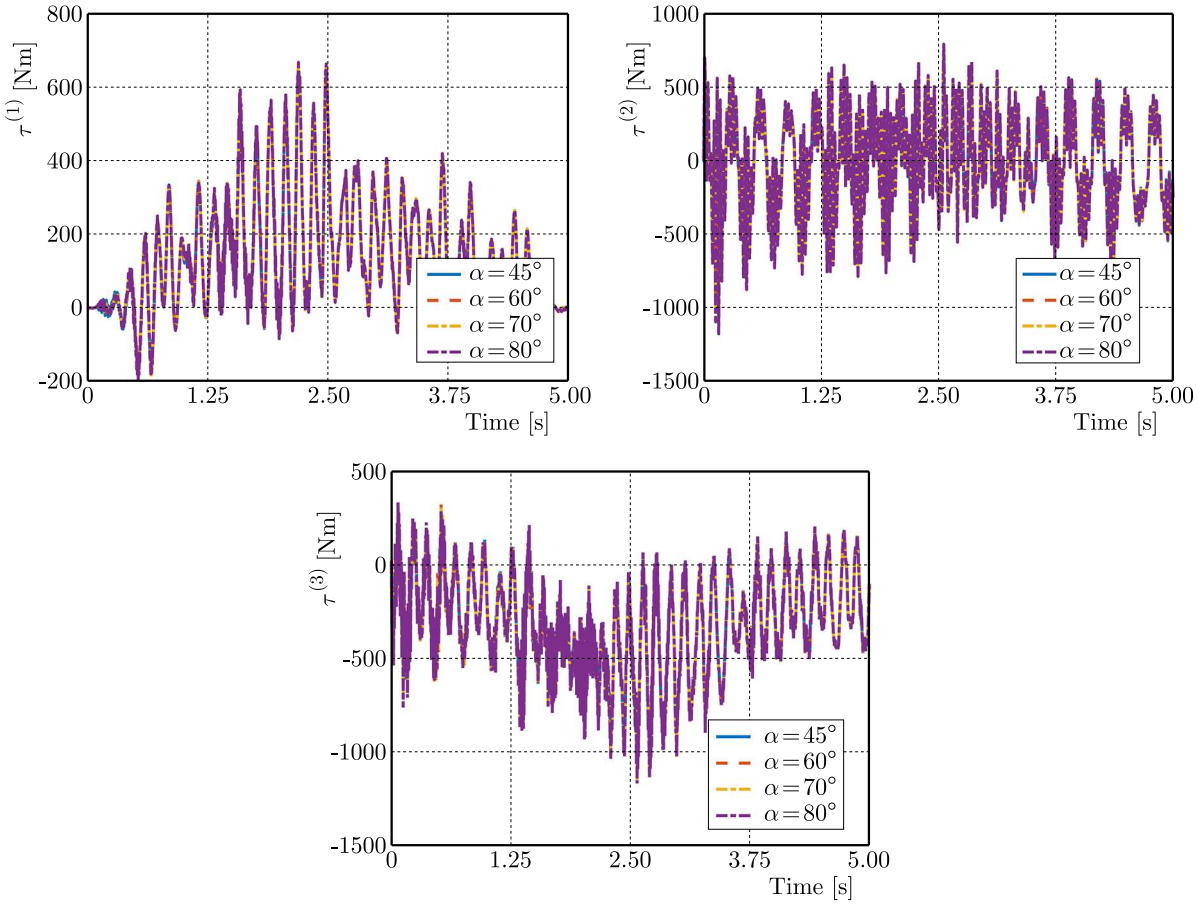

Fig. 8. Time courses of driving torques and the force

References

1. Armstrong-Hlouvry B., 1991, *Control of Machines with Friction*, Springer International Series in Engineering and Computer Science, New York
2. Banaszuk A., Mehta P.G, Hagen G., 2007, The role of control in design: From fixing problems to the design of dynamics, *Control Engineering Practice*, **15**, 10, 1292-1305
3. Bounini F., Gingras D., Pollart H., Gruyer D., 2017, Modified artificial potential field method for online path planning applications, *IEEE Intelligent Vehicles Symposium*, (IV), LA, CA, USA
4. Chiang H.-T., Malone N., Lesser K., Oishi M., Tapia L., 2015, Path-guided artificial potential fields with stochastic reachable sets for motion planning in highly dynamic environments, *IEEE International Conference on Robotics and Automation (ICRA)*, Washington, USA
5. Dixon W.E., Behal A., Dawson D.M., Nagarkatti S.P., 2003, *Nonlinear Control of Engineering Systems: A Lyapunov-Based Approach*, Springer
6. Do T.-T., Vu V.-H., Liu Z., 2021, Symbolic differentiation algorithm for inverse dynamics of serial robots with flexible joints, *ASME Journal of Mechanisms and Robotics*, **13**, 6
7. Feyzabadi S., Carpin S., 2016, Multi-objective planning with multiple high level task specifications, *IEEE International Conference on Robotics and Automation (ICRA)*, Stockholm, Sweden
8. Huang Y., van Gelder J.M., Wen Y., 2018, Velocity obstacle algorithms for collision prevention at sea, *Ocean Engineering*, **151**, 308-321
9. Jarzebowska E., 2008, Advanced programmed motion tracking control of nonholonomic mechanical systems, *IEEE Transactions on Robotics*, **24**, 6, 1315-1328
10. Jarzębowska E., 2009, Quasi-coordinates based dynamics modeling and control design for nonholonomic systems, *Nonlinear Analysis: Theory, Methods and Applications*, **71**, 12, 118-131
11. Jarzębowska E., 2012, *Model-Based Tracking Control of Nonlinear Systems*, Boca Raton: CRC Press, Taylor & Francis Group
12. Jarzębowska E., Augustynek K., Urbaś A., 2018a. Automated generation of reference dynamical models for constrained robotic systems in the presence of friction and damping effects, *Concurrency and Computation: Practice and Experience*, 4452
13. Jarzębowska E., Augustynek K., Urbaś A., 2018b, Development of a computational based reference dynamics model of a flexible link manipulator, *Springer Proceedings Mathematics and Statistics Series, Dynamical Systems in Applications*, **249**, 169-180
14. Jarzębowska E., Augustynek K., Urbaś A., 2023, Dynamics modeling method dedicated to system models with open- and closed-loop structures subjected to kinematic and task based constraints, *Nonlinear Dynamics*, **111**, 13, 12053-12080
15. Jarzębowska E., Cichowski M., 2018, Dynamics modeling and performance analysis of underwater vehicles based on the Boltzmann-Hamel equations approach, *MATEC Web of Conferences*, **148**, 03005
16. Kane T.R., Levinson D.L., 1983, The use of Kane's dynamical equations in robotics, *International Journal of Robotics Research*, **2**, 3, 3-21
17. Khalil W., Boyer F., Morsli F., 2017, General dynamic algorithm for floating base tree structure robots with flexible joints and links, *ASME Journal of Mechanisms and Robotics*, **9**, 3
18. LaValle S., 2006, *Planning Algorithms*, Cambridge University, Cambridge
19. Lee B.H., Jeon J.D., Oh J.H., 2017, Velocity obstacle based local collision avoidance for a holonomic elliptic robot, *Autonomous Robots*, **41**, 6, 1347-1363
20. Liu J., Liu R., 2016, Simple method to the dynamic modeling of industrial robot subject to constraint, *Advances in Mechanical Engineering*, **8**, 4, 1-9

21. Lu Y., Xi Z., Lien J.-M., 2016, Online collision prediction among 2D polygonal and articulated obstacles, *The International Journal of Robotics Research*, **35**, 5, 476-500

22. Macfarlane S., Croft E.A., 2003, Jerk bounded manipulator trajectory planning: Design for real-time applications, *IEEE Transactions on Robotics and Automation*, **19**, 1, 42-52

23. Sayers M.W., 1990, Symbolic computer methods to automatically formulate vehicle simulation codes, Ph.D. Thesis, Dept. of Mechanical Engineering, University of Michigan

24. Van den Berg J., Overmars M., 2008, Planning time-minimal safe paths amidst unpredictably moving obstacles, *International Journal of Robotics Research*, **27**, 11-12, 1274-1294

25. Yang X., Zhang X., Xu S., Ding Y., Zhu K., Liu X., 2019, An approach to the dynamics and control of uncertain robot manipulators, *Algorithms*, **12**, 3

Manuscript received October 26, 2023; accepted for print February 21, 2024

JOURNAL OF THEORETICAL AND APPLIED MECHANICS
62, 3, pp. 631-635, Warsaw 2024
https://doi.org/10.15632/jtam-pl/191182

TOWARDS THE PREDICTION OF PLAQUE ONSET AND GROWTH IN CAROTID ARTERIES

Jaskaran Singh
University of Pisa, Dipartimento di Ingegneria Civile ed Industriale, Pisa, Italy
corresponding author, email: jaskaran.singh@phd.unipi.it

Katia Capellini, Benigno Marco Fanni
Fondazione Toscana G. Monasterio, BioEngineering Unit, BioCardioLab, Massa, Italy

Alessandro Mariotti, Maria Vittoria Salvetti
University of Pisa, Dipartimento di Ingegneria Civile ed Industriale, Pisa, Italy

Simona Celi
Fondazione Toscana G. Monasterio, BioEngineering Unit, BioCardioLab, Massa, Italy

We describe a computational platform to predict atherosclerotic plaque onset and growth in carotids. It integrates *in-vivo* data, Computational Fluid Dynamics (CFD) simulations and a model for plaque growth linearly correlating the plaque progression with low values of time-averaged Wall Shear Stresses (WSS). We show that steady CFD simulations give the same averaged-WSS values as unsteady simulations. Therefore, the model for plaque growth can be coupled with steady simulations, reducing the computational costs. Finally, by comparing the numerical predictions with the *in-vivo* data, we show that a modification must be introduced in the plaque growth model to obtain acceptable results.

Keywords: hemodynamic simulations, atherosclerotic plaque, carotid arteries

1. Introduction

Cardiovascular Diseases (CVD) have emerged as a significant concern for global public health in recent decades due to their high risk, elevated mortality rates, and challenges associated with the diagnosis (Townsend *et al.*, 2016). Atherosclerotic plaque in the carotid arteries is a specific CVD condition that causes the narrowing of the vessel lumen, due to the deposition of substances on the arterial wall. This process obstructs the delivery of blood to downstream organs (Ross, 1999). Consequently, it is imperative to develop strategies aimed at preventing the onset of plaque by identifying key factors and providing healthcare professionals with reliable information (Rafieian-Kopaei *et al.*, 2014). Computational Fluid Dynamics (CFD) simulations, conducted on both idealized and patient-specific geometries, have become a widely utilized tool for analyzing blood flow dynamics and hemodynamic parameters that influence plaque growth. Some of these parameters, such as Wall Shear Stresses (WSS), are challenging to measure directly *in-vivo* (Lopes *et al.*, 2020). CFD simulations, however, need proper geometry definition and boundary conditions. We consider herein the patient-specific geometry and cardiac-cycle flow-rate waveform from *in-vivo* data. Moreover, realistic simulations are three-dimensional in complex geometries and unsteady following the cardiac cycle; therefore, the related computational costs and times are large. Since the growth of atherosclerotic plaques occurs over times much larger than the cardiac cycle period, a possible simplification of the steady flow assumption can be adopted for blood circulation, and the results used to predict plaque growth (Lopes *et al.*, 2020; Marshall *et al.*, 2004). This may allow for a more computationally efficient analysis,

allowing one to model the progression of plaque development over an extended period without prohibitive computational costs (Tang *et al.*, 2008; Gessaghi *et al.*, 2011). Finally, CFD simulations must be coupled with a model predicting the plaque growth.

In this work, we integrate the WSS model by Tang *et al.* (2008) into CFD simulations of patient-specific geometries. To the best of our knowledge, this is the first time this model has been utilized to predict atherosclerotic plaque growth in patient-specific carotid arteries. The plaque growth model establishes a linear correlation between the thickening of the innermost intimal layer of the arterial vessel and the time-averaged WSS exerted on the wall. The thickening of the carotid intimal layer is implemented through morphing (Biancolini *et al.*, 2020; Capellini *et al.*, 2021). We first investigate whether accurate values of WSS can be provided by steady simulations, reducing in this way the computational costs. We evaluate then the capability of this approach in predicting the plaque onset and growth in the considered patient-specific carotid geometry, and we propose a modified version of the model for plaque growth, aimed at improving the agreement with clinical data.

2. Materials and methods

The clinical dataset includes *in-vivo*-measured geometries and flow rates of the diseased right and left carotid arteries from a 78-year-old male patient (Fig. 1a). The diseased geometry is obtained through segmentation of Computed Tomography (CT) scans. The corresponding healthy geometries are derived from the diseased ones by applying an idealized endarterectomy (Fig. 1b). The volumetric flow rates at the inlet Common Carotid Artery (CCA) and the outlets, Internal Carotid Artery (ICA), and External Carotid Artery (ECA) are obtained by interpolating 4D-flow Magnetic Resonance Imaging (4D-MRI) data (Fig. 2).

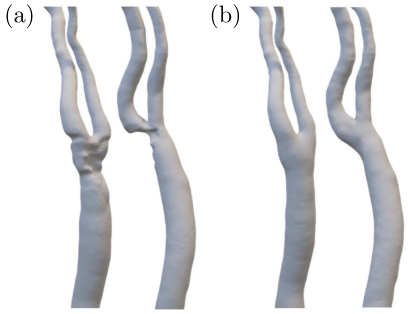

Fig. 1. Patient-specific (a) diseased and (b) healthy right and left carotids geometrical models

CFD simulations are carried out for a laminar and incompressible blood flow ($\rho = 1050\,\mathrm{kg/m^3}$). Blood is considered as a non-Newtonian fluid to capture the shear-thinning effect near the arterial wall that influences the WSS field in medium-small vessels like carotids; the Carreau-Yasuda model is adopted (Weddell *et al.*, 2015). We carry out CFD simulations using a finite-volume commercial code. For simulations involving patient-specific flow-rate waveforms, we conducted unsteady simulations. Conversely, when employing a time-constant inflow condition, we conducted steady-state simulations since the flow remains constant over time. In steady-state simulations, the Navier-Stokes equations are solved in their steady-state formulation, neglecting time derivatives. Conversely, unsteady simulations solve the Navier-Stokes equations as they are, considering time-dependent variables. The fluid domain is discretized by using a polyhedric grid defined after the grid independence study, and the 3D Navier-Stokes equations are discretized through finite volumes. An implicit unsteady time scheme is applied for unsteady simulations. In the steady simulations, we impose a constant fully-developed parabolic velocity profile at the inlet based on the cycle-averaged mean value of the flow rate, as shown in Fig. 2. Furthermore,

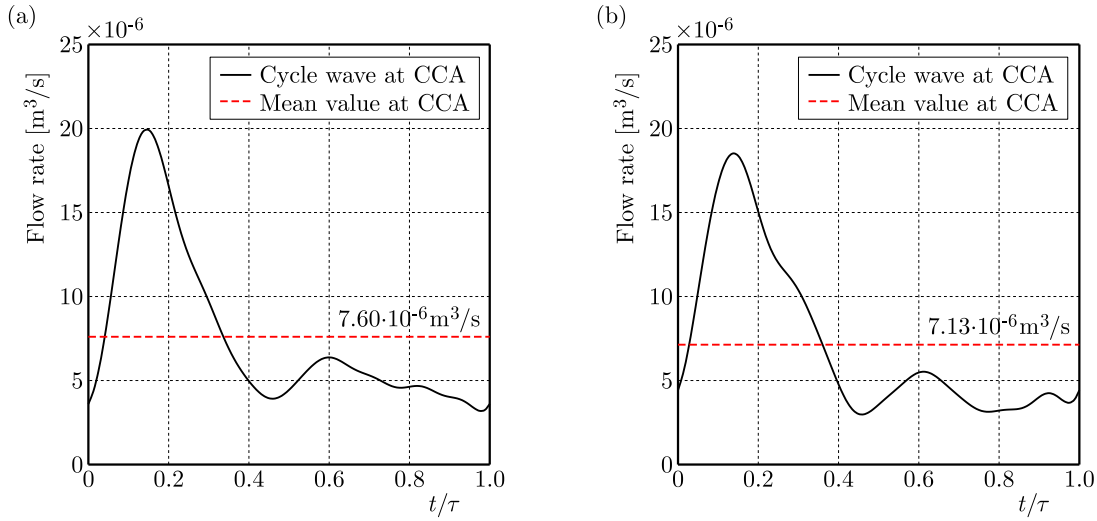

Fig. 2. Patient-specific flow rates: (a) right carotid at CCA and (b) left carotid at CCA

a flow rate split ratio is imposed at the two outlets, ICA : ECA = 0.66 : 0.34 for the right and ICA : ECA = 0.61 : 0.39 for the left carotid (Marshall *et al.*, 2004) with a reference pressure equal to 12438.98 Pa.

CFD simulations are coupled with the WSS-based model of plaque growth from Tang *et al.* (2008) which computes the plaque growth rate $\dot{e}$ as

$$\dot{e} = k_1 - k_2\tau \tag{2.1}$$

where $k_1 = 1.85 \cdot 10^{-2}$ cm/(3months) and $k_2 = 1.73 \cdot 10^{-3}$ cm/(3 months·Pa). Moreover, we have developed a modified version of the model, the WSS_{th} model, that incorporates a threshold value τ_{th}, which confines the plaque growth to regions with low values of τ, thereby preventing plaque onset in the straight portions of vessels, which is unrealistic. The threshold value is set to $\tau_{th} = 0.3$ Pa as suggested in Gessaghi *et al.* (2011). Thus, the updated version of the model is as follows

$$\dot{e} = \begin{cases} k_1 - k_2\tau & \text{for} \quad \tau < \tau_{th} \\ 0 & \text{for} \quad \tau > \tau_{th} \end{cases} \tag{2.2}$$

3. Results and discussion

In Fig. 3, we compare the results of steady and unsteady simulations. Specifically, Fig. 3a shows the time-averaged WSS fields $\overline{\tau}$ obtained from patient-specific unsteady simulations. In Fig. 3b, the WSS field τ for the steady simulation is depicted, and in Fig. 3c, the difference $\overline{\tau} - \tau$ is illustrated. The differences are negligible. Therefore, we can conclude that steady simulations with the time-averaged patient-specific inflow flow rate give WSS that are identical to time-averaged WSS obtained in realistic unsteady simulations. Thus, in the following, the plaque growth will be evaluated on τ with reduced computational costs.

The CFD-predicted values for the plaque onset and early-stage growth are shown in Figs. 4a,c for the WSS-based model from Tang *et al.* (2008) and in Figs. 4b,d for the modified version. The results report the displacement Δe of the intimal layer thickness over a year.

The original version of the WSS-model from Tang *et al.* (2008) lacks precision in predicting the onset location, as it suggests the plaque growth throughout, including in the straight branches of the carotid with high values of τ. Conversely, the modified version of the WSS-model,

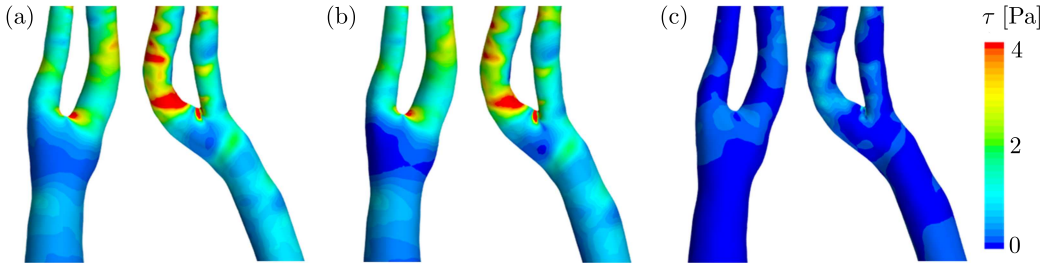

Fig. 3. WSS fields for right and left carotids: (a) $\overline{\tau}$, (b) τ, and (c) $\overline{\tau} - \tau$

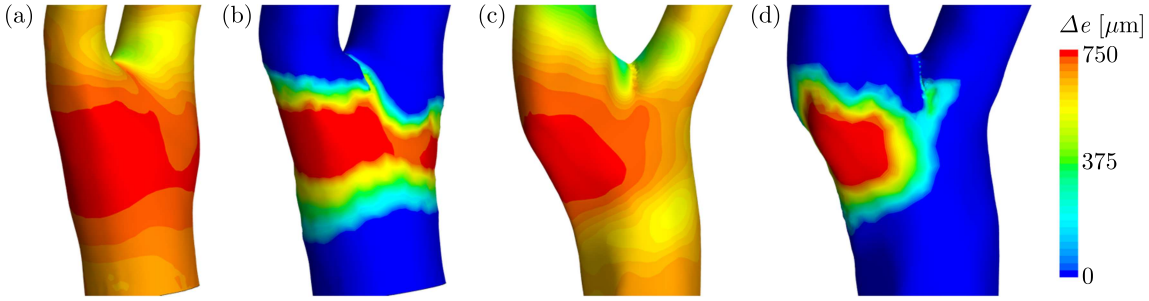

Fig. 4. Displacement fields of the plaque for right and left carotids: (a) WSS model, (b) WSS_{th} model, (c) WSS model, and (d) WSS_{th} model

incorporating the threshold, better delineates and identifies the onset region. The plaques indeed tend to develop near the bifurcation with low values of τ, where the plaques have actually formed in the patient (refer to Fig. 1a). Regarding the plaque growth, both versions of the WSS-model provide overestimated predictions for the plaque growth rate $\dot{e}$, and consequently, for Δe after one year (in comparison, for instance, with the data from the review paper by Lopes *et al.* (2020)). Therefore, while the modified WSS-model effectively identifies the plaque onset, both are inadequate for precise quantitative predictions of the plaque growth without additional calibration of the model constants. Therefore, future work could be devoted to (i) calibrating the constants of the WSS-based model to obtain a more accurate growth rate and (ii) considering more complete plaque growth models, such as the one proposed in Gessaghi *et al.* (2011).

Acknowlegements

This paper was presented at WECM'23-2nd Workshop on Experimental and Computational Mechanics (Pisa, Italy, 20-22 September 2023). Based on the evaluation by a Selection Committee chaired by Prof. Jerzy Warmiński, Lublin University of Technology, Poland, and composed of Prof. Simone Camarri and Prof. Luigi Lazzeri, University of Pisa, Italy, this work was awarded the "WECM'23 Best Paper Award in Fluid Dynamics". The authors gratefully acknowledge the University of Pisa for the organisation of the workshop and for the payment of the publication fee.

This research is supported by PNRR M4C2 – HPC, Big data and Quantum Computing (Simulazioni, calcolo e analisi dei dati e altre prestazioni – CN1) – CUP I53C22000690001 SPOKE 6 Multiscale modelling & Engineering applications and by the National Recovery and Resilience Plan, Mission 4 Component 2 Investment 1.3.

References

1. Biancolini M.E., Capellini K., Costa E., Groth C., Celi S., 2020, Fast interactive CFD evaluation of hemodynamics assisted by RBF mesh morphing and reduced order models: The case of aTAA modelling, *International Journal on Interactive Design and Manufacturing (IJIDeM)*, **14**, 1227-1238

2. Capellini K., Gasparotti E., Cella U., Costa E., Fanni B.M., Groth C., Porziani S., Biancolini M.E., Celi S., 2021, A novel formulation for the study of the ascending aortic fluid dynamics with in vivo data, *Medical Engineering and Physics*, **91**, 68-78
3. Gessaghi V.C., Raschi M.A., Tanoni D.Y., Perazzo C.A., Larreteguy A.E., 2011, Growth model for cholesterol accumulation in the wall of a simplified 3D geometry of the carotid bifurcation, *Computer Methods in Applied Mechanics and Engineering*, **200**, 23-24, 2117-2125
4. Lopes D., Puga H., Teixeira J., Lima R., 2020, Blood flow simulations in patient-specific geometries of the carotid artery: A systematic review, *Journal of Biomechanics*, **111**, 110019
5. Marshall I., Papathanasopoulou P., Wartolowska K., 2004, Carotid flow rates and flow division at the bifurcation in healthy volunteers, *Physiological Measurement*, **25**, 3, 691-697
6. Rafieian-Kopaei M., Setorki M., Doudi M., Baradaran A., Nasri H., 2014, Atherosclerosis: process, indicators, risk factors and new hopes, *International Journal of Preventive Medicine*, **5**, 8, 927
7. Ross R., 1999, Atherosclerosis – an inflammatory disease, *New England Journal of Medicine*, **340**, 2, 115-126
8. Tang D., Yang C., Mondal S., Liu F., Canton G., Hatsukami T.S., Yuan C., 2008, A negative correlation between human carotid atherosclerotic plaque progression and plaque wall stress: in vivo MRI-based 2D/3D FSI models, *Journal of Biomechanics*, **41**, 4, 727-736
9. Townsend N., Wilson L., Bhatnagar P., Wickramasinghe K., Rayner M., Nichols M., 2016, Cardiovascular disease in Europe: epidemiological update 2016, *European Heart Journal*, **37**, 42, 3232-3245
10. Weddell J.C., Kwack J., Imoukhuede P.I., Masud A., 2015, Hemodynamic analysis in an idealized artery tree: differences in wall shear stress between Newtonian and non-Newtonian blood models, *PloS One*, **10**, 4, e0124575

Manuscript received December 29, 2023; accepted for print March 5, 2024

JOURNAL OF THEORETICAL AND APPLIED MECHANICS
62, 3, pp. 637-649, Warsaw 2024
https://doi.org/10.15632/jtam-pl/191234

COUPLING EFFECT OF HOLE ENLARGEMENT AND DIFFUSION IN THE GROUTING PROCESS IN A WEAK STRATUM BASED ON ANALYTICAL RESEARCH

Zenghui Zhao

College of Energy and Mining Engineering, Shandong University of Science and Technology, Qingdao, China; and State Key Laboratory of Mining Disaster Prevention and Control Co-founded by Shandong Province and the Ministry of Science and Technology, Shandong University of Science and Technology, Qingdao China

Zhe Meng

College of Energy and Mining Engineering, Shandong University of Science and Technology, Qingdao, China

Longfei Li

College of Energy and Mining Engineering, Shandong University of Science and Technology, Qingdao, China; and State Key Laboratory of Mining Disaster Prevention and Control Co-founded by Shandong Province and the Ministry of Science and Technology, Shandong University of Science and Technology, Qingdao China
correspondinc author, e-mail: lilongfei@sdust.edu.cn

Canlin Li, Peng Yang

College of Energy and Mining Engineering, Shandong University of Science and Technology, Qingdao, China

According to the tail grouting of a double shield TBM tunnel in a soft stratum, the spherical hole model with small and large diffusion radius were established respectively considering the slurry diffusion and slurry displacement effect in the grouting compaction stage. Analytical solutions of the spherical hole expansion stress and displacement field under the hole expansion-diffusion coupling effect are deduced. The interaction among plastic zone radius, reaming radius, initial radius of the spherical hole, and the seepage radius were analyzed. The results show that the larger the seepage pressure of grouting, the smaller the plastic radius. The larger the reaming radius is, the larger the plastic zone radius is. When the reaming radius reaches a certain value, the plastic radius tends to be stable, and the smaller the grouting seepage pressure, the earlier it tends to be stable. The above conclusions have important guiding significance for optimizing grouting parameters in weak strata.

Keywords: weak stratum, shielding, grouting, reaming diffusion, coupling mechanical effect

1. Introduction

The shield construction is widely used in urban rail transit engineering due to its small disturbance to the environment and high speed. However, many urban subway lines pass through prosperous areas, the underground pipelines are crisscrossed, the ground buildings are complex and changeable, and the construction environment is extremely harsh. The shield construction can easily cause uneven subsidence of the stratum, resulting in surface subsidence and building cracking (Epel *et al.*, 2021; Khetwal *et al.*, 2020; Han *et al.*, 2022). As the main method of shield backfilling, the grouting can effectively control deformation of the formation and prevent uneven stress on the segment. However, if the grouting effect is not good, the segment will float,

be damaged, and the surface will rise or sink. Therefore, revealing the mechanical mechanism of shield grouting in weak strata is of great significance to reduce the shield disturbance in weak strata and reduce the surface subsidence and tunnel deformation.

The shield backfill grouting can be divided into four stages: grouting filling, infiltration, compaction and splitting. Regarding the diffusion effect of grouting, Bezuijen and Talmon (2004) and Bezuijen *et al.* (2004) conducted on-site monitoring research and analyzed in detail the slurry diffusion process and the changes in slurry pressure at different stages. Based on the Navier--Stokes equation, Mu *et al.* (2019) established a water glass slurry diffusion model considering the coupling between the slurry and fracture. Boschi *et al.* (2020) studied the interaction between soil particles and grout during grouting from the perspective of meso-mechanics. Zhou *et al.* (2021) established diffusion models for a single-hole and porous grouting based on fractal geometry and seepage effects. Liu *et al.* (2021) revealed the fluid motion law of a synchronous grouting along the unconventional path in the shield tail gap, and obtained the axial and longitudinal pressure distribution patterns. Li *et al.* (2020) proposed the SDS numerical simulation method considering temporal and spatial evolution factors of slurry viscosity, and studied the diffusion law of water glass slurry in cracks under different dynamic water conditions. Xu *et al.* (2021) developed a simulator that could simulate the whole process of grouting reinforcement based on the numerical manifold method.

In the late stage of grouting diffusion, the slurry around the hole has initially coagulated. When the grouting pressure continues to increase, the grouting enters the grouting compaction stage. Squeezing and compacting causes the phenomenon of hole expansion at the orifice. In view of the grouting reaming effect, Li *et al.* (2019) established an improved compaction grouting model considering three-dimensional shear failure to predict the ultimate grouting pressure of compaction grouting. Shrivastava *et al.* (2017) considered grouting compaction as an expansion process of a cylindrical cavity in a finite medium, and provided its analytical solution. Pachen *et al.* (2005) studied the mechanism and effectiveness of medium pressure grouting in loose filled sand through model experiments. El-Kelesh *et al.* (2012) explored the effects of soil parameters, soil compression rate, replacement rate, and injection sequence on the grouting effect of grouting compaction through on-site experiments. Wang *et al.* (2015) conducted numerical simulations of radial expansion and uplift caused by grouting compaction in noncohesive soil. Wang and Zheng (2022) used the pore fluid diffusion/stress coupling analysis method to simulate the grouting compaction process of two on-site tests, and conducted parameter studies on the uplift and settlement caused by grouting and tunnel excavation. Wu *et al.* (2022) considered the compaction effect of grouting under the condition of soil unloading, and established a compaction grouting model considering the effect of soil unloading. Nishimura *et al.* (2011) demonstrated the importance of stress changes in increasing liquefaction resistance by simulating the grouting compaction process in a geocentrifuge.

In the grouting diffusion stage, the pore water in the formation has been displaced within a certain range as the slurry seeps and diffuses into the formation. The formation already contains slurry at this time, and the influence of slurry diffusion on expansion should not be ignored when analyzing the grouting compaction. Most of the scholars' research on the slurry infiltration diffusion and grouting compaction is idealized to separate the grouting stage, but in fact, seepage, compaction and splitting often occur simultaneously in the grouting process, and various stages of grouting are mutually coupled. The existing research rarely considers the interaction between the grouting compaction and grouting diffusion. Therefore, in this paper, considering the slurry diffusion-compaction coupling effect, analytical formulas of stress field and displacement fields in the elastic-plastic zone of soil around the hole are derived, and the effects of groundwater seepage and slurry diffusion radius on the reaming pressure and plastic zone radius are analyzed.

2. Grouting diffusion-compact spherical hole model

The mechanical effect of grouting is manifested in two aspects (Vesić *et al.*, 2021): one is the reaming effect of the grouting hole under the grouting pressure P_k; the other is the diffusion effect of the grout in the formation under the seepage pressure P_j. Assuming that P_w is the pore water pressure, the final reaming radius is r_0. The slurry diffusion radius is r_c, and slurry seepage field is shown in Fig. 1.

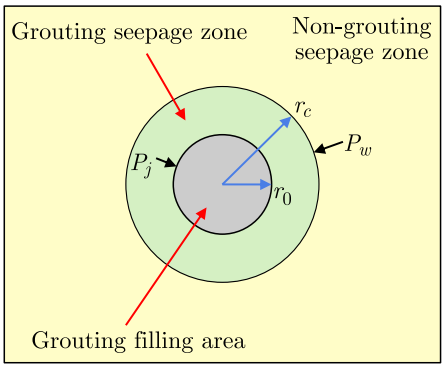

Fig. 1. Seepage field of slurry diffusion

When P_k is small, the soil around the hole has only elastic deformation. When P_k reaches a certain value, the soil will produce plastic deformation, forming a grouting seepage plastic zone. If P_k continues to increase, the plastic zone radius will exceed the slurry diffusion radius to form a plastic zone without grouting seepage. To this end, the analytical model shown in Fig. 2 has been established. It has been assumed that the in-situ stress is P_0, and the plastic zone radius is r_p. When $r_c < r_p$, the plastic zone of the surrounding rock is divided into two regions, namely the grouting seepage plastic zone and the non-grouting seepage plastic zone, which is defined as a small diffusion radius model. When $r_c > r_p$, the plastic zone is the grouting seepage plastic zone, which can be considered as $r_c = r_p$ and defined as the large diffusion radius model.

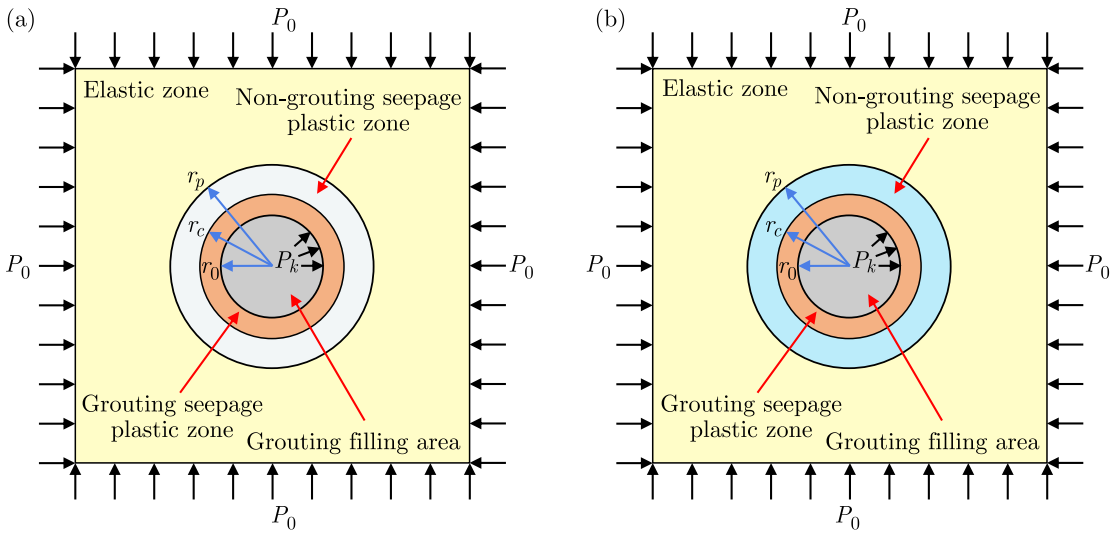

Fig. 2. Coupling model of grouting considering the reaming-diffusion effect: (a) small diffusion radius model, (b) large diffusion radius model

For convenience in analysis, the following assumptions are made:

(1) The stratum is regarded as isotropic and compressible, the compressibility of the slurry is ignored, and the influence of self-weight is not considered;

(2) The slurry diffusion mode is hemispherical diffusion, and the diffusion process follows Darcy's law;
(3) The change of formation permeability during the diffusion process and the influence of slurry diffusion on formation properties are ignored.

3. Analytical solutions of the coupled effect of expansion and diffusion during grouting

3.1. Basic formula

Stress and strain take pressure as positive and tension as negative, considering the influence of grouting seepage and pore water pressure. The spherically symmetric equilibrium differential equation can be uniformly expressed as

$$\frac{\mathrm{d}\sigma_r}{\mathrm{d}r} + 2\frac{\sigma_r - \sigma_\theta}{r} + \frac{\mathrm{d}P_f}{\mathrm{d}r} = 0 \tag{3.1}$$

where σ_r and σ_θ are stresses in the radial and circumferential directions, and P_f is fluid pressure.

The geometric equation is

$$\varepsilon_r = -\frac{\mathrm{d}u_r}{\mathrm{d}r} \qquad \varepsilon_\theta = -\frac{u_r}{r} \tag{3.2}$$

where ε_r and θ are strains in the radial and circumferential directions, u_r is radial displacement.

Using the above equation, the spherically symmetric strain coordination equation can be obtained

$$\frac{\mathrm{d}\varepsilon_\theta}{\mathrm{d}r} + \frac{\varepsilon_\theta - \varepsilon_r}{r} = 0 \tag{3.3}$$

Generalized Hooke's law of spherically symmetric problems is used in the elastic region, i.e.

$$\varepsilon_r = -\frac{\sigma_r - 2\nu\sigma_\theta}{E} \qquad \varepsilon_\theta = -\frac{(1-\nu)\sigma_\theta - \nu\sigma_r}{E} \tag{3.4}$$

where E is elastic Young's modulus, and ν is Poisson's ratio.

In the spherically symmetric model, the hoop stress is equal everywhere, and the stress state is the same as that of the pseudo-triaxial test of the rock. Assuming that the formation yielding behavior satisfies the Mohr-Coulomb criterion, it can be expressed as

$$\sigma_\theta = M\sigma_r + \sigma_0 \tag{3.5}$$

where $M = (1+\sin\theta)/(1-\sin\theta)$, $\sigma_0 = 2c\cos\theta/(1-\sin\theta)$, θ is the internal friction angle, c is cohesion.

The dynamic equilibrium is satisfied at the grouting seepage boundary, that is, differential pressure $\Delta P = P_{gm}\big|_{r=r_c} - P_w = 0$. The seepage boundary condition is

$$P_f\Big|_{r=r_0} = P_j \qquad P_f\Big|_{r=r_c} = P_w \qquad P_f\Big|_{r=\infty} = 0 \tag{3.6}$$

The stable seepage equation (Vesić, 1972) is

$$\frac{\partial^2}{P_f}\partial r^2 + \frac{2}{r}\frac{\partial P_f}{\partial r} = 0 \tag{3.7}$$

Solving the above equation and using boundary condition Eq. (3.6), we can get

$$P_f = \begin{cases} \dfrac{r_0 r_c(P_j - P_w)}{(r_c - r_0)r} + \dfrac{r_c P_w - r_0 P_j}{r_c - r_0} & \text{for} \quad r_0 < r < r_c \\ \dfrac{r_c P_w}{r} & \text{for} \quad r > r_c \end{cases} \tag{3.8}$$

3.2. Solution of the spherical hole model with small diffusion radius for grouting

3.2.1. Elastic zone

Let $\sigma_r = \Phi/r$, by substituting it into Eq. (3.1), we can obtain $\sigma_\theta = [\mathrm{d}\Phi/\mathrm{d}r + (\Phi - k_0)/r]/2$, where k is an intermediate constant that can be eliminated later. Substituting Eq. (3.4) into Eq. (3.3) and substituting $\sigma_r = \Phi/r$, $\sigma + \theta = [\mathrm{d}\Phi/\mathrm{d}r + (\Phi - k_0)/r]/2$ into the resulting expression, the control equation of stress definite solution can be obtained as

$$r^2\frac{\mathrm{d}^2\Phi}{\mathrm{d}r^2} + 2r\frac{\mathrm{d}\Phi}{\mathrm{d}r} - 2\Phi = 0 \tag{3.9}$$

Using Eq. (3.9), the general solution of elastic stress can be obtained as

$$\sigma_r = k_1\frac{1}{r^3} + k_2 \qquad \sigma_\theta = -\frac{1}{2}\frac{k_1}{r^3} + k_2 \tag{3.10}$$

where k_1 and k_2 can be determined by the stress boundary conditions.

Assume that the radial stress of the elastic-plastic boundary is P_{yg}, by using $\sigma_r\big|_{r=r_p} = P_{yg}$, $\sigma_r\big|_{r\to\infty} = P_0$, the stress solutions in the elastic zone are available

$$\sigma_{rse} = (P_{yg} - P_0)\Big(\frac{r_p}{r}\Big)^3 + P_0 \qquad \sigma_{\theta se} = -\frac{1}{2}(P_{yg} - P_0)\Big(\frac{r_p}{r}\Big)^3 + P_0 \tag{3.11}$$

By substituting Eqs. (3.11) and $r = r_p$ into Eq. (3.5), the radial stress of the elastic-plastic boundary can be obtained as

$$P_{yg} = \frac{3MP_0 + 2\sigma_0}{2 + M} \tag{3.12}$$

By substituting Eqs. (3.11) into Eq. (3.4) and subtracting the strain generated by the in-situ stress $\varepsilon_0 = P_0(1 - 2\nu)/E$, and then substituting the resulting expression into Eq. (3.2), the displacement solution of elastic zone can be obtained

$$u_{rse} = -(\varepsilon_\theta - \varepsilon_0)r = \frac{r}{4G}(P_{yg} - P_0)\Big(\frac{r_p}{r}\Big)^3 \tag{3.13}$$

3.2.2. Plastic zone

(1) Non-grouting seepage plastic zone

By substituting Eq. (3.5) and the second expression of Eq. (3.8) into Eq. (3.1), and using the boundary condition $\sigma_r\big|_{r=r_p} = P_{yg}$, the stresses in the non-grouting seepage plastic zone can be obtained as

$$\begin{aligned}
\sigma_{rsp} &= \Big(P_{yg} - \frac{r_cP_w}{r_p(1-2M)} + \frac{\sigma_0}{M-1}\Big)\Big(\frac{r}{r_p}\Big)^{2(M-1)} + \frac{r_cP_w}{(1-2M)r} - \frac{\sigma_0}{M-1} \\
\sigma_{\theta sp} &= M\Big(P_{yg} - \frac{r_cP_w}{r_p(1-2M)} + \frac{\sigma_0}{M-1}\Big)\Big(\frac{r}{r_p}\Big)^{2(M-1)} + \frac{Mr_cP_w}{(1-2M)r} - \frac{\sigma_0}{M-1}
\end{aligned} \tag{3.14}$$

At the grouting seepage boundary, the radial stress is

$$\sigma_{rsp}\Big|_{r=r_c} = \Big(P_{yg} - \frac{r_cP_w}{r_p(1-2M)} + \frac{\sigma_0}{M-1}\Big)\Big(\frac{r_c}{r_p}\Big)^{2(M-1)} + \frac{P_w}{1-2M} - \frac{\sigma_0}{M-1} \tag{3.15}$$

Using the associated flow criteria

$$\mathrm{d}\varepsilon_{ij}^p = \mathrm{d}\lambda\frac{\partial f}{\partial\sigma_{ij}} \tag{3.16}$$

where ε_{ij}^{p} is the plastic strain tensor, substituting Eq. (3.5) into Eqs. (3.14), we can get

$$\mathrm{d}\varepsilon_r^p = \mathrm{d}\lambda\frac{\partial f}{\partial\sigma_r} = \mathrm{d}\lambda \qquad \mathrm{d}\varepsilon_\theta^p = \mathrm{d}\lambda\frac{\partial f}{\partial\sigma_\theta} = -M\mathrm{d}\lambda \tag{3.17}$$

It can be obtained from the above equation

$$\frac{\mathrm{d}\varepsilon_r^p}{\mathrm{d}\varepsilon_\theta^p} = -\frac{1}{M} \tag{3.18}$$

The strain relationship in the plastic zone is

$$\varepsilon_r = \varepsilon_r^e + \varepsilon_r^p \qquad \varepsilon_\theta = \varepsilon_\theta^e + \varepsilon_\theta^p \tag{3.19}$$

Substituting Eqs. (3.18) and (3.18) into Eq. (3.3), one gets

$$\frac{\mathrm{d}\varepsilon_\theta^p}{\mathrm{d}r} + \Big(1+\frac{1}{M}\Big)\frac{\varepsilon_\theta^p}{r} + \frac{\varepsilon_\theta^e - \varepsilon_r^e}{r} + \frac{\mathrm{d}\varepsilon_\theta^e}{\mathrm{d}r} = 0 \tag{3.20}$$

Substituting Eqs. (3.14) into Eq. (3.4), the elastic strain in the plastic zone is

$$\begin{aligned}
\varepsilon_{rsp}^e &= \frac{2\nu M-1}{E}\left(\Big(P_{yg} - \frac{r_c P_w}{r_p(1-2M)} + \frac{\sigma_0}{M-1}\Big)\Big(\frac{r}{r_p}\Big)^{2(M-1)} + \frac{r_c P_w}{(1-2M)r}\right) \\
&\quad + \frac{(1-2\nu)\sigma_0}{E(M-1)} \\
\varepsilon_{\theta sp}^e &= \frac{\nu-(1-\nu)M}{E}\left(\Big(P_{yg} - \frac{r_c P_w}{r_p(1-2M)} + \frac{\sigma_0}{M-1}\Big)\Big(\frac{r}{r_p}\Big)^{2(M-1)} + \frac{r_c P_w}{(1-2M)r}\right) \\
&\quad + \frac{(1-2\nu)\sigma_0}{E(M-1)}
\end{aligned} \tag{3.21}$$

Substituting Eqs. (3.21) into Eq. (3.20) and using the boundary condition $\varepsilon_{\theta sp}^{p}\big|_{r=r_p} = 0$, the circumferential plastic strain can be written as

$$\begin{aligned}
\varepsilon_{\theta sp}^p &= -\frac{M(1+2M)(1-M)(1-\nu)}{2M^2-M+1}\Big(P_{yg} - \frac{r_c P_w}{r_p(1-2M)} + \frac{\sigma_0}{M-1}\Big)\Big(\frac{r}{r_p}\Big)^{2(M-1)} \\
&\quad - \frac{M(1-2\nu M)r_c P_w}{(1-2M)r} + \frac{M(1-2\nu M)r_c P_w}{(1-2M)r_p}\Big(\frac{r_p}{r}\Big)^{1+\frac{1}{M}} \\
&\quad + \frac{M(1+2M)(1-M)(1-\nu)}{2M^2-M+1}\Big(P_{yg} - \frac{r_c P_w}{r_p(1-2M)} + \frac{\sigma_0}{M-1}\Big)\Big(\frac{r_p}{r}\Big)^{1+\frac{1}{M}}
\end{aligned} \tag{3.22}$$

Using Eq. (3.22), the plastic strain at the junction of the two plastic regions can be obtained

$$\begin{aligned}
\varepsilon_{\theta sp}^p\Big|_{r=r_c} &= -\frac{M(1+2M)(1-M)(1-\nu)}{2M^2-M+1}\Big(P_{yg} - \frac{r_c P_w}{r_p(1-2M)} + \frac{\sigma_0}{M-1}\Big)\Big(\frac{r_c}{r_p}\Big)^{2(M-1)} \\
&\quad - \frac{M(1-2\nu M)P_w}{1-2M} + \frac{M(1-2\nu M)P_w}{1-2M}\Big(\frac{r_p}{r_c}\Big)^{\frac{1}{M}} \\
&\quad + \frac{M(1+2M)(1-M)(1-\nu)}{2M^2-M+1}\Big(P_{yg} - \frac{r_c P_w}{r_p(1-2M)} + \frac{\sigma_0}{M-1}\Big)\Big(\frac{r_p}{r_c}\Big)^{1+\frac{1}{M}}
\end{aligned} \tag{3.23}$$

Similar to Eq. (3.13), combining Eqs. (3.2), (3.19), (3.21) and (3.22), the displacement solution of non-grouting seepage plastic zone can be obtained

$$u_{rsp} = -(\varepsilon_\theta - \varepsilon_0)r \tag{3.24}$$

(2) Grouting seepage plastic zone

By substituting Eq. (3.5) and the first expression of Eq. (3.8) into Eq. (3.1) and using boundary condition Eq. (3.15), the stresses in the grouting seepage plastic zone can be obtained as

$$\begin{aligned}\sigma_{rsg} &= \Big(P_{yg} - \frac{r_c P_w}{r_p(1-2M)} + \frac{\sigma_0}{M-1}\Big)\Big(\frac{r}{r_p}\Big)^{2(M-1)} \\ &\quad + \Big(\frac{P_w}{1-2M} - \frac{r_0(P_j-P_w)}{(1-2M)(r_c-r_0)}\Big)\Big(\frac{r}{r_c}\Big)^{2(M-1)} + \frac{r_0 r_c(P_j-P_w)}{(r_c-r_0)(1-2M)r} - \frac{\sigma_0}{M-1} \\ \sigma_{\theta sg} &= M\Big(P_{yg} - \frac{r_c P_w}{r_p(1-2M)} + \frac{\sigma_0}{M-1}\Big)\Big(\frac{r}{r_p}\Big)^{2(M-1)} \\ &\quad + M\Big(\frac{P_w}{1-2M} - \frac{r_0(P_j-P_w)}{(1-2M)(r_c-r_0)}\Big)\Big(\frac{r}{r_c}\Big)^{2(M-1)} + \frac{M r_0 r_c(P_j-P_w)}{(r_c-r_0)(1-2M)r} - \frac{\sigma_0}{M-1}\end{aligned} \tag{3.25}$$

Substituting Eqs. (3.25) into Eq. (2.4), the elastic strain in the plastic zone is obtained as

$$\begin{aligned}\varepsilon^e_{rsg} &= \frac{2\nu M-1}{E}\Bigg(\Big(P_{yg} - \frac{r_c P_w}{r_p(1-2M)} + \frac{\sigma_0}{M-1}\Big)\Big(\frac{r}{r_p}\Big)^{2(M-1)} + \frac{r_0 r_c(P_j-P_w)}{(r_c-r_0)(1-2M)r} \\ &\quad + \Big(\frac{P_w}{1-2M} - \frac{r_0(P_j-P_w)}{(1-2M)(r_c-r_0)}\Big)\Big(\frac{r}{r_c}\Big)^{2(M-1)}\Bigg) + \frac{(1-2\nu)\sigma_0}{E(M-1)} \\ \varepsilon^e_{\theta sg} &= \frac{\nu-(1-\nu)M}{E}\Bigg(\Big(P_{yg} - \frac{r_c P_w}{r_p(1-2M)} + \frac{\sigma_0}{M-1}\Big)\Big(\frac{r}{r_p}\Big)^{2(M-1)} + \frac{r_0 r_c(P_j-P_w)}{(r_c-r_0)(1-2M)r} \\ &\quad + \Big(\frac{P_w}{1-2M} - \frac{r_0(P_j-P_w)}{(1-2M)(r_c-r_0)}\Big)\Big(\frac{r}{r_c}\Big)^{2(M-1)}\Bigg) + \frac{(1-2\nu)\sigma_0}{E(M-1)}\end{aligned} \tag{3.26}$$

Substituting Eq. (3.26) into Eq. (3.20) and using the boundary condition $\varepsilon^p_{\theta sg}\big|_{r=r_c} = \varepsilon^p_{\theta sp}\big|_{r=r_c}$, i.e. Eq. (3.23), the circumferential plastic strain can be written as

$$\begin{aligned}\varepsilon^p_{\theta sg} &= \frac{M(1+2M)(1-M)(1-\nu)}{2M^2-M+1}\Bigg[\Big(P_{yg} - \frac{r_c P_w}{r_p(1-2M)} \\ &\quad + \frac{\sigma_0}{M-1}\Big)\Bigg(\Big(\frac{r_p}{r}\Big)^{1+\frac{1}{M}} - \Big(\frac{r}{r_p}\Big)^{2(M-1)}\Bigg) \\ &\quad + \Big(\frac{P_w}{1-2M} - \frac{r_0(P_j-P_w)}{(1-2M)(r_c-r_0)}\Big)\Bigg(\Big(\frac{r_c}{r}\Big)^{1+\frac{1}{M}} - \Big(\frac{r}{r_c}\Big)^{2(M-1)}\Bigg)\Bigg] \\ &\quad - \frac{M(1-2\nu M)r_0 r_c(P_j-P_w)}{(r_c-r_0)(1-2M)r} \\ &\quad + \frac{M(1-2\nu M)}{1-2M}\Bigg(P_w\Big(\frac{r_p}{r_c}\Big)^{\frac{1}{M}} - P_w + \frac{r_0(P_j-P_w)}{(r_c-r_0)}\Bigg)\Big(\frac{r_c}{r}\Big)^{1+\frac{1}{M}}\end{aligned} \tag{3.27}$$

Similar to Eq. (3.13), using Eqs. (3.2), (3.19), (3.26) and (3.27), the relative displacement can be obtained as

$$u_{rsg} = -(\varepsilon_\theta - \varepsilon_0)r \tag{3.28}$$

When the injected stratum is sandy soil or a soft stratum with similar physical properties to sandy soil, the diffusion radius considering the displacement effect can be calculated by the following equation (Ye *et al.*, 2022)

$$r_c = r_0 + r_c' = 3\frac{tK(P_k - P_w)}{\phi[(\mu_g - \mu_w)r_c' + \mu_w l_w]} \tag{3.29}$$

where r_c' is diffusion radius under displacement, μ_g, μ_w are slurry viscosity and groundwater viscosity, K is permeability, ϕ is soil porosity, P_w is groundwater pressure at l_w, t is grouting time, r_0 is reaming radius.

3.3. Grouting compaction-solution of the spherical hole model with a large diffusion radius

At this time, there is only a grouting seepage plastic zone in the plastic zone of the surrounding rock. It can be considered that $r_c = r_p$, then the stress boundary condition is

$$\sigma_r\Big|_{r=r_0} = P_k \tag{3.30}$$

Similar to the above derivation, the stress solution in the plastic zone can be obtained

$$\begin{aligned}
\sigma_{rg} &= \Big(P_k - \frac{r_0 r_c(P_j - P_w)}{r_0(r_c - r_0)(1-2M)} + \frac{\sigma_0}{M-1}\Big)\Big(\frac{r}{r_0}\Big)^{2(M-1)} + \frac{r_0 r_c(P_j - P_w)}{(r_c - r_0)(1-2M)r} - \frac{\sigma_0}{M-1} \\
\sigma_{\theta lg} &= M\Big(P_k - \frac{r_0 r_c(P_j - P_w)}{r_0(r_c - r_0)(1-2M)} + \frac{\sigma_0}{M-1}\Big)\Big(\frac{r}{r_0}\Big)^{2(M-1)} + \frac{M r_0 r_c(P_j - P_w r)}{(r_c - r_0)(1-2M)r} - \frac{\sigma_0}{M-1}
\end{aligned} \tag{3.31}$$

And the plastic zone strain solution can be expressed as

$$\begin{aligned}
\varepsilon_{rlg}^e &= \frac{2\nu M - 1}{E}\Bigg(\Big(P_k - \frac{r_c(P_j - P_w)}{(r_c - r_0)(1-2M)} + \frac{\sigma_0}{M-1}\Big)\Big(\frac{r}{r_0}\Big)^{2(M-1)} \\
&\quad + \frac{r_0 r_c(P_j - P_w)}{(r_c - r_0)(1-2M)r}\Bigg) + \frac{(1-2\nu)\sigma_0}{E(M-1)} \\
\varepsilon_{\theta lg}^e &= \frac{\nu - (1-\nu)M}{E}\Bigg(\Big(P_k - \frac{r_c(P_j - P_w)}{(r_c - r_0)(1-2M)} + \frac{\sigma_0}{M-1}\Big)\Big(\frac{r}{r_0}\Big)^{2(M-1)} \\
&\quad + \frac{r_0 r_c(P_j - P_w)}{(r_c - r_0)(1-2M)r}\Bigg) + \frac{(1-2\nu)\sigma_0}{E(M-1)} \\
\varepsilon_{\theta lg}^p &= -\frac{M(1+2M)(1-M)(1-\nu)}{2M^2 - M + 1}\Big(P_k - \frac{r_c(P_j - P_w)}{(r_c - r_0)(1-2M)} + \frac{\sigma_0}{M-1}\Big)\Big(\frac{r}{r_0}\Big)^{2(M-1)} \\
&\quad - \frac{M(1-2\nu M)r_0 r_c(P_j - P_w)}{(r_c - r_0)(1-2M)r} + \frac{M(1-2\nu M)r_0(P_j - P_w)}{(r_c - r_0)(1-2M)}\Big(\frac{r_c}{r}\Big)^{1+\frac{1}{M}} \\
&\quad + \frac{M(1+2M)(1-M)(1-\nu)}{2M^2 - M + 1}\Big(P_k - \frac{r_c(P_j - P_w)}{(r_c - r_0)(1-2M)} + \frac{\sigma_0}{M-1}\Big)\Big(\frac{r_c}{r_0}\Big)^{2(M-1)}\Big(\frac{r_c}{r}\Big)^{1+\frac{1}{M}}
\end{aligned} \tag{3.32}$$

Similar to Eq. (3.13), using Eqs. (3.2), (3.19) and (3.32), the displacement solution can be obtained

$$u_{rlg} = -(\varepsilon_\theta - \varepsilon_0)r \tag{3.33}$$

4. Model discussion

4.1. Large diffusion radius model

Taking the physical and mechanical parameters of the formation as shown in Table 1, the relationship between the reaming radius and the plastic zone radius is analyzed.

Table 1. Physical and mechanical parameters of strata

Elastic Young's modulus E [MPa]	Diffusion radius r_c [m]	Porosity K	Poisson's ratio μ	Initial geostress P_0 [kPa]	Internal friction angle θ [°]	Cohesion c [kPa]	Initial grouting radius r_k [m]
26	1.33	0.3	0.3	100	25	20	0.1

Figure 3 shows the relationship between the reaming radius and the plastic zone radius obtained by using the model in this paper when P_j is 0 kPa, 30 kPa and 50 kPa. The calculation results of the model have a similar change trend to the results of Mei *et al.* (2017), but the upward trend of the results in this paper is relatively slow and the value is small. This is because the results of Mei *et al.* (2017) only consider the effect of the lower grout seepage on the plastic zone of the surrounding rock. In fact, in the grouting diffusion stage, the grout has penetrated and diffused into the formation, which has a strengthening effect on the formation, which reduces the plastic zone of the surrounding rock. The larger P_j is, the smaller the plastic radius is, and the slurry has a certain improvement on the surrounding rock during the diffusion stage.

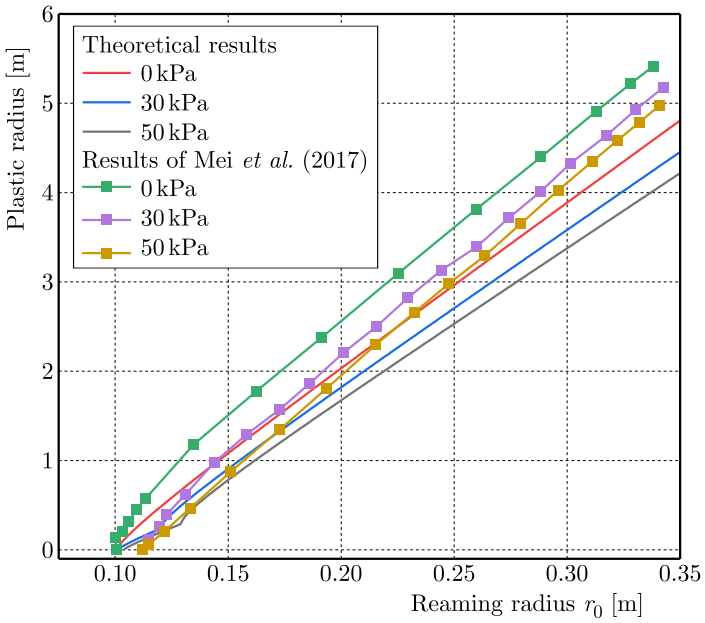

Fig. 3. Comparison of the theoretical calculation of seepage diffusion in grouting with Mei *et al.* (2017)

Figure 4a shows the relationship between the reaming pressure and the reaming radius. It can be seen that the reaming pressure increases rapidly in the range of the reaming radius of 0 m-1 m, and the slurry diffusion has a certain influence on the reaming pressure. When P_j is 0 kPa, 30 kPa and 50 kPa, respectively, the reaming pressure is stable at 4.38 MPa, 4.22 MPa and 4.1 MPa. Figure 4b shows the effect of the reaming radius r_0 on r_p/r_0. The plastic zone radius increases with an increase in reaming radius. It increases rapidly at the beginning of reaming, then the growth trend is slow, and finally reaches a steady state. r_p/r_0 finally stabilized between 15 and 17, while increasing P_j would make the ratio decrease.

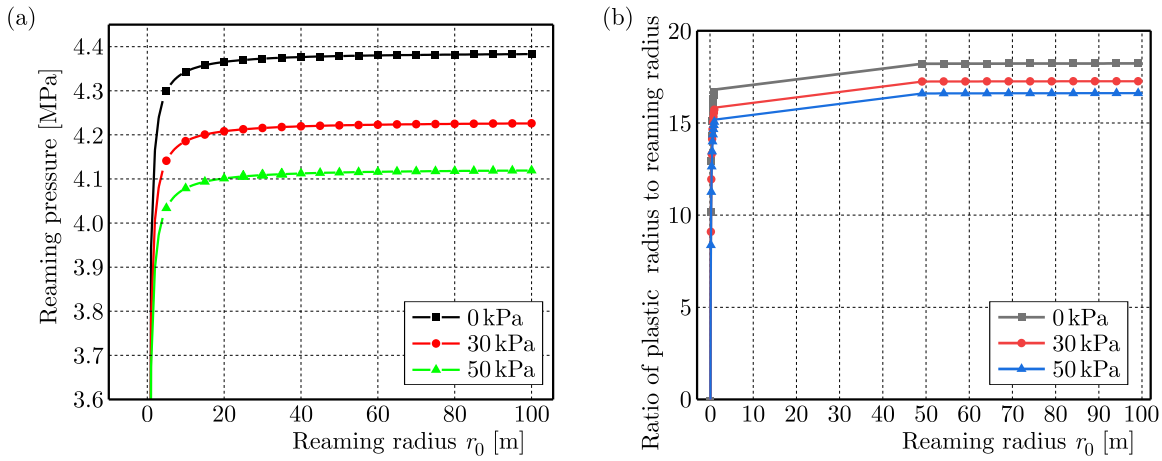

Fig. 4. (a) Expansion pressure curve and (b) influence of reaming on the ratio of plastic zone radius

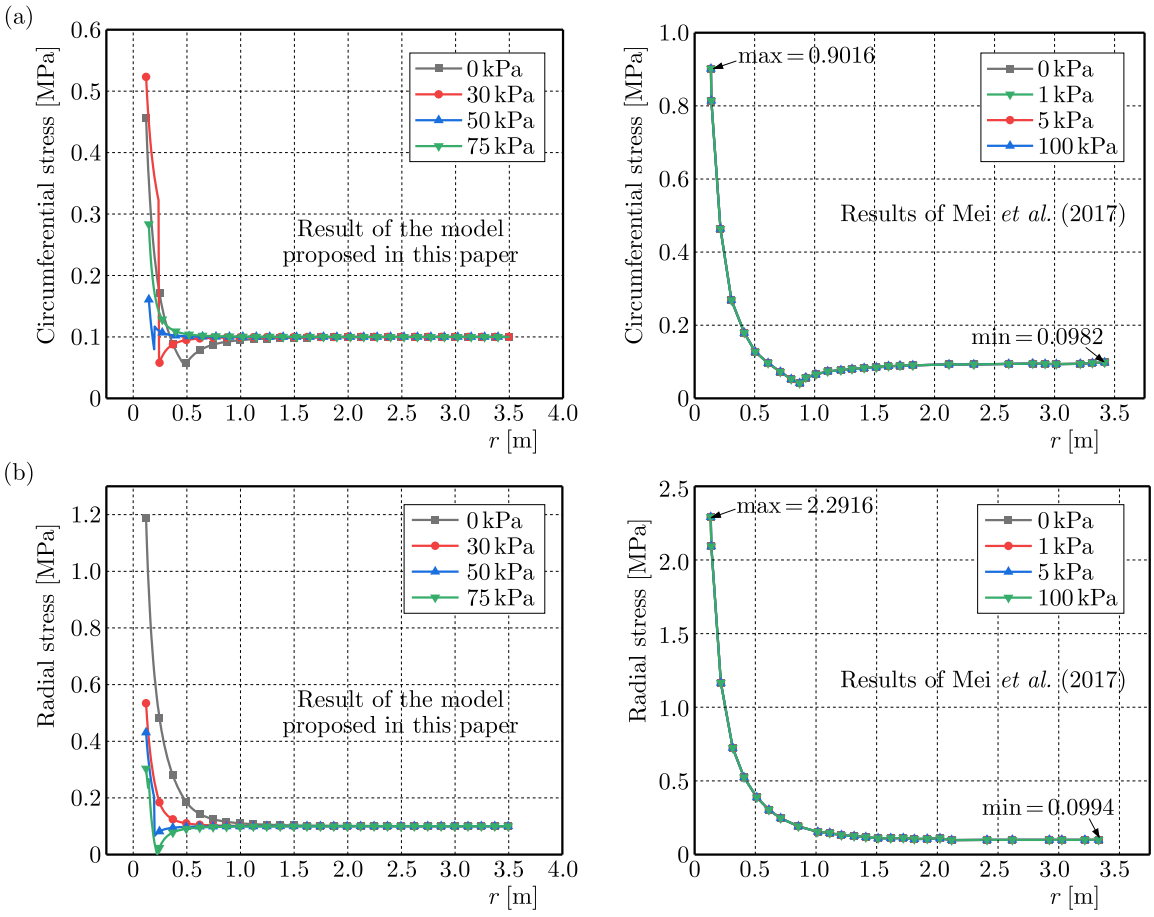

Fig. 5. Stress distribution curve along the radial direction without considering the displacement effect: (a) circumferential stress, (b) radial stress

Figure 5 shows the stress evolution law under different grouting infiltration pressures in the hole when the reaming radius $r_0 = 0.12$ m. The larger the P_j, the smaller the plastic zone. When the P_j increases from 0 to 75 kPa, the radius of the plastic zone decreases from 0.48 m to 0.143 m. This is because after the slurry penetrates and diffuses, it has a certain reinforcement effect on the soil, so that the plastic zone of the surrounding rock is reduced to a certain extent in the compaction stage. Compared with the literature (Mei *et al.*, 2017), it is found that the

two change trends are consistent, but after considering the grouting diffusion stage, the stress in the plastic zone of the surrounding rock decreases compared with the stage without considering the slurry diffusion, and the stress reaches the minimum value at the radius of the plastic zone. Therefore, the slurry diffusion has some influence on the grouting compaction stage.

4.2. Small diffusion radius model

If the displacement effect is not considered, the diffusion radius is only related to the permeability. If the displacement effect is considered, there are many factors affecting the permeability radius, and the grouting pressure will also affect the permeability radius. In the following analysis, the displacement effect is considered, and the calculation parameters at $l_w = 5\,\text{m}$ are selected, as shown in Table 2, and the formation-related parameters are shown in Table 1. Using the formula in Section 3, it can be obtained that when $P_j = 0\,\text{kPa}$, $r_c = 5.45\,\text{m}$; when $P_j = 30\,\text{kPa}$, $r_c = 5.66\,\text{m}$; when $P_j = 50\,\text{kPa}$, $r_c = 5.66\,\text{m}$.

Table 2. Grouting calculation parameters considering displacement effect

Water pressure P_w [MPa]	Porosity ϕ	Water viscosity μ_w [Pa·s]	Grouting time t [s]	Slurry viscosity μ_g [Pa·s]	Permeability coefficient m [cm/s]	Initial grouting radius r_k [m]	Grouting time [min]
0.05	0.3	0.00101	3000	0.0047	0.03	0.1	50

Figure 6 shows the effect of the reaming radius on plastic radius under the displacement effect. The grouting plastic zone is still nonlinear, and the non-grouting plastic zone is greatly affected by the grouting pressure. The greater the grouting pressure, the greater the penetration radius. With an increase in the reaming radius, the ratio of the plastic zone radius to the reaming radius finally approaches a constant, and this constant gradually decreases with an increase in the grouting pressure. This is because when the grouting pressure is constant, with an increase in the grouting osmotic pressure, the volume of the grout entering the soil increases, and the disturbed zone of the surrounding rock continuously expands, resulting in an increase in the radius of the plastic zone. When the reaming radius reaches a certain value, the plastic radius tends to be stable, and the smaller P_j is, the sooner it tends to be stable, which is relatively consistent with the actual situation of grouting.

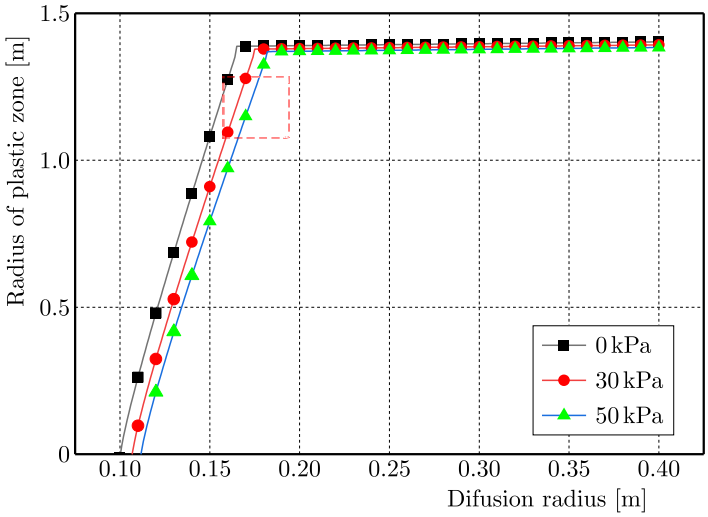

Fig. 6. Effect of grounting diffusion on plastic radius under the displacement effect

Comparing Figs. 4b and 6, it can be seen that when the displacement effect is not considered, the grouting pressure has little effect on the radius of the plastic zone and cannot play a decisive role. When the displacement effect of groundwater and grout is considered, the reaming radius and the plastic zone radius in the non-grouting plastic zone show a nonlinear relationship. With a gradual increase of the reaming radius, the radius of the plastic zone shows a trend of rapid growth at first, and then a slow growth. At the same time, with an increase in the grouting pressure, the radius of plastic zone does not have a large gap, so the grouting pressure does not play a decisive role in the change of the radius of the plastic zone.

5. Conclusion

Considering the slurry diffusion and slurry displacement effect in the grouting compaction stage, a diffusion-compaction model of shield backfill grouting was established. The stress and displacement fields of spherical hole expansion problem considering the coupling effect of reaming and diffusion in grouting process were established. The main conclusions are as follows:

- When the displacement effect of groundwater and grouting slurry is considered, the surrounding rock stress is the same as when only the slurry diffusion is considered, but the displacement of the plastic zone is significantly reduced, and the stress has a minimum point, which corresponds to the radius of the plastic zone.
- The grouting pressure and reaming radius have influence on the radius of plastic zone during the seepage and diffusion of slurry. The larger P_j is, the smaller the plastic radius is, and the larger the cavity expansion radius is, the larger the radius of plastic zone is. When the cavity expansion radius reaches a certain value, the plastic radius tends to be stable, and the smaller P_j is, the sooner it tends to be stable, which is relatively consistent with the actual situation of shield backfill grouting.
- The groundwater flow is more complex. In order to facilitate the analysis, this paper simplifies the groundwater to laminar flow and does not consider turbulence. Therefore, further research on this issue should be conducted in the future.

Acknowledgements
This work was supported by Shandong Provincial Natural Science Foundation (No. ZR2023ME086).

References

1. Bezuijen A., Talmon A., 2004, Grout pressures around a tunnel lining, influence of grout consolidation and loading on lining, *Tunnelling. a Decade of Progress. GeoDelft 1995-2005*, 109-114
2. Bezuijen A., Talmon A., Kaalberg F.J., Plugge R., 2004, Field measurements of grout pressures during tunnelling of the Sophia Rail Tunnel, *Soils and Foundations*, **44**, 1, 39-48.
3. Boschi K., Di Prisco C.G., Ciantia M.O., 2020, Micromechanical investigation of grouting in soils, *International Journal of Solids and Structures*, **187**, 121-132
4. El-Kelesh Adel M., Matsui T., 2012, Effect of soil and grouting parameters on the effectiveness of compaction grouting, *Grouting and Ground Treatment*, 1056-1070
5. Epel T., Mooney M.A., Gutierrez M., 2021, The influence of face and shield annulus pressure on tunnel liner load development, *Tunnelling and Underground Space Technology*, **117**, 104096
6. Han X., Liang X., Ye F., Wang X., Chen Z., 2022, Statistics and construction methods for deep TBM tunnels with high geostress: A case study of Qinling Tunnel in Hanjiang-Weihe River Diversion Project, *Engineering Failure Analysis*, **138**, 106301

7. Khetwal A., Rostami J.I., Nelson P., 2020, Investigating the impact of TBM downtimes on utilization factor based on sensitivity analysis, *Tunnelling and Underground Space Technology*, **106**, 103586
8. Li L., Xiang Z.-C., Zou J.-F., Wang F., 2019, An improved model of compaction grouting considering three-dimensional shearing failure and its engineering application, *Geomechanics and Engineering*, **19**, 3, 217
9. Li S., Pan D., Xu Z., Lin P., Zhang Y., 2020, Numerical simulation of dynamic water grouting using quick-setting slurry in rock fracture: the Sequential Diffusion and Solidification (SDS) method, *Computers and Geotechnics*, **122**, 103497
10. Liu J., Li P., Shi L., Fan J., Kou X., Huang D., 2021, Spatial distribution model of the filling and diffusion pressure of synchronous grouting in a quasi-rectangular shield and its experimental verification, *Underground Space*, **6**, 6, 650-664
11. Mei B.X., Yang M., Jia S.H., 2017, Mohr-Coulomb criterion-based theoretical solutions of spherical cavity expansion considering seepage (in Chinese), *Journal of Tongji University (Natural Science)*, **45**, 3, 309-316
12. Mu W., Li L., Yang T., Yu G., Han Y., 2019, Numerical investigation on a grouting mechanism with slurry-rock coupling and shear displacement in a single rough fracture, *Bulletin of Engineering Geology and the Environment*, **78**, 8, 6159-6177
13. Nishimura S., Takehana K., Morikawa Y., Takahashi H., 2011, Experimental study of stress changes due to compaction grouting, *Soils and Foundations*, **51**, 6, 1037-1049
14. Pachen H., Meijers P., Korff M., Maertens J., 2005, Effect of compaction grouting in loosely packed sand on density, *Stand Alone*, **0**, 1241-1244
15. Shrivastava N., Zen K., Shukla S.K., 2017, Modeling of compaction grouting technique with development of cylindrical cavity expansion problem in a finite medium, *International Journal of Geosynthetics and Ground Engineering*, **3**, 4, 40
16. Shukla M., Gottumukkala B., Nagabhushana M.N., Chandra S., Shaw A., Das S., 2021, Design and evaluation of mechanical properties of cement grouted bituminous mixes (CGBM), *Construction and Building Materials*, **269**, 121805
17. Vesić A.S., 1972, Expansion of cavities in infinite soil mass, *Journal of the Soil Mechanics and Foundations Division*, **98**, 3, 265-290
18. Wang D., Xing X., Qu H., Zhang L.M., 2015, Simulated radial expansion and heave caused by compaction grouting in noncohesive soils, *International Journal of Geomechanics*, **15**, 4, 04014069
19. Wang L., Zheng G., 2022, Numerical evaluation of the upheave and soil arching associated with compaction grouting in shield tunneling and loading process, *Tunnelling and Underground Space Technology*, **128**, 104664
20. Wu Y., Zhao C., Zhao C., Liu F., Zhang J., 2022, Modeling of compaction grouting considering the soil unloading effect, *International Journal of Geomechanics*, **22**, 6, 04022061
21. Xu X., Wu Z., Sun H., Weng L., Chu Z., Liu Q., 2021, An extended numerical manifold method for simulation of grouting reinforcement in deep rock tunnels, *Tunnelling and Underground Space Technology*, **115**, 104020
22. Ye F., Qin N., Liang X., Han X.B., Han X., 2022, Microscopic model analysis of shield tunnel backfill grouting based on displacement effect (in Chinese), *Journal of Southwest Jiaotong University*, **57**, 2, 339-345
23. Zhou Z., Wang K., Feng H., Tian Y., Zhu S., 2021, Centrifugal model test of post-grouting pile group in loess area, *Soil Dynamics and Earthquake Engineering*, **151**, 106985

Manuscript received September 21, 2023; accepted for print Marcn 11, 2024

INFORMATION FOR AUTHORS

Journal of Theoretical and Applied Mechanics (***JTAM***) is devoted to all aspects of solid mechanics, fluid mechanics, thermodynamics and applied problems of structural mechanics, mechatronics, biomechanics and robotics. Both theoretical and experimental papers as well as survey papers can be proposed.

JTAM accepts full-text articles (max. 12 pages) as well as the short communications with all the requirements concerning standard publications, except a volume that is limited to 4 pages.

We accept articles in English only. The text of JTAM paper should not exceed 12 pages of standard format A4 (11-point type size, standard margins – 2.5 cm, single line spacing) including abstract, figures, tables and references.

The material for publication should be sent to the Editorial Office via electronic journal system: http://www.editorialsystem.com/jtam

Papers are accepted for publication after the review process. Blind review model is applied, which means that the reviewers' names are kept confidential to the authors. Reviewer(s) declare that there is no interpersonal relation with the author(s) that would affect the opinion and recommendation of the article for publication in JTAM. The final decision on paper acceptance belongs to the Editorial Board.

Starting from January 1, 2020, the Publisher of *Journal of Theoretical and Applied Mechanics* introduces a fee for published articles.

This applies only to papers submitted after this date and accepted by the Editorial Board for publication.

A payment of 700 EUR will be a condition for commencing the editorial procedure for upcoming articles.

After qualifying your paper for publication we will require LaTeX or TeX or Word document file and figures.

The best preferred form of figures are files obtained by making use of editorial environments employing vector graphics.

Requirements for paper preparation

Contents of the manuscripts should appear in the following order:

- Title of the paper.
- Authors' full name, affiliation and e-mail.
- Short abstract (maximum 100 words) and 3-5 key words (1 line).
- Article text (equations should be numbered separately in each section; each reference should be cited in the text by the last name(s) of the author(s) and the publication year).
- References (maximum 25) in alphabetical order.
- Titles of references originally published not in English, should be translated into English.

All the data should be reported in SI units.